Studying the Effects of Galactic and Extragalactic Foregrounds on Cosmic Microwave Background Observations

Maximilian Henri Abitbol

Submitted in partial fulfillment of the
requirements for the degree of
Doctor of Philosophy
in the Graduate School of Arts and Sciences

COLUMBIA UNIVERSITY

2018

ABSTRACT

Studying the Effects of Galactic and Extragalactic Foregrounds on Cosmic Microwave Background Observations

Maximilian Henri Abitbol

Cosmic microwave background observations have been fundamental in forming the standard model of cosmology. Ongoing and upcoming cosmic microwave background experiments aim to confirm this model and push the boundaries of our knowledge to the very first moments of the Universe. Non-cosmological microwave radiation from the Galaxy and beyond, called foregrounds, obscures and contaminates these measurements. Understanding the sources and effects of foregrounds and removing their imprint in cosmic microwave background observations is a major obstacle to making cosmological inferences. This thesis contains my work studying these foregrounds. First, I will present observations of a well-known but poorly understood foreground called anomalous microwave emission. Second, I will present results forecasting the capability of a next-generation satellite experiment to detect cosmic microwave background spectral distortions in the presence of foregrounds. Third, I will present results studying the effect of foregrounds on the cosmic microwave background self-calibration method, which allows experiments to calibrate the telescope polarization angle using the cosmic microwave background itself. Fourth, I will present my analysis characterizing the performance of and producing maps for the E and B Experiment. Fifth, I will present my research contributions to the readout system that used in the laboratory to operate kinetic inductance detectors, which are being developed for cosmic microwave background observations. Lastly, I will conclude with future prospects in the field of foregrounds and cosmic microwave background cosmology.

Contents

List of Figures

List of Tables

Acknowledgments

The completion of this thesis would not have been possible without the support and encouragement of my friends and family. I would like to thank my advisor, Brad Johnson, for his ideas and guidance throughout my graduate education. I would also like to give my sincerest thanks to Jens Chluba, Joy Didier, Colin Hill, Glenn Jones, Michele Limon, Heather McCarrick, and Amber Miller for all of their help, work, perseverance, and insight that has helped me grow as a physicist and as a person.

Overview

This thesis contains my work on several different research projects all related to the cosmic microwave background (CMB). My research focuses on enabling measurements of the CMB in various ways, focusing on the problem of non-cosmological foreground signals obscuring our view of the CMB. The thesis is divided into three parts: i) Science Introduction and Motivation, ii) CMB Foreground Research, and iii) Experimental CMB Research. Part I of the thesis serves to introduce the field of CMB cosmology and motivate the research in my thesis. Part II of the thesis contains my work related to CMB foregrounds including observations, forecasting, and analysis methods. Part III of the thesis contains my work on CMB data analysis and hardware development. The thesis is outlined as follows.

Part I Science Introduction and Motivation

- Chapter 1 of the thesis reviews the state of the field of CMB science. I introduce the main concepts and scientific motivation behind the research in this thesis.
- Chapter 2 presents an overview of CMB foregrounds, which contaminate our observations. Much of my research is focused on the impact of foregrounds on CMB observations.

Part II CMB Foreground Research

- Chapter 3 presents observations and analysis of data acquired using the Green Bank Telescope of a region with anomalous microwave emission. This chapter was accepted for publication in The Astrophysical Journal, 2018 [6] and reproduced by permission of the American Astronomical Society.

- Chapter 4 presents forecasts for the capability of future space-based CMB satellite missions to measure spectral distortions of the CMB blackbody due to energy releases in the early Universe. This chapter was published in the Monthly Notices of the Royal Astronomical Society, 471:1126-1140, October 2017 [5], by Oxford University Press on behalf of the Royal Astronomical Society.

- Chapter 5 presents research studying the effect of foregrounds on the self-calibration technique for CMB polarization experiments. This chapter was published in the Monthly Notices of the Royal Astronomical Society, 457:1796-1803, April 2016 [3], by Oxford University Press on behalf of the Royal Astronomical Society.

Part III Experimental CMB Research

- Chapter 6 presents my research in CMB data analysis for the E and B Experiment (EBEX). I worked on detector noise estimation and map-making for EBEX. Part of these results were published in The EBEX Collaboration et al. [300].

- Chapter 7 summarizes my laboratory research for CMB Microwave Kinetic Inductance Detector (MKID) readout. I worked on part of the readout electronics and associated software to operate the MKIDs that are being developed by the Columbia Experimental Cosmology Group. This work contributed to these publications: McCarrick et al. [199], Johnson et al. [158], Flanigan et al. [110, 109], Johnson et al. [159], Jones et al. [160], McCarrick et al. [200].

- Chapter 8 contains the conclusion and future prospects.

Part I

Science Introduction and Motivation

Chapter 1

The Cosmic Microwave Background

The cosmic microwave background (CMB) is remnant radiation from the beginning of the Universe. Observations of the CMB have uncovered a vast amount of cosmological information and solidified the Hot Big Bang model of cosmology. The existence of the CMB was first proposed in the 1940s by George Gamow, Ralph Alpher, and Robert Herman [14, 13, 116] and confirmed with observations by Arno Penzias and Robert Wilson in 1965 [221]. Since then, properties of the CMB have been characterized by a variety of experiments and revealed that the large-scale properties of the Universe can be described by a six parameter cosmological model [139, 238]. In particular, the CMB was observed to be nearly isotropic blackbody radiation in 1990 by the Cosmic Background Explorer (COBE) satellite, implying that the entire Universe was once in thermal equilibrium [192]. The Far-InfraRed Absolute Spectrometer (FIRAS) instrument on COBE found that the current CMB temperature is $T = 2.725 \pm 0.002$ K [108, 106]. Distortions from a blackbody spectrum have not yet been detected but would give us insight into the thermal history of the Universe beginning at the earliest moments [284, 286, 285]. The Differential Microwave Radiometer (DMR) instrument on COBE detected the first hints of anisotropies in the CMB [174], which were later confirmed and studied extensively by an array of experiments, in particular the Wilkinson Microwave Anisotropy Probe (WMAP) and *Planck* satellites [29, 239].

These anisotropies contain imprints of the initial conditions of the Universe and allow us to measure precisely the six parameters that dictate the evolution of the Universe [238, 2]. Ongoing and upcoming experimental efforts are focused primarily on measuring the polarization of the CMB in order to constrain inflationary model that describe the first moments the Universe [4, 32, 127, 104, 301, 115]. Experiments are also targeting late-time features in the CMB that are imprinted by galaxy clusters and weak gravitational lensing of the CMB by large-scale structure [209, 170]. In the future, CMB experiments could aim to revisit the measurement of the CMB energy spectrum, constraining thermal processes during recombination and studying the thermodynamic properties of matter at late times [176, 178].

In this chapter I aim to motivate the research in my thesis by introducing the scientific background and goals of the field of CMB cosmology. I begin by reviewing the state of CMB cosmology and introduce how observations of the CMB are used to constrain cosmological models and estimate cosmological parameters. I will then summarize current efforts to measure the imprint of primordial gravitational waves from inflation on the polarization of the CMB. I will end by introducing spectral distortions of the CMB and the cosmological implications for detecting these features.

1.1 Overview of CMB Cosmology

The Universe is observed to be flat, homogeneous, isotropic, and expanding [29, 239]. We can determine the evolution of the Universe using the Friedmann-Lemaître-Robertson-Walker (FLRW) metric and Einstein's equation for a perfect fluid, resulting in the Friedmann equations [305]. The FLRW metric is given by,

$$ds^2 = -dt^2 + a^2(t)(dx^2 + dy^2 + dz^2)\,, \tag{1.1}$$

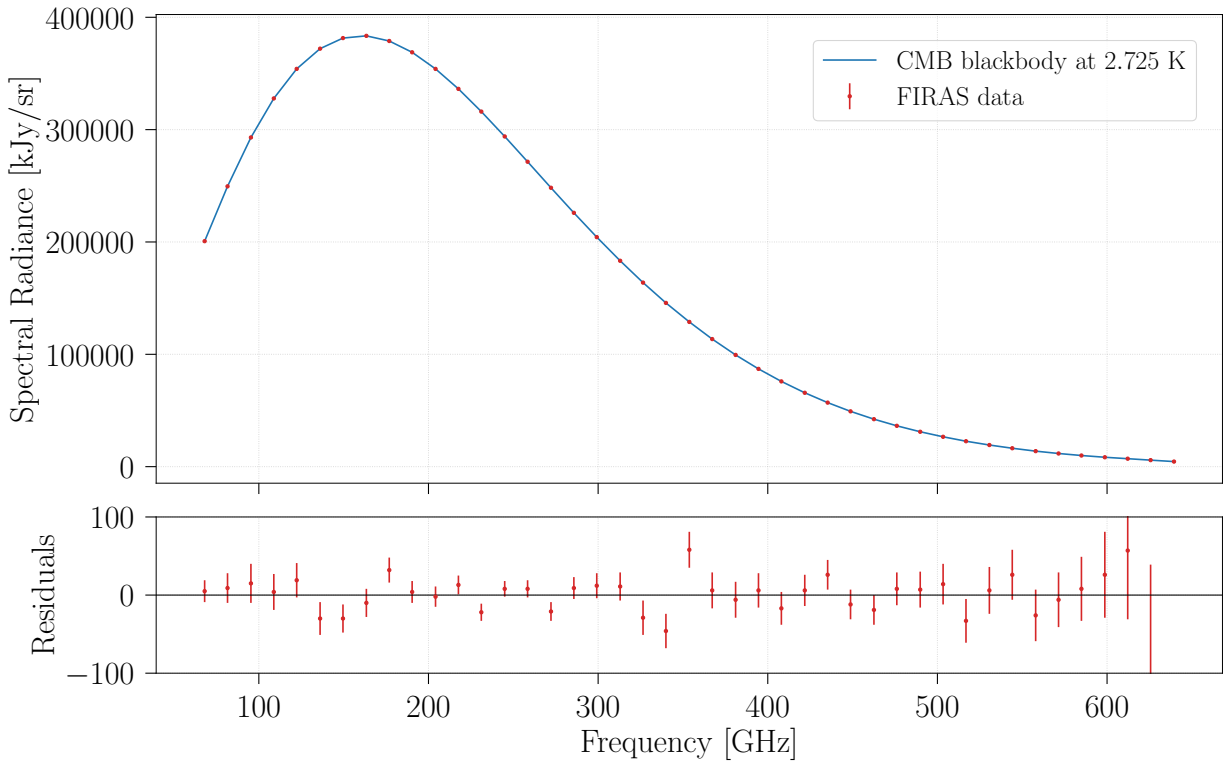

Figure 1.1: CMB blackbody spectrum as determined by COBE FIRAS. The CMB temperature is 2.725 K. The residuals are plotted below to show the size of the uncertainties. Deviations from a blackbody are limited to 1 part in 10^5.

where $a(t)$ is the scale factor that describes the expansion of the Universe. The Friedmann equations are,

$$H^2 = \frac{8\pi G}{3} \sum_i \rho_i \tag{1.2}$$

and

$$\frac{\ddot{a}}{a} = -\frac{4\pi G}{3} \sum_i \left(\rho_i + \frac{3P_i}{c^2} \right) \tag{1.3}$$

where $H = \frac{1}{a}\frac{da}{dt}$ is the Hubble parameter as a function of time, ρ is the energy density, P is the pressure, and the index i labels the constituents of cold dark matter, baryons, radiation, or the cosmological constant (I have excluded the potential for curvature here and in the metric for simplicity). The quantities ρ and P are related by the appropriate equation of state for each constituent. The equation of state for a perfect fluid is generally parameterized

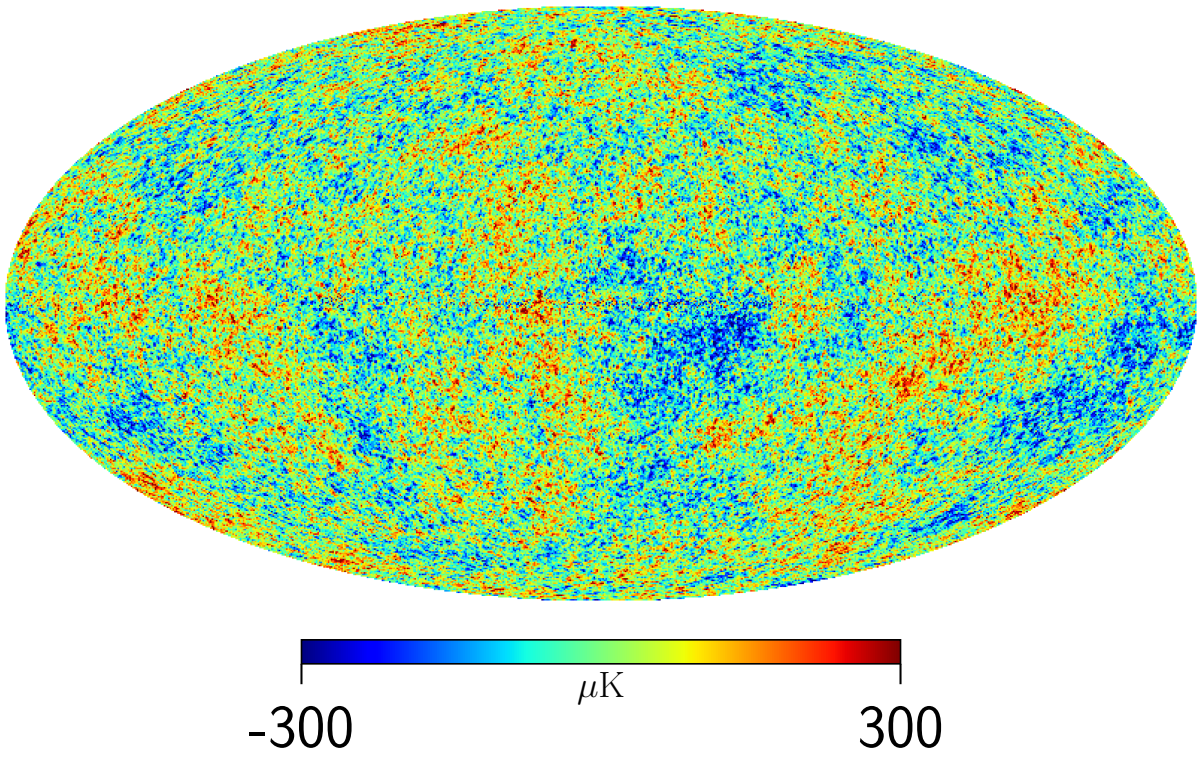

Figure 1.2: CMB temperature anisotropies map as measured by *Planck*. The resolution of the map is $5'$.

as,

$$w = \frac{\rho}{P}\,, \tag{1.4}$$

where $w = 0$ for dark and baryonic matter, $w = 1/3$ for relativistic particles, and $w = -1$ for the cosmological constant. These equations can be combined to relate the Hubble parameter and the constituent densities,

$$\left(\frac{H}{H_0}\right)^2 = \frac{\Omega_c + \Omega_b}{a^3} + \frac{\Omega_r}{a^4} + \Omega_\Lambda\,, \tag{1.5}$$

where Ω_i is the fractional energy density evaluated today of the respective constituents. These densities are part of the six parameter cosmological model and can be measured by observations of the CMB, as we discuss later.

The history of the universe as we know it begins with a rapid expansion from inflation

and the production of photons and elementary particles during reheating [89]. At this time matter and CMB photons were tightly coupled and in thermal equilibrium. As the Universe expanded and cooled, hadrons formed during nucleosynthesis and eventually protons combined with electrons to produce the first atoms (mostly hydrogen, helium and their isotopes) during recombination. The CMB energy spectrum at recombination was a thermal blackbody at around 3000 K. CMB photons stream relatively freely after recombination and carry in imprint of the primordial Universe as it was at 380,000 years old. This imprint from end of recombination and the beginning of free-streaming photons is called the surface of last scattering. The Universe continued to expand and cool and today we observe a CMB blackbody spectrum at a temperature of 2.725 K.

The CMB is nearly isotropic however small fluctuations exist, carrying an imprint of a variety of cosmological processes with them. These anisotropies occur on many different angular scales and the spatial distribution of the CMB intensity and polarization anisotropies can be studied to reveal cosmological information. The anisotropies trace both the initial conditions of perturbations on the largest scales and the ensuing time evolution of these perturbations all the way down to the formation of structure and galaxy clusters. Anisotropies in the CMB are typically broken into primary and secondary anisotropies, referring to whether they occurred at early or late cosmological times. The primary anisotropies are from perturbations in the initial conditions in the universe. Secondary anisotropies come mainly from the epoch of reionization and interactions with massive galaxy clusters at late times. Observationally, the way we can study these perturbations is by measuring spatial anisotropies in the CMB sky in intensity and polarization and studying the distribution of these features as a function of angular scale.

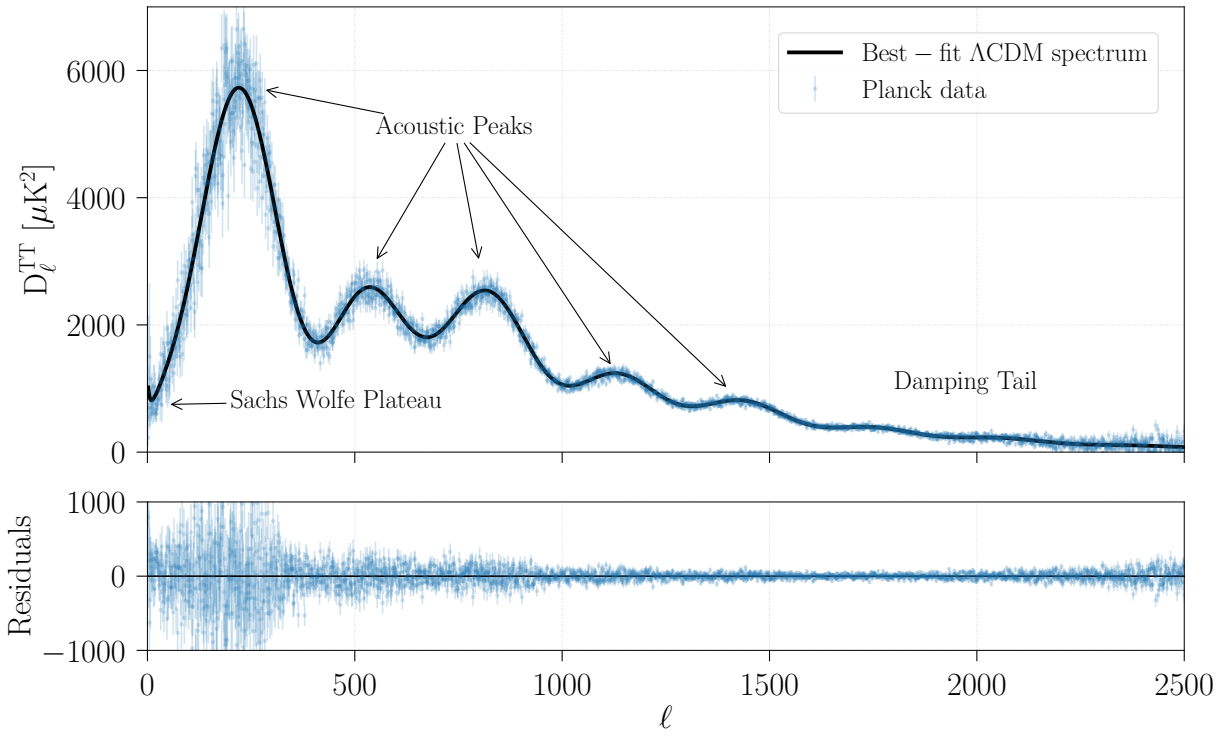

Figure 1.3: CMB TT power spectrum as measured by *Planck*. The solid black curve represents the best-fit ΛCDM model. The model residuals are plotted below.

1.2 CMB Temperature Anisotropies

To infer cosmological parameters from CMB anisotropies, the CMB sky is projected onto spherical harmonics, and spatial correlations in the CMB are calculated by taking the angular power spectrum of temperature fluctuations, defined as C_ℓ^{TT} [89]. The power spectra are then related to predicted models. We can relate C_ℓ^{TT} to the distribution and evolution of primordial density fluctuations. The calculation of the CMB angular power spectrum as it relates to cosmological parameters was developed in a series of publications; in particular Bond and Efstathiou [37], Hu et al. [148], Hu and Sugiyama [144], Kosowsky [180], Seljak and Zaldarriaga [268], Hu and White [145], Kamionkowski et al. [162], Zaldarriaga and Seljak [312], Seljak and Zaldarriaga [269]. For a review of these calculations see Hu et al. [149], Scott and Smoot [266], Bucher [42], Challinor [50], Hu and Dodelson [141], Zaldarriaga [311]. The cosmological power spectrum calculation is done numerically using the widely ac-

cepted CMBFAST, CAMB, and CLASS codes [313, 186, 187]. To understand qualitatively how the CMB power spectrum relates to cosmological parameters we present a brief summary of how this is done. We begin by introducing perturbations in the initial distribution of energy densities on the FRWL metric for the background cosmology (we will follow the notation in Dodelson [89] for the following equations). For a scalar density fluctuation the perturbed metric can be written as (in the conformal Newtonian gauge),

$$ds^2 = a^2(\eta)[-(1+2\Psi)d\eta^2 + (1-2\Phi)dx^2] \tag{1.6}$$

where $\eta = \int_0^t dt'/a(t')$ is the conformal time (or the comoving distance that light has traveled) and Ψ and Φ describe the primordial scalar fluctuations. In the Newtonian limit $\Psi = -\Phi$. We will see that the distribution of these fluctuations is directly measured in the CMB power spectrum. The source of the perturbations is the topic of current research, which will be discussed in the next section. The current paradigm is that quantum fluctuations from inflation evolved into these perturbations. The evolution of Ψ and Φ is calculated assuming linear perturbation theory and using Einstein's equation and the Friedmann equations. The Boltzmann equation is then used to calculate the interactions between photons, dark matter, baryons, and neutrinos [89].

The Boltzmann equation for photons is solved in two limits, the tight-coupling or free-streaming limit, corresponding to the times before and after recombination and the surface of last scattering. Let us examine the tight-coupling solution (before recombination and the surface of last scattering), which in Fourier space can be reduced to,

$$\ddot{\Theta}_0 + \frac{\dot{a}}{a}\frac{R}{1+R}\dot{\Theta}_0 + k^2 c_s^2 \Theta_0 = \frac{-k^2}{3}\Psi - \frac{\dot{a}}{a}\frac{R}{1+R}\dot{\Phi} - \ddot{\Phi}\,, \tag{1.7}$$

where $\Theta = \frac{\Delta T}{T}$ describes the fluctuations in the CMB. The speed of sound in the plasma is $c_s^2 = 1/3(1+R)$, $R = \frac{3\rho_b}{4\rho_\gamma}$ is the ratio of the equilibrium baryon to photon densities, and k describes the Fourier wavelength. The terms on the left of Equation 1.7 describe a damped

harmonic oscillator with independent modes and the terms on the right are interpreted as a forcing term. This produces the acoustic oscillations that are ultimately observed in the CMB power spectrum. In the free-streaming limit, the Boltzmann equation can be integrated and rearranged into, now in configuration space,

$$\Theta(\vec{x}_0, \hat{p}, \eta_0) = [\Theta_0 + \Psi]\,(\vec{x}(\eta_R), \eta_R) + \int_0^{\eta_0} d\eta\,[\Psi' - \Phi']\,(\vec{x}(\eta), \eta) e^{-\tau} + [\hat{p} \cdot \vec{v}_b]\,\vec{x}(\eta_R), \eta_R) + \dots . \tag{1.8}$$

Here Θ_0 is the local monopole of the temperature anisotropy, η_R is the time of recombination, τ is the optical depth, $\hat{p}$ is photon propagation direction, and $\vec{v}_b$ is the baryon velocity. The additional terms are independent of $\hat{p}$ and depend on the local quadrupole of the temperature field and the monopole and quadrupole of the polarization field. The first term on the right of Equation 1.8 is the term from primordial gravitational fluctuations called the Sachs-Wolfe Effect [261]. The second term involving derivatives of the potential is the integrated Sachs-Wolfe effect and the last term is the Doppler effect. We will describe these effects qualitatively later on.

To relate the time evolution equations with the initial conditions of scalar perturbations we can calculate the angular power spectrum of the CMB,

$$C_\ell^{TT} = \frac{2}{\pi} \int_0^\infty dk k^2 \mathcal{P}_\Phi(k) \left| \frac{\Theta_\ell(k)}{\delta(k)} \right|^2 . \tag{1.9}$$

C_ℓ^{TT} is the quantity that is measured by observations of the CMB and this relation allows us to estimate cosmological parameters. In Equation 1.9, $\mathcal{P}_\Phi(k)$ describes the initial conditions of scalar perturbations. Θ_ℓ is the ℓ-th multipole moment of the temperature field, calculated by projecting Θ onto the Legendre polynomial of order ℓ,

$$\Theta_\ell = \frac{1}{(-i)^\ell} \int_{-1}^{1} \frac{d\mu}{2} \mathcal{P}_\ell(\mu) \Theta(\mu) \tag{1.10}$$

The initial conditions of the perturbations depends on the inflationary scenario and its statis-

tics are typically given by a power law with departures from scale-invariance parameterized by n_s,

$$\mathcal{P}_\Phi(k) = A_S \left(\frac{k}{k_*}\right)^{n_s - 1} . \tag{1.11}$$

For $n_s = 1$ the spectrum of perturbations is scale invariant, meaning the power in the flucutuations is the same at all wavelengths. Current observations show the spectrum is not scale invariant, with slightly more power on large scales than small scales. Departures from this power law spectrum have not been detected. This concludes the summary of calculations necessary to determine the CMB angular power spectrum and how the angular power spectrum is related to the cosmological parameters.

The standard cosmological model is currently described by six parameters for a spatially flat Universe with a power law spectrum of adiabatic scalar perturbations, as described above. From the perspective of CMB experiments, *Planck* has best constrained these parameters [238]. The six parameters are the baryon density ($\Omega_b h^2$), cold dark matter density ($\Omega_c h^2$), scalar spectral index (n_s), optical depth (τ), angular acoustic scale ($100\theta_*$), and amplitude of primordial perturbations (A_S). The latest (and final) *Planck* release has constrained these parameters to $\Omega_b h^2 = 0.02237 \pm 0.00015$, $\Omega_c h^2 = 0.1200 \pm 0.0012$, $n_s = 0.9649 \pm 0.0042$, $\tau = 0.0544 \pm 0.0073$, $100\theta_* = 1.04092 \pm 0.00031$, $\ln 10^{10} A_S = 3.044 \pm 0.014$ [238]. Additional model dependent late time parameters such as the Hubble constant (H_0) can be derived from these parameters. Further cosmological information can be determined with the use of external datasets such as baryon acoustic oscillation (BAO) observations. For example, the effective number of relativistic degrees of freedom (N_{eff}) and sum of neutrino masses ($\sum m_\nu$) can be measured.

We briefly provide a physical description of the source of CMB anisotropies and their effect on the CMB angular power spectrum. The temperature fluctuations are mainly sourced by three effects, the Sachs-Wolfe effect, acoustic oscillations, and Silk Damping.

The Sachs-Wolfe effect refers to the temperature fluctuations and gravitational redshifting on large scales at last scattering, as in the first term of Equation 1.8. Anisotropies on

Table 1.1: Cosmological parameters determined by *Planck*. The scalar-to-tensor ratio, r, is evaluated at a pivot scale $k_* = 0.002$ Mpc^{-1} and includes polarization data from BICEP. This is a 95% confidence upper bound.

Parameter	Value	Description
$\Omega_b h^2$	0.02237 ± 0.00015	baryon density
$\Omega_c h^2$	0.1200 ± 0.0012	cold dark matter density
n_s	0.9649 ± 0.0042	scalar spectral index
τ	0.0544 ± 0.0073	optical depth
$100\theta_*$	1.04092 ± 0.00031	angular acoustic scale
$\ln 10^{10} A_S$	3.044 ± 0.014	amplitude of primordial perturbations
$r_{0.002}$	< 0.064	Scalar-to-tensor ratio

scales larger than the horizon at last scattering have not evolved significantly and represent directly the initial conditions of the perturbations. In the CMB angular power spectrum this corresponds to anisotropies on scales larger than $\ell < 100$. For scale invariant density fluctuations this would lead to a flat spectrum at low ℓs, as in Figure 1.3. There is an additional effect, called the integrated Sachs-Wolfe effect, that occurs if there is a time dependence in the gravitational potentials, as in the second term in Equation 1.8. This effect is present on the largest scales in the CMB as the Universe became Dark Energy dominated at low redshifts.

On scales within the horizon at last scattering we see acoustic oscillations as gravity and radiation pressure produce competing forces on the initial perturbations, as described by Equation 1.7. In the temperature angular power spectrum these appear at $100 < \ell < 1000$. At that time, photons are tightly coupled with matter so as matter over-densities gravitationally attract, photons are dragged along as well. As the photon density increases with the matter density, the radiation pressure increases, which then repulsively forces away the matter, producing oscillations. After the Universe becomes neutral these oscillations freeze out, producing correlations on the scale of the horizon at last scattering. The main peak in the CMB occurs where the acoustic oscillations went through 1/4 of a cycle, corresponding to a maximum in a harmonic oscillator. The next peak (and all even numbered peaks) then

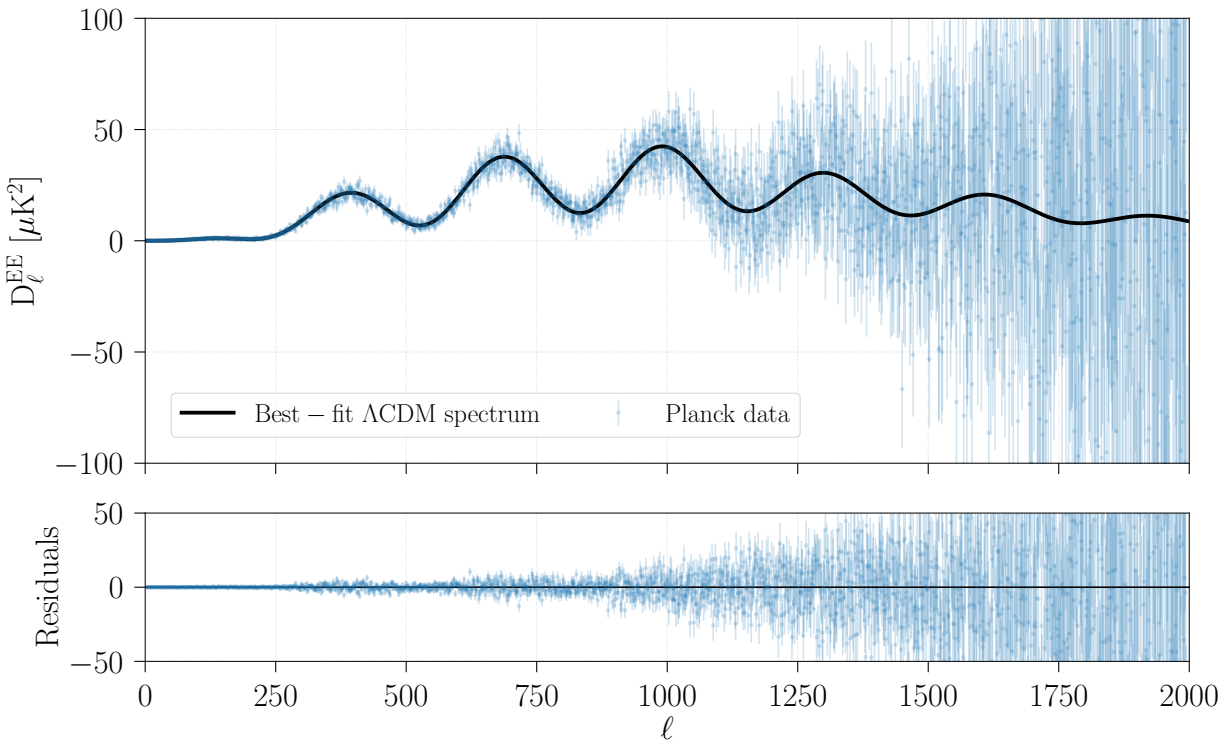

Figure 1.4: CMB *EE* power spectrum as measured by *Planck*. The solid black curve represents the best-fit ΛCDM model. The model residuals are plotted below. The peaks in the polarization spectrum are exactly out of phase with the peaks in the temperature spectrum (see Figure 1.3). Polarization is created by velocity gradients in the primordial plasma which will appear where there are troughs in the temperature spectrum.

correspond to maximal under-densities. In between the peaks, the troughs have non-zero power because they are at a velocity maximum. The velocity maxima produce a Doppler effect in the CMB, imparting back some energy into the photons, seen in the third term in Equation 1.8. When used in conjunction with BAO data, the location of the peaks can be used to determine the spatial flatness of the Universe.

On small scales, damping is evident in the oscillations. Silk Damping occurs at $\ell > 1000$ as the photons and baryons are not perfectly coupled [273]. Additionally, late time effects occur from gravitational lensing from non-linear structure growth at low redshifts and photon-electron interactions in galaxy clusters, called the Sunyaev-Zeldovich Effect [314, 287].

1.3 CMB Polarization Anisotropies

Current CMB experiments are focusing on measuring the polarization of the CMB to constrain inflationary scenarios. The intensity and polarization of the CMB is represented by I, Q, and U Stokes parameters (the CMB is not expected to be circularly polarized and therefor V is often not measured), where the Q and U maps describe the polarization. As with the temperature anisotropy maps, an angular power spectrum of the polarization data is calculated to enable cosmological inferences on CMB data. The angular power spectrum in polarization is split into two fields called E and B fields [162]. In real space both E and B are invariant under rotations. Under reflections, E is invariant (even parity) while B changes sign (odd parity). The E and B fields therefore represent "curl-free" and "curl-like" modes. Power spectra and cross spectra are calculated from the T, E, and B fields to allow for cosmological studies. We will drop the C_ℓ notation and call the angular power spectra by which fields are being correlated (e.g. TT for C_ℓ^{TT}). The TT, TE, EE, and BB spectra are generally the ones of cosmological interest. In standard cosmological scenarios the TB and EB spectra are zero (this will be important and revisited in Chapter 5).

The CMB becomes polarized by Thompson scattering during recombination and again during reioniziation. In both cases the polarization arises from an anisotropic CMB field incident on a free electron. In particular, a CMB photon field with a quadrupole moment incident on a free electron will generate linear polarization. These quadrupole moments in the CMB photons can be generated in two ways: (i) by density fluctuations that produce velocity gradients in the photon-baryon fluid and (ii) by a background of gravitational waves. These produce scalar and tensor perturbations respectively. The velocity gradients from scalar density perturbations produce only E-mode CMB polarization. The background of gravitational waves produces B-mode polarization in the CMB.

E-Mode Polarization

The peaks in the temperature angular power spectrum are due to the baryon-photon acoustic

oscillations in the recombination plasma. The temperature spectrum receives contributions from both the density perturbations and velocity gradients. The peaks in the E-mode polarization are due only to the velocity gradients. This results in sharp peaks in the EE angular power spectrum that are out of phase with the temperature peaks. Because the polarization is sourced mainly from velocity gradients in the field, the magnitude of the CMB polarization is significantly lower than the temperature anisotropies. The polarization measurements and EE spectrum provide an independent check on the cosmology separate from the TT spectrum, although most of the parameter constraints come from temperature since it is brighter.

B-Mode Polarization

The primary reason to measure polarization is to detect a stochastic background of gravitational waves generated by inflation. The amplitude of the gravitational waves is proportional to the Hubble constant during inflation which is related to the energy scale of inflation, which we will describe in the next section. As photons travel through a background of gravitational waves they are redshifted or blue shifted, depending on the relation between the photon propagation direction and the gravitational waves polarization and propagation direction. As a result, the gravitational waves produce a quadrupole anisotropy in the intensity of CMB field. Therefore, polarization is again generated by Thompson scattering of the CMB field with quadrupole anisotropy. The BB angular power spectrum generated by primordial gravitational waves peaks at $\ell = 100$ because gravitational waves with wavelengths longer than the photon mean free-path at decoupling cannot generate quadruples necessary for polarization. Gravitational waves decay when they enter the horizon and this limits the small-scale polarization. Density perturbation (scalar field) cannot generate B-mode polarization patterns in the CMB, so B-mode polarization on these scales is uniquely generated by primordial gravitational waves. The BB spectrum signal is plotted in Figure 1.5. This primordial B-mode signal from gravitational waves is currently being targeted by a variety of CMB experiments

.

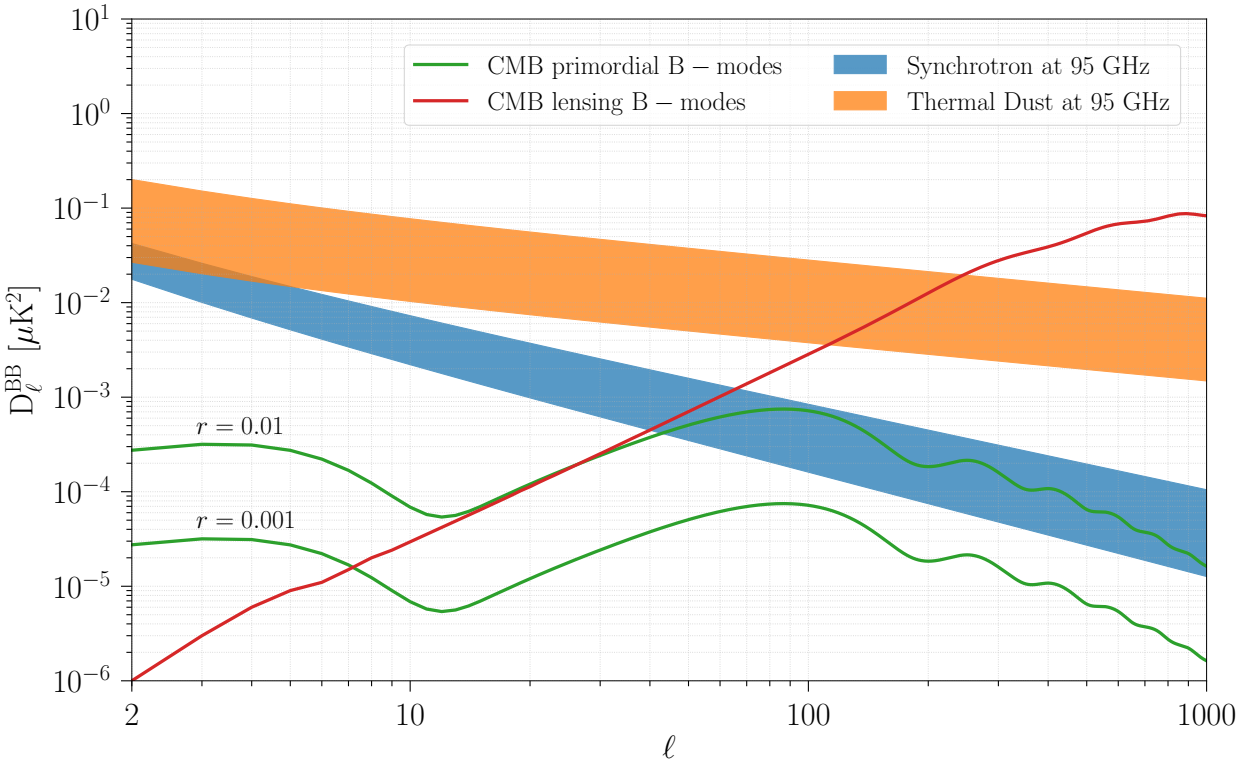

Figure 1.5: Expected BB signals including CMB primordial and lensing B-modes and synchrotron and thermal dust foregrounds.

1.3.1 Inflation

The current understanding of cosmology suffers from the fact that the Universe is extremely homogeneous without a mechanism to generate this property [166]. Inflation is the idea that the observable Universe was initially extremely small and exponentially expanded to produce the initial conditions of the Universe that we observer today [279, 124]. Specifically, inflation solves the "horizon", "flatness", and "monopole" problems and creates an initial spectrum of density fluctuations [165, 99, 190]. These density perturbations then grew into the Universe that we see today. In addition to scalar perturbations, many inflation scenarios lead to tensor perturbations as well. These tensor perturbations could be visible in the polarization of the CMB. The same method to derive the temperature anisotropies described previously is used

to calculate the primordial gravitational wave signal in the polarization spectrum.

The metric for tensor perturbations is [305],

$$ds^2 = -dt^2 + a^2(t)((1+h_+)dx^2 + (1-h_+)dy^2 + 2h_\times dxdy + dz^2)\,. \tag{1.12}$$

From this one can derive the equation for gravitational wave propagation,

$$\ddot{h_\alpha} + 2\frac{\dot{a}}{a}\dot{h_\alpha} + k^2 h_\alpha = 0\,, \tag{1.13}$$

where α denotes the $+$ or $\times$ gravitational wave polarizations. The power spectrum for primordial tensor (gravitational waves) perturbations is

$$\mathcal{P}_h(k) = A_T \left(\frac{k}{k_*}\right)^{n_T - 3}\,, \tag{1.14}$$

where k_* is usually taken to be 0.05 or 0.002 Mpc^{-1}. The scalar-to-tensor ratio is defined as,

$$r = \frac{A_T}{A_S}\,, \tag{1.15}$$

where A_S and A_T is the amplitude of scalar and tensor perturbations respectively. The scalar-to-tensor ratio can be directly measured by polarization measurements of the CMB. This ratio can then be related to the inflationary field parameters.

$$\left(\frac{r}{0.01}\right)^{1/4} \approx \frac{V^{1/4}}{10^{16} GeV}\,. \tag{1.16}$$

Planck and BICEP have constrained the scalar-to-tensor ratio to $r_{0.002} < 0.064$ [238].

The current state of CMB experiments is that we aim to measure the polarization spectrum well enough to characterize the BB power spectrum and therefore constrain inflation scenarios. A detection of r could provide strong evidence for inflation and solidify our understanding of the early Universe.

1.4 CMB Spectral Distortions

Spectral distortions of the CMB are deviations from a perfect blackbody spectrum created by energy releases in the early Universe. Measurements of CMB spectral distortions have implications for our understanding of physical processes taking place over a vast period in cosmological history [142, 64, 283, 292, 274, 56, 80]. Observations show that the CMB is a nearly perfect blackbody at $T_0 = 2.725 \pm 0.002\ K$. The only observed spectral distortion so far is from the anisotropic Sunyaev-Zeldovich (SZ) effect, from CMB scattering of hot electrons in galaxy clusters. All-sky spectral distortions produced by processes dating back to recombination are expected in the standard cosmological model and can reveal information about the thermal history of the Universe at early times [284, 316, 151, 74]. Future CMB experiments could more precisely measure the spectral energy density of the CMB in an effort to detect spectral distortions [176, 178, 58], as we will discuss in Chapter 4.

Spectral distortions are caused by energy or photon injection processes that affect the thermal equilibrium between matter and radiation [314, 286, 151, 43, 142, 64, 57]. There are two standard distortions which are called the Compton y distortion and the chemical potential μ distortion. The Compton y distortion is created by the inefficient transfer of energy between electrons and photons at redshifts $z < 5 \times 10^4$. In the standard model this distortion is produced by inverse-Compton scattering of photons and high-energy electrons during the epoch of reionization and structure formation [288, 147, 248, 138]. Chemical potential μ distortions are created much earlier on, at redshifts between $5 \times 10^4 < z < 2 \times 10^6$ [286, 142]. During this period, photons and matter are able to reach kinetic equilibrium, but photon production processes are unable to maintain full thermal equilibrium, producing a distribution with a chemical potential. A detection of the μ distortion would place tight constraints on the amplitude of the small-scale scalar perturbation power spectrum and rule out many alternative models of inflation, as well as provide new constraints on decaying particle scenarios [285, 73, 146, 67, 262, 100, 143, 55].

The CMB spectrum is a blackbody due to scattering processes which thermalize the

CMB with matter up to the time of last scattering. The thermalization process requires kinetic collisions to allow for energy transfer as well as photon producing processes (photon creation and annihilation) to change the photon number. The thermalization processes in the early Universe are Compton scattering, bremsstrahlung, and double Compton scattering and these must be efficient in order to maintain thermal equilibrium. Compton scattering involves kinetic collisions of photons and electrons,

$$e^- + \gamma \rightarrow e^- + \gamma \,. \tag{1.17}$$

Bremsstrahlung and double Compton scattering (inelastic scattering) are the photon producing processes given by,

$$e^- + X \rightarrow e^- + X + \gamma \tag{1.18}$$

$$e^- + \gamma \rightarrow e^- + \gamma + \gamma \tag{1.19}$$

Spectral distortions of the CMB are possible because each process becomes more or less efficient depending on the temperature of the Universe and densities of particles at that time. The balance of these mechanisms as a function of redshift produces separate stages of possible spectral distortion production.

In the very early universe, $z > 10^7$, both the photon production and kinetic equilibrium processes are efficient and thermalize any energy released into the baryon-photon plasma. After $z < 2 \times 10^6$, bremsstrahlung and double Compton scattering become inefficient at photon production, enabling spectral distortions to be created. Double Compton is the dominant photon production mechanism at this time because the bremsstrahlung interaction is dependent on the baryon density, which is small in the early Universe. Compton scattering is an efficient process and keeps baryons and photons in a kinetic equilibrium, producing a Maxwell distribution of photons and baryons with an equal temperature for both. Compton scattering conserves photon number, therefore any energy injection into the primordial plasma only changes the photon energy distribution as the electrons and photons

come to kinetic equilibrium. This can result in a Bose-Einstein distribution with a chemical potential when the photon production processes are inefficient, as photons are upscattered in energy and leave a deficiency of low energy photons with respect to a blackbody. At later times, $z < 1000$, Compton scattering becomes inefficient, while bremsstrahlung will maintain the low-energy photon population, allowing for a Compton y-distortion.

Chemical Potential μ-Distortion and Recombination Line Emission

During recombination but later than $z < 2 \times 10^6$, Compton scattering is efficient and can produce kinetic equilibrium. Double Compton scattering is the main photon production mechanism but can only provide low-energy photons. This results in a chemical potential μ-distortion if there is an energy release during this time. In the early universe, adiabatic cooling of the CMB produces a negative μ-distortion, while diffusion damping heats up the primordial plasma and creates a positive μ-distortion. Additional, non-standard cosmology sources are possible as well from unstable relic particles, primordial black holes, cosmic strings, or particle annihilation. The μ-distortion equation, relative to the CMB blackbody is given by,

$$\Delta I_\nu^\mu = I_o \frac{x^4 \mathrm{e}^x}{(\mathrm{e}^x - 1)^2} \left[\frac{1}{\beta} - \frac{1}{x} \right] \mu \,, \tag{1.20}$$

where μ is the amplitude of the distortion, $\beta \approx 2.1923$, $x = h\nu/kT_0$, and $I_o = (2h/c^2)\,(kT_0/h)^3 \approx 270\,\mathrm{M}Jy/sr$. The expected amplitude from Silk Damping is $\mu \approx 2 \times 10^{-8}$. An additional distortion comes from the hydrogen and helium recombination line spectrum as these elements are produced. Detection of the μ distortion would reveal information about the thermal history of the Universe dating back to $z \approx 2 \times 10^6$.

Compton y-Distortion

After recombination, $z \approx 1000$, Compton scattering does not reach full kinetic equilibrium and energy injection into CMB produces a y-distortion, similar to the SZ effect. Known energy release scenarios after this time include contributions from the intracluster medium

of galaxy groups and clusters, the intergalactic medium, and reionization. The y distortion equation is given by the standard SZ effect equation,

$$\Delta I_\nu^y = I_o \frac{x^4 \mathrm{e}^x}{\left(\mathrm{e}^x - 1\right)^2} \left[x \coth\left(\frac{x}{2}\right) - 4 \right] \, y \,, \tag{1.21}$$

where $y = 1.77 \times 10^{-6}$ is expected. An additional relativistic correction to it is given by,

$$\Delta I_\nu^{rel-SZ} = I_o \frac{x^4 \mathrm{e}^x}{\left(\mathrm{e}^x - 1\right)^2} \left\{ Y_1(x)\, \theta_\mathrm{e} + Y_2(x)\, \theta_\mathrm{e}^2 + Y_3(x)\, \theta_\mathrm{e}^3 + \left[Y_2(x)\, \theta_\mathrm{e}^2 + 3 Y_3(x)\, \theta_\mathrm{e}^3 \right] \, \omega_2^{eSZ} \right\} \, y \,, \tag{1.22}$$

where $\theta_\mathrm{e} = kT_\mathrm{eSZ}/m_e c^2$, $kT_\mathrm{eSZ} = 1.282$ keV and $\omega^{\mathrm{eSZ}_2} = 1.152$. The $Y_i(x)$ are obtained by an asymptotic expansion of the relativistic SZ signal. A measurement of the all-sky averaged relativistic and non-relativistic Compton y-distortion would constrain galaxy formation models and provide information on the total thermal energy of electrons in the Universe, as well as the electron temperature distribution and total baryon density at low redshifts. These signals are shown in Figure 1.6.

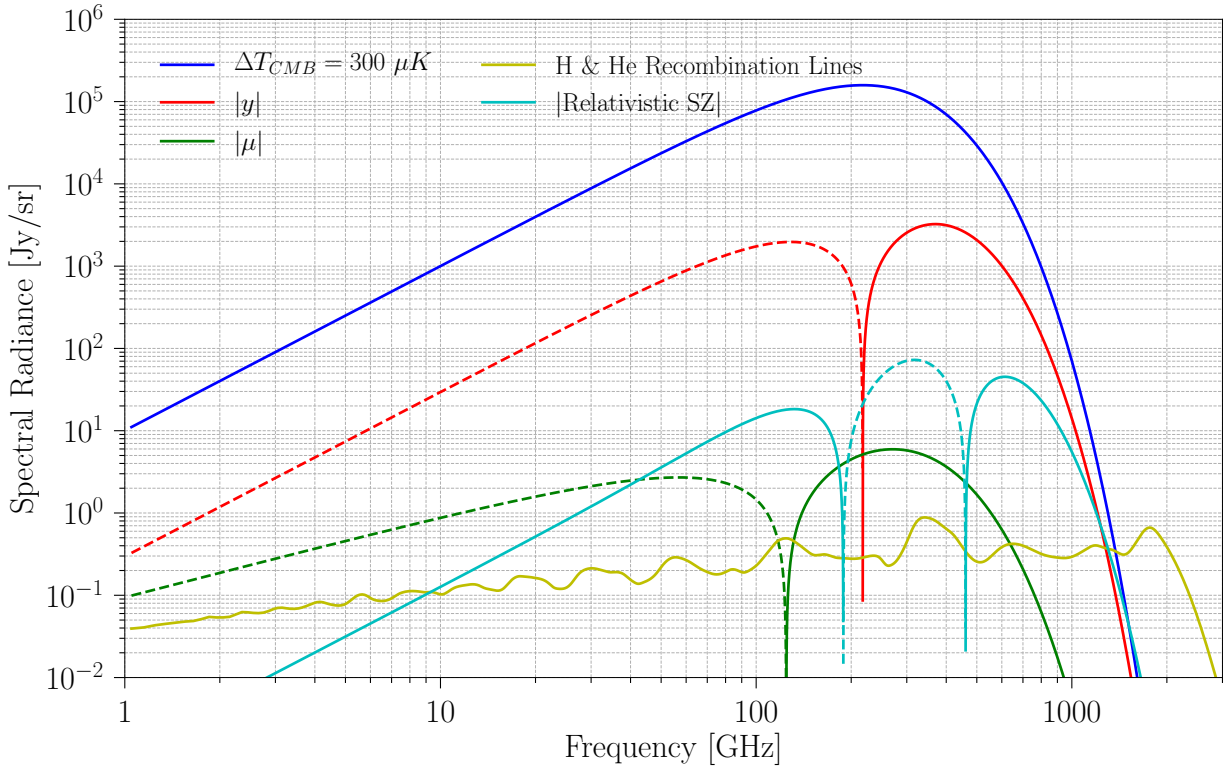

Figure 1.6: CMB spectral distortions as expected from ΛCDM. The signals are plotted in reference to the assumed CMB blackbody at 2.725 K. The signals can be negative in this respect and the negative portions are plotted as dotted lines to accommodate the use of a log scale. The blue curve is an example monopole distortion, set at a level just inside the COBE FIRAS uncertainty. The Compton y distortion is the brightest spectral distortion (red), followed by it's relativistic correction (cyan). The chemical potential μ distortion (green) and the hydrogen and helium recombination lines (yellow) are at the bottom. The total intensity foregrounds are brighter than all the distortion signals as will be discussed in Chapter 4.

Chapter 2

CMB Foreground Signals

Foregrounds are signals that arise naturally in our Solar System, Galaxy, and beyond, that happen to emit in the same frequency range as the CMB. Foregrounds pose one of the biggest problems for ongoing and future CMB observations [97, 35, 102, 256]. Current research is concentrated on studying the effects of foregrounds in CMB maps and improving the measurements of CMB foregrounds in order to remove the foregrounds and uncover the CMB B-mode and spectral distortion signals [240, 241, 132, 317, 281, 302, 132, 242].

My thesis covers both foreground observations and analysis, in addition to forecasting the capabilities of future experiments given the foreground problem. In this section I will introduce each of the common foregrounds that will be discussed in this thesis. I will describe the physical mechanism that creates each foreground, current observations of each foreground, and the parametric models that describe the observed emission. I will list parametric models for both the Rayleigh-Jeans approximation to the brightness temperature and the model for the spectral radiance of each foreground (the brightness temperature models are typically used for foreground subtraction because CMB maps are usually calibrated in these units).

Foregrounds are typically divided into the ones relevant for intensity studies and the ones relevant for polarization studies [241]. An example of all the intensity foregrounds is plotted in Figure 2.1. There are a variety of foregrounds in intensity of varying importance to CMB

missions. The primary intensity foregrounds are synchrotron, free-free (bremsstrahlung), and thermal dust radiation [241, 256]. Additionally there is also anomalous microwave emission and Galactic atomic and molecular emission lines [226]. Other signals include zodiacal emission from the Solar System, as well as the integrated effect of extragalactic thermal dust (called the cosmic infrared background) and integrated extragalactic atomic and molecular emission lines [228, 229]. There are also planets, stars, and a variety of other Galactic and extragalactic point sources that are detected by CMB experiments [227]. All of these signals are interesting on their own from an astrophysical or even cosmological perspective and there is a mutually beneficial relationship of studying them from as foregrounds. Modern CMB experiments such as *Planck* (and a variety of others) produce incredibly detailed maps on these astrophysical signals as a product of their CMB research [237]. The most important 'foreground' of all, for ground and even balloon based telescopes, is the atmosphere itself, however the atmosphere is typically treated as correlated noise in the detectors and not as a foreground since it is time varying (see Chapter 6 for a discussion about correlated noise in the detectors).

Fortunately there are only two major polarized foregrounds for CMB B-mode studies: synchrotron and thermal dust [240, 12]. Both trace the Galactic magnetic field and synchrotron and thermal dust emission are spatially correlated. The polarized foregrounds are plotted against the relevant CMB signals in Figure 2.4. The polarized foregrounds are the center of much research (and controversy [1]) in order to enable B-mode studies. The polarization of certain foregrounds actually simplifies the foregrounds problem because only synchrotron and thermal dust are expected to be polarized. Nonetheless foreground observations in both intensity and polarization are helpful for understanding the emission mechanism and subtracting the signals from CMB maps. They are the same foregrounds after all.

[1] See nytimes.com, nytimes.com, and nature.com.

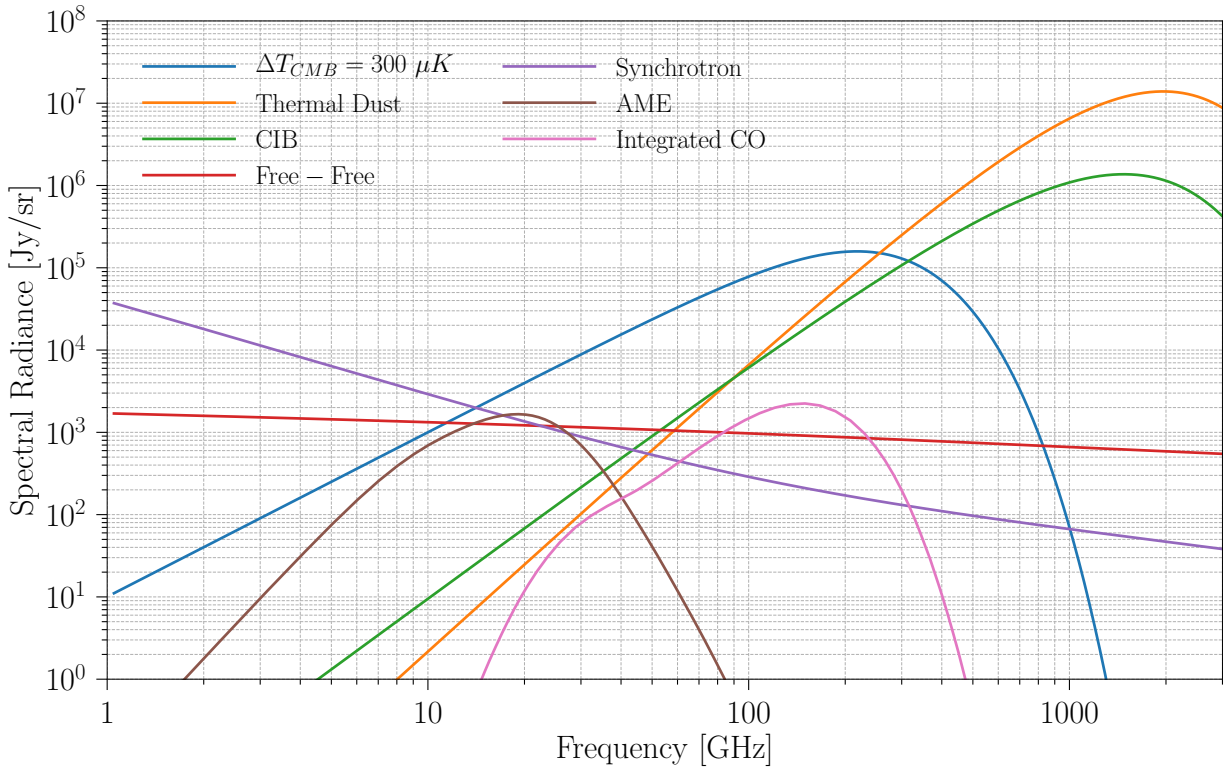

Figure 2.1: Example foreground intensity spectra. The CMB curve corresponds approximately to the size of the CMB temperature anisotropies.

2.1 Synchrotron

Synchrotron radiation is Galactic emission from cosmic ray electrons spiraling in the Galactic magnetic field. The physical mechanism for synchrotron is very well understand and can be analytically derived using electromagnetism. The complexity comes in understanding the Galactic magnetic field (direction and magnitude) and the underlying cosmic ray spectrum [79, 264]. Synchrotron spectrum in brightness temperature can be described by a power law decreasing in frequency (it is the same model in spectral radiance but with different parameter values),

$$T_{\text{synchroton}} = A_s \left(\frac{\nu}{\nu_0}\right)^{\beta_s}, \tag{2.1}$$

where A_s is the amplitude defined at a reference frequency ν_0 and β_s is the spectral index. The spectral index is typically near $\beta_s \approx -3$ in temperature units ($\beta_s \approx -1$ in spectral

radiance units) depending on the sky patch. Curvature of the power law (an additional index) is a common extension of the model. Here we write the model with curvature (in either units),

$$I_{\text{synchroton}} = A_s \left(\frac{\nu}{\nu_0}\right)^{\beta_s} \left[1 + \frac{1}{2}\omega_s \log^2\left(\frac{\nu}{\nu_0}\right)\right] , \tag{2.2}$$

where ω_s describes the curvature. Full models of the synchrotron emission which incorporate knowledge about the cosmic ray energy spectrum and Galactic magnetic field have been implemented by codes such as GALPROP [207]. Synchrotron is brightest at low frequencies and is typically the dominant source below around 70 GHz [97]. Synchrotron observations on the full sky come from the Haslam 408 MHz (intensity only), WMAP 20-90 GHz, and Planck 30-70 GHz observations [128, 129, 254, 29, 241]. Additional observation on large sky fractions have been conducted (and are ongoing) by S-PASS (2.4 GHz), C-BASS (5 GHz), QUIJOTE (10-30 GHz), CLASS (30 GHz), BICEP (30/40 GHz) and ACT (30/40 GHz) [181, 161, 117, 119, 103, 277, 276]. Synchrotron is polarized with a high polarization fraction as the emission is aligned perpendicular to the magnetic fields. Synchrotron is observed to be polarized at a level of 10 - 40% [240, 241, 29].

2.2 Thermal Dust

Galactic thermal dust emission is the brightest foreground in both intensity and polarization at frequencies above 100 GHz [97, 256, 241]. The radiation is due to blackbody radiation from dust grains in the interstellar medium (ISM), modified by the emissivity of the grains [132]. The nature of the grains can vary widely depending on the local ISM environment surrounding the grains. The grains are composed primarily of hydrogen, carbon, oxygen, magnesium, silicon, and/or iron [90]. The size of the grains can vary from several angstrom to tens of microns [189, 306]. For CMB studies, the effects of the different grains populations are modeled by assuming a power law spectrum of emissivities which leads to the modified blackbody spectrum that is commonly used to model dust [240, 132, 256, 242].

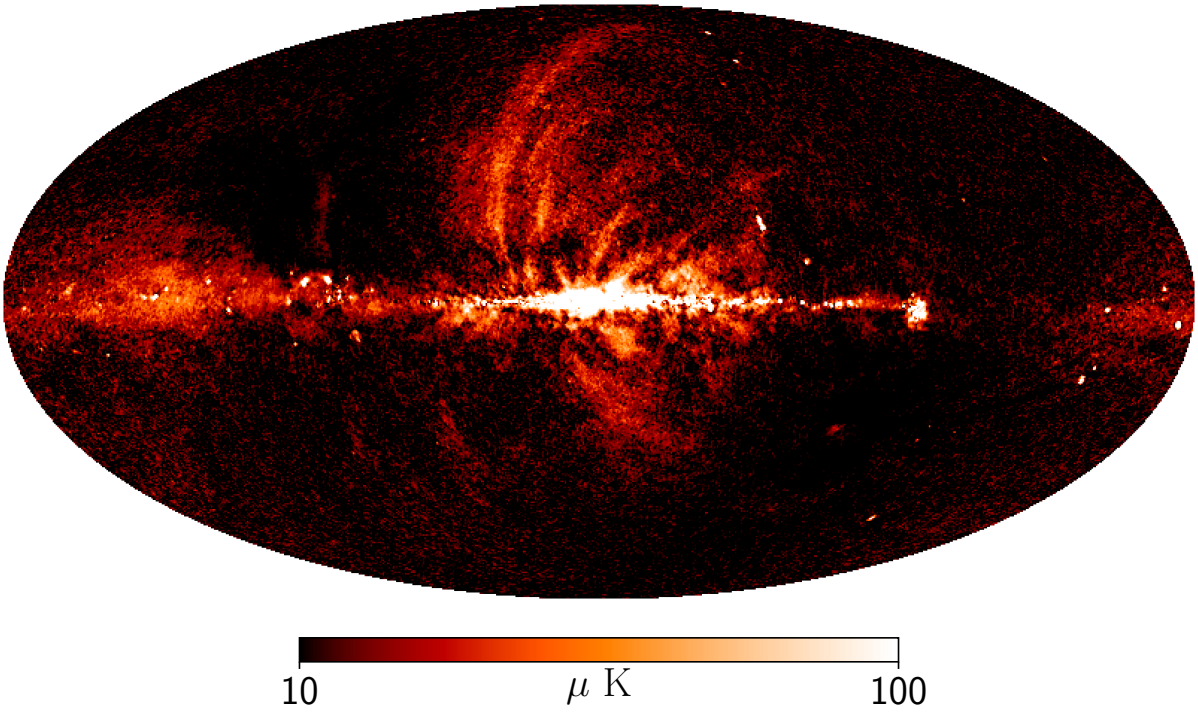

Figure 2.2: Polarized synchrotron emission map determined by Planck at 30 GHz at 40' resolution.

The model is given by,

$$x = \frac{h\nu}{kT_{\mathrm{D}}} \tag{2.3}$$

$$T_{\mathrm{dust}}(\nu) = A_{\mathrm{D}} \left(\frac{x}{x_0}\right)^{\beta_{\mathrm{D}}+1} \frac{\mathrm{e}^{x_0} - 1}{\mathrm{e}^{x} - 1}\,, \tag{2.4}$$

where A_{D} is the amplitude, β_{D} is the index and T_{D} is the dust temperature. The index is typically $\beta_{\mathrm{D}} \approx 1.5$ and the temperature is $T_{\mathrm{D}} \approx 20$ K. The model is defined such that A_{D} is the brightness of the dust at frequency ν_0. The spectrum behaves approximately like a power law until THz frequencies, where the exponential cutoff is determined by T_{D}. We can write the model in spectral radiance and rearrange terms to get,

$$x = \frac{h\nu}{kT_{\mathrm{D}}} \tag{2.5}$$

$$I_{\rm dust}(\nu) = A_{\rm D} x^{\beta_{\rm D}} \frac{x^3}{e^x - 1}\,. \tag{2.6}$$

Typically a single modified blackbody spectrum is used to describe the thermal dust emission in a given region, although two temperature dust models are commonly tested as well [172, 203]. Dust is polarized at the level of 5 - 20%. The dust angular power spectra observationally seem to obey several interesting properties [240, 163]. The spectra follow a power law in ℓ. The dust EE to BB ratio is around 0.5 across the whole sky. There is a dust TB correlation that is not expected for parity observing radiation. Thermal dust is polarized as the grains align with the local magnetic field, however, the higher the dust column integrated along the line-of-sight, the smaller the level of polarization. This is because the polarization is canceled out by spatial variations of the magnetic fields. Therefore, regions that are low in intensity are not necessarily also low in polarization and in fact usually exhibit higher polarization fractions than bright regions.

2.3 Free-Free

Free-free emission comes from electron-ion collisions in hot ionized regions in the Galaxy, typically HII regions [90]. The free-free spectrum in brightness temperature can be parameterized as,

$$g_{\rm FF} = \log\left(\frac{0.04955}{(\nu/10^9)}\right) + 1.5\,\log(T_{\rm e}) \tag{2.7}$$

$$T_{\rm FF} = 0.0314\,\frac{T_{\rm e}^{-1.5}}{(\nu/10^9)^2}\,{\rm EM}\,g_{\rm FF} \tag{2.8}$$

$$T_{\rm FF}(\nu) = T_{\rm e}\,\left(1 - e^{-T_{\rm FF}}\right) \tag{2.9}$$

The parameters of the model are the electron temperature, $T_{\rm e}$ of the region and the effective emission measure, EM, (which is related to the column density) of the region. The spectrum is weakly dependent on the electron temperature and is typically around 8000 K [235]. The spectrum is flat and appears nearly as a power law with the amplitude set by the emission

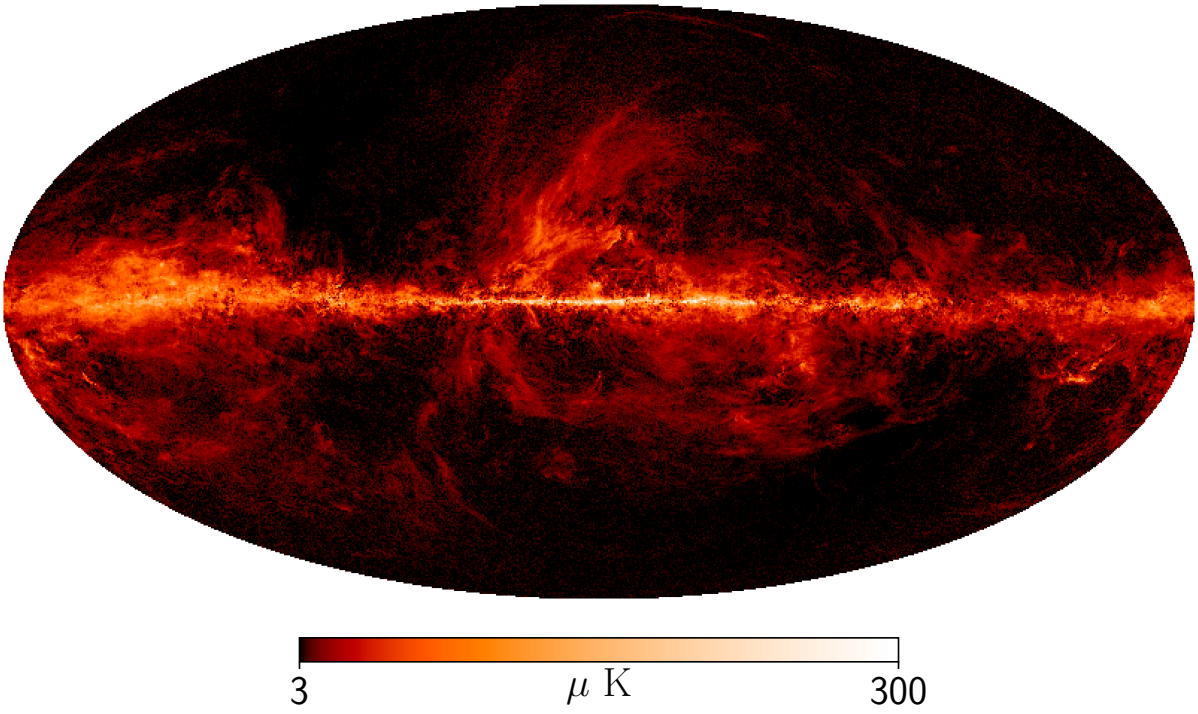

Figure 2.3: Polarized thermal dust emission map determined by Planck at 353 GHz at 5' resolution.

measure. We can simplify the model and write it in spectral radiance units as,

$$\nu_{\rm FF} = \nu_0 \left(\frac{T_{\rm e}}{10^3 K} \right)^{3/2} \tag{2.10}$$

$$I_{\rm FF}(\nu) = A_{\rm FF} \left(1 + \log \left(1 + \left(\frac{\nu_{\rm FF}}{\nu} \right)^{\sqrt{3}/\pi} \right) \right) , \tag{2.11}$$

where $A_{\rm FF}$ sets the amplitude. Due to absorption, the free-free spectrum becomes optically thick at low frequencies (around 1-10 GHz depending on the emission measure). Free-free is intrinsically unpolarized as the emission comes from random thermal collisions of electrons and ions (and the velocities are not correlated). Free-free is correlated with the emission from the $H\alpha$ line (the transition from n=3 to n=2 in the hydrogen Balmer series), as electrons are captured by protons. Optical $H\alpha$ observations can be used to estimate the free-free emission, after correcting for dust extinction [105].

2.4 AME

Anomalous microwave emission is Galactic radiation that peaks between $20 - 60$ GHz and is not explained by synchrotron, thermal dust or free-free radiation [173, 93, 184, 85]. The mechanism for AME is currently the topic of much research [133, 91, 9, 11, 140]. The leading model for AME is spinning dust emission that is sourced by small asymmetrical rapidly rotating dust grains with an electromagnetic dipole moment. AME is spatially correlated with thermal dust emission, hence the popularity of the spinning dust grains theory [225]. Other models for AME include thermal magnetic dust grains and compact HII (free-free that is optically thick until about 10 GHz). The size and composition of the dust grain is important for spinning dust models and far-infrared and mid-infrared observations can reveal emission lines correlated with the size of the grain [134]. AME is observationally not polarized, however the limits are not strong across the whole sky [119]. Depending on the emission mechanism, there are theoretical models for both unpolarized and polarized AME [91, 94]. Spinning dust is expected to be unpolarized while magnetic dust emission could be polarized. Spinning dust models for the AME are derived from the SPDust code [11, 275]. For reference the shape of the spectrum looks approximately like a concave quadratic peaking around 30 GHz. AME models will be discussed extensively in Chapter 3.

2.5 Other

There are a variety of other foregrounds that are important for CMB observations. For intensity observations, atomic and molecular emission lines, in particular CO, CII, and NII lines are present in relevant millimeter-wave frequencies [226]. The integrated emission from distant dusty star forming galaxies produces a foreground signal, the cosmic infrared background (CIB) [228]. Integrated atomic and molecular lines from distant galaxies and the intragalactic medium (IGM) are also considered a foreground [257]. These signals are important for other cosmological research and are used in intensity mapping to measure the

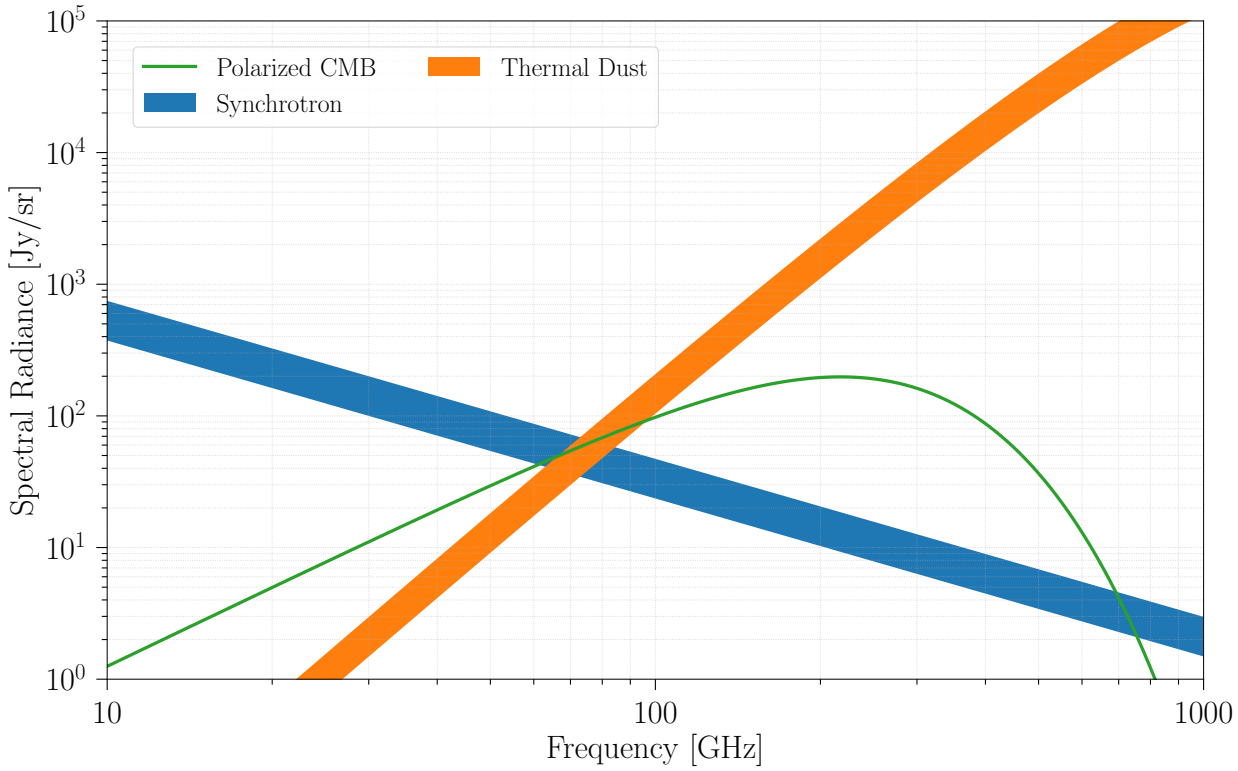

Figure 2.4: Example foreground polarization spectra. The CMB curve is dominated by the E-mode polarization of the CMB. The B-mode signal lies at least an order of magnitude below the E-mode signal, potentially off the plot. Ground-based observations are typically made from 20 to 300 GHz in order to constrain and remove the foreground contamination. Space-based missions like Planck can observe even higher frequencies to further constrain the thermal dust emission.

3-D structure and evolution of the Universe [47, 291, 191]. Within our Solar system, zodiacal emission is sunlight that is reflected of local interstellar dust grains, producing a foreground that lies in the ecliptic plane [229]. A variety of point sources (planets, stars, galaxies) are also typically masked from CMB angular power spectra calculations [227]. Some of these point sources are polarized and this is a topic of current research [246].

Part II

CMB Foreground Research

Chapter 3

Studying the Anomalous Microwave Emission Mechanism in the S140 Region with Green Bank Telescope Observations

Anomalous microwave emission (AME) is a category of Galactic signals that cannot be explained by synchrotron radiation, thermal dust emission, or optically thin free-free radiation. Spinning dust is one variety of AME that could be partially polarized and therefore relevant for ongoing and future cosmic microwave background polarization studies. The *Planck* satellite mission identified candidate AME regions in approximately 1° patches that were found to have spectra generally consistent with spinning dust grain models. The spectra for one of these regions, G107.2+5.2, was also consistent with optically thick free-free emission because of a lack of measurements between 2 and 20 GHz. Follow-up observations were needed. Therefore, we used the C-band receiver (4 to 8 GHz) and the VEGAS spectrometer at the Green Bank Telescope to constrain the AME mechanism. For this study, we produced three band averaged maps at 4.575, 5.625, and 6.125 GHz and used aperture photometry to

measure the spectral flux density in the region relative to the background. We found if the spinning dust description is correct, then the spinning dust signal peaks at 30.9 ± 1.4 GHz, and it explains the excess emission. The morphology and spectrum together suggest the spinning dust grains are concentrated near S140, which is a star forming region inside our chosen photometry aperture. If the AME is sourced by optically thick free-free radiation, then the region would have to contain HII with an emission measure of $5.27^{+2.5}_{-1.5} \times 10^8$ cm^{-6} pc and a physical extent of $1.01^{+0.21}_{-0.20} \times 10^{-2}$ pc. This result suggests the HII would have to be ultra or hyper compact to remain an AME candidate.

3.1 Introduction

Diffuse Galactic signals obscure our view of the cosmic microwave background (CMB). Ongoing and future CMB polarization studies will likely be limited by these Galactic foreground signals [102]. Component separation analysis methods currently being used for CMB polarization studies commonly consider only Galactic dust emission and synchrotron radiation [see 235, for example]. There may be additional signals to consider as well.

Diffuse Galactic microwave signals that are not synchrotron radiation, optically thin free-free emission, or thermal dust emission are commonly referred to as anomalous microwave emission (AME) [85]. AME was first observed by the COBE satellite [173, 174] and later identified in observations near the north celestial pole [185]. Since then, evidence for AME has been reported in many other regions as well [see 126, and references therein]. The reported AME signals have been detected between approximately 10 and 60 GHz, and active AME research is focused on understanding the emission mechanisms [133, 91]. The emission mechanism models that are currently being considered include (i) flat-spectrum synchrotron radiation [28, 173], (ii) optically thick free-free emission from, for example, ultra compact HII (UCHII) regions [83, 183], (iii) thermal magnetic dust emission [94], and (iv) emission from rapidly rotating dust grains that have an electric dipole moment [101, 93, 92].

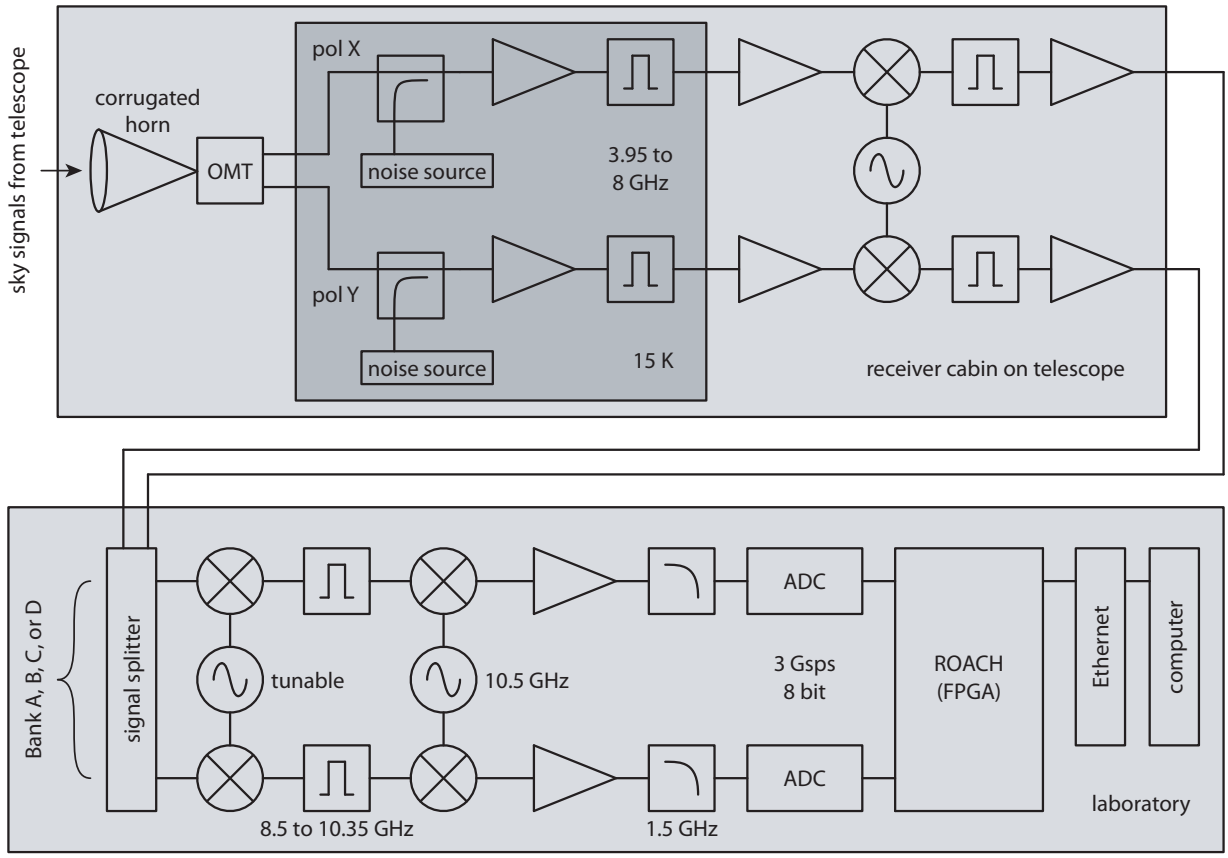

Figure 3.1: A schematic of the GBT instrument we used for this study. The C-band receiver elements in the receiver cabin on the telescope are shown in the box on the top. The digital spectrometer elements in the laboratory are shown in the box on the bottom. For clarity, just one spectrometer bank is shown. More details are given in Section 3.2.1.

Spinning dust grains could potentially produce linearly polarized signals [see 184, 91, for example], and the theoretical emission spectrum for spinning dust grains can extend up to frequencies above 80 GHz, where the CMB polarization anisotropy is commonly being observed. Therefore, spinning-dust emission could be a third important polarized Galactic foreground signal that should be considered for CMB polarization studies [135, 255, 17]. Observational evidence to date suggests the AME signal can be partially polarized, if at all, with upper bounds at the level of 0.5 percent or less [119, 236, 84]. However, this detected level of polarization is still appreciable because the CMB polarization anisotropy signals are polarized at a level of $\sim 10^{-6}$ or less [see 278, and references therein]. More investigation is required to see if polarized AME would bias future CMB polarization anisotropy

measurements.

Active spinning-dust research focuses on searching for and characterizing regions with spinning dust signal. Discovering spinning-dust regions is challenging because they need to be detected both spectroscopically and morphologically [27, 217]. Using multi-wavelength analyses members of the Planck Collaboration have identified several regions that could contain spinning-dust signal [224, 230]. However, there are limited observations between 2 and 20 GHz [118], so there is some remaining uncertainty in the AME emission mechanism in these regions. As a result, these Planck-discovered regions are excellent targets for follow-up spinning-dust studies. One target is near the star-forming region S140 [271], and it is centered on $(l, b) = (107.2°, 5.20°)$, which we will refer to in this Chapter as G107.2+5.20. Previous analysis of this region showed that both spinning dust and UCHII models fit the data well [223, 230]. In an effort to further constrain the emission mechanism in this region and possibly expand the catalog of known spinning-dust regions, we made spectropolarimetric measurements of the region using the the 100-m Green Bank Telescope (GBT) in West Virginia [156]. Specifically, we used the C-band receiver (4 to 8 GHz) and the Versatile GBT Astronomical Spectrometer (VEGAS), which is a digital back-end [244]. During our 18 hours of observing (10 hours mapping and 8 hours calibrating) we measured all four Stokes parameters of a nearly circular region centered on G107.2+5.20.

In this Chapter, we first describe the instrument and the observations in Section 3.2. The analysis methods are described in Section 3.3. Our measurements of the spatial morphology of the intensity of the region (the Stokes I parameter) and the derived spectroscopic results are presented in Section 3.4. Our polarization results (the Stokes Q, U, and V maps) will be published in a future study.

Table 3.1: Definition of the four spectral banks. Each bank is divided into 16,384 channels that are 91.552 kHz wide yielding the raw bandwidth, $\Delta\nu_r$. The subscript c denotes center frequency. We ultimately used 6,400 channels in each bank (see Section 3.3.1), so the selected bandwidth for map making is $\Delta\nu_s$. The estimated beam full-width at half-maximum (FWHM) for each bank is listed as well.

Bank	ν_c [GHz]	$\Delta\nu_r$ [GHz]	$\Delta\nu_s$ [GHz]	FWHM$_c$ [arcmin]
A	4.575	3.975 - 5.225	4.407 - 4.993	2.75
B	5.625	5.025 - 6.275	5.457 - 6.043	2.25
C	6.125	5.525 - 6.775	5.957 - 6.543	2.05
D	7.175	6.575 - 7.825	7.007 - 7.593	1.75

3.2 Observations

3.2.1 Receiver and Spectrometer

GBT is a fully steerable off-axis Gregorian reflecting antenna designed for observations below approximately 115 GHz. The prime focus of the parabolic primary mirror is directed into a receiver cabin using an elliptical secondary mirror. The C-band receiver we used for our observations is mounted in this receiver cabin. The unblocked aperture diameter is 100 m, so the beam size for our observations was between 1.8 and 2.8 arcmin, depending on frequency. The VEGAS back-end electronics used to measure the spectra are housed in a laboratory approximately 2 km from the telescope.

A schematic of the receiver and the digital spectrometer we used for this study is shown in Figure 3.1. The telescope first feeds a corrugated horn. An orthomode transducer (OMT) at the back of the horn splits the sky signals into two polarizations (polarization X and polarization Y). The two outputs of the OMT are routed to a cryogenic stage that is cooled to approximately 15 K. At this cryogenic stage, directional couplers are used to insert calibration signals from a noise diode. These calibration signals were switched on and off during our observations to help monitor time-dependent gain variations. The sky signals were then (i) amplified with a cryogenic low-noise amplifier (LNA), (ii) band-pass filtered, (iii) amplified a second time with a room-temperature amplifier, (iv) mixed down in frequency, and (v)

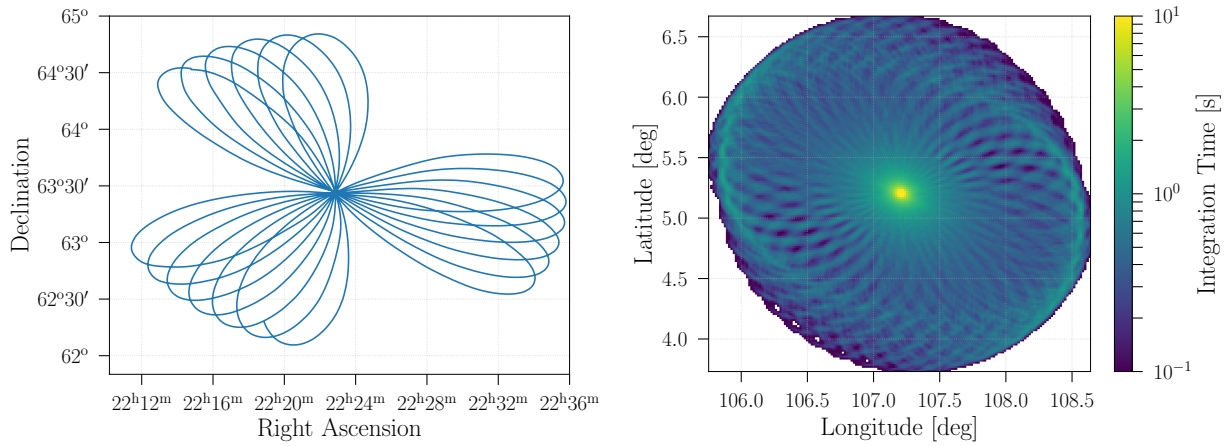

Figure 3.2: **Left:** The "daisy" scan pattern used for our observations. Five minutes of pointing data are plotted as an example to show the three "petals." A full cycle is completed every 25 minutes. The scan strategy densely fills in a circle of radius 1.5°. **Right:** Map of the total integration time per pixel for our observations. The pixels are $1' \times 1'$, and the median integration time per pixel is 0.4 s. Note that the color bar uses a log scale.

routed to the laboratory via optical fibers.

In the laboratory, the signals were split into four banks: Bank A, B, C, and D. Each bank used its own hardware chain to measure the spectrum of that bank. For clarity, only one of the four spectrometer chains is shown in Figure 3.1. The spectral band for each bank is determined by mixing up the signal in that bank using a tunable local oscillator (LO) and then band-pass filtering. The chosen LO frequency ultimately defines the spectral band. The pass band of the filter is between 8.50 and 10.35 GHz. The signals were then mixed down using a fixed 10.5 GHz LO. At this stage, each bank has 1.85 GHz of bandwidth. The signals were then (i) amplified, (ii) low-pass filtered to avoid aliasing (edge at 1.5 GHz), and (iii) sampled at 3 Gsps with an 8-bit analog to digital converter (ADC) that is connected to a Reconfigurable Open Architecture Computing Hardware 2 (ROACH2) board[1]. The ROACH2 board uses a field-programmable gate array (FPGA) to compute the spectrum of the sampled data. Each bank has 16,384 raw spectral channels that are each 91.552 kHz wide. Spectra are integrated in the ROACH2, and one average spectrum is saved to disk every 40 ms. In the following sections, we use the term ADC count to refer to the power

[1]https://casper.berkeley.edu/

measurement in each filter bank channel. The spectral banks are defined in Table 3.1.

3.2.2 Scan Strategy and Calibration

Our GBT observations were conducted in April and June of 2017. Ten total hours of mapping data were collected during observing sessions on April 5, April 10, and June 4. Eight total hours of polarization calibration data were collected on April 3 and June 3. We refer to these as Sessions 1 through 5 chronologically, so Sessions 1 and 4 are the polarization calibration sessions, and Sessions 2, 3, and 5 are the mapping sessions. At the beginning of each session, the system temperature was measured. For our five sessions, the mean system temperature was 19.5 ± 1 K.

We chose to use the "daisy" scan strategy available at GBT, which is typically used for MUSTANG mapping observations [179]. The daisy scan traces out three "petals" on the sky every 30 seconds (see Figure 3.2). Every 25 minutes, this scan strategy completes a full cycle densely covering both the innermost and the outermost portions of a nearly circular region. This approach works well with our map-making algorithm (see Section 3.3.3) because map pixels are revisited and sampled multiple times. Given that we want a densely sampled map, we scanned GBT close to the speed and acceleration limits of the telescope[2] and were able to observe a nearly circular region 3.0° in diameter centered on G107.2+5.20. Our maximum scan speed was 21.6 arcmin s^{-1}, and the root mean squared (RMS) speed was 10 arcmin s^{-1}. The scan pattern is calculated in an astronomical coordinate system to ensure the center is always on G107.2+5.20.

To convert our measurements into flux units, we calibrated using observations of 3C295. 3C295 is an unpolarized radio galaxy that has a power-law-with-curvature spectrum [222, 216]. To mitigate the effects of any gain fluctuations, we switched the noise diode on and off at 25 Hz during all observations. With this approach, every other spectrum output by VEGAS was a measurement of the noise-diode spectrum. By comparing the noise-diode spectrum

[2]The maximum scan speed for GBT is 36 arcmin s^{-1} in azimuth and 18 arcmin s^{-1} in elevation. The maximum acceleration is 3 arcmin s^{-2}, and it is only possible to accelerate twice per minute.

Table 3.2: Data sets used in this study. We used a circular aperture with a radius of $45'$ to determine the spectral flux density (SFD).

Experiment	Frequency [GHz]	Beam FWHM [arcmin]	Aperture SFD [Jy]	Reference
CGPS	0.408	2.8	17.0 ± 3	[303]
Reich	1.42	36.0	18.9 ± 2	[251]
GBT (Bank A)	4.575	2.75	18.1 ± 2	This work
GBT (Bank B)	5.625	2.24	17.5 ± 2	"
GBT (Band C)	6.125	2.05	17.7 ± 2	"
Planck	28.4	32.3	30.3 ± 1	[234]
Planck	44.1	27.1	26.8 ± 1	"
Planck	70.4	13.3	26.1 ± 1	"
Planck	100	9.7	-	"
Planck	143	7.3	88.7 ± 5	"
Planck	217	5.0	-	"
Planck	353	4.8	$1,550 \pm 70$	"
Planck	545	4.7	$5,190 \pm 200$	"
Planck	857	4.3	$18,100 \pm 700$	"
DIRBE	1249	39.5	$44,000 \pm 1,000$	[131]
DIRBE	2141	40.4	$74,600 \pm 2,000$	"
DIRBE	2997	41.0	$41,900 \pm 800$	"
IRIS (100 μm)	3000	4.3	-	[205]
IRIS (60 μm)	5000	4.0	-	"
IRIS (25 μm)	12000	3.8	-	"
IRIS (12 μm)	25000	3.8	-	"

to the 3C295 spectrum, we calibrated the measured G107.2+5.20 spectra to the 3C295 calibration spectrum at every point in time during the observation session. To calibrate the noise diode into flux units, at the beginning and end of each observation session we pointed the antenna directly at 3C295 and collected data for two minutes. We then pointed 1 degree in RA away from 3C295 and collected two minutes of data. These on-source/off-source measurements yielded the desired calibration spectrum, which was measured relative to the background. Note that we assume the the on-source measurement includes signal from 3C295 plus the unknown background, while the nearby off-source measurement includes only the background signal.

3.2.3 Ancillary Data

To measure the spectral flux density of the AME region G107.2+5.2 and to inspect its morphology at different frequencies we compiled data from a range of observatories. A list of all the data sets used in our study is given in Table 3.2. Data processing and unit conversions are required for each data set as described below.

For the radio observations we used the Canadian Galactic Plane Survey (CGPS) data [295, 303] at 408 MHz as well as the Reich all sky survey at 1.420 GHz [252, 249, 251]. The CGPS map was produced using Haslam data [128, 129, 254, 255], which is widely used to trace synchrotron and optically thin free-free emission on 1 degree angular scales. The CGPS data[3] has arcminute resolution, which is useful for morphological comparisons. To convert from thermodynamic units to flux units we used the Rayleigh Jeans approximation,

$$I = \frac{2\nu^2 k_B}{c^2} T_B \times \Omega_p \times 10^{26}\,, \tag{3.1}$$

where $\nu = 408$ MHz for the CGPS data and 1.420 GHz for the Reich data, and Ω_p is the solid angle of a pixel in steradians. This conversion brings the maps into spectral flux density units (Jy pixel^{-1}). The Reich data required a calibration correction factor of 1.55 to compensate for the full-beam to main-beam ratio, based on comparisons with bright calibrator sources [250]. We included an estimated 10% calibration uncertainty on all the radio data.

We used Planck observations for measurements between 30 and 857 GHz [234]. To convert Planck data from $K_{\rm CMB}$ to spectral radiance we used the Planck unit conversion and color correction code available on the Planck Legacy Archive[4]. Note that molecular CO lines have biased the 100 and 217 GHz Planck results, so these points are not included in the model fitting (see Section 3.4).

Far-infrared information was provided by IRIS (improved IRAS) and DIRBE data [205,

[3]The CGPS data is available online at http://www.cadc-ccda.hia-iha.nrc-cnrc.gc.ca/en/cgps/
[4]https://pla.esac.esa.int/pla/

131]. For our spectrum analysis we only used the DIRBE data up to 3 THz because of complexities from dust grain absorption and emission lines at higher frequencies. The IRIS data was used for morphological comparisons only (see Section). We applied color corrections to the DIRBE data according to the DIRBE explanatory supplement [131]. For this analysis we did not use Haslam or WMAP [29] data due to the low spatial resolution of those datasets. However we did check that our aperture photometry results using CGPS and Planck were consistent with the results using Haslam and WMAP.

3.3 GBT Data Analysis

The data processing algorithm consists of five steps: (i) data selection, (ii) noise diode calibration, (iii) data calibration, (iv) map making, and (v) aperture photometry. Each of these steps is described in the subsections below. The time-ordered data from each mapping session are processed with steps (i), (ii), (iii), and (iv). Data from Sessions 3 and 5 are processed with step (v). The results presented in this Chapter come from data collected during Session 5, which was 4.5 hours long. The data from Sessions 2 and 3 are used for jackknife tests. The mapping observations are stored in files containing 25 minutes of data arranged in 5 minute long segments. Some of the steps in the data processing algorithm operate on these 5 minute long segments.

3.3.1 Data Selection

Parts of the data sets are corrupted by radio frequency interference (RFI), transient signals, and instrumental artifacts. These spurious signals need to be removed before making maps. The transient signals and instrumental artifacts are excised by hand after inspection. To find RFI corrupted spectral channels we search for high noise levels and non-Gaussianity using two statistics: the coefficient of variation and the spectral kurtosis [211]. The RFI removal techniques based on these statistics are described below.

The subscript ν denotes the frequency channel index and t denotes the time index. For example, $\xi_{\nu,t}$ is data in ADC counts in frequency channel ν at time t.

For each 5 minute long data segment, we calculated the coefficient of variation in each spectral channel, which is the the inverse signal-to-noise ratio (NSR_ν). This statistic finds spectral channels with persistently high noise levels. We define the mean and the standard deviation in time per channel as

$$\mu_\nu = \langle \xi_{\nu,t} \rangle_t \tag{3.2}$$

$$\sigma_\nu = \sqrt{\left\langle (\xi_{\nu,t} - \mu_\nu)^2 \right\rangle_t}, \tag{3.3}$$

therefore

$$NSR_\nu = \frac{\sigma_\nu}{\mu_\nu}. \tag{3.4}$$

We masked channels with NSR_ν greater than 7.5 times the median absolute deviation of the NSR_ν. We empirically chose this cutoff level because it corresponds to approximately 5σ and effectively detects outliers. In addition, we calculated the spectral kurtosis (or the fourth standardized moment),

$$K_\nu = \frac{\left\langle (\xi_{\nu,t} - \mu_\nu)^4 \right\rangle_t}{\left\langle (\xi_{\nu,t} - \mu_\nu)^2 \right\rangle_t^2}. \tag{3.5}$$

This statistic finds channels with non-Gaussian noise properties. Again we mask spectral channels with K_ν greater than 7.5 times the median absolute deviation of K_ν.

Finally, we only used the selected bandwidth that is listed in Table 3.1 for each bank because at the spectral bank edges the band-pass filters in the receiver (see Figure 3.1) attenuate the sky signals and the gain is low. In total, for Banks A, B, and C in Session 5, 0.7% of the bandwidth-selected data was excised because of RFI contamination, 2% was excised because of transient signals, and 7% was excised because of instrumental artifacts. The signal-to-noise ratio (SNR) for Bank D was low so the data in this bank was ultimately unusable.

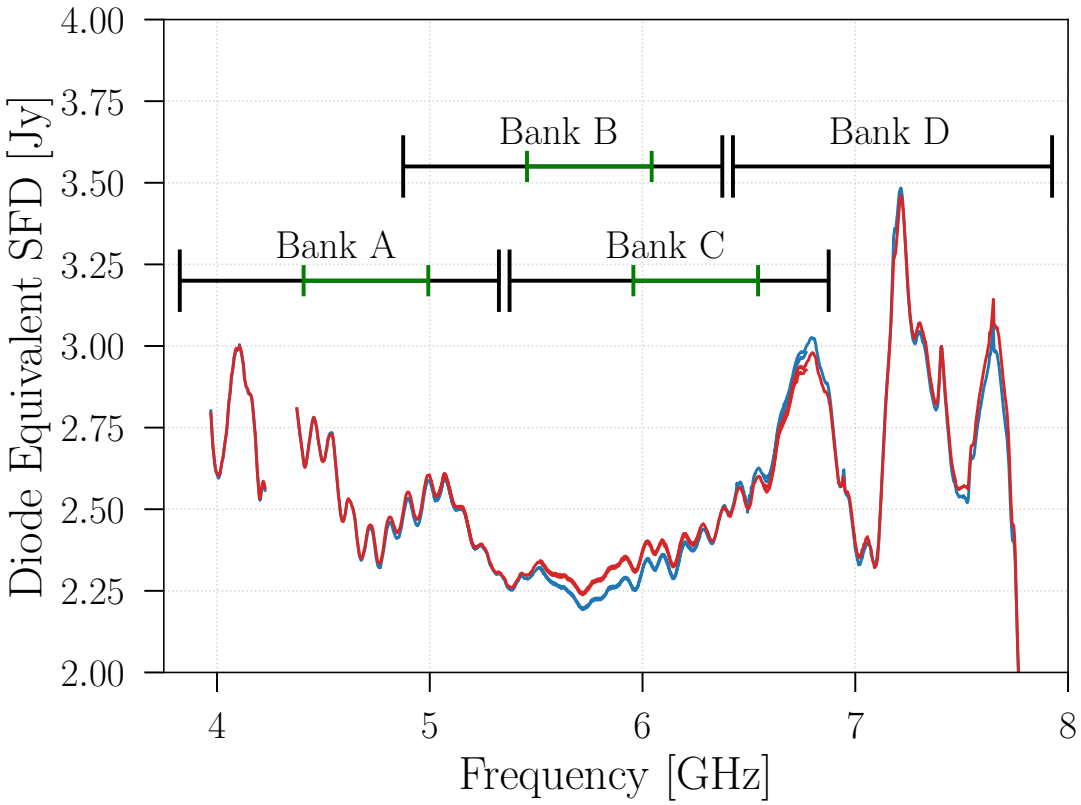

Figure 3.3: Equivalent spectral flux density (SFD) of the noise diode. The noise diode brightness was calibrated on 3C295 at the beginning (red) and end (blue) of Session 5. The amplitude of the noise-diode spectrum used for calibration is very stable in time throughout the observations. The RMS of the difference between the two calibrations during Session 5 over banks A to C is 30 mJy, approximately a 1% difference. The full bandwidth of Bank A through D is shown in black, and the selected bandwidth for Bank A, B, and C is shown in green (see Table 3.1).

3.3.2 Calibration

To convert the mapping data from ADC units to spectral radiance (Jy sr^{-1}), we first calibrate the noise diode using the point source 3C295 and then calibrate the mapping data using the noise diode (see Section 3.2.2). The point source observations take place at the beginning and the end of the observing sessions, and they allow us to convert the data to Janskys. The noise diode is flashed at 25 Hz during both the point source and the mapping observations, so the noise diode is used as a calibration signal to track gain stability. The assumptions are the noise diode spectrum is stable in time and the gain is linear as a function of signal

brightness over the observing session.

In this subsection, we now define x as calibration data while pointing away from 3C295 (off-source), y as calibration data while pointing at 3C295 (on-source), and z as mapping data, scanning G107.2+5.2. We use the superscripts on or off to denote whether the noise diode is on or off. For example, $x^{on}_{\nu,t}$ is off-source calibration data at time t for channel ν while the noise diode is on. We calculated the average noise diode level in a spectral channel as

$$D_\nu = \langle\, x^{on}_{\nu,t} - x^{off}_{\nu,t} \,\rangle_t \,, \tag{3.6}$$

which has units of ADC counts. We computed the average source level in a spectral channel as

$$S_\nu = \langle\, y^{off}_{\nu,t} - x^{off}_{\nu,t} \,\rangle_t \,, \tag{3.7}$$

which also has units of ADC counts. Both D_ν and S_ν were averaged over two minutes, which was the total duration of the point source calibration observations. The noise diode signal was calibrated using the known spectral flux density of 3C295 [222] in the following way:

$$P_\nu = \frac{I_\nu}{S_\nu} D_\nu. \tag{3.8}$$

Here P_ν is the calibrated noise diode signal in units of Janskys (see Figure 3.3) and I_ν is the spectral flux density of 3C295. We then used P_ν to calibrate the mapping data z into Janskys.

Let $z^{on}_{\nu,t}$ and $z^{off}_{\nu,t}$ be the mapping data at time t and frequency channel ν with the noise diode on and off, respectively. We calculated the inverse receiver gain

$$G_\nu = \frac{P_\nu}{\langle\, z^{on}_{\nu,t} - z^{off}_{\nu,t} \,\rangle_t} \,, \tag{3.9}$$

which has units of Janskys per ADC count. G_ν was calculated for every 5 minute long data segment. When making maps of diffuse sky signals we divide the data by the beam solid

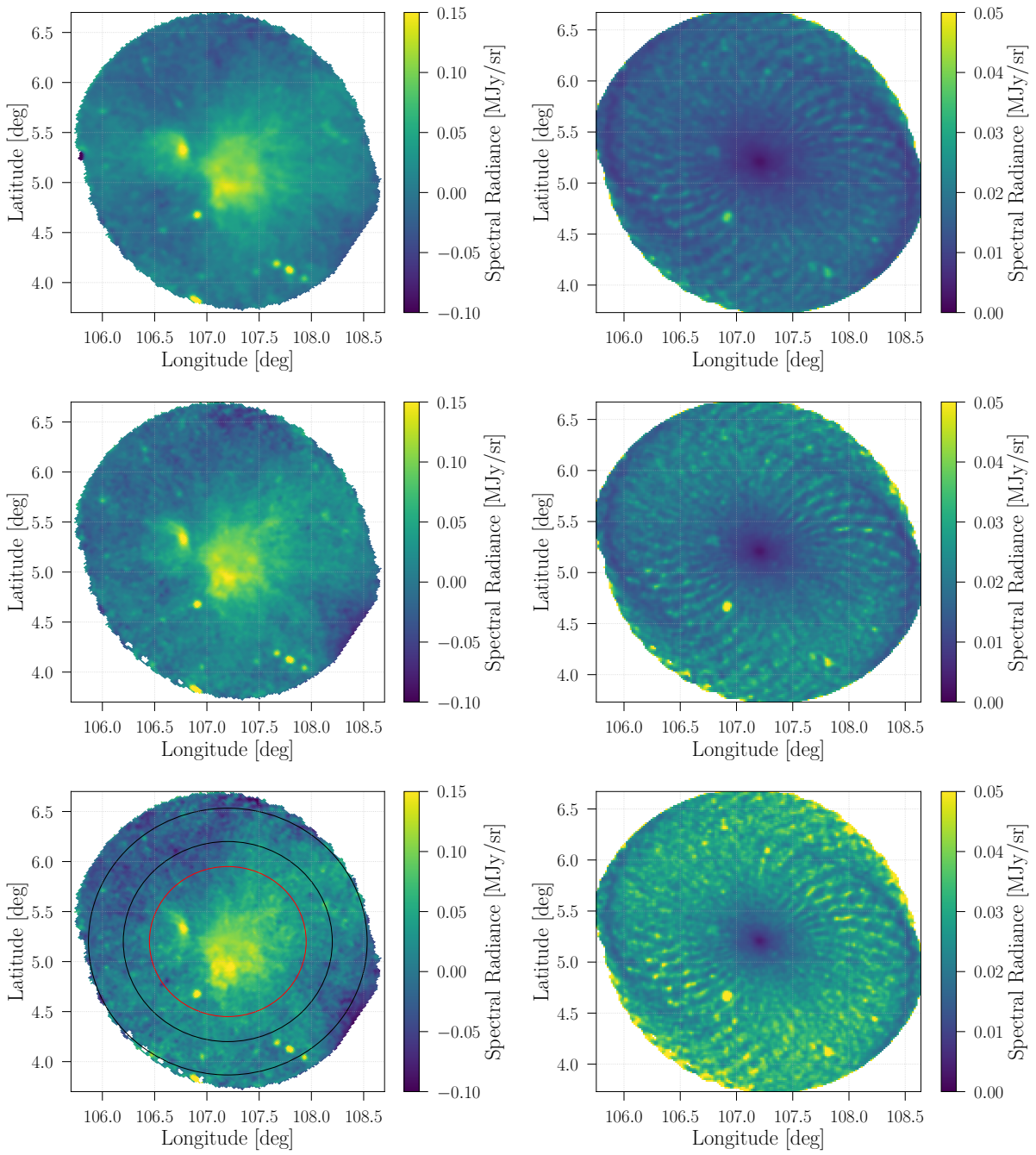

Figure 3.4: Maps of the AME region centered on G107.2+5.2. The left column shows the destriped maps (see Section 3.3.3) and the right column shows the estimated uncertainty map. The top, middle, and bottom rows correspond to Bank A, B, and C, respectively. The star-forming region, S140, is the bright feature located at $(l, b) = (106.80°, +5.31°)$, and G107.2+5.20 is the center of each map. The aperture (inside the red circle) and annulus (between the black circles) for photometry are shown in the Bank C map. The stripes in the uncertainty maps come from the visible stripes in the integration time map (see Figure 3.2), and they are not map-making artifacts. The peak SNR is 40, 36, and 26, and the median SNR inside the photometry aperture is 3.2, 2.6, and 1.9 for Bank A, B, and C, respectively.

angle,

$$\Omega_\nu = \frac{\pi}{4 \log 2} \, \mathrm{FWHM}_\nu^2. \tag{3.10}$$

Here, FWHM_ν is the beam full-width at half-maximum at the frequency channel ν and we assume a Gaussian beam profile. The FWHM values for the center frequencies of the four Banks are given in Table 3.1. The calibrated time-ordered mapping data were then calculated as

$$d_t = \left\langle \frac{G_\nu \, z_{\nu,t}^{off}}{\Omega_\nu} \right\rangle_\nu , \tag{3.11}$$

which have units of spectral radiance (Jy sr^{-1}). The average is taken over the selected bandwidth in a given spectral bank (see Table 3.1) after data selection (see Section 3.3.1).

3.3.3 Map Making

Variations in the gain and system temperature of a receiver result in a form of correlated noise that is often referred to as $1/f$ noise. To separate the sky signal from the $1/f$ noise we implemented a form of the destriping map-making method as described in Delabrouille [81], Sutton et al. [289, 290]. The aim of the destriping map-making method is to solve for the $1/f$ noise in the time-ordered data as a series of linear offsets. To do this the time-ordered data from a receiver system is defined as

$$\mathbf{d} = \mathbf{P}\,\mathbf{m} + \mathbf{F}\,\mathbf{a} + \mathbf{n}_w, \tag{3.12}$$

where the $\mathbf{m}$ is a the map vector of the true sky signal, $\mathbf{P}$ is the pointing matrix that transforms pixel locations on the sky into time positions in the data stream, $\mathbf{Fa}$ describes the $1/f$ noise linear offsets and $\mathbf{n}_w$ is the white noise vector. For our GBT data, the $\mathbf{d}$ is populated with d_t, which is the calibrated time-ordered data for a spectral bank given in Equation 3.11.

Solving for the amplitudes of the $1/f$ noise linear offsets ($\mathbf{a}$) requires minimizing

$$\chi^2 = (\mathbf{d} - \mathbf{P}\,\mathbf{m} - \mathbf{F}\,\mathbf{a})^{\mathrm{T}}\,\mathbf{N}^{-1}\,(\mathbf{d} - \mathbf{P}\,\mathbf{m} - \mathbf{F}\,\mathbf{a})\,, \tag{3.13}$$

where $\mathbf{N}$ is a diagonal matrix describing the receiver white noise. By minimizing derivatives of Equation 3.13 with respect to the sky signal $\mathbf{m}$ and $1/f$ noise amplitude $\mathbf{a}$, it is possible to derive the following maximum-likelihood estimate for the amplitudes

$$\hat{\mathbf{a}} = \left(\,\mathbf{F}^{\mathrm{T}}\,\mathbf{Z}^{\mathrm{T}}\,\mathbf{N}^{-1}\,\mathbf{Z}\,\mathbf{F}\,\right)^{-1}\mathbf{F}^{\mathrm{T}}\,\mathbf{Z}^{\mathrm{T}}\,\mathbf{N}^{-1}\,\mathbf{Z}\,\mathbf{d}. \tag{3.14}$$

Here, we have made the substitution

$$\mathbf{Z} = \mathbf{I} - \mathbf{P}\left(\,\mathbf{P}^{\mathrm{T}}\,\mathbf{N}^{-1}\,\mathbf{P}\,\right)^{-1}\mathbf{P}\,\mathbf{N}^{-1}. \tag{3.15}$$

Once the $1/f$ noise amplitudes have been computed the, $1/f$ noise can be subtracted in the time domain, and the sky map becomes

$$\hat{\mathbf{m}} = \left(\,\mathbf{P}^{\mathrm{T}}\,\mathbf{N}^{-1}\,\mathbf{P}\,\right)^{-1}\mathbf{P}^{\mathrm{T}}\,\mathbf{N}^{-1}\,\left(\,\mathbf{d} - \mathbf{F}\,\mathbf{a}\,\right), \tag{3.16}$$

which is a noise weighted histogram of the data.

For our GBT observations a linear offset length of 1 second was chosen, which removes $1/f$ noise on scales larger than $10'$. The noise weights for each data point were calculated by subtracting neighboring pairs of data and taking the running RMS within 2-second chunks of the auto-subtracted data. The destriped sky maps and the associated uncertainty-per-pixel maps for Bank A, B, and C are shown in Figure 3.4.

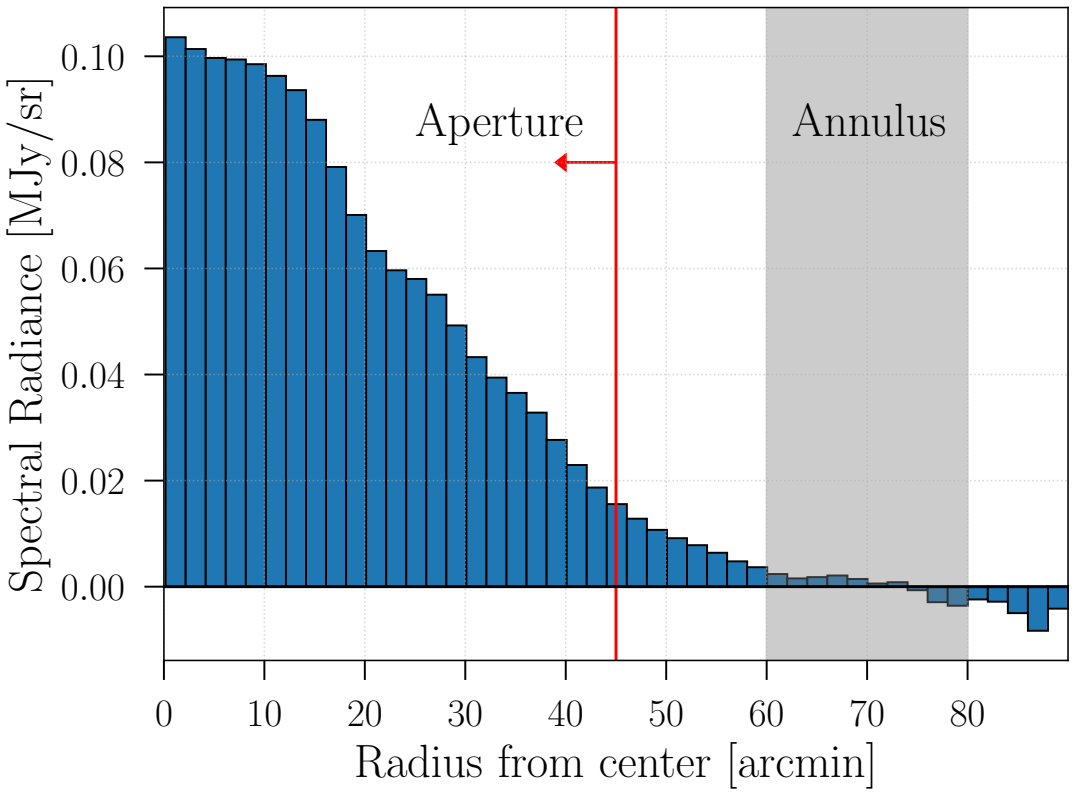

Figure 3.5: Mean spectral radiance per pixel as a function of radial distance from G107.2+5.20 for the Bank A map shown in Figure 3.4. The histogram bins are annuli 2′ wide centered on G107.2+5.20. The zero-point annulus and the aperture radius are highlighted.

3.3.4 Aperture Photometry

We used aperture photometry [230, 119] to measure the spectral flux density (Jy) of the AME region centered on G107.2+5.2. This analysis used seventeen total maps including our GBT maps and maps from CGPS, Reich, Planck, and DIRBE (see Table 3.2). This aperture photometry procedure involves five key steps. First, we removed a spatial gradient and smoothed all the maps in the study to a common resolution of 40′ by convolving the maps with a two-dimensional Gaussian with

$$\mathrm{FWHM} = \sqrt{(40')^2 - \Theta^2}\,, \tag{3.17}$$

Table 3.3: Measured spectral flux density in an aperture 45′ in radius centered on G107.2+5.20. Here, σ_r is the random error from noise in the measurement, σ_s is the systematic error from uncertainty in the calibration, and σ_t is the total uncertainty. These points are plotted in Figure 3.6 and 3.7.

Bank	ν_c [GHz]	Aperture SFD [Jy]	σ_r [Jy]	σ_s [Jy]	σ_t [Jy]
A	4.575	18.09	0.08	1.81	1.81
B	5.625	17.51	0.10	1.75	1.75
C	6.125	17.75	0.15	1.78	1.79
D	7.175	32.39	0.77	3.24	3.33

where Θ is the beam FWHM of each data set. The common 40′ resolution is set by DIRBE, which has the largest beam of all of the data sets used in this study. The beam sizes are given in Table 3.2. Second, we integrated the spectral radiance over the solid angle of a map pixel Ω_p to convert the units to Jy pixel^{-1}. For our GBT maps,

$$\Omega_p = s_p^2 \,, \tag{3.18}$$

where $s_p = 1'$ is the length of the side of each square pixel in the map. Third, the map offsets needed to be subtracted because the aperture photometry technique references a common zero point among all the maps. We determined this zero point by calculating the median value of all the pixels in an annulus with an inner radius of 60′ and an outer radius of 80′ centered on G107.2+5.2. We found the results do not strongly depend on the precise annulus dimensions as long as it is away from the aperture and within the boundaries of our maps (see Figure 3.5). Fourth, we summed all the pixels inside a circular aperture with a radius of 45′ centered on G107.2+5.2 to get the spectral flux density of the AME region. The aperture radius we chose is well matched to the map resolution after smoothing. Fifth, we estimated the uncertainty in the aperture spectral flux density by computing the standard deviation of the pixel values in the annulus and propagating this uncertainty through to each pixel within the aperture. See Equations 4 and 5 in Génova-Santos et al. [118]. An additional systematic error for the GBT data was estimated using jack-knife tests of the

mapping data taken on different days. We found a 10% variation from this jack-knife test and included this as a systematic uncertainty (see Table 3.3). A breakdown of the statistical and systematic uncertainty of the spectral flux density measurements from our GBT maps is listed in Table 3.3. The spectral flux density values from all maps computed with this aperture photometry technique are listed in Table3.2 and plotted in Figures 3.6 and 3.7. All of the maps and the smoothed versions of the maps are shown in Figures 3.10, 3.11, and 3.12.

3.4 Results

To understand the emission mechanism in the G107.2+5.2 AME region, we fit model spectra to the data points from our aperture photometry analysis. These models are composed of CMB, thermal dust emission, optically thin free-free emission, and one AME component. The AME component is either spinning dust emission or optically thick free-free emission. These component models are the same used in Planck Collaboration et al. [230]. We fit the models to the data using the affine invariant Markov chain Monte Carlo (MCMC) ensemble sampler from the `emcee` package [112], which gives model parameter values and parameter posterior probability distributions. The maximum-likelihood parameter values are given in Table 3.5 and the marginalized posteriors are plotted in Figures 3.8 and 3.9. A physical description of the model components is given below in Section 3.4.1, and the functional form of each model component is given in Table 3.4. We also compare the angular morphology of all the maps, which are plotted in Figures 3.10 to 3.14. Our interpretation of the results is given in Section 3.4.3.

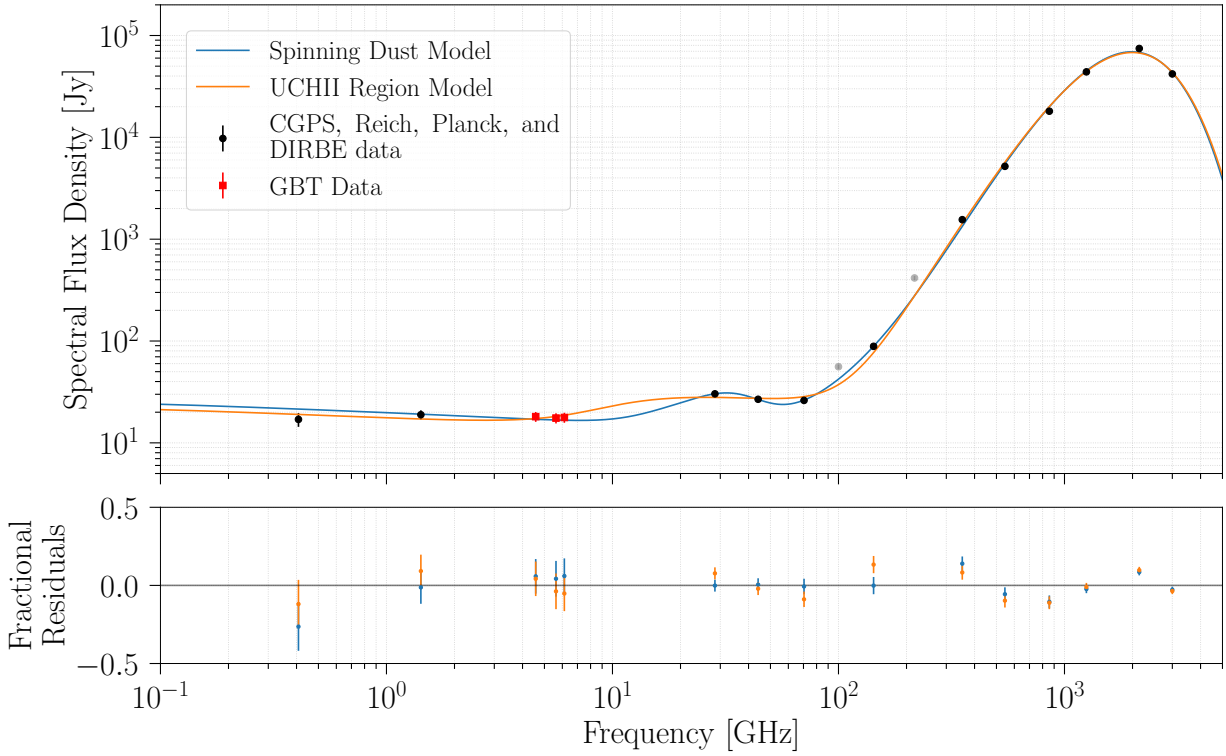

Figure 3.6: Spectral flux density for G107.2+5.2. The aperture radius used for each point in the spectrum is 45′ with the zero-point annulus extending from 60′ to 80′ (see Section 3.3.4). The data points in black come from CGPS, Reich, Planck, and DIRBE (see references in Table 3.2). Our new data points from this GBT study are shown in red. The gray points are from Planck (100 and 217 GHz), but contain known CO contamination and are not used in the fit. The solid curves correspond to the best-fit foreground models. These models include optically thin free-free emission, thermal dust emission, the CMB, and one AME component. If the included AME component is spinning dust, then the best-fit model is the blue curve. If the included AME component is UCHII free-free, then the best-fit model is the orange curve. The fractional residuals for both models are shown as well (blue points for the spinning dust and orange points for the UCHII fractional residuals). The foreground models are given in Table 3.4, and the best-fit model parameters are given in Table 3.5. A close-up view of the result between 300 MHz and 200 GHz is shown in Figure 3.7.

Table 3.4: Foreground models.

Foreground	Spectral Radiance Model [Jy/sr]	Free Parameters	Additional Information
Conversion	$I_{RJ} = \dfrac{2k_B\nu^2}{c} \times 10^{26}$		from K to Jy/sr
Thermal Dust	$x = \dfrac{h\nu}{kT_{\rm D}}$	$A_{\rm D}$ [K]	
	$I_{\rm D}(\nu) = A_{\rm D} \left(\dfrac{x}{x_0}\right)^{\beta_{\rm D}+1} \dfrac{{\rm e}^{x_0}-1}{{\rm e}^{x}-1} \times I_{RJ}$	$\beta_{\rm D}$	$\nu_0 = 545$ GHz
		$T_{\rm D}$ [K]	
Free-Free	$g_{\rm FF} = \log\left(\dfrac{0.04955}{(\nu/10^9)}\right) + 1.5\,\log(T_{\rm e})$	EM [$\rm cm^{-6}pc$]	$T_{\rm e} = 8000$ K
	$T_{\rm FF} = 0.0314\,\dfrac{T_{\rm e}^{-.15}}{(\nu/10^9)^2}\,{\rm EM}\,g_{\rm FF}$		
	$I_{\rm FF}(\nu) = T_{\rm e}\,\left(1 - e^{-T_{\rm FF}}\right) \times I_{RJ}$		
Spinning Dust	$\Theta_{\rm SD}(\nu) = {\rm SD\ template}(\nu)$	$A_{\rm SD}$ [K]	$\nu_0 = 22.8$ GHz
	$\Delta I_{\rm SD}(\nu) = A_{\rm SD}\left(\dfrac{\nu_0}{\nu}\right)^2 \dfrac{\Theta_{\rm SD}(\nu\nu_{p_0}/\nu_p)}{\Theta_{\rm SD}(\nu_0\nu_{p_0}/\nu_p)} \times I_{RJ}$	ν_p [GHz]	$\nu_{p_0} = 30.0$ GHz
CMB	$X = \dfrac{h\nu}{k_B T_{\rm CMB}}$	$A_{\rm CMB}$ [K]	$T_{CMB} = 2.7255$ K
	$g_f = \dfrac{(e^X-1)^2}{X^2 e^X}$		
	$I_{\rm CMB} = A_{\rm CMB}/g_f \times I_{RJ}$		

3.4.1 Emission Mechanisms

Free-Free

Free-free emission is electron-ion collision radiation in our Galaxy, typically in HII regions. The model we used in this study was derived by Draine [90]. We used the same model for optically thin and optically thick free-free emission. The optically thin free-free emission is the diffuse signal commonly considered in CMB foreground analyses, while the optically thick free-free emission, which could be the source of the AME signal, has a much higher emission measure and is spatially compact. In both cases we found the spectrum is very weakly dependent on the electron temperature, and therefore we set it to the commonly used value of 8000 K. Since the optically thick signal is compact, we do not resolve it, and an additional solid angle parameter is added to the model to account for the size of the compact region. HII regions of the size and density we are considering are typically classified as ultra compact, so in this Chapter we commonly call the optically thick free-free emission UCHII. The difference between the optically thin and the optically thick spectra is shown in the right panel of Figure 3.7.

Thermal Dust

Thermal dust emission is the dominant radiation source above approximately 100 GHz. The model we used is a modified blackbody spectrum with a power law emissivity. The dust grain properties can widely vary, which is accounted for by the emissivity power law. This results in the 3-parameter modified black body spectrum we used. In principle, several different grain populations at different temperatures may be present in the G107.2+5.2 region and could be described by the inclusion of several modified blackbody spectra with different parameters. The presence of the star forming region S140 as well as the surrounding diffuse emission indeed could harbor grains at different temperatures, but the high-frequency data does not allow us to constrain multiple modified blackbody models and a model with

a different dust temperature would only affect the dust SFD at higher frequencies above 100 GHz. Additionally, the DIRBE beam size is $40'$ which does not allow us to spatially identify different regions within the beam.

CMB

The temperature of the CMB varies between our annulus and aperture because of the angular anisotropy. To account for this fact we included a CMB spectrum in our fit described by the first derivative of a blackbody with respect to the temperature. The amplitude of this derivative spectrum is a free parameter.

Spinning Dust

We used the spinning dust template from the Planck analysis [230], that is derived from the SPDust code [11, 275] using the warm ionized medium (WIM) spinning-dust parameters. The free parameters in the model are the amplitude and peak frequency. Spinning dust emission is typically correlated with thermal dust emission because the two signals are produced by the same dust grains. We searched for radio/infrared map-domain correlations (see Section 3.4.2), but this study was limited by the comparatively low resolution of the 28 GHz Planck data.

Other

We considered but ruled out other AME models including hard synchrotron radiation and thermal magnetic dust emission. Hard synchrotron radiation has a falling spectral flux density, which was ruled out because the spectrum would have to be increasing instead to produce the observed excess near 30 GHz. Note that we did not include conventional synchrotron radiation in our analysis for two reasons. First, synchrotron radiation is not expected to vary appreciably on scales less than 1 degree, so it would appear as an offset in the map and should not effect the detected signal morphology. Second, the shallowness

Table 3.5: Best-fit AME parameter values for an aperture region 45′ in radius. The associated models are given in Table 3.4, and the posteriors are plotted in Figures 3.8 and 3.9.

UCHII Model						
$\mathrm{EM_{Diffuse}}$	$\mathrm{EM_{UCHII}}$	θ_{UCHII}	A_{D}	β_{D}	T_{D}	A_{CMB}
$[\,\mathrm{cm^{-6}pc}\,]$	$[\,\mathrm{cm^{-6}pc}\,]$	$[\,\mathrm{arcsec}\,]$	$[\,\mu\mathrm{K}\,]$	$[\,-\,]$	$[\,\mathrm{K}\,]$	$[\,\mu\mathrm{K}\,]$
300^{+22}_{-24}	$5.27^{+2.5}_{-1.5} \times 10^8$	$2.49^{+0.47}_{-0.44}$	1160^{+27}_{-27}	$1.83^{+0.057}_{-0.056}$	$20.0^{+0.35}_{-0.34}$	-20.9^{+27}_{-28}
Spinning Dust Model						
$\mathrm{EM_{Diffuse}}$	A_{SD}	ν_p	A_{D}	β_{D}	T_{D}	A_{CMB}
$[\,\mathrm{cm^{-6}pc}\,]$	$[\,\mu\mathrm{K}\,]$	$[\,\mathrm{GHz}\,]$	$[\,\mu\mathrm{K}\,]$	$[\,-\,]$	$[\,\mathrm{K}\,]$	$[\,\mu\mathrm{K}\,]$
339^{+16}_{-16}	1380^{+160}_{-150}	$30.9^{+1.4}_{-1.4}$	1110^{+27}_{-27}	$1.94^{+0.057}_{-0.056}$	$19.4^{+0.32}_{-0.31}$	142^{+20}_{-20}

of the measured spectrum below approximately 10 GHz is not consistent with the common $\beta \approx -1$ spectral index in Jansky units [235], so if there is any background synchrotron radiation, then it has to be negligible. Thermal magnetic dust is a possible AME source, but this signal is expected to have a spectrum that peaks near 70 GHz [85, 94], so it can not produce the observed excess near 30 GHz.

3.4.2 Maps and Spatial Morphology

Our GBT maps show diffuse emission inside the photometry aperture, which extends out to approximately 45′ away from G107.2+5.2 (see Figure 3.4). This diffuse emission spatially correlates very well visually with the high resolution CGPS data at 408 MHz. Inside the photometry aperture we see the star forming region S140, a diffuse cloud centered on G107.2+5.2 (hereafter the cloud), and one bright radio point source. Outside the photometry aperture, we also detected three additional bright radio point sources and several other point sources with low SNR.

The diffuse emission centered on G107.2+5.2 appears in all of the maps from 408 MHz up to 100 GHz. This seems to indicated that this emission is diffuse free-free plus possibly AME near 30 GHz. Above 100 GHz the diffuse signal in this region is faint when compared with the signal from S140. This seems to indicate S140 contributes the majority of the thermal dust emission that appears in the measured spectrum. Since S140 appears all the

way down to 408 MHz, this seems to indicated that it contains a range of signals because thermal dust emission should be negligible below 70 GHz and effectively zero below 10 GHz (see Figure 3.7).

3.4.3 Interpretation of Results

The spectrum shows a clear deviation from a simple model consisting of only optically thin free-free emission and thermal dust emission near 30 GHz indicating there is AME somewhere in the region defined by our photometry aperture. The AME could be either in S140 or in the cloud or both. Given the varied angular resolutions of all of the data in this study – in particular the coarse resolution at 28 GHz – it is difficult to say which case is correct. Our GBT measurements near 5 GHz suggest the signal from the cloud is predominantly optically thin free-free emission. Therefore, viable AME models must rapidly rise above approximately 5 GHz, peak near 30 GHz, and then remain sub dominant to thermal dust emission above 100 GHz. Models based on both the spinning dust signal and the UCHII signal match this description. However, this new information puts a tighter constraint on the angular size and emission measure of viable UCHII AME scenarios.

Fitting the combined model with the UCHII AME component to the observed spectrum results in a best-fit emission measure of $5.27^{+2.5}_{-1.5} \times 10^8$ cm^{-6}pc and an angular size of $2.49^{+0.47}_{-0.44}$ arcseconds. Given that S140 is 910 pc away, the angular size from the fit corresponds to an HII region with a physical extent of $1.01^{+0.21}_{-0.20} \times 10^{-2}$ pc. Note that an UCHII region of this size and emission measure might be better classified as a hyper-compact HII region [208]. High-resolution, interferometric measurements of S140 at 15 GHz from AMI did indeed reveal a rising spectrum but did not conclusively resolve any UCHII regions and the AMI collaboration concluded the AME signal is likely from spinning dust [223]. Our spectrum fit suggests that, if it is present, we have enough sensitivity to see the UCHII signal in our GBT maps, however our maps do not conclusively show compact discrete sources in the the cloud. Therefore, if the AME signal is from UCHII emission in the cloud, then it

seems there must be multiple UCHII sources that together look like the single diffuse region we detected.

The combined model with the spinning dust AME component also explains the AME excess. The best-fit model gives a spinning-dust peak frequency of 30.9 ± 1.4 GHz, with a peak amplitude of $15.2^{+1.8}_{-1.7}$ Jy. Spinning dust should correlate well with thermal dust emission. The spinning-dust AME signal could be from S140, where there is obviously a significant amount of thermal dust emission, or it could be from the cloud or both. However, the Planck maps show that any thermal dust emission in the cloud is small. Therefore, if the AME is from spinning dust it seems likely that it is coming from S140. The resulting emission at 28 GHz is then both spinning dust emission emanating from around S140 and optically thin free-free emission from the diffuse cloud present at 28 GHz. The comparatively low angular resolution of the 28 GHz map results in the bright region over both S140 and the cloud as seen in Figure 3.10. To estimate the relative goodness-of-fit between the two models we calculated the Akaike Information Criteria [7] (AIC),

$$\mathrm{AIC} = 2\mathrm{k} - 2\ln(\hat{\mathcal{L}})\,, \tag{3.19}$$

where k is the number of model parameters (7 in both cases) and $\hat{\mathcal{L}}$ is the maximum value of the likelihood function. The AIC is an estimate of information loss and is used to select between two models, but does not reveal information on the absolute quality of the models. We found for the spinning dust model AIC = 54 and for the UCHII model AIC = 70. The AIC relative likelihood estimated that the UCHII model is 0.04% as likely as the spinning dust model to minimize the information loss and therefore strongly favors the spinning dust model.

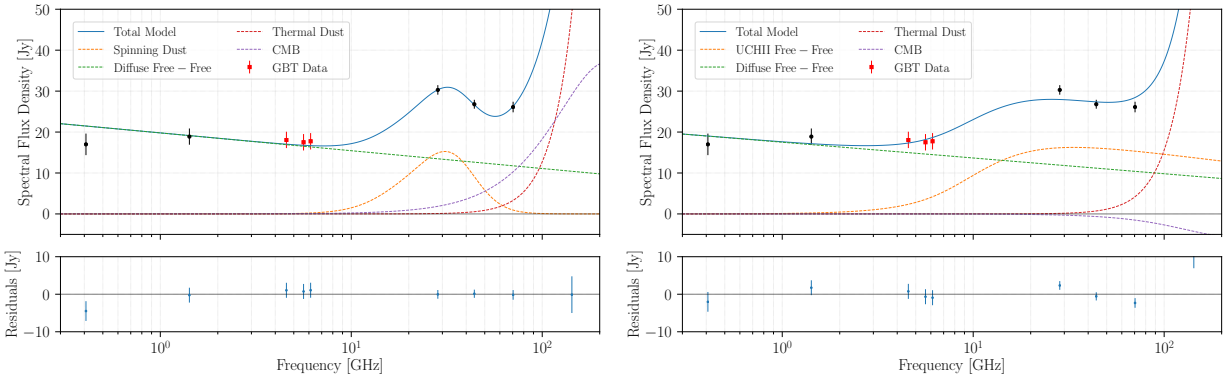

Figure 3.7: Data and best-fit models plotted between 300 MHz and 200 GHz. As in Figure 3.6, the models include diffuse free-free emission, thermal dust emission, the CMB, and one AME component – either spinning dust (left) or UCHII free-free (right). The residuals for both models are shown as well. The foreground models are given in Table 3.4, the best-fit model parameters are given in Table 3.5, and the posteriors are plotted in Figures 3.8 and 3.9.

3.5 Discussion

The goal for this study was to determine the AME mechanism in the G107.2+5.2 region. Our measurements are consistent with and further support the spinning dust scenario, and they conclusively ruled out some of parameter space for the UCHII scenario. Additional measurements are needed to concretely determine the emission mechanism.

High angular resolution measurements near 30 GHz are ideal. Ku-band (12.0 to 15.4 GHz) observations at GBT, for example, would provide valuable spectral information where the AME signal rises. If the AME signal is in fact from spinning dust, then polarization measurements in Ku band could convincingly reveal the polarization fraction of this spinning-dust signal. Additionally, the angular resolution in Ku band would be higher, providing a better view of the morphology of the region. Our original project proposal requested both C-band and Ku-band observations. Unfortunately, the Ku-band receiver was not available in the 17A semester at GBT when we observed. Therefore, we are planning a follow-up observing proposal for these Ku-band observations.

High resolution H-alpha measurements would also help because H-alpha is a tracer of free-free emission. We investigated the Finkbeiner composite H-alpha map that uses data

from the Wisconsin H $-$ α Survey and Virginia Tech Spectral Lines Survey [105]. However, in the G107.2+5.2 region the resolution of the survey is approximately 1 degree, which makes spatial comparisons difficult, and significant dust extinction is present.

3.6 Conclusions

In this study, we performed follow-up C-band observations of the region G107.2+5.2 and fit two potential AME models to the resulting spectra to explain the excess microwave emission at 30 GHz. We find that spinning dust emission or optically thick free-free emission can explain the AME in this region. Additional studies including higher spatial resolution data between 10 and 30 GHz as well as high resolution H-alpha data are necessary disentangle the two emission mechanics. Our analysis of the C-band polarization data are ongoing. We also plan to look at radio recombination lines between 4-8 GHz, using the high spectral resolution of the GBT data.

3.7 Parameter Posterior Distributions and External Maps

In this section we show the posterior probability distributions from the spectral flux density model fits (see Section 3.4) and all of the maps used in this study. The posteriors are shown in Figures 3.8 and 3.9, and the associated maximum-likelihood model parameter values are given in Table 3.5. The maps are shown in Figures 3.10 to 3.14. The left column of Figure 3.11 shows the Bank A, B, and C maps from this GBT study. These three maps are the same three maps shown in the left column of Figure 3.4, but smoothed with a $10'$ FWHM beam to remove noise and point sources. A contour plot of the smoothed Bank A map in this Figure (the top left panel) is overplotted on all of the maps in Figures 3.10 to 3.14 for a morphological comparison. This Bank A contour plot clearly shows S140 and the AME cloud centered on G107.2+5.2. The right column of Figures 3.10 to 3.12 shows the associated map in the left column smoothed to a resolution of $40'$; the photometry aperture

and the zero-point annulus are overplotted for comparison. The aperture photometry details are given in Section 3.3.4). For a morphological comparison (see Section 3.4.2), the nine highest-frequency maps (143 GHz to 25 THz) are shown in Figures 3.13 and 3.14.

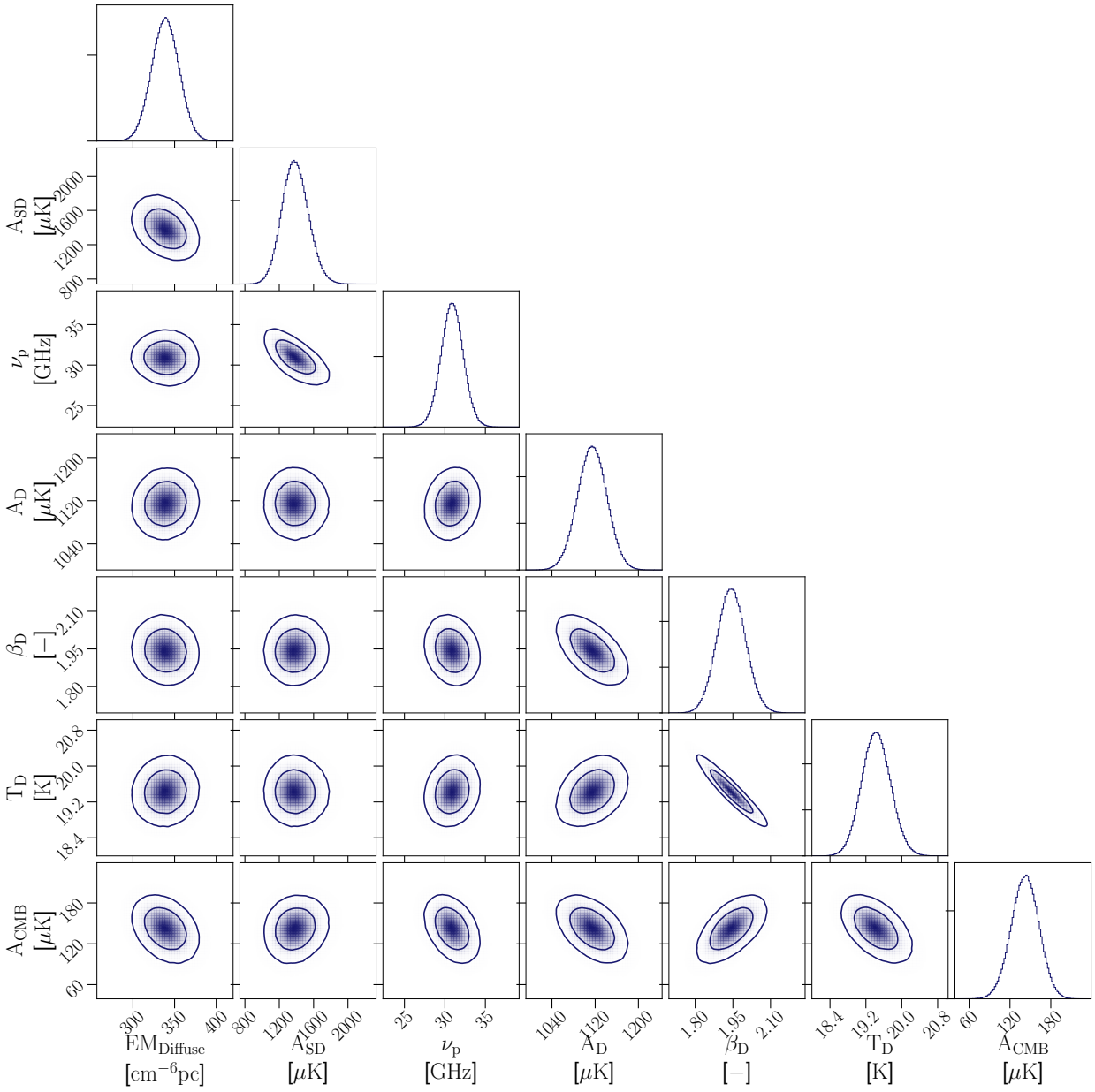

Figure 3.8: Posterior from fit using the spinning-dust model. The foreground models are given in Table 3.4, and the best-fit model parameters are given in Table 3.5.

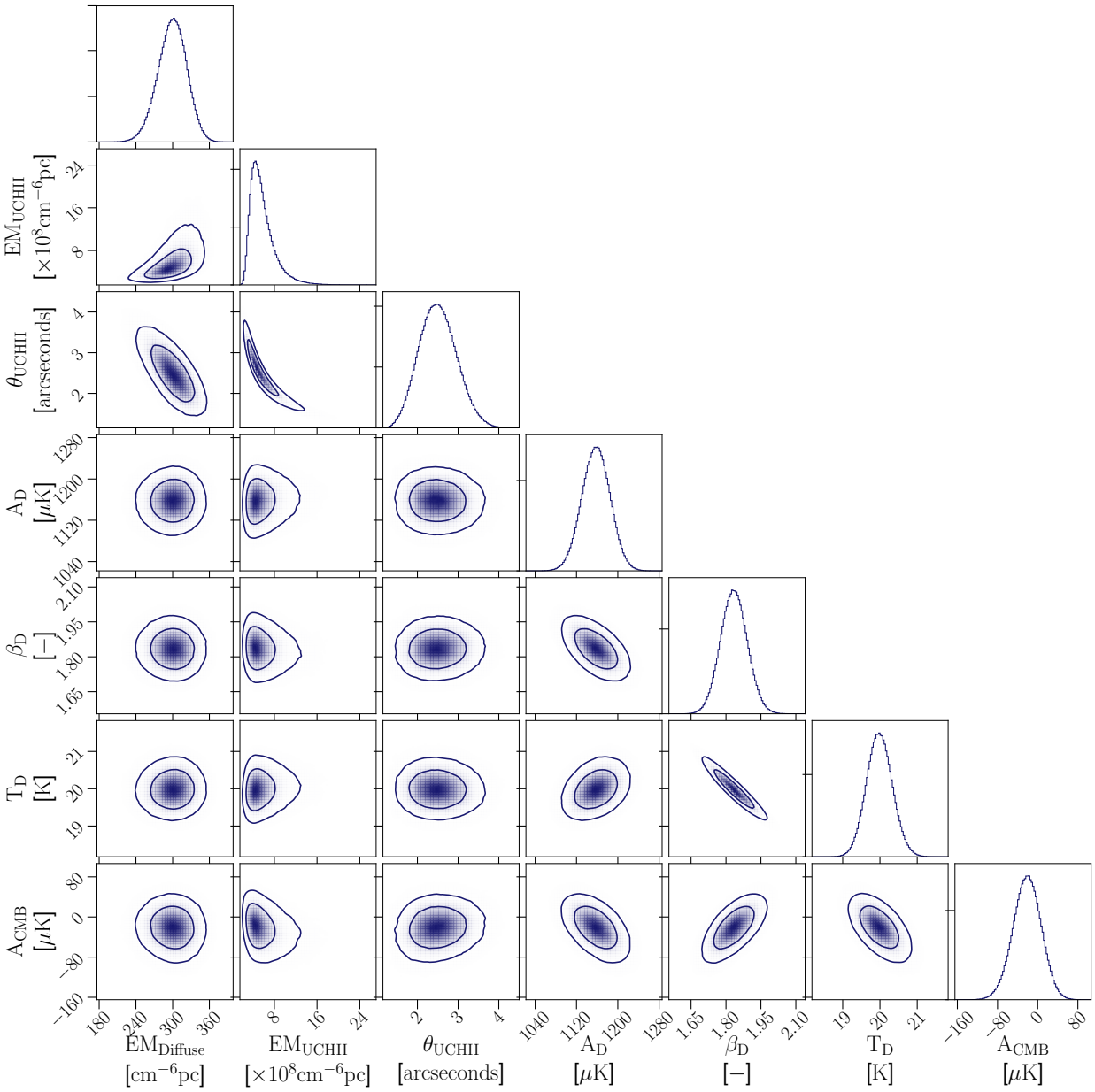

Figure 3.9: Posterior from fit using the UCHII model. The foreground models are given in Table 3.4, and the best-fit model parameters are given in Table 3.5.

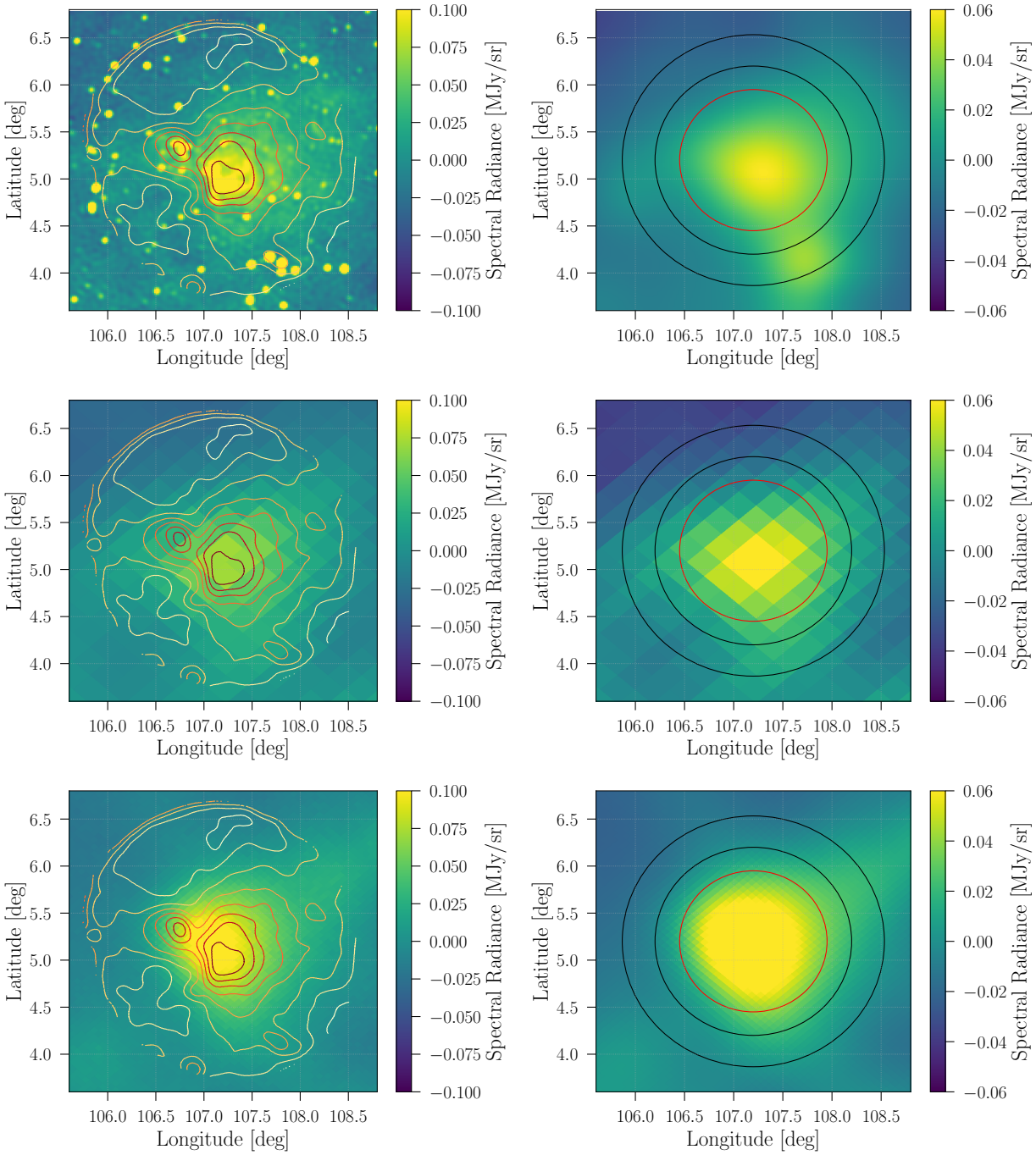

Figure 3.10: Maps used in this study. The left column shows the map with contours from our Bank A (4.575 GHz) map oveplotted for comparison. There are 12 contours from light to dark evenly spaced between -0.10 MJy sr^{-1} and 0.1 MJy sr^{-1} The right column shows the map on the left smoothed to 40′ resolution. Here, the aperture (circle 45′ radius) and the zero-point annulus (60′ to 80′) are overplotted. From top to bottom, the rows are CGPS (0.408 GHz), Stocker (1.42 GHz), and Planck (28 GHz). Maps in each column are plotted with the same color scale for straightforward comparison. References are given in Table 3.2.

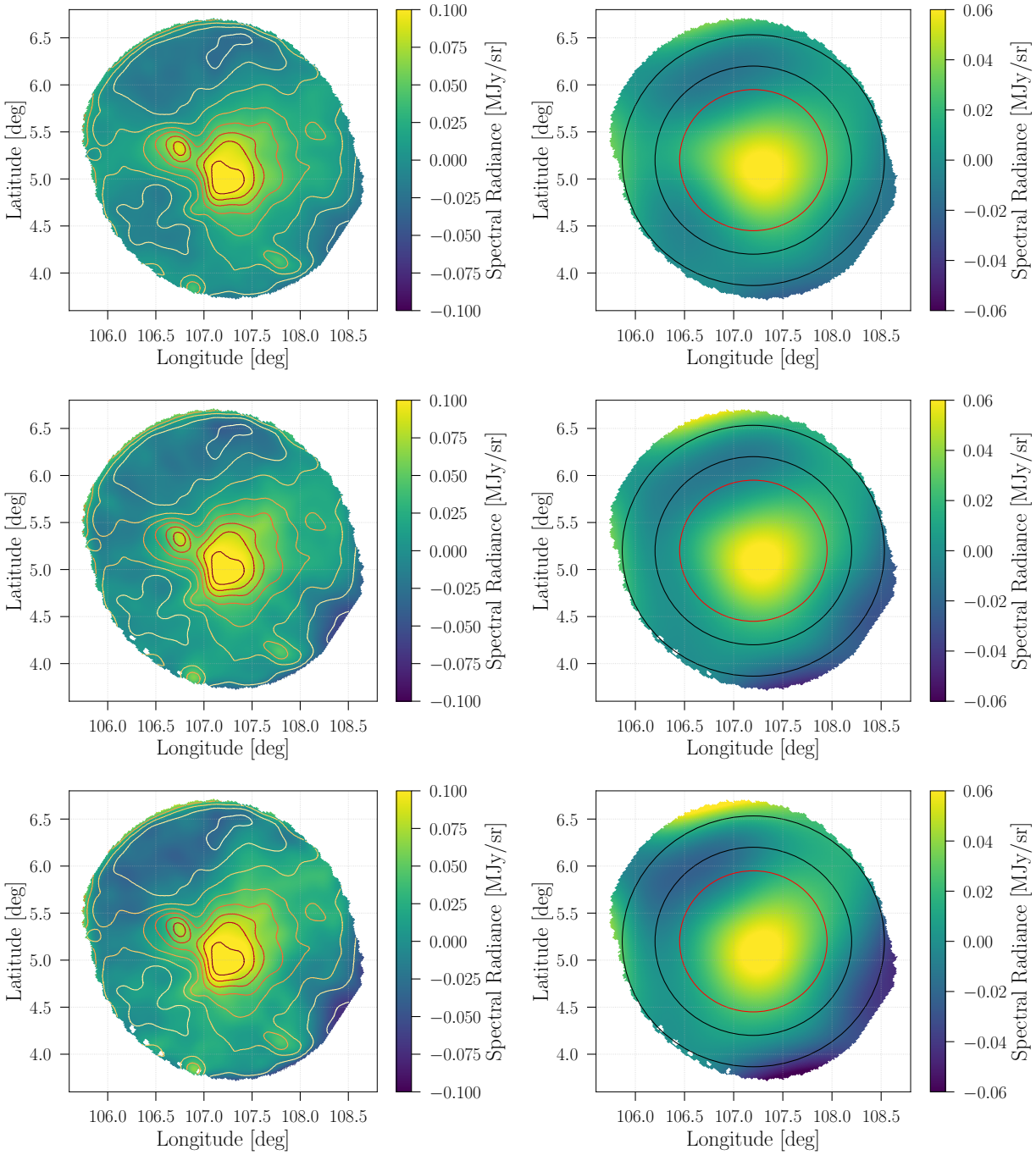

Figure 3.11: Maps used in this study. The left column shows the map with contours from our Bank A (4.575 GHz) map oveplotted for comparison. The right column shows the map on the left convolved with a 40′ Gaussian. Here, the aperture (circle 45′ radius) and the zero-point annulus (60′ to 80′) are overplotted. From top to bottom, the rows are GBT Bank A (4.575 GHz), GBT Bank B (5.625 GHz), and GBT Bank C (6.125 GHz). Maps in each column are plotted with the same color scale for straightforward comparison. References are given in Table 3.2.

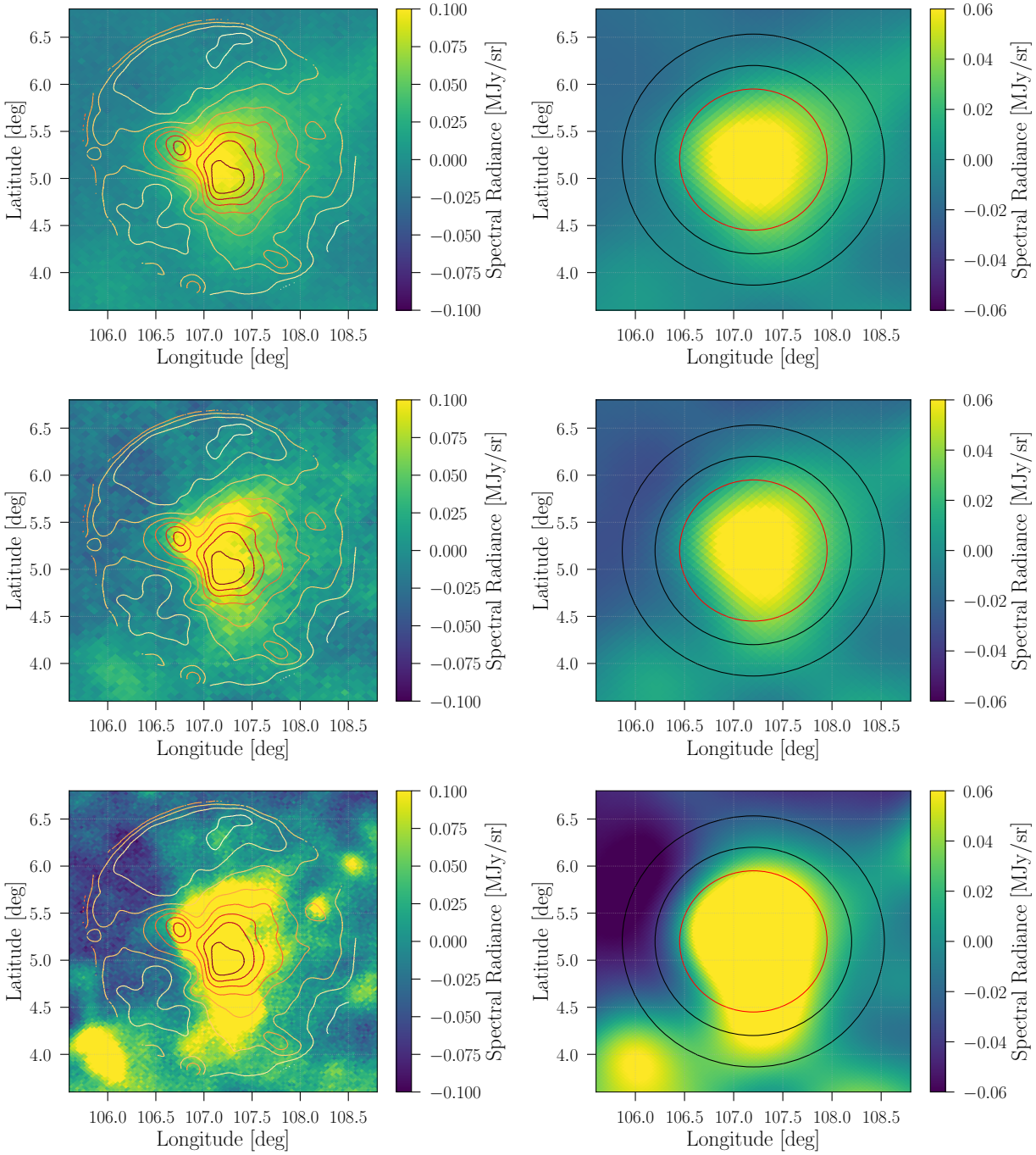

Figure 3.12: Maps used in this study. As in Figure 3.10, the left column shows the given map with our GBT contours oveplotted for comparison, while the right column shows the map on the left convolved with a 40′ Gaussian. Again, the aperture (45′ radius) and the zero-point annulus (60′ to 80′) are overplotted. From top to bottom, the rows are Planck 44 GHz, Planck 70 GHz, and Planck 100 GHz. Maps in each column are plotted with the same color scale for straightforward comparison. References are given in Table 3.2.

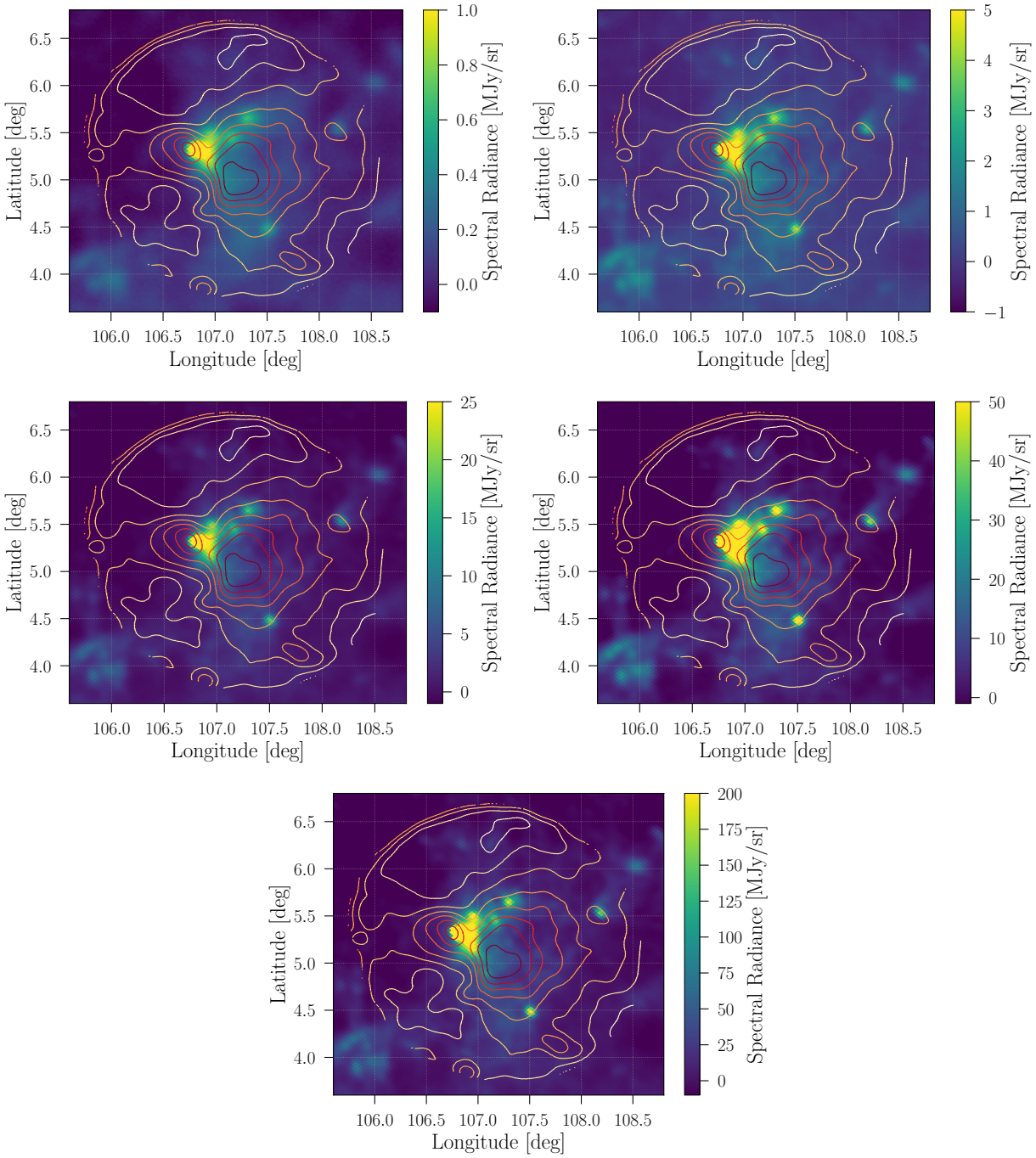

Figure 3.13: Morphological comparison between our GBT maps and the Planck maps between 143 GHz and 857 GHz. **Top Row:** Planck 143 GHz and 217 GHz maps. **Middle Row:** Planck 353 GHz and 545 GHz maps. **Bottom Row:** Planck 857 GHz map. The overplotted contours come from our Bank A (4.575 GHz) GBT map. References are given in Table 3.2.

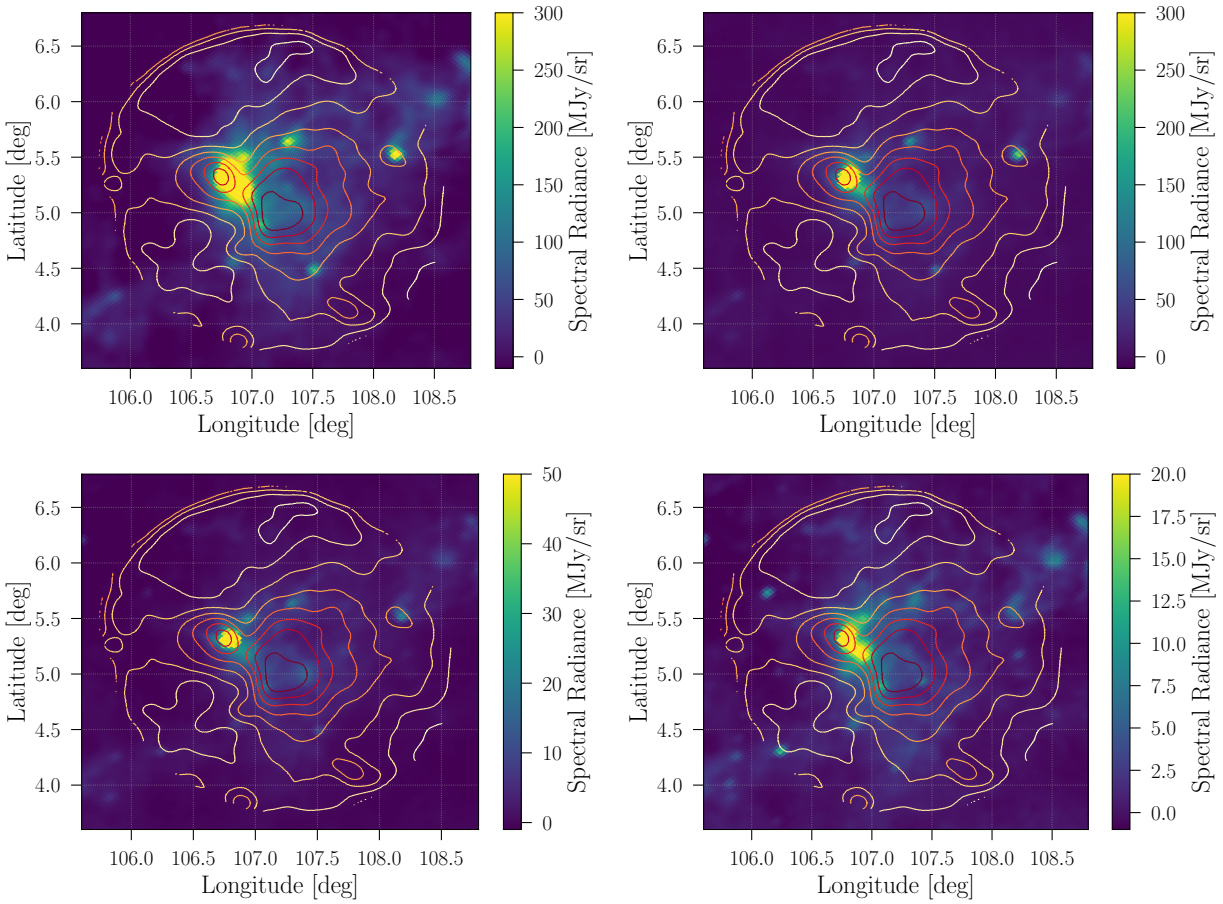

Figure 3.14: Morphological comparison between our GBT maps and the IRIS maps between 3 THz and 25 THz. **Top Row:** IRIS 3 THz and 5 THz maps. **Middle Row:** IRIS 12 THz and 25 THz maps. The overplotted contours come from our Bank A (4.575 GHz) GBT map. References are given in Table 3.2.

Chapter 4

Prospects for Measuring CMB Spectral Distortions in the Presence of Foregrounds

Measurements of cosmic microwave background spectral distortions have profound implications for our understanding of physical processes taking place over a vast window in cosmological history. Foreground contamination is unavoidable in such measurements and detailed signal-foreground separation will be necessary to extract cosmological science. In this Chapter, we present MCMC-based spectral distortion detection forecasts in the presence of Galactic and extragalactic foregrounds for a range of possible experimental configurations, focusing on the *Primordial Inflation Explorer* (*PIXIE*) as a fiducial concept. We consider modifications to the baseline *PIXIE* mission (operating $\simeq$ 12 months in distortion mode), searching for optimal configurations using a Fisher approach. Using only spectral information, we forecast an extended *PIXIE* mission to detect the expected average non-relativistic and relativistic thermal Sunyaev-Zeldovich distortions at high significance (194σ and 11σ, respectively), even in the presence of foregrounds. The ΛCDM Silk damping μ-type distortion is not detected without additional modifications of the instrument or external data. Galactic

synchrotron radiation is the most problematic source of contamination in this respect, an issue that could be mitigated by combining *PIXIE* data with future ground-based observations at low frequencies ($\nu \lesssim 15 - 30\,\mathrm{GHz}$). Assuming moderate external information on the synchrotron spectrum, we project an upper limit of $|\mu| < 3.6 \times 10^{-7}$ (95% c.l.), slightly more than one order of magnitude above the fiducial ΛCDM signal from the damping of small-scale primordial fluctuations, but a factor of $\simeq 250$ improvement over the current upper limit from *COBE/FIRAS*. This limit could be further reduced to $|\mu| < 9.4 \times 10^{-8}$ (95% c.l.) with more optimistic assumptions about extra low-frequency information and would rule out many alternative inflation models as well as provide new constraints on decaying particle scenarios.

4.1 Introduction

Spectral distortions of the cosmic microwave background (CMB) are one of the next frontiers in CMB science [64, 283, 292, 274, 56, 80]. The intensity spectrum of the CMB was precisely measured by *COBE/FIRAS* over two decades ago [192, 108] and is consistent with a blackbody at temperature $T_0 = 2.72548 \pm 0.00057$ K from $\nu \simeq 3\,\mathrm{GHz}$ to 3,000 GHz [106]. This agrees with a variety of other CMB observations including COBRA, TRIS, and ARCADE [123, 120, 175, 267]. These impressive measurements already place very tight constraints on the thermal history of the Universe [e.g., 284, 316, 151, 74], limiting early energy release to $\Delta\rho_\gamma/\rho_\gamma \lesssim 6 \times 10^{-5}$ (95% c.l.) relative to the CMB energy density [108, 107].

Most of our detailed current cosmological picture stems from measurements of the CMB temperature and polarization anisotropies, which have been well characterized by WMAP [139], *Planck* [232], and many sub-orbital experiments [e.g., 210, 258, 220, 253, 169, 98]. More precise measurements of the polarization anisotropies are being targeted by an array of ongoing experiments including BICEP2/3 and the KECK array, ACTPol, SPTPol, POLARBEAR, CLASS, SPIDER, and the Simons Array [32, 209, 170, 127, 104], all with the goal to fur-

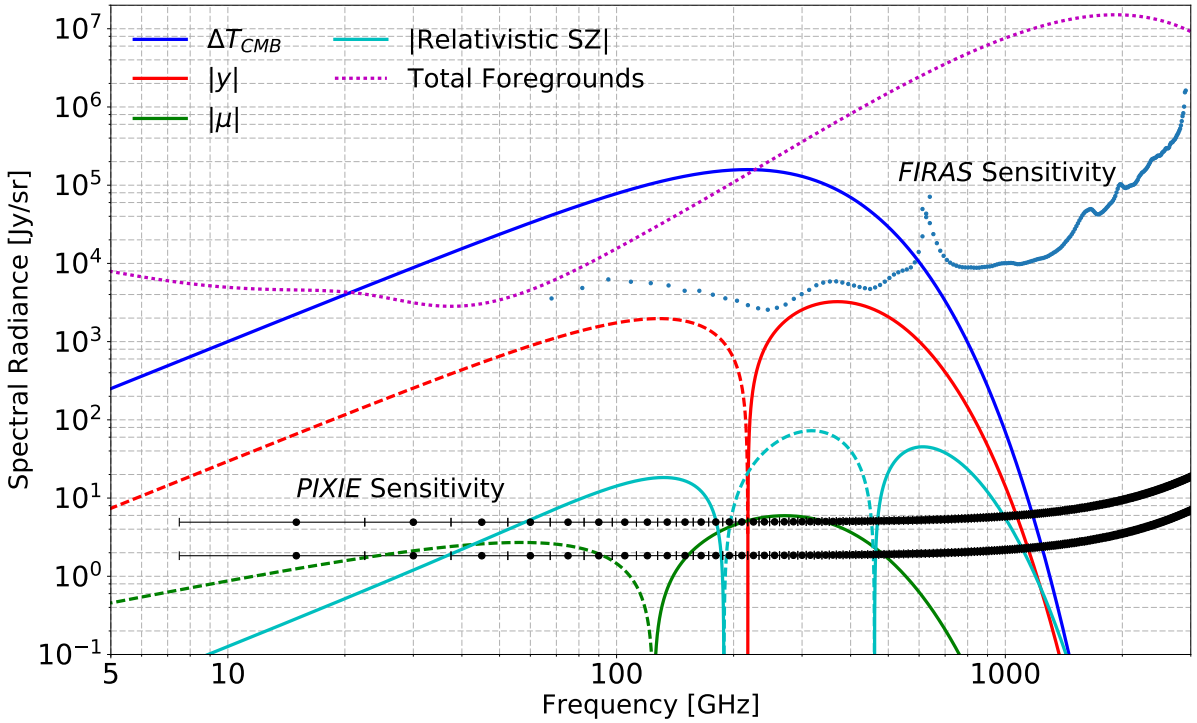

Figure 4.1: Spectral distortion signals compared to the *PIXIE* sensitivity and foregrounds. The signals include the CMB blackbody (blue) as well as the ΛCDM-predicted Compton-y (red), relativistic SZ (cyan), and μ (green) spectral distortions. The dashed and solid curves indicate negative and positive values, respectively. The total foreground model, which dominates over all non-blackbody signals, is shown in dotted magenta. The black points represent the *PIXIE* sensitivity for the nominal and extended mission, assuming $f_{sky} = 0.7$ and 12 or 86.4 months of integration time, respectively. The horizontal error bars on the noise curve points represent the width of the 15 GHz *PIXIE* frequency bins. For comparison, the *COBE/FIRAS* raw detector sensitivity is illustrated by the blue dots.

ther refine our understanding of the Universe and its constituents. Measurements of CMB spectral distortions could complement these efforts and provide access to qualitatively new information that cannot be probed via the angular anisotropy [see 58, for an overview of the standard ΛCDM distortions].

Spectral distortions are caused by processes (e.g., energy or photon injection) that affect the thermal equilibrium between matter and radiation [314, 286, 151, 43, 142, 64, 57]. One of the standard distortions, known as the Compton y-distortion, is created in the regime of inefficient energy transfer between electrons and photons, relevant at redshift $z \lesssim 5 \times$

10^4. Processes creating this type of distortion include the inverse-Compton scattering of CMB photons off hot electrons during the epoch of *reionization and structure formation* [288, 147, 248, 138], also known in connection with the thermal Sunyaev-Zeldovich (tSZ) effect [314], but can also be related to non-standard physics, e.g., the presence of *long-lived decaying particles* [262, 100, 143, 55].

Chemical potential or μ-type distortions [286], on the other hand, are generated by energy release at earlier stages ($z \gtrsim 5 \times 10^4$), when interactions are still extremely efficient and able to establish kinetic equilibrium between electrons and photons under repeated Compton scattering and photon emission processes (i.e., double Compton and Bremsstrahlung).

The latter are particularly important at $z \gtrsim 2 \times 10^6$, leading to a strong suppression of the distortion amplitude [e.g., 142]. Expected sources of μ-distortions include the *Silk damping of small-scale acoustic modes* in the early Universe [285, 73, 146, 67] and the extraction of energy from the photon bath due to the adiabatic cooling of ordinary matter [53, 64].

The *Primordial Inflation Explorer* (*PIXIE*) is a proposed satellite mission designed to constrain the primordial B-mode polarization power spectrum and target spectral distortions of the CMB [177, 178]. The instrument is a polarizing Michelson interferometer spanning 15 to 6,000 GHz with a mirror stroke length corresponding to $\simeq 15\,\mathrm{GHz}$ channels. In order to detect the small spectral distortion signals, Galactic and extragalactic foreground emission has to be precisely modeled, characterized, and marginalized over in the cosmological analysis. In this Chapter we forecast the capabilities of *PIXIE*-like experimental concepts for detecting spectral distortions in the presence of known foregrounds, extending simpler forecasts presented earlier [e.g., by 177, 60, 138].[1]

Our analysis solely considers the spectral energy distribution (SED) of the sky monopole, relying on the spectral behavior of different components in order to separate them. In contrast, we note that the *COBE/FIRAS* analysis relied on spatial information in order to separate the extragalactic monopole from Galactic foregrounds [and the CMB dipole] [108].

[1]Forecasts for the polarization sensitivity of *PIXIE* were described most recently in [45] and will not be addressed here.

An optimal analysis would combine spectral and spatial information, with the latter primarily helping to isolate Galactic foregrounds. We shall leave a more rigorous assessment to future work and for now focus on the available spectral information.

We apply a Fisher matrix approach to the fiducial *PIXIE* instrument configuration, spectral distortion signals, and standard foreground models to estimate uncertainties on the CMB signal parameters. We consider a range of foreground models and vary the *PIXIE* mission configuration to search for an optimal instrument setup based on the assumed sky signals. We compare part of the results to full Monte Carlo Markov Chain (MCMC) analyses, which do not rely on the assumption of Gaussian posteriors, finding good agreement. The considered signals and total foreground emission are illustrated in Fig. 4.1 and will be discussed in detail below.

The Chapter is organized as follows. We describe the *PIXIE* mission, fiducial CMB spectral distortions, and foreground models in Sections 4.2, 4.3, and 4.4, respectively. We summarize the forecasting calculations in Section 4.5. The CMB-only forecast is presented in Section 4.6. Forecasts with foregrounds are discussed in Section 4.7. We search for an optimal mission configuration in Section 4.7.3 and conclude in Section 4.8.

4.2 *PIXIE* Mission Configuration

We use the nominal *PIXIE* mission configuration as described in [176]. (A slightly updated concept was recently proposed[2] but the modifications do not significantly change the forecast.) The center of the lowest frequency bin is 15 GHz, with a corresponding 15 GHz bin width. The highest frequency bin in the nominal design is $\simeq$ 6 THz; however, due to the complexity of dust emission at such high frequencies, we use 3 THz as the highest bin edge, yielding a total of 200 channels for distortion science. This choice does not affect the forecasted uncertainties because the high-frequency foregrounds are not the limiting factor. In addition, the spectral distortion signals cut off well below 3 THz (see Fig. 4.1).

[2] Al Kogut, priv. comm.

Assuming 12 months of spectral distortion mode integration time (*PIXIE* will also spend time in polarization observation mode), the noise per $1^\circ \times 1^\circ$ pixel is $\simeq$ 747 Jy at low frequencies, which we convert to Jy/sr and assume 70% of the sky is used in the analysis. The projected noise increases at frequencies above 1 THz due to a low-pass filter in the instrument. For most of the forecasting below, we scale the sensitivity to an extended mission with 86.4 months of integration time (representing a 9 year mission with 80% of the observation time spent in distortion mode), with the noise scaling down as the square root of the mission duration. For a Fourier Transform Spectrometer (FTS) such as *PIXIE*, the lowest frequency bin is set by the size of the instrument. The mirror stroke length determines the frequency resolution. Additionally, increasing the bin width (i.e., reducing the mirror stroke) by a multiplicative factor decreases the noise by the same factor. This is due to the fact that the noise scales with the square root of the bandwidth and the square root of the integration time, both of which increase when increasing the bin size. We discuss the trade-off between frequency resolution and sensitivity in Section 4.7.3.

4.3 CMB Spectral Distortion Modeling

At the level of *PIXIE*'s expected sensitivity, the average CMB spectral distortion signal can be efficiently described by only a few parameters. We model the sky-averaged spectral radiance relative to the assumed CMB blackbody, ΔI_ν, as:

$$\Delta I_\nu = \Delta B_\nu + \Delta I_\nu^y + \Delta I_\nu^{rel-tSZ} + \Delta I_\nu^\mu + \Delta I_\nu^{\rm fg} \,. \tag{4.1}$$

Here, $\Delta B_\nu = B_\nu\left(T_{CMB}\right) - B_\nu(T_0)$ represents the deviation of the true CMB blackbody spectrum, $B_\nu(T_{\rm CMB})$, at a temperature $T_{CMB} = T_0(1+\Delta_T)$, from that of a blackbody with temperature $T_0 = 2.726\,{\rm K}$; ΔI_ν^y is the y-type distortion; $\Delta I_\nu^{\rm rel-tSZ}$ is the relativistic temperature correction to the tSZ distortion; ΔI_ν^μ is the μ-type distortion; and ΔI_ν^{fg} represents the sum of all foreground contributions. We describe our fiducial models for these signal

components below. The results are shown in Figure 4.1 in comparison to the *PIXIE* (nominal/extended mission) sensitivity and the total foreground level (described in Sect. 4.4).

Blackbody Component. The average CMB blackbody temperature must be determined in the analysis, as it is not currently known at the necessary precision [e.g., see 60]. We work to first order in $\Delta_T = (T_{CMB} - T_0)/T_0$, describing the temperature shift spectrum as

$$\Delta B_\nu \approx I_o \frac{x^4 \mathrm{e}^x}{(\mathrm{e}^x - 1)^2} \Delta_T \,, \tag{4.2}$$

with $I_o = (2h/c^2)\,(kT_0/h)^3 \approx 270\,\mathrm{MJy/sr}$ and $x = h\nu/kT_0$. For illustration, we assume a fiducial value $\Delta_T = 1.2 \times 10^{-4}$, consistent with current constraints [106]. The analysis is not affected significantly by this choice.

While simple estimates indicate that *PIXIE* is expected to measure T_{CMB} to the $\simeq \mathrm{n}K$ level [60], an improvement over *COBE/FIRAS* does not immediately provide new cosmological information simply because there is no cosmological prediction for the average photon temperature. By comparing the local ($\leftrightarrow$ current) value of T_{CMB} with measurements at earlier times, e.g., at recombination [232] or during BBN [280], constraints on entropy production can be deduced [280, 155]; however, these are not limited by the current $\simeq \mathrm{m}K$ uncertainty of T_{CMB}.

Cumulative Thermal SZ (y) Distortion. We adopt the model for the sky-averaged thermal SZ signal from [138], including both the standard non-relativistic (Compton-y) and relativistic contributions.[3] The Compton-y signal (tSZ) includes contributions from the intracluster medium (ICM) of galaxy groups and clusters (which dominate the overall signal), the intergalactic medium, and reionization, yielding a total value of $y = 1.77 \times 10^{-6}$ [138]. This is a conservative estimate as with increased AGN feedback larger values for y could be feasible [80]. Note that the actual monopole y value measured by *PIXIE* or other experiments

[3] *PIXIE* may also have sufficient sensitivity to constrain the sky-averaged *non-thermal* SZ signal, but we do not investigate this possibility here.

will also contain a primordial contribution in general, but this is expected to be 2–3 orders of magnitude smaller than the structure formation contributions [67]. We furthermore assume that the average y-distortion caused by the CMB temperature dipole, $y_{sup} = (2.525 \pm 0.012) \times 10^{-7}$ [61, 58], is subtracted. The non-relativistic tSZ signal takes the standard Compton-y form [314]:

$$\Delta I_\nu^y = I_o \frac{x^4 \mathrm{e}^x}{(\mathrm{e}^x - 1)^2} \left[x \coth\left(\frac{x}{2}\right) - 4 \right] y \,, \tag{4.3}$$

with cross-over frequency $\nu \simeq 218\,\mathrm{GHz}$.

We model the sky-averaged relativistic corrections to the tSZ signal, $\Delta I_\nu^{rel-tSZ}$, using the moment-based approach described in [138], whose calculation used the results of [213] up to fourth order in the electron temperature. For the MCMC calculations below, we generate the signal using moments of the optical-depth-weighted ICM electron temperature distribution of `SZpack` [68], with parameter values identical to those in [138], to which we refer the reader for more details. However, at *PIXIE*'s sensitivity, the SZ signal can be represented most efficiently using moments of the y-weighted ICM electron temperature distribution. In particular, using only the first two y-weighted moments is sufficient to reproduce the relativistic correction signal for our purpose. This is explained in more detail by [26] and greatly simplifies comparisons to the results of cosmological hydrodynamics simulations.

While we emphasize that the fiducial signal is generated using the more accurate optical-depth-weighted approach (in the MCMC case), the Fisher forecasts and MCMC fits below use the y-weighted moment approach in the analysis. The two approaches are equivalent in the limit of many temperature moments, but to reduce the number of parameters, the y-weighted approach provides an efficient re-summation of the signal templates. We denote the first moment of the y-weighted ICM electron temperature distribution as $kT_{\mathrm{e}SZ}$. The fiducial value is $kT_{\mathrm{e}SZ} = 1.245\,\mathrm{keV}$, which is recovered in noiseless estimates of the full signal (including all higher temperature moments) for *PIXIE* channel settings.

One can think of all-sky SZ observations as the ultimate stacking method for SZ halos. In foreground-free forecasts, the second moment of the underlying relativistic electron temper-

ature distribution, $\omega_2^{\mathrm{e}SZ}$, is also detectable with an extended *PIXIE* mission (see Table 4.2). In this case, the recovered noiseless relativistic correction parameters are $kT_{\mathrm{e}SZ} = 1.282\,\mathrm{keV}$ and $\omega_2^{\mathrm{e}SZ} = 1.152$ (again, for default *PIXIE* channel settings). The spectral templates for the relativistic tSZ signal can be expressed as

$$\Delta I_\nu^{rel-SZ} = I_o \frac{x^4 \mathrm{e}^x}{(\mathrm{e}^x-1)^2} \left\{ Y_1(x)\,\theta_\mathrm{e} + Y_2(x)\,\theta_\mathrm{e}^2 + Y_3(x)\,\theta_\mathrm{e}^3 + \left[Y_2(x)\,\theta_\mathrm{e}^2 + 3Y_3(x)\,\theta_\mathrm{e}^3 \right] \omega_2^{\mathrm{e}SZ} \right\} y \tag{4.4}$$

to sufficient precision for our analysis. Here, $\theta_\mathrm{e} = kT_{\mathrm{e}SZ}/m_\mathrm{e}c^2$ and $Y_i(x)$ are the usual functions obtained by asymptotic expansions of the relativistic SZ signal [265, 51, 154]. By characterizing the relativistic tSZ contribution one can learn about feedback processes during structure formation [138, 26].

Primordial μ Distortion. Chemical potential μ-type distortions [286] can be generated by many forms of energy release at redshifts $5 \times 10^4 \lesssim z \lesssim 2 \times 10^6$, including decaying or annihilating particles [e.g., 262, 143, 201, 55], the damping of small-scale density fluctuations [e.g., 285, 73, 23, 67], and injection from cosmic strings [215, 293, 294] or primordial black holes [48, 10]. A negative μ distortion is also generated by the Compton-cooling of CMB photons off the adiabatically evolving electrons [53, 64].

Here, we assume only the "vanilla" sources exist in our Universe, in particular the μ signals from acoustic damping and adiabatic cooling [67, 58]. The latter signal is expected to be roughly one order of magnitude smaller than the former. We adopt a fiducial value of $\mu = 2 \times 10^{-8}$, consistent with current constraints on the primordial power spectrum [67, 60, 44, 58]. The spectral dependence of the μ-distortion is given by [e.g., 67, 54]:

$$\Delta I_\nu^\mu = I_o \frac{x^4 \mathrm{e}^x}{(\mathrm{e}^x-1)^2} \left[\frac{1}{\beta} - \frac{1}{x} \right] \mu\,. \tag{4.5}$$

with $\beta \approx 2.1923$. This distortion has a shape that is similar to that of the y-type distortion,

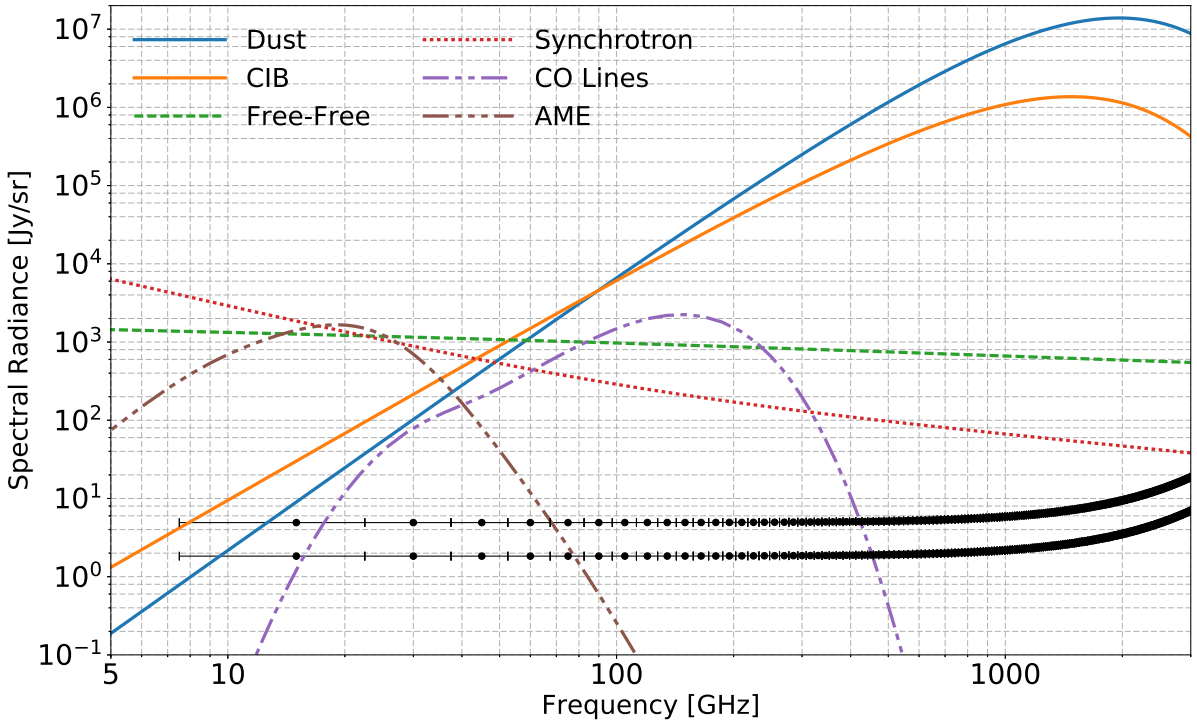

Figure 4.2: Foreground spectral radiance relative to the CMB blackbody, ΔI_ν^{fg}, for the components in our model (as labeled in the figure). The black points with horizontal error bars represent the *PIXIE* sensitivity and bin width for the nominal and extended mission duration, as in Figure 4.1. Galactic and extragalactic dust emission dominates at high frequencies, but multiple components are important at low frequencies ($\nu \lesssim 100$ GHz).

but with a zero-crossing at $\nu \simeq 125\,\mathrm{GHz}$ rather than $\nu \simeq 218\,\mathrm{GHz}$ (see Fig. 4.1). By measuring the μ-distortion parameter one can place tight limits on the amplitude of the primordial power spectrum at small scales corresponding to wavenumber $k \simeq 10^3\,\mathrm{Mpc}^{-1}$ [e.g., 67, 66, 71].

Residual Distortions. For a given energy release history, in general spectral distortions are generated which are not fully described by the sum of the μ- and y-type shapes [64, 171, 54], yielding the so-called "residual" or r-type distortion. However, for the concordance ΛCDM cosmology, the lowest-order r-type distortion is expected to be well below *PIXIE*'s sensitivity [60, 58]. Thus, we neglect this contribution in the forecasts carried out below. In an analysis of actual *PIXIE* data, it will be interesting to search for and constrain this signal, as it can be sizeable in non-standard scenarios, e.g., those related to energy release from decaying particles [60].

Cosmological Recombination Spectrum. The cosmological recombination process occurring at $z \simeq 10^3$ also causes a very small distortion of the CMB spectrum visible at $\nu \simeq 1\,\mathrm{GHz} - 3\,\mathrm{T}Hz$ through photon injection [315, 96, 282]. Thïs signal can now be accurately computed [260, 62, 65, 8, 59] and would provide a novel way to constrain cosmological parameters, such as the baryon density and primordial helium abundance [63, 282]. However, since this signal is about one order of magnitude below the sensitivity of *PIXIE* [82], we neglect it in our analysis. A detection of the recombination signal could become feasible in the future using ground-based detector arrays operating at low frequencies, $\nu \simeq 2 - 6\,\mathrm{GHz}$ [263].

Table 4.1: Foreground model motivated by *Planck* data. All SEDs, $\Delta I_{\rm X}$, are in units of Jy/sr. For each component, we also give the value of $\Delta I_{\rm X}(\nu_r)$ at $\nu_r = 100\,\mathrm{GHz}$ for reference.

Foreground	Spectral Radiance [Jy/sr]	Free Parameters and Values	Additional Information
Thermal Dust	$x = \frac{h\nu}{kT_{\rm D}}$ $\Delta I_{\rm D}(\nu) = A_{\rm D}\, x^{\beta_{\rm D}}\, \frac{x^3}{{\rm e}^x - 1}$	$A_{\rm D} = 1.36 \times 10^6$ Jy/sr $\beta_{\rm D} = 1.53$ $T_{\rm D} = 21$ K	$\Delta I_{\rm D}(\nu_r) = 6,608$ Jy/sr
CIB	$x = \frac{h\nu}{kT_{CIB}}$ $\Delta I_{CIB}(\nu) = A_{CIB}\, x^{\beta_{CIB}}\, \frac{x^3}{{\rm e}^x - 1}$	$A_{CIB} = 3.46 \times 10^5$ Jy/sr $\beta_{CIB} = 0.86$ $T_{CIB} = 18.8$ K	$\Delta I_{CIB}(\nu_r) = 6,117$ Jy/sr
Synchrotron	$\Delta I_{\rm S}(\nu) = A_{\rm S} \left(\frac{\nu}{\nu_0}\right)^{\alpha_{\rm S}} \left[1 + \frac{1}{2}\omega_{\rm S} \ln^2\left(\frac{\nu}{\nu_0}\right)\right]$	$A_{\rm S} = 288.0$ Jy/sr $\alpha_{\rm S} = -0.82$ $\omega_{\rm S} = 0.2$	$\Delta I_{\rm S}(\nu_r) = 288$ Jy/sr 10% prior assumed on $A_{\rm S}$ and $\alpha_{\rm S}$ $\nu_0 = 100$ GHz
Free-Free	$\nu_{ff} = \nu_{FF}\,(T_{\rm e}/10^3\ {\rm K})^{3/2}$ $\Delta I_{FF}(\nu) = A_{FF}\left(1 + \ln\left[1 + \left(\frac{\nu_{ff}}{\nu}\right)^{\sqrt{3}/\pi}\right]\right)$	$A_{FF} = 300$ Jy/sr	$\Delta I_{FF}(\nu_r) = 972$ Jy/sr $\{T_{\rm e}, \nu_{FF}\} = \{7000\ {\rm K},\ 255.33\,{\rm GHz}\}$
Integrated CO	$\Theta_{CO}(\nu) = \text{CO template}(\nu)$ $\Delta I_{CO}(\nu) = A_{CO}\Theta_{CO}(\nu)$	$A_{CO} = 1$	$\Delta I_{CO}(\nu_r) = 1,477$ Jy/sr Template in Jy/sr
Spinning Dust	$\Theta_{SD}(\nu) = \text{SD template}(\nu)$ $\Delta I_{SD}(\nu) = A_{SD}\Theta_{SD}(\nu)$	$A_{SD} = 1$	$\Delta I_{SD}(\nu_r) = 0.25$ Jy/sr Template in Jy/sr

4.4 Foreground Modeling

We consider six main astrophysical foregrounds which contaminate CMB measurements in the frequency range from 10 GHz to 3 THz: Galactic thermal dust, cosmic infrared background (CIB), synchrotron, free-free, integrated CO, and spinning dust emission (anomalous microwave emission, or AME). We use the *Planck* results to estimate each component's SED [235]. While *Planck* measured intensity fluctuations, *PIXIE* will measure the absolute sky intensity. We assume that the SEDs of the fluctuations measured by *Planck* can be used to model the monopole SED for each foreground.

Figure 4.2 shows each foreground SED and Table 4.1 lists the relevant parameters. All SEDs are given in absolute intensity units of spectral radiance [Jy/sr]. The results presented below do not depend strongly on the amplitudes of the foregrounds (within reasonable ranges), but they do depend on the spectral shapes of the foregrounds and the associated number of free parameters (see Sect. 4.7.1 for discussion). The foreground-to-signal level sets the calibration requirement for the instrument, but we ignore instrumental systematics for the purposes of this work. Our results hold as long as the shapes of the foreground emission do not deviate strongly from the assumed models.

An important note is that for this analysis we assume these SEDs represent the sky-averaged spectra of the foregrounds. The foreground emission varies across the sky and the average of a specific SED model over a distribution of parameter values is not in general represented by the same SED with a single set of parameter values. For example, averaging many modified blackbody spectra with different temperatures does not correspond exactly to a modified blackbody with a single temperature [similarly, averaging over the CMB temperature anisotropy itself produces a small y-distortion [61]]. A moment expansion approach could appropriately handle the effects of different averaging processes [69]. Spatial information about the Galactic foreground emission could also help in separating signals from foregrounds. We limit the scope of this study to understanding how the shapes of known foreground SEDs impact our ability to measure spectral distortions and leave spatial consid-

erations to future work. In addition, we do not consider effects due to imperfect modeling, as described for example in [136] for a polarization forecast.

For *PIXIE*, we find below that the limiting foregrounds are those which dominate at low frequency, specifically synchrotron and free-free emission, and spinning dust to a lesser extent. Additional measurements of these signals below 100 GHz will be necessary for a detection of the standard ΛCDM μ-type spectral distortion. *PIXIE* will set the most stringent constraints to date on the thermal dust and CIB emission and these limits could only be improved by increasing the effective integration time of the experiment. We consider including information from external datasets in the form of priors on select foreground parameters in Section 4.7.2. In total there are 12 free foreground parameters. We describe our model for each foreground SED in the following.

Thermal Dust and Cosmic Infrared Background. The brightest foregrounds at frequencies above 100 GHz are due to Galactic thermal dust and the cumulative redshifted emission of thermal dust in distant galaxies, called the cosmic infrared background (CIB). The physical characteristics of dust grains, such as the molecular composition, grain size, temperature, and emissivity, vary widely in the Galaxy, but for CMB analyses this is often summed into a modified blackbody spectrum. *Planck* finds empirically that a single-temperature modified blackbody describes the observed emission well, and we therefore adopt this model [235]. We similarly use a modified blackbody to represent the CIB emission, and use data from *Planck* to determine the parameters [228]. Due to the more complex emission and absorption spectra of dust at frequencies near and above 1 THz, the *Planck* analysis cautions against the use of the model at such high frequencies. However, for the purpose of this forecast we extend the model to 3 THz. Cutting the forecast off at 1 THz only marginally affects the forecasted *PIXIE* performance.

Each modified blackbody is characterized by 3 parameters: the amplitude, spectral index, and dust temperature, for a total of 6 thermal dust and CIB foreground parameters. This

list can be extended using a moment expansion method [69]; however, in this case the use of spatial information, possibly from future high-resolution CMB imagers [297, 15], is essential but beyond the scope of this work, so that we limit ourselves to a 6-parameter model.

Synchrotron. The most dominant low-frequency foreground comes from the synchrotron emission of relativistic cosmic ray electrons deflected by Galactic magnetic fields. The shape of this emission is predicted to obey a power law with a spectral index of approximately $\alpha_{sync} \simeq -1$ in intensity units (i.e., approximately $\alpha^T_{sync} \simeq -3$ in brightness temperature). Empirically, *Planck* finds a power law with a flattening at low frequencies to best fit the data [235]. Additional low-frequency SED modeling is discussed in [79] and [264], with the latter introducing physically-motivated SED approximations.

To avoid the use of a template and allow for a more general SED we use a power law with logarithmic curvature to describe the Galactic synchrotron emission. Such spectral curvature generically arises when averaging over power-law SEDs with different spectral indices [e.g., 69]. There are thus 3 free parameters in our model: the amplitude, spectral index, and curvature index. Spectral curvature is usually neglected for single-pixel SED modeling; however, line-of-sight and beam averages cannot be avoided and thus require its inclusion at the level of sensitivity reached by *PIXIE* [69].

We estimate the synchroton parameters by fitting this model to the *Planck* synchrotron spectrum. Unless stated otherwise, we impose a 10% prior on the synchrotron amplitude and spectral index throughout the forecasting to represent the use of external datasets such as the Haslam 408 MHz map, *WMAP*, *Planck*, C-BASS, QUIJOTE, or future observations [128, 129, 254, 29, 235, 153, 117]. We find that in particular future low-frequency ($\lesssim 15-30$ GHz) observations that can constrain the synchrotron SED or limit its contribution using spatial information to better than 1% will be very valuable for tightening the constraints on μ.

Free-free Emission. The next brightest foreground at low frequencies, following a relatively shallow spectrum, is the thermal free-free ($\leftrightarrow$ Bremsstrahlung) emission from electron-

ion collisions within the Galaxy (for example in HII regions). The shape of the spectrum is derived from [90]. We neglect the small high-frequency suppression (at $\nu \gtrsim 1\,\mathrm{T}Hz$) caused by the presence of CMB photons in the spectral template [69]. At the relevant frequencies, the spectrum is very weakly dependent on the electron temperature, and we therefore only allow for one free parameter, corresponding to the overall amplitude in intensity units. We estimate the amplitude by fitting this model to the free-free spectrum from *Planck* [235].

Cumulative CO. The cumulative CO emission from distant galaxies adds another foreground that will interfere with CMB spectral distortion measurements. From the theoretical point of view, the exact spectral shape is very uncertain and depends on the star-formation history [257]. Recent observations with *ALMA* place a lower limit on the integrated cosmic CO signal [47], which is consistent with these models.

Here, we take the spectra calculated by [191] and produce a template with one free amplitude parameter to model the average CO emission. In principle, one could allow the spectral shape of each individual line to vary (with some relative constraints on the amplitudes), but for simplicity we use only one template. We note that cross-correlations with galaxy redshift surveys could provide an independent estimate of the CO SED (and other lines) via intensity mapping [270, 291], which could be used to improve the modeling.

Spinning Dust Grains. Lastly, we consider AME, which is non-negligible at $\nu \simeq 10 - 60\,\mathrm{GHz}$ and thought to be sourced by spinning dust grains with an electric dipole moment [93]. We adopt the model used by *Planck*, which generates a template from a theoretically calculated SED [235] [see also [9] and references therein]. We allow one free parameter for the amplitude of the AME template. This is a relatively rigid parameterization, but the AME is not a dominant source of error in the forecast and we find that expanding the model does not significantly change the results. We furthermore anticipate that future ground-based observations will help to improve the modeling of this component, given its potential relevance to ongoing and planned B-mode searches [153, 117].

Table 4.2: CMB-only MCMC forecasts. This table gives noise-limited constraints for CMB spectral distortion parameters in a no-foreground scenario, derived via MCMC methods. The fiducial parameter values are $\Delta_T^{\rm f} = 1.2 \times 10^{-4}$, $y^{\rm f} = 1.77 \times 10^{-6}$, $\mu^{\rm f} = 2.0 \times 10^{-8}$, and $kT_{{\rm e}SZ}^{\rm f} = 1.245\,{\rm keV}$. The table lists the MCMC-recovered values with 1σ uncertainties, as well as detection significances in parentheses (fiducial parameter value divided by 1σ error). We illustrate the improvement resulting from an extended nine-year *PIXIE* mission (86.4 months of integration time in spectral distortion mode). We consider spectral distortion models of increasing complexity to examine potential biases in the parameters. Parameter values that are left blank were not included in the model. The small biases seen in μ and Δ_T are due to the fact that the relativistic SZ signal includes contributions from higher-order temperature moments. This bias disappears when including the y-weighted temperature dispersion, $\omega_2^{{\rm e}SZ}$, in the analysis. In this case, one expects to find $kT_{{\rm e}SZ} \simeq 1.282\,{\rm keV}$ and $\omega_2^{{\rm e}SZ} \simeq 1.152$ in noiseless observations (see Sect. 4.6 for more discussion).

Parameter	Baseline	Extended	Baseline
$(\Delta_T - \Delta_T^{\rm f})\,[10^{-9}]$	$0.0^{+2.3}_{-2.3}$	$0.00^{+0.85}_{-0.85}$	$-0.5^{+2.3}_{-2.3}$
$y\,[10^{-6}]$	$1.7700^{+0.0012}_{-0.0012}\,(1475\sigma)$	$1.77000^{+0.00044}_{-0.00044}\,(4023\sigma)$	$1.7692^{+0.0012}_{-0.0012}\,(1474\sigma)$
$\mu\,[10^{-8}]$	$2.0^{+1.3}_{-1.3}\,(1.5\sigma)$	$2.00^{+0.50}_{-0.50}\,(4.0\sigma)$	$2.3^{+1.4}_{-1.4}\,(1.6\sigma)$
$kT_{{\rm e}SZ}\,[{\rm keV}]$	–	–	$1.244^{+0.029}_{-0.030}\,(42\sigma)$
$\omega_2^{{\rm e}SZ}$	–	–	–

Parameter	Extended	Extended
$(\Delta_T - \Delta_T^{\rm f})\,[10^{-9}]$	$-0.53^{+0.84}_{-0.86}$	$0.00^{+0.87}_{-0.87}$
$y\,[10^{-6}]$	$1.76921^{+0.00044}_{-0.00044}\,(4021\sigma)$	$1.76996^{+0.00050}_{-0.00050}\,(3540\sigma)$
$\mu\,[10^{-8}]$	$2.30^{+0.53}_{-0.52}\,(4.3\sigma)$	$2.00^{+0.53}_{-0.53}\,(3.8\sigma)$
$kT_{{\rm e}SZ}\,[{\rm keV}]$	$1.244^{+0.011}_{-0.011}\,(113\sigma)$	$1.281^{+0.016}_{-0.016}\,(80\sigma)$
$\omega_2^{{\rm e}SZ}$	–	$1.14^{+0.32}_{-0.33}\,(3.5\sigma)$

Other Components. For the purpose of our forecast, we only include the above foregrounds, which are well-known and (relatively) well-characterized. We neglect several other potential foreground signals, such as additional spectral lines [e.g., CII; see 47, 270] or intergalactic dust [152]. In an effort to capture the dominant effects of the known foregrounds, we also do not include more general models for our foreground signals, with some possible generalizations being discussed in [69]. One could also use physical models instead of templates for the CO and AME, or extended dust models with distributions of temperatures and emissivities [e.g., 172, 69]. This will be studied in the future and also requires taking spectral-spatial information into account.

4.5 Forecasting Methods

We implement two methods to estimate the capability of *PIXIE* (or other CMB spectrometers) to constrain the signals described above. First, we use a Markov Chain Monte Carlo (MCMC) sampler to calculate the parameter posterior distributions. This allows us to determine the most likely parameter values and the parameter uncertainties, even in the case of highly non-Gaussian posteriors, as can be encountered close to the detection threshold. Second, we employ a Fisher matrix calculation to determine the parameter uncertainties, assuming Gaussian posteriors. The Fisher method has the benefit of running much more quickly than the MCMC, which allows us to more easily explore the effects of modifying the instrument configuration. In the high-sensitivity limit (i.e., when Gaussianity is an excellent approximation), the two methods converge to identical results. The Fisher information matrix is calculated as

$$F_{ij} = \sum_{a,b} \frac{\partial(\Delta I_\nu)_a}{\partial p_i} C_{ab}^{-1} \frac{\partial(\Delta I_\nu)_b}{\partial p_j} \,. \tag{4.6}$$

Here the sum is over frequency bins indexed by $\{a, b\}$, p_i stands for parameter i, and C_{ab} is the *PIXIE* noise covariance matrix, which we assume to be diagonal. The parameter covariance matrix is then calculated by inverting the Fisher information, F_{ij}.

For the MCMC sampling, we use the `emcee` package [112], with wrappers developed previously as part of `SZpack` [68] and `CosmoTherm` [55]. This method allows us to obtain realistic estimates for the detection thresholds when non-Gaussian contributions to the posteriors become noticeable. It also immediately reveals parameter biases introduced by incomplete signal modeling. We typically use $N \simeq 200$ independent walkers and vary the total number of samples to reach convergence in each case. Unless stated otherwise, flat priors over a wide range around the input values are assumed for each parameter. We impose a lower limit $A_{sync} > 0$, as in many of the estimation problems this unphysical region would otherwise be explored due to the large error on A_{sync}. For high-dimensional cases (14 and 16 parameters), we find the convergence of the affine-invariant ensemble sampler in the `emcee` package to

become extremely slow, so that in the future alternative samplers should be used.

4.6 CMB-Only Distortion Sensitivities

To estimate the maximal amount of information that *PIXIE* could extract given its noise level, we perform several MCMC forecasts omitting foreground contamination. The CMB parameters are $\Delta_T = (T_{CMB} - T_0)/T_0$, y, kT_{eSZ}, and μ. Considering the cases with only Δ_T, y, and μ (i.e., neglecting the relativistic SZ temperature corrections), the baseline mission (12 months spent in distortion mode) yields a significant detection of the y-parameter, but only a marginal indication for non-zero μ (see Table 4.2). This situation improves for an extended mission (86.4 months in distortion mode), suggesting that a $\simeq 4\sigma$ detection of μ would be possible. In both cases, the constraints are driven by channels at $\nu \lesssim 1\,\mathrm{T}Hz$.

When adding the relativistic temperature correction to the SZ signal and modeling the data using Δ_T, y, μ, and the y-weighted electron temperature $kT_{eSZ} = \langle y\, kT_e \rangle \,/\, \langle y \rangle$, only a small penalty is paid in the constraint on μ: the error increases from $\sigma_\mu \simeq 1.3 \times 10^{-8}$ to $\sigma_\mu \simeq 1.4 \times 10^{-8}$ for the baseline mission, consistent with the results of [138]. A very significant measurement of kT_{eSZ} is expected. The central value of μ is biased high by $\Delta\mu \simeq 0.3 \times 10^{-8}$, since the relativistic SZ correction model includes contributions from higher-order moments that are not captured by only adding kT_{eSZ} (see Sect. 4.3). When also adding the second moment of the y-weighted electron temperature to the analysis (ω_2^{eSZ}), this bias disappears. The main penalty for adding this parameter is paid by kT_{eSZ}, for which the detection significance degrades by a factor of $\simeq 1.4$. The second temperature moment is seen at a similar level of significance as μ. The relativistic distortion signal receives extra information from frequencies $\nu \simeq 1\,\mathrm{T}Hz - 2\,\mathrm{T}Hz$, which makes it distinguishable from μ without impacting its constraint. For baseline settings, we find $\mu = (2.0 \pm 1.4) \times 10^{-8}\,(\simeq 1.4\sigma)$, $kT_{eSZ} = (1.279 \pm 0.042)\,\mathrm{keV}\,(\simeq 31\sigma)$ and $\omega_2^{eSZ} = 1.12^{+0.84}_{-0.93}\,(\simeq 1.1\sigma)$, and practically unaltered constraints on Δ_T and y. Overall, we conclude that for an extended mission and a

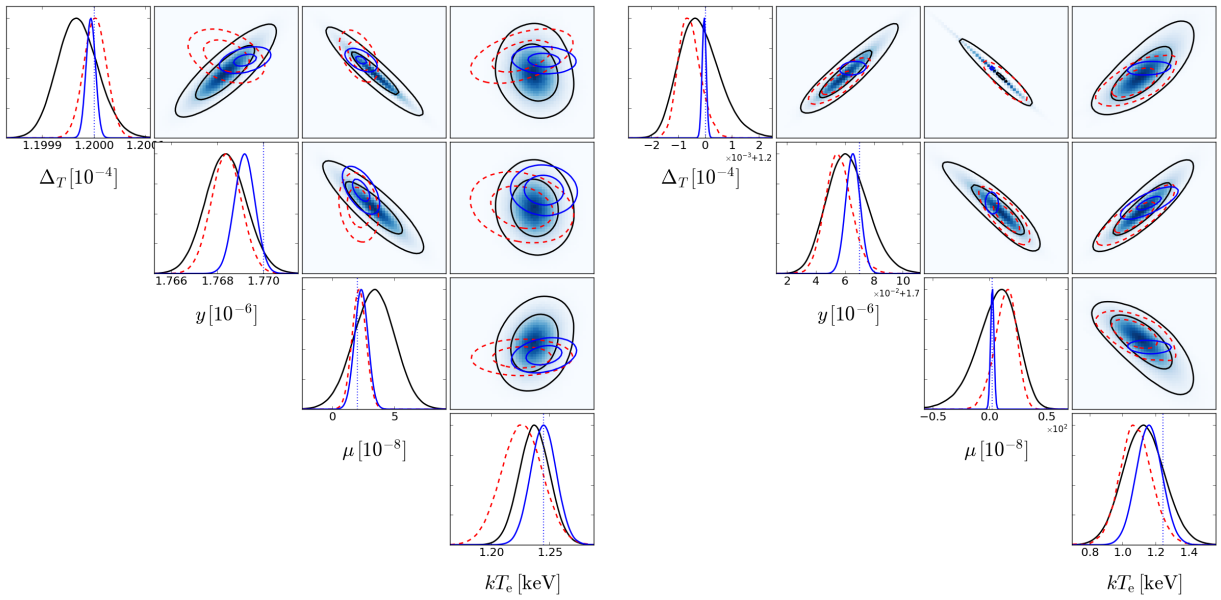

Figure 4.3: Comparison of the CMB spectral distortion parameter contours for varying foreground complexity. – Left panel: CMB-only (blue), CMB+Dust+CO (red), and CMB+Sync+FF+AME (black) parameter cases. Adding Dust+CO has a small effect on μ, while adding Sync+FF+AME has a moderate effect on kT_{eSZ}. – Right panel: CMB+Dust+CIB+CO (blue), CMB+Sync+FF+Dust+CIB (red), and all foreground (black) parameter cases. The degradation of μ due to the foregrounds is more severe than that for the other parameters. The axis scales are different between the left and right panels and offsets are added.

foreground-free sky, the noise level of *PIXIE* would be sufficient to detect the standard ΛCDM μ distortion at moderate significance, as well as the y and kT_{eSZ} signals at high significance. As we show below, the presence of foregrounds significantly changes the conclusion for μ, but the outlook for the y and kT_{eSZ} signals is still very positive.

4.7 Foreground-Marginalized Distortion Sensitivity Estimates

We estimate the capability of a *PIXIE*-like experiment to detect the Δ_T, y, kT_{eSZ}, and μ spectral distortion parameters in the presence of the foregrounds described in Sect. 4.4. To understand the effect of each individual foreground on the distortion parameter forecast,

Table 4.3: Forecasts with foregrounds, using MCMC. All results are for the extended mission (86.4 months), except for the first column (12 months). The given numbers represent the average of the two-sided 1σ marginalized uncertainty on each parameter. The models for the extended mission are sorted using the errors on y and $kT_{\rm e}$. Values in parentheses are the detection significance (i.e., fiducial parameter value divided by 1σ error). We assume a 10% prior on the synchrotron amplitude and spectral index, $A_{\rm S}$ and $\alpha_{\rm S}$, to represent external datasets. This only has a noticeable effect for the 14 and 16 parameter cases. No band average is included, but this is found to have only a small effect.

Sky Model	CMB (baseline)	CMB	Dust, CO	Sync, FF, AME	Sync, FF, Dust
# of parameters	4	4	8	9	11
$\sigma_{\Delta_T}[10^{-9}]$	2.3	0.86	2.2	3.9	9.7
$\sigma_y[10^{-9}]$	1.2 (1500σ)	0.44 (4000σ)	0.65 (2700σ)	0.88 (2000σ)	2.7 (660σ)
$\sigma_{kT_{eSZ}}[10^{-2}$ keV$]$	2.9 (42σ)	1.1 (113σ)	1.8 (71σ)	1.3 (96σ)	4.1 (30σ)
$\sigma_\mu[10^{-8}]$	1.4 (1.4σ)	0.53 (3.8σ)	0.55 (3.6σ)	1.7 (1.2σ)	2.6 (0.76σ)
Sky Model	Dust, CIB, CO	Sync, FF, Dust, CIB	Sync, FF, AME Dust, CIB, CO		
# of parameters	11	14	16		
$\sigma_{\Delta_T}[10^{-9}]$	5.3	59	75		
$\sigma_y[10^{-9}]$	4.8 (370σ)	12 (150σ)	14 (130σ)		
$\sigma_{kT_{eSZ}}[10^{-2}$ keV$]$	7.8 (16σ)	11 (11σ)	12 (10σ)		
$\sigma_\mu[10^{-8}]$	0.75 (2.7σ)	14 (0.15σ)	18 (0.11σ)		

we compare the effects of each component in Table 4.3. The forecasts assume an extended *PIXIE* mission and a 10% prior on the synchrotron amplitude and index, $A_{\rm S}$ and $\alpha_{\rm S}$, unless stated otherwise. We find that in general the μ and kT_{eSZ} signals are the most obscured by foregrounds, which is expected since they are the faintest distortion signals. Δ_T and y are measured with high significance even in the worst cases. We therefore focus on the impact of the foregrounds on the kT_{eSZ} and μ spectral distortion parameters. As a reference point, note that for the CMB-only extended mission, we found in the previous section that kT_{eSZ} is measured at 113σ and μ at 3.8σ. Including all foreground parameters, this degrades to 10σ for kT_{eSZ} and 0.11σ for μ (Table 4.3).

We find that the kT_{eSZ} measurement is mainly affected by the high-frequency foregrounds

Table 4.4: Errors on CMB parameters as a function of synchrotron parameter priors, using MCMC. These results assume an extended *PIXIE* mission and various priors (deduced from external data sets) on the synchrotron spectral index and amplitude, as indicated by the percentage values in the first row, respectively. In the final four columns, the μ parameter is not included in the data analysis (although it is present in the signal), yielding improved constraints on kT_{eSZ}. For comparison, we also show the CMB-only (foreground-free) constraints (4^{th} and 8^{th} column).

Parameter	1% / –	10% / 10%	1% / 1%	CMB only
$\sigma_{\Delta_T}[10^{-9}]$	194	75	18	0.86
$\sigma_y[10^{-9}]$	32 (55σ)	14 (130σ)	5.9 (300σ)	0.44 (4000σ)
$\sigma_{kT_{eSZ}}[10^{-2}\,keV]$	23 (5.5σ)	12 (10σ)	8.6 (14σ)	1.1 (113σ)
$\sigma_\mu[10^{-8}]$	47 (0.04σ)	18 (0.11σ)	4.7 (0.43σ)	0.53 (3.8σ)
Parameter	10% / 10% (no μ)	1% / 1% (no μ)	CMB only	none (no μ)
$\sigma_{\Delta_T}[10^{-9}]$	4.4	3.7	0.42	17
$\sigma_y[10^{-9}]$	4.6 (380σ)	4.6 (390σ)	0.28 (6200σ)	9.1 (194σ)
$\sigma_{kT_{eSZ}}[10^{-2}\,keV]$	7.9 (16σ)	7.6 (17σ)	1.0 (120σ)	12 (11σ)
$\sigma_\mu[10^{-8}]$	–	–	–	–

of Galactic thermal dust and CIB, bringing the detection significance down to 16σ when including these components. The integrated CO emission and dust alone have a more marginal effect (compare the 8 and 11 parameter dust cases in Table 4.3). This degradation is also illustrated in Fig. 4.3, where we show the CMB distortion parameter posteriors for various sky models. It appears to be related to the fact that a superposition of modified blackbody spectra (thermal dust and CIB) produces a signal that mimics a Compton-y distortion and relativistic correction in the Wien tail of the spectrum [69].

The μ distortion measurement is primarily obscured by the low-frequency synchrotron and free-free foregrounds (this will be further illustrated in Sect. 4.7.2). The three synchrotron parameters are poorly constrained by *PIXIE* and significantly degrade the μ detection significance. The free-free spectrum is relatively flat in this frequency range and parameterized by only its amplitude, which is better measured than the synchrotron parameters by *PIXIE*. AME, the other low-frequency foreground, affects only a fairly narrow band and thus only has a small effect on μ. These three foregrounds alone bring the μ detection

Table 4.5: Percent errors on foreground parameters, using MCMC. These results assume an extended *PIXIE* mission and various priors on the synchrotron spectral index and amplitude, as labeled in the first column. The average of the two-sided errors is quoted. The recovered parameter posterior distributions for the final three cases (no μ in the analysis) are shown in Figure 4.8. The synchrotron and free-free parameters are the least well constrained by *PIXIE*, suggesting that low-frequency ($\lesssim 15$ GHz) ground-based measurements could provide important complementary information.

Prior $\alpha_{\rm S}$ / $A_{\rm S}$	$A_{\rm S}$	$\alpha_{\rm S}$	$\omega_{\rm S}$	A_{FF}	A_{AME}	$A_{\rm d}$	$\beta_{\rm d}$	$T_{\rm d}$
1% / –	34.0%	1.0%	106.0%	23.0%	1.7%	0.35%	0.087%	0.0051%
10% / 10%	9.6%	9.3%	52.0%	7.3%	0.9%	0.18%	0.051%	0.0046%
1% / 1%	0.99%	1.0%	5.5%	1.1%	0.77%	0.13%	0.04%	0.0045%
none (no μ)	33.0%	29.0%	93.0%	8.9%	1.3%	0.18%	0.048%	0.0049%
10% / 10% (no μ)	7.3%	7.0%	21.0%	2.2%	0.85%	0.14%	0.043%	0.0046%
1% / 1% (no μ)	0.95%	0.95%	5.1%	0.47%	0.61%	0.12%	0.038%	0.0042%
	A_{CIB}	β_{CIB}	T_{CIB}	A_{CO}				
1% / –	1.2%	0.32%	0.1%	0.33%				
10% / 10%	0.58%	0.17%	0.053%	0.23%				
1% / 1%	0.3%	0.11%	0.031%	0.22%				
none (no μ)	0.6%	0.17%	0.069%	0.33%				
10% / 10% (no μ)	0.35%	0.12%	0.029%	0.21%				
1% / 1% (no μ)	0.29%	0.1%	0.028%	0.16%				

significance down to 1.2σ for an extended mission (see Table 4.3 and Fig. 4.3). Combining the four brightest components – synchrotron, free-free, thermal dust, and CIB – reduces the kT_{eSZ} detection significance to 11σ and completely obscures the μ distortion (0.15σ). In the presence of all six foreground components, the kT_{eSZ} distortion is still detected at 10σ significance (see Figure 4.3 and the last column of Table 4.3). However, the ΛCDM μ-distortion seems to be out of reach without additional information.

For completeness, we list the forecasts for the baseline *PIXIE* mission with 12 months of spectral distortion mode integration time. With no priors (including, in this case, no priors on the synchrotron parameters) and all foreground components included, the 1σ uncertainties are: $\sigma_{\Delta T} = 6.9 \times 10^{-7}$, $\sigma_y = 1.2 \times 10^{-7}$, $\sigma_{kT_{eSZ}} = 0.9$ keV, and $\sigma_\mu = 1.5 \times 10^{-6}$. Comparing to the 1σ limits of *COBE/FIRAS*, $\sigma_{\Delta T} \simeq 2.0 \times 10^{-4}$, $\sigma_y \simeq 7.5 \times 10^{-6}$ and $\sigma_\mu \simeq 4.5 \times 10^{-5}$,

shows that with 12 months in spectral distortion mode *PIXIE* will improve the parameter constraints by more than a factor of $\simeq 30$. However, this comparison is not precisely valid, as the *COBE/FIRAS* limits are derived on combinations of two parameters only ($\sigma_{\Delta T}$ and y or μ). For example, omitting μ and kT_{eSZ} we find the baseline sensitivities $\sigma_{\Delta T} = 4.1 \times 10^{-8}$ and $\sigma_y = 8.7 \times 10^{-9}$, which highlights the large improvement in the raw sensitivity ($\gtrsim 1000$ times better than *COBE/FIRAS*; see Fig. 4.1.).[4]

Assuming 10% priors on the synchrotron index and amplitude and the baseline mission sensitivity gives: $\sigma_{\Delta T} = 9.6 \times 10^{-8}$, $\sigma_y = 2.1 \times 10^{-8}$, $\sigma_{kT_{eSZ}} = 0.25$ keV, and $\sigma_\mu = 2.3 \times 10^{-7}$. The priors carry a significant amount of information about the low-frequency foregrounds. In the framework of this analysis, the biggest gains on CMB parameters come from better constraining these foregrounds, in particular the synchrotron emission. A side effect of including external priors is that they necessarily reduce the efficiency of increasing the mission sensitivity in a Fisher analysis. The extended mission has $\approx \sqrt{86.4/12} \approx 2.68$ times better sensitivity than the baseline mission, but we see only a factor of ≈ 1.3 improvement in the CMB parameter constraints due to the external priors dominating the information on the synchrotron SED. When comparing the baseline and extended mission without priors, we find an improvement of almost exactly 2.68, but the constraints are of course better with the external priors applied, as seen in Figures 4.5, 4.6, and 4.7 (discussed in detail below).

4.7.1 Foreground Model Assumptions

We consider the effects of varying the foreground models and parameter values on the spectral distortion forecast using the Fisher method. First, we vary each foreground amplitude parameter by up to a factor of 5 and find very little change in the projected spectral dis-

[4]We show the raw sensitivity of the *COBE/FIRAS* mission in Fig. 4.1, but the cosmological parameter constraints quoted in the text include additional degradation due to systematic errors. Furthermore, as mentioned in Sect. 4.1, the *COBE/FIRAS* analysis methodology differs significantly from ours. In particular, that analysis relies entirely on spatial information to separate Galactic foregrounds from the extragalactic monopole, while ours relies entirely on spectral information to separate different components at the level of the monopole SED. An optimal analysis would combine both sets of information, but this requires the simulation of detailed sky maps at each *PIXIE* frequency.

tortion uncertainties. Next, we find that the forecasts are still accurate when varying the spectral indices or component temperatures by up to $\approx 20\%$. Further modification of the spectral shape parameters, in particular the synchrotron spectral index and curvature, can noticeably change the forecast estimates, but these modifications are not consistent with current observations [e.g., 29, 235] which indicate that α_{sync} only varies at the $\simeq 5-10\%$ level across the sky.

We also consider simplifying the synchrotron model to a two-parameter power law, which improves the detection significance by about a factor of 2 on μ and by 1.3 on $kT_{\mathrm{e}SZ}$. This is expected, since we saw previously that low-frequency foregrounds mainly degrade the detection significance of μ (e.g., Fig. 4.3). However, this scenario is again unrealistic, as the curvature of the synchrotron spectrum is an inevitable result of the average of the synchrotron emission over the sky and along the line-of-sight. Spatial information on α_{sync} could be used to further constrain ω_{sync}, but the effects of line-of-sight and beam averaging will not be separable in this way. In addition, due to the rather low angular resolution of *PIXIE*, a combination with other experiments might be required in this case, so that we leave this aspect for future explorations.

Removing the CIB emission entirely results in the largest (factor of $\simeq 5$) improvement in the detection of all CMB parameters, but this is also unrealistic. Rather, we expect a more complicated model for the dust components to be required, which directly handles and models the information from spatial variations of the SED parameters. Allowing the peak frequency of the spinning dust SED to be a free parameter negligibly affects the μ and $kT_{\mathrm{e}SZ}$ detection significance when assuming the 10% prior on A_{sync} and α_{sync}. In fact with this synchrotron prior, the entire spinning dust SED provides only a marginal ($< 20\%$) reduction in CMB parameter detections. Even when relaxing the synchrotron priors, the spinning dust affects the CMB parameters' detection significance by less than a factor of 2. Overall, we find that the forecast is robust to moderate variations in the assumed foreground model and parameters. Rather than the specific amplitude of the signals, the shapes and covariance

with the distortion parameters is most important in driving the CMB parameter limits.

4.7.2 Addition of External Data Using Priors

We examine the use of external information in the form of *a priori* knowledge of the foreground SED parameters. The biggest improvements can be expected for the low-frequency foreground parameters, as the high-frequency components generally are found to be constrained with high precision ($\lesssim 1\%$) due to the large number of high-frequency channels in FTS concepts. We thus compare results using combinations of 10% and 1% priors on the synchrotron amplitude and spectral index in Tables 4.4 and 4.5. This is meant to mimic information from future ground-based experiments similar to C-BASS and QUIJOTE, possibly with extended capabilities related to absolute calibration, or when making use of extra spatial information in the analysis.

Focusing on Table 4.4, the ΛCDM μ distortion is still not detectable even with tightened priors, but the kT_{eSZ} detection significance could be improved to 14σ when imposing 1% priors on A_{sync} and α_{sync}. In this case, an upper limit of $|\mu| < 9.4 \times 10^{-8}$ (95% c.l.) could be achieved. Comparing this with the CMB-only constraints reveals that foregrounds introduce about one order of magnitude degradation of the constraint. To detect the ΛCDM μ distortion at 2σ requires a $\simeq 0.1\%$ prior on the synchrotron amplitude, index, curvature, and the free-free amplitude. This is not met by *PIXIE* alone, but could possibly be achieved by adding constraints from ground-based observations at lower frequencies. In particular the steepness of the synchrotron SED might help in this respect, with increasing leverage as lower frequencies are targeted. Performing similar measurements with a space mission will be very challenging due to constraints on the size of the instrument.

Nevertheless, *PIXIE* could significantly improve the existing limit from *COBE/FIRAS*, placing tight constraints on the amplitude of the small-scale scalar power spectrum, $A_{\rm s}$,

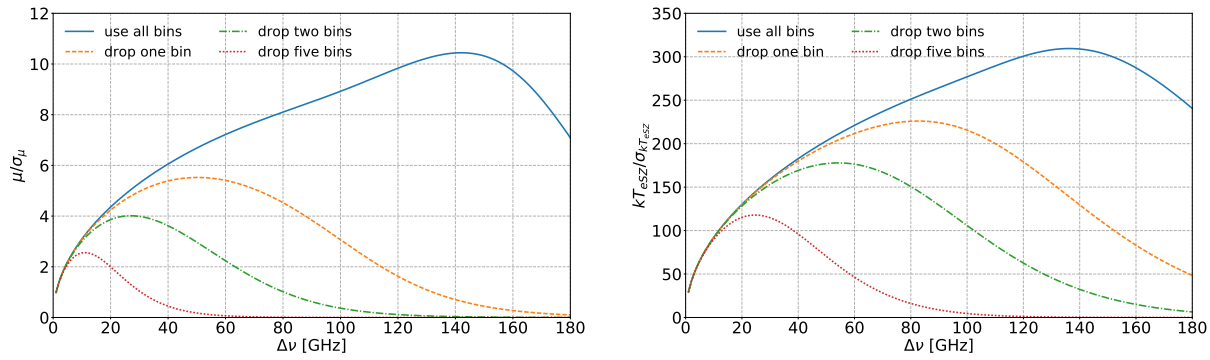

Figure 4.4: Estimated CMB-only (i.e., no foregrounds; extended mission) detection significance for the ΛCDM μ (upper panel) and kT_{eSZ} (lower panel) signals as a function of the frequency resolution, $\Delta\nu$. The different curves show the effect of dropping a varying number of the lowest-frequency channels to mimic systematic-related channel degradation.

around wavenumber $k \simeq 740\,\mathrm{Mpc}^{-1}$, corresponding to [cf., 60]

$$A_\mathrm{s}(k \simeq 740\,\mathrm{Mpc}^{-1}) < 2.8\times10^{-8}\left[\frac{|\mu|}{3.6\times10^{-7}}\right]\ (95\%\ \mathrm{c.l.}), \tag{4.7}$$

when assuming a scale-invariant (spectral index $n_\mathrm{s} = 1$) small-scale power spectrum. Here, $|\mu|$ is the 2σ upper limit on the chemical potential. This would already rule out many alternative early-universe models with enhanced small-scale power [66, 71]. Assuming 1% priors on A_{sync} and α_{sync}, one could obtain $A_\mathrm{s}(k \simeq 740\,\mathrm{Mpc}^{-1}) < 7.3\times10^{-9}(95\%\ \mathrm{c.l.})$, bringing us closer to the value obtained from CMB anisotropy observations, $A_\mathrm{s}(k \simeq 0.05\,\mathrm{Mpc}^{-1}) \simeq 2.2\times10^{-9}$ [232] at much larger scales.

As mentioned above, the biggest issue for the μ detection indeed lies in the synchrotron emission. Table 4.5 shows the expected uncertainties on foreground parameters with various assumed synchrotron SED priors. The thermal dust, CIB, and CO parameters are all measured to $< 1\%$, while the low-frequency foregrounds have much larger uncertainties. This implies that the largest gains in terms of CMB distortion science can be expected by improving ground-based measurements at low frequencies. These measurements will also be required to complement CMB B-mode experiments, aiming at detection of a tensor-to-scalar ratio $r < 10^{-3}$.

Generally, we also find that imposing a prior on α_{sync} alone does not significantly improve the results. For example, we find the distortion constraints with 10% and 1% prior on α_{sync} to be practically the same (the 1% prior on α_{sync} case is shown in Table 4.4). This is due to the strongly non-Gaussian posteriors of the model parameters (see Fig. 4.8 for the cases without μ) and adding a 10% prior on A_{sync} immediately improves the CMB distortion constraints by a factor $\simeq 2$. This means that it will be crucial to obtain additional low-frequency constraints on the absolute sky-intensity, while simple differential measurements will only help in constraining the spatially-varying contributions to ω_{sync}.

Further improvements for $kT_{\rm e}{}_{SZ}$ are seen when μ is excluded from the parameter analysis (although the signal is still present in the sky model). In this case, the $kT_{\rm e}{}_{SZ}$ detection significance can reach 17σ (see Table 4.5). The addition of 10% priors on A_{sync} and α_{sync} are sufficient to achieve this. This can also be seen in Fig. 4.8 and stems from the highly non-Gaussian tails of the $kT_{\rm e}{}_{SZ}$ posterior without external prior. We also find small biases in the deduced distortion parameters (see Fig. 4.8). For example, for the case with 1% priors on A_{sync} and α_{sync}, we obtain $y = (1.7676 \pm 0.0045) \times 10^{-6}$ and $kT_{\rm e}{}_{SZ} = (1.182 \pm 0.075)\,{\rm k}eV$, corresponding to marginal biases of $\simeq -0.5\,\sigma$ and $\simeq -0.8\,\sigma$, respectively. These can usually be neglected. CMB spectral distortion measurements are thus expected to yield robust constraints on $kT_{\rm e}{}_{SZ}$.

4.7.3 Optimal Mission Configuration Search

In an effort to optimize the instrument configuration in the presence of foregrounds, we study the effect of varying the mission parameters, such as sensitivity, frequency resolution, and frequency coverage, all assuming an FTS concept. Aside from extending the mission duration, the overall sensitivity can only be increased by increasing the aperture and detector array (to increase the étendue), as concepts like *PIXIE* are already photon-noise-limited. The FTS mirror stroke controls the frequency resolution and the physical size of the detector array limits the lowest frequency channels. This implies that changing the above experimental

parameters is a strong cost driver, and complementarity between different experimental concepts needs to be explored.

We characterize the mission in terms of the detection significance for the CMB spectral distortion fiducial ΛCDM μ and kT_{eSZ} parameters (y and Δ_T are detected at high significance in all scenarios and will not be further highlighted). We assume the extended mission and consider varying the priors on the synchrotron amplitude and spectral index, A_S and α_S. The lower edge of the lowest frequency channel is set to $\nu_{min} \simeq 7.5\,\mathrm{GHz}$ (similar to *PIXIE*), determined by the physical dimension of the instrument. We assume an otherwise ideal instrument with a top-hat frequency response[5] and, in terms of systematics, consider white noise only.

Optimal setup without foregrounds

In Figure 4.4, we show the estimated CMB-only detection significance for the ΛCDM μ and kT_{eSZ} signals as a function of the frequency resolution, $\Delta\nu$, which in principle can be varied in-flight by adjusting the mirror stroke. The sensitivity per channel scales as $\simeq \Delta\nu/15\,\mathrm{GHz}$ (i.e., wider frequency bins have higher sensitivity). The lowest frequency channels are susceptible to instrument-related systematic errors, so we also consider forecasts in which we drop a fixed number of the lowest frequency bins. When ignoring foreground contamination, the optimal configuration for measuring the μ distortion is $\Delta\nu \simeq 142$ GHz when all channels are included, yielding a 10.4σ detection of the standard ΛCDM value, $\mu \simeq 2\times10^{-8}$. This drops steeply to $\simeq 5.5\sigma$, 4.0σ, 2.6σ for optimal resolutions $\Delta\nu \simeq 50\,\mathrm{GHz}$, $27\,\mathrm{GHz}$, $11\,\mathrm{GHz}$, if the lowest one, two, or five frequency channels cannot be used, respectively.

A similar trend is found for the optimal configuration aiming to detect kT_{eSZ} (lower panel, Fig. 4.4), with the optimal resolution being $\Delta\nu \simeq 135$ GHz when all channels are included in the analysis, giving a $> 300\sigma$ detection of the signal. This degrades to $\simeq 226\sigma$, 178σ, 118σ for

[5]For large $\Delta\nu$, the band average becomes very important.

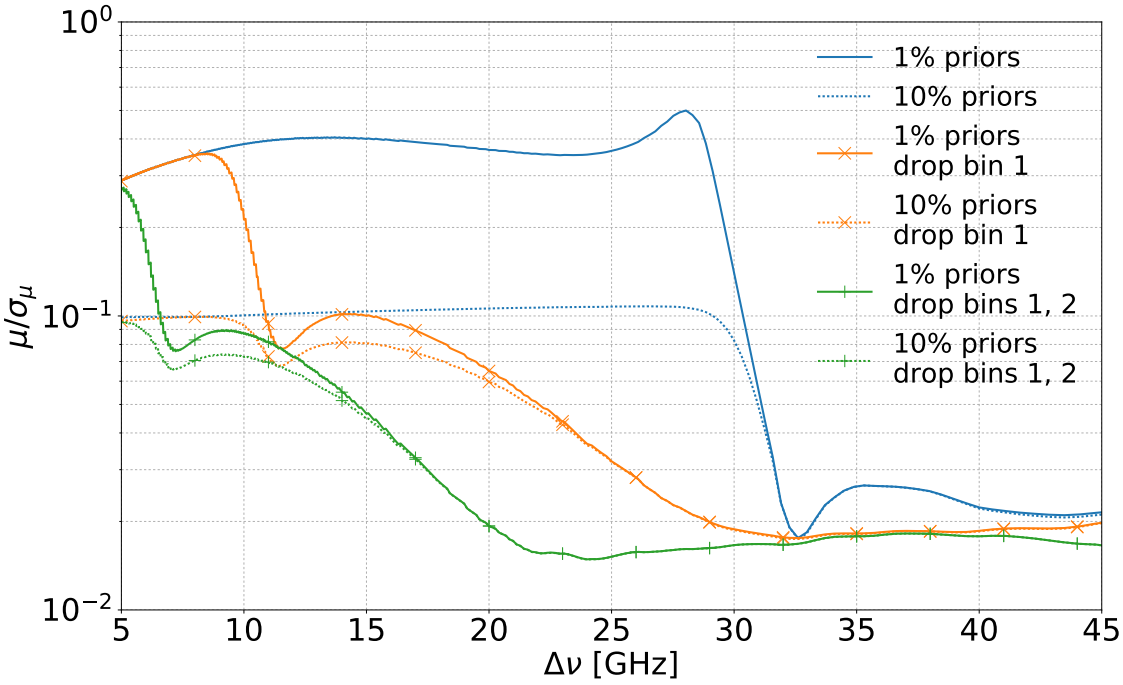

Figure 4.5: Estimated detection significance (foregrounds included; extended mission) for the ΛCDM μ-distortion signal as a function of the frequency resolution, $\Delta\nu$ (note the logarithmic scale on the vertical axis). The different curves show the effect of dropping the lowest-frequency channels and changing the priors on A_{sync} and α_{sync}.

optimal resolutions $\Delta\nu \simeq 83\,\mathrm{GHz}$, $54\,\mathrm{GHz}$, $25\,\mathrm{GHz}$, if the lowest one, two or five frequency channels cannot be used, respectively.

The error is mainly driven by the competition between sensitivity per channel ($\leftrightarrow$ frequency bin size) and frequency coverage ($\leftrightarrow$ lowest frequency bin) to allow the separation of the distortion parameters, with kT_{eSZ} and μ usually most strongly correlated. In particular, the sensitivity to μ drops when the design is near a regime in which no independent frequency channel is present below the null of the μ-distortion signal at $\nu \simeq 130\,\mathrm{GHz}$. For instance, assuming all channels can be included, one would expect a configuration with one bin between $7.5\,\mathrm{GHz}$ and $130\,\mathrm{GHz}$, giving $\Delta\nu \simeq 120\mathrm{GHz}$, to be roughly optimal. Dropping the lowest frequency bin, one would expect a configuration with two bins between $7.5\,\mathrm{GHz}$ and $130\,\mathrm{GHz}$, giving $\Delta\nu \simeq 120\mathrm{GHz}/2 \simeq 60\,\mathrm{GHz}$, to be optimal, and so on. These numbers are in good agreement with the true optimal frequency bin widths found above.

Optimal setup with foregrounds

When including foreground contamination, the picture changes significantly. Focusing on the detection significance for μ (Fig. 4.5), we see that when including all channels the optimal frequency resolution is $\Delta\nu \lesssim 27\,\mathrm{GHz}$, independent of the chosen prior on the synchrotron parameters (blue curves in Fig. 4.5). The sensitivity remains rather constant in this regime, since most of the information is already delivered by including external data as represented by the 10% or 1% priors on A_{sync} and α_{sync}. A sharp drop in the μ-sensitivity is found around $\Delta\nu \simeq 30\,\mathrm{GHz}$. This is roughly where in our model the transition between low- and high-frequency foreground components occurs (see Fig. 4.2), driving the trade-off in the frequency resolution toward lower frequencies. For $\Delta\nu \simeq 30\,\mathrm{GHz}$ all of the low-frequency foreground information is contained in one channel, which limits the ability of such a setup to separate individual components. This feature is also seen in Figures 4.6 and 4.7 (discussed below).

The sensitivity, even for the extended mission, is not sufficient to detect the ΛCDM μ distortion, but greatly improved limits of $|\mu| \lesssim few \times 10^{-7}$ are within reach. The increase in detection significance at lower frequencies is due primarily to better constraining the synchrotron and free-free SEDs. Dropping the lowest frequency channels further pushes the optimal frequency resolution to $\Delta\nu \lesssim 15$ GHz. This statement is relatively independent of the assumed synchrotron priors and indicates that the μ-distortion sensitivity of *PIXIE* is relatively robust with respect to the inclusion of the lowest FTS channels. However, modest improvements are seen when choosing $\Delta\nu \lesssim 10\,\mathrm{GHz}$.

Figure 4.6 shows the detection significance for $kT_{\mathrm{e}SZ}$ when varying experimental parameters as above. We also show the constraints when μ is excluded from the analysis (lower panel). For the relativistic tSZ parameter, the optimal frequency resolution is $\Delta\nu \simeq 27\,\mathrm{GHz}$ or $\simeq 37\,\mathrm{GHz}$ when all channels are included in the analysis. For $\Delta\nu \simeq 27\,\mathrm{GHz}$, the sensitivity to μ is also optimized. Although this is not the default resolution of *PIXIE*, the improvement in the distortion sensitivity over $\Delta\nu \simeq 15\,\mathrm{GHz}$ is only $\simeq 15\%$. $\Delta\nu \simeq 27\,\mathrm{GHz}$ is also optimal when dropping the lowest frequency channel, but in this case drops off rapidly

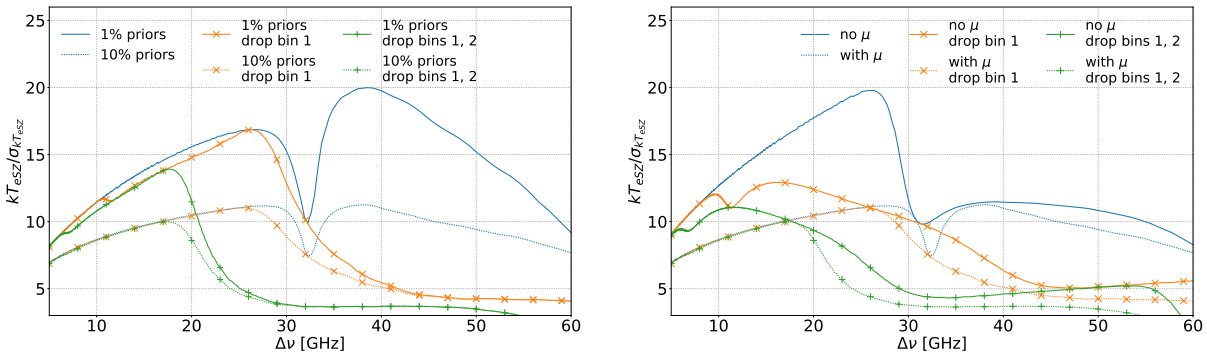

Figure 4.6: Estimated detection significance (foregrounds included; extended mission) for the ΛCDM kT_{eSZ} signal as a function of the frequency resolution, $\Delta\nu$. The different curves show the effect of omitting the lowest-frequency channels and changing the priors on A_{sync} and α_{sync}. The upper panel illustrates the results when μ is included in the analysis, while in the lower panel the cases for 10% priors are compared with and without μ included.

for $\Delta\nu \gtrsim 30\,\mathrm{GHz}$. When dropping the lowest two frequency channels, the optimal frequency resolution is $\Delta\nu \simeq 17\,\mathrm{GHz}$, which is very close to the default setting of *PIXIE*. In this case, the sensitivity to kT_{eSZ} furthermore drops strongly for $\Delta\nu \gtrsim 20\,\mathrm{GHz}$.

Ignoring μ in the parameter analysis generally yields improved constraints on kT_{eSZ} (lower panel, Fig. 4.6). In particular, gains are seen for $\Delta\nu \lesssim 30\,\mathrm{GHz}$, as low-frequency information can be used to improve the constraint without competition from μ. Again, $\Delta\nu \simeq 15\,\mathrm{GHz}$ is found to optimize the overall trade-offs when the lowest frequency channel is omitted, and $\Delta\nu \simeq 11\,\mathrm{GHz}$ is optimal when dropping the lowest two channels.

We also study the dependence of the μ constraints on the overall sensitivity of the instrument, which could be modified by increasing the total aperture and detector array (e.g., by replicating the instrument) or further extending the mission duration. As expected, this improves the spectral distortion measurements (Fig. 4.7). In particular, increasing the mission sensitivity by a factor of 100 enables a $\simeq 3-4\sigma$ detection of the expected ΛCDM μ distortion, $\mu \simeq 2\times10^{-8}$, for the default setup. This implies an étendue 10,000 times greater than that of *PIXIE*, which is prohibitively expensive with current technology. Combining *PIXIE* with 1% synchrotron index and amplitude priors performs as well as an experiment with 10 times the sensitivity and no priors when focusing on the μ constraints, for $\Delta\nu \lesssim 30\,\mathrm{GHz}$.

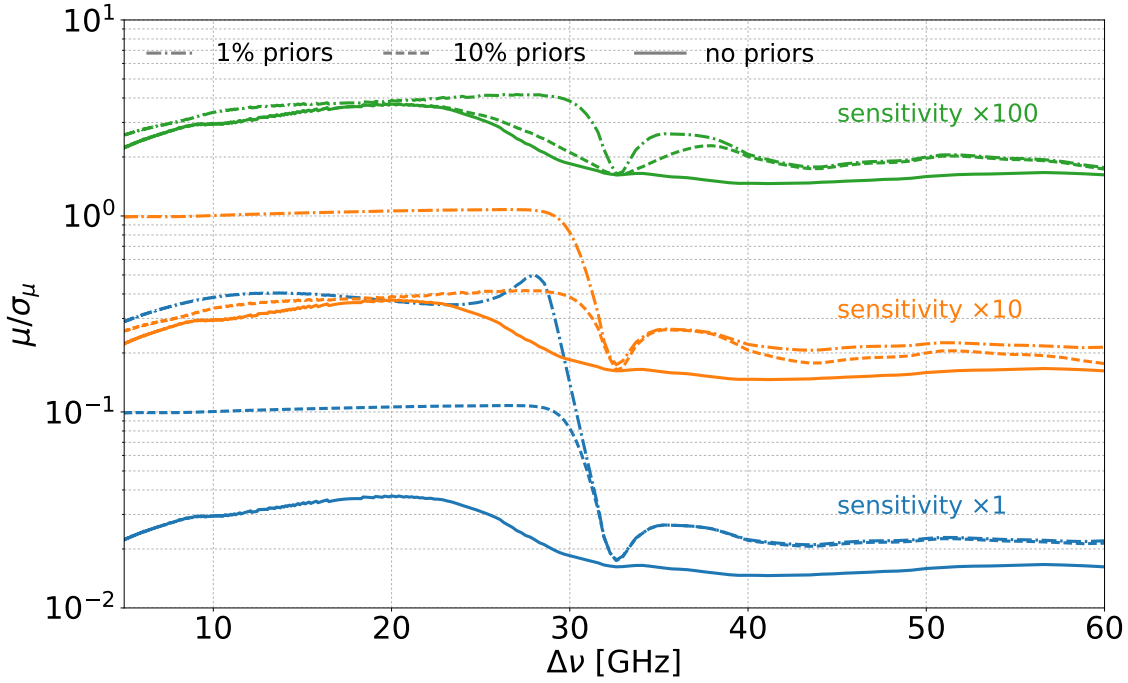

Figure 4.7: Estimated detection significance (foregrounds included; extended mission) for the ΛCDM μ-distortion signal as a function of the frequency resolution, $\Delta\nu$, and for varying priors on A_{sync} and α_{sync} and increasing the overall mission sensitivity (note the logarithmic scale on the vertical axis).

This emphasizes the impact external synchrotron datasets, possibly also exploiting spatial information, could have when combined with *PIXIE*.

Our analysis shows that ultimately the biggest hurdle to measuring μ comes down to the low-frequency foregrounds, in particular the synchrotron and free-free emission. A dedicated ground-based, low-frequency instrument with spatial resolution at least as good as *PIXIE* will be essential in constraining these foregrounds. Alternatively, one could think about adding a low-frequency instrument not based on the FTS concept to the payload. A detailed analysis of these ideas is left to future work, but a rough estimate with the Fisher method seems to indicate that tens of spectral channels between $\simeq 1$ and 30 GHz with sensitivity equal to or better than the baseline *PIXIE* mission would be required. This leads to $< 1\%$ constraints on the synchrotron, free-free, and spinning dust SEDs and could yield $|\mu| < 2.0 \times 10^{-8}$ (95% c.l.).

4.8 Conclusions

Measurements of CMB spectral distortions will shed new light on physics in both the early ($\leftrightarrow$ μ distortion) and late ($\leftrightarrow$ y and $kT_{\rm eSZ}$ signals) periods of cosmic history. This will open a new era in CMB cosmology, with clear distortion signals awaiting us. However, detecting spectral distortions will require extreme precision and control of systematics over large bandwidths. Our analysis shows that foregrounds strongly affect the expected results and demand dedicated observations and experimental designs, particularly with improved sensitivity at low frequencies ($\nu \lesssim 15 - 30\,{\rm GHz}$).

We considered foreground models motivated by available CMB observations to forecast the capability of *PIXIE* or other future missions to detect spectral distortions, focusing on FTS concepts. We find that *PIXIE* has the capability to measure the CMB temperature to $\simeq$ nK precision and to detect the Compton-y and relativistic tSZ distortions at high significance (see Table 4.4). With conservative assumptions about extra information at low frequencies from external data, we expect detections at 194σ and 11σ for y and $kT_{\rm eSZ}$, respectively. We emphasize that $kT_{\rm eSZ}$ is detected at above 5σ with no modification of the *PIXIE* mission and no external data. The $kT_{\rm eSZ}$ detection significance is increased to $> 11\sigma$ when μ is ignored in the parameter analysis (shown in the last 3 columns of Table 4.4 and in Figure 4.8). These measurements would provide new constraints on models of baryonic structure formation, thus providing novel information about astrophysical feedback mechanisms [138, 26].

Due to its many high-frequency channels, *PIXIE* will provide the best measurements of thermal dust and CIB emission to date (see Table 4.5). These sub-percent absolute measurements will provide invaluable information for the modeling of CMB foregrounds relevant to B-mode searches from the ground. They will furthermore allow improvements in the channel inter-calibration, potentially allowing us to reach sensitivities required to extract resonant scattering signals caused by atomic species [e.g., 25, 259]. They will also greatly advance our understanding of Galactic dust properties and physics, providing invaluable absolutely calibrated maps in many bands.

The fiducial ΛCDM μ distortion ($\mu \simeq 2 \times 10^{-8}$) is unlikely to be detected in the presence of known foregrounds without better sensitivity or additional high-fidelity datasets that constrain the amplitude and shape of low-frequency foregrounds. Nevertheless, *PIXIE* could improve upon the existing limit from *COBE/FIRAS* by a factor of 250, yielding $|\mu| < 3.6 \times 10^{-7}$ (95% c.l.) for conservative assumptions about available external data. This would place tight constraints on the amplitude of the small-scale scalar power spectrum at wavenumber $k \simeq 740\,\mathrm{Mpc}^{-1}$ (Sect. 4.7.2) and would rule out currently allowed parameter space for long-lived decaying particles with lifetimes $\simeq 10^6 - 10^{10}\,\mathrm{s}$ [e.g., see 60].

We find *PIXIE*'s frequency resolution of $\Delta\nu \simeq 15\,\mathrm{GHz}$ to be close to optimal, although for μ slight improvements could be expected when using $\Delta\nu \simeq 10\,\mathrm{GHz}$, depending on the quality of the low-frequency channels (Sect. 4.7.3). A similar choice seems optimal for $kT_{\mathrm{e}SZ}$, in particular if the lowest frequency channels cannot be used in the data analysis due to systematic errors (see Fig. 4.7).

The most practical way to improve the μ results from a *PIXIE*-like experiment is to complement it with ground-based observations of the low-frequency synchrotron, free-free, and AME foregrounds. Measuring the synchrotron and free-free SEDs to 0.1% would enable *PIXIE* to detect μ at $\simeq 2\sigma$. Some of the challenges could be avoided by selecting specific patches on the sky with low foreground contamination, but we generally find that the distortion sensitivity is mostly limited by the lack of constraints on the *shape* of the foreground SEDs rather than their amplitude (Sect. 4.7.1).

Our analysis only uses spectral information to separate different components. Adding spatial information would yield a reduction in the total contribution of fluctuating foreground components (e.g., Galactic contributions) to the sky-averaged spectrum. In addition, a more optimal sky-weighting scheme could be implemented for the monopole measurement, as opposed to the simple average taken on 70% of the sky assumed in our analysis. Extragalactic signals (e.g., CIB) will, however, not be significantly reduced by considering spatial information, unless high-resolution and high-sensitivity measurements become available. In this

case, extended foreground parameterizations, which explicitly include the effects of spatial averages across the sky and along the line-of-sight [69], should be used. Since *PIXIE* has a fairly low angular resolution ($\Delta\theta \simeq 1.6^\circ$), a combination with future high-resolution CMB imagers might also be beneficial. A more detailed analysis is required to assess the overall trade-offs in these directions.

We close by mentioning that information from the CMB dipole spectrum could also help in extracting the CMB distortion signals [75, 21]. In particular, these measurements do not require absolute calibration and thus can also be carried out in the *PIXIE* anisotropy observing mode. This can furthermore be used to test for systematic effects. Also, Galactic ($\leftrightarrow$ comoving) and extragalactic foregrounds are affected in a different way by our motion with respect to the CMB rest frame, so that this could provide additional leverage for foreground separation. All this is left to future analysis.

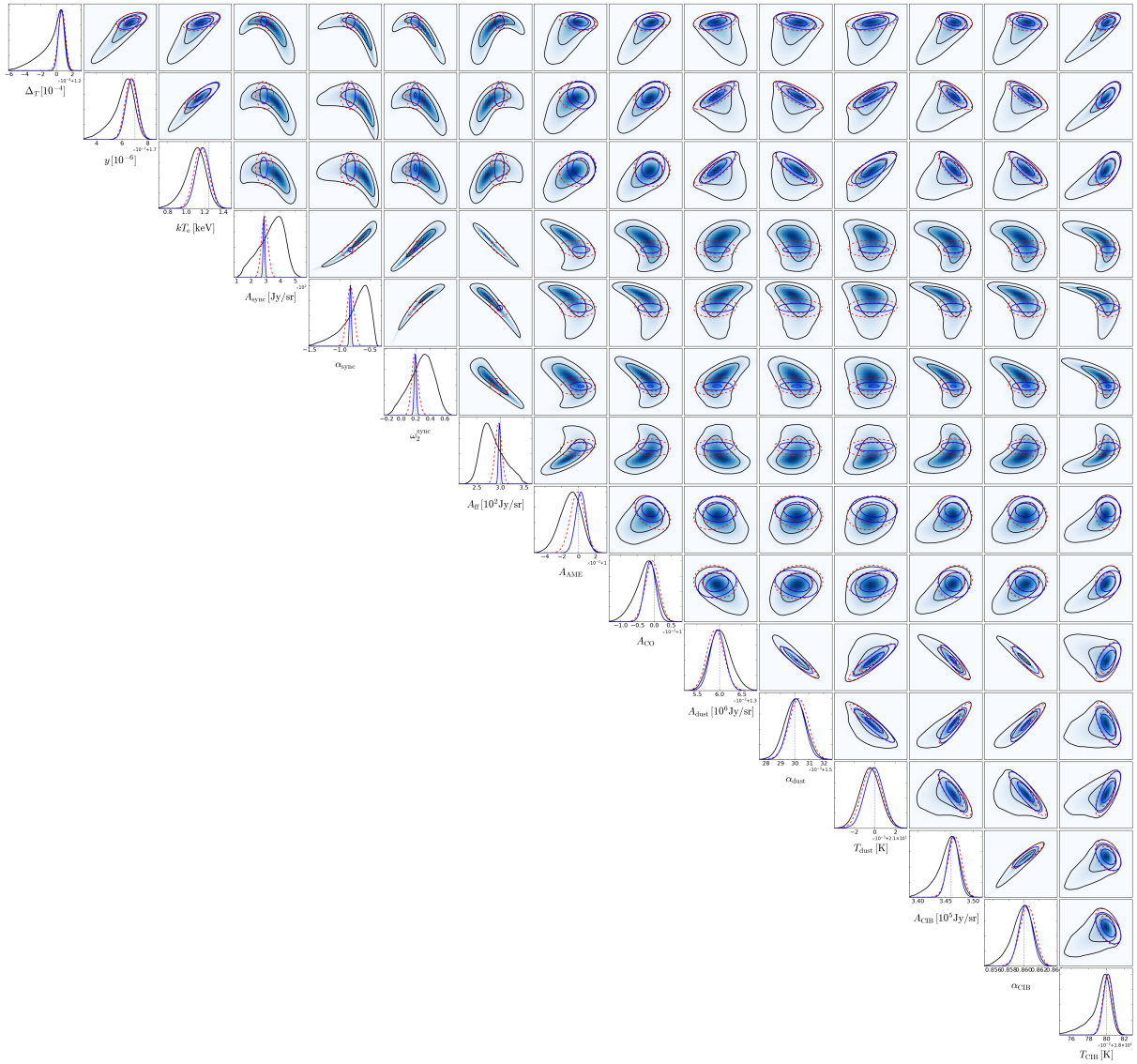

Figure 4.8: Posteriors obtained with MCMC runs for the full foreground model without μ in the analysis. The case without priors on the foreground parameters (black line / blue contours) is highly non-Gaussian. Including 10% priors on $A_{\rm S}$ and $\alpha_{\rm S}$ (red dashed line) leads to much more Gaussian posteriors, improving the CMB parameter constraints by a factor of $\simeq 2$. Tightening the priors on $A_{\rm S}$ and $\alpha_{\rm S}$ to 1% (blue line) improves the constraints on low-frequency foreground parameters, but only marginally affects the CMB parameter constraints. Details about the error estimates for these cases can be found in Tables 4.4 and 4.5.

Chapter 5

Foreground Biases in CMB Polarimeter Self-Calibration

Precise polarization measurements of the cosmic microwave background (CMB) require accurate knowledge of the instrument orientation relative to the sky frame used to define the cosmological Stokes parameters. Suitable celestial calibration sources that could be used to measure the polarimeter orientation angle are limited, so current experiments commonly 'self-calibrate.' The self-calibration method exploits the theoretical fact that the EB and TB cross-spectra of the CMB vanish in the standard cosmological model, so any detected EB and TB signals must be due to systematic errors. However, this assumption neglects the fact that polarized Galactic foregrounds in a given portion of the sky may have non-zero EB and TB cross-spectra. If these foreground signals remain in the observations, then they will bias the self-calibrated telescope polarization angle and produce a spurious B-mode signal. In this paper we estimate the foreground-induced bias for various instrument configurations and then expand the self-calibration formalism to account for polarized foreground signals. Assuming the EB correlation signal for dust is in the range constrained by angular power spectrum measurements from *Planck* at 353 GHz (scaled down to 150 GHz), then the bias is negligible for high angular resolution experiments, which have access to CMB-dominated

high ℓ modes with which to self-calibrate. Low-resolution experiments observing particularly dusty sky patches can have a bias as large as 0.5°. A miscalibration of this magnitude generates a spurious BB signal corresponding to a tensor-to-scalar ratio of approximately $r \sim 2 \times 10^{-3}$, within the targeted range of planned experiments.

5.1 Introduction

The cosmic microwave background (CMB) is a primordial bath of photons that permeates all of space and carries an image of the universe as it was 380,000 years after the Big Bang. Physical processes that operated in the early universe left various imprints in the CMB. These imprints appear today as angular anisotropies, and the primordial angular anisotropies have proven to be a trove of cosmological information. The precise characterization of the intensity (or temperature) anisotropy of the CMB has helped reveal that space-time is flat, the universe is 13.8 billion years old, and the energy content of the universe is dominated by cold dark matter and dark energy [29, 232]. The associated 'E-mode' polarization anisotropy signal has been observed at the theoretically expected level [29, 233, 247, 209, 72]. Experimental CMB polarization research is currently focused on (i) searching for the primordial 'B-mode' polarization anisotropy signal from inflationary gravitational waves (IGW) [312, 162] and (ii) characterizing the detected non-primordial B-mode signal generated when E-modes are gravitationally lensed by large-scale structures in the Universe [125, 76, 33, 31, 32, 170, 1, 35]. A key challenge for B-mode studies is disentangling foreground signals from CMB observations because they can appreciably bias the results in a variety of ways [111]. In this Chapter we address biases to polarimeter calibration.

Precise measurements of the polarization properties of the CMB require accurate knowledge of the relationship between the instrument frame and the reference frame on the sky that is used to define the cosmological Stokes parameters. We refer to this relative orientation angle as the polarization angle of the telescope, $\psi = \psi_{design} + \Delta\psi$, where ψ_{design}

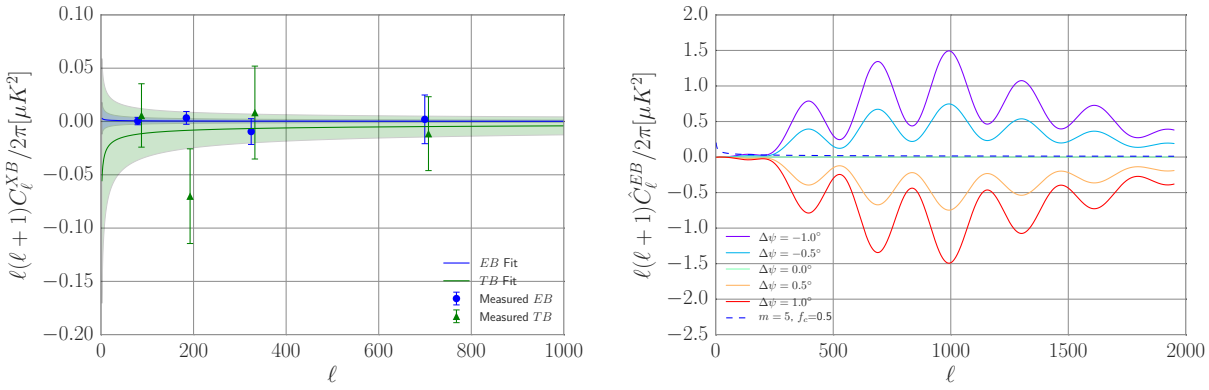

(a) (b)

Figure 5.1: (a) Measured EB and TB dust cross-spectra with best-fitting power laws. The blue and green data points show the EB and TB dust cross-spectra, respectively, as measured on *Planck* 353 GHz data in the BICEP2 region using PolSpice and scaled to 150 GHz using the dust grey-body spectrum (plotted with a slight offset for clarity). The solid lines are the best-fitting power laws with a fixed index and the shading represents the uncertainty of the best-fitting amplitude. (b) Rotated CMB EB cross-spectra and dust EB cross-spectra as a correlation fraction. The solid rainbow lines show the rotated EB spectra given an experiment observing only the CMB but misaligned by various angles $\Delta\psi$. The dashed line is an upper bound on the dust EB spectrum, determined by a correlated fraction of the E- and B-mode power (see Equation 5.3 with $m = 5$ and $f_c = 0.5$). At $\ell \gtrsim 300$ even the brightest dust EB spectrum is negligible compared to the rotated CMB spectra for $\Delta\psi > 0.5°$.

is the intended orientation and $\Delta\psi$ is a small misalignment. Calculations show that ψ must be measured to arcminute precision for IGW searches targeting tensor-to-scalar ratios $r \lesssim 0.01$ [150, 214, 204]. Ideally, celestial sources would be used to measure the polarization angle [19, 193, 209, 301]. At millimetre wavelengths, the best celestial source appears to be Tau A, though it is not ideal because (i) it is not bright enough to give a high signal-to-noise ratio measurement with a short integration time, (ii) the source is extended with a complicated polarization intensity morphology, (iii) the millimetre-wave spectrum of Tau A is not precisely known, which is important for polarimeters that have frequency-dependent performance, and (iv) Tau A is not observable from Antarctica where many ground-based and balloon-borne experiments are sited (see [157] and references therein). Since an ideal celestial calibration source does not exist, many current experiments [164, 22, 209, 301, 34]

use a 'self-calibration' method [167].

The self-calibration method exploits the fact that the EB and TB cross-spectra of the CMB vanish for parity-conserving inflaton fields [312], so any detected EB and TB signals are interpreted as systematic effects that can be used to de-rotate instrument-induced biases. However, this assumption neglects the fact that polarized Galactic foregrounds in a given portion of the sky may have non-zero EB and TB cross-spectra. If these foreground signals remain in the observations, then they will bias the derived polarization angle and produce a spurious BB signal even if the instrument was perfectly mechanically aligned before self-calibration [150, 272, 307].

In this Chapter, we consider the case where the EB and TB cross-spectra for Galactic dust are non-zero, and estimate the foreground-induced bias produced by different levels of polarized dust intensity for various instrument configurations. We then expand the formalism to mitigate the effect of polarized foreground signals. The Chapter is structured as follows. In Section 5.2.1, we discuss the data used to establish the likely range of polarized foreground signals. In Section 5.2.2, we review the self-calibration method and add foregrounds to the rotated power spectra. Miscalibration results for different levels of dust and instrument designs are presented in Section 5.3. We then estimate the bias on r due to miscalibration in Section 5.3.2. Section 5.4 corrects the self-calibration formalism to account for foregrounds in the observations. We show that this recovers the telescope polarization angle at the cost of increased statistical error on $\Delta\psi$. We summarize and conclude in Section 5.5.

5.2 Methods

5.2.1 Estimating Foreground Power Spectra

To perform the self-calibration calculation and estimate the foreground bias we require CMB and foreground power spectrum measurements. We use CAMB[1] to generate theoretical CMB

[1] http://camb.info

power spectra [188], with the *Planck* best-fitting ΛCDM cosmological parameters [232]. We include gravitational lensing and set the tensor-to-scalar ratio $r = 0.0$.

To assess the impact of dust foregrounds on the self-calibration procedure, we require estimates of realistic dust EE, TE, TB, EB, and BB power spectra. For this purpose, we consider the BICEP2 field, in which foregrounds have been particularly well-studied (e.g., [113, 111, 225, 35, 31]), and in which the foreground levels are low but non-negligible. Later we also consider different scenarios for the dust amplitude. To measure the power spectra, we use the *Planck* 353 GHz T, Q, and U half-mission split maps and an angular mask approximating the BICEP2 region from [111]. We also apply a polarized point source mask constructed from *Planck* High Frequency Instrument data. The combined mask is apodized using a Gaussian with FWHM = 30 arcmin, yielding an effective sky fraction $f_{sky} = 0.013$. Our power spectrum estimator is based on PolSpice [70], with parameters calibrated using 100 simulations of polarized dust power spectra consistent with recent *Planck* measurements [225]. The power spectra are estimated from cross-correlations of the *Planck* half-mission splits, such that no noise bias is present in the results. We bin the measured power spectra in four multipole bins matching those used in [225], spanning $40 < \ell < 1000$. Error bars are estimated in the Gaussian approximation from the auto-power spectra of the half-mission splits. We then re-scale the 353 GHz measurements to 150 GHz using the best-fitting greybody dust SED from [225], which corresponds to a factor of 0.041 for polarization and 0.043 for temperature.

Our measured BB power spectrum is consistent with that measured in the BICEP2 patch in [225] (small deviations are expected due to the slightly different masks employed). The measured EB and TB power spectra are shown in Figure 5.1a. Both spectra are consistent with zero. The observed amplitudes are smaller than those measured in [225] for EB and TB spectra on large sky fractions containing more dust, as expected (see Appendix 5.6 here and figs. B.2 and B.3 of [225]). We note that even on the large sky fractions studied in [225], the dust EB and TB spectra are generally consistent with zero, except for masks

with $f_{sky} \gtrsim 0.5$, which show evidence of a signal on roughly degree angular scales. We take the results measured in the BICEP2 patch as fiducial dust power spectra and consider variations around this scenario below. For simplicity, we fit a simple power-law template to all dust power spectra (see below), such that each spectrum is completely characterized by an overall amplitude. We then vary the amplitudes to produce two additional sets of dust power spectra to represent different possible observations:

$$C_\ell^{dust,XY} = A^{XY}\left(\frac{\ell}{80}\right)^{-2.42} \tag{5.1}$$

$$C_{\ell,mult}^{dust,XY} = mC_\ell^{dust,XY} \tag{5.2}$$

$$C_{\ell,corr}^{dust,ZB} = f_c\sqrt{C_{\ell,mult}^{dust,ZZ}C_{\ell,mult}^{dust,BB}}, \tag{5.3}$$

where A^{XY} is the best-fitting amplitude, m is a multiplicative factor, f_c is a correlation fraction, $X, Y \in \{T, E, B\}$ and $Z \in \{T, E\}$.

Data set 1 is calculated by fitting for the amplitude of a power law spectrum to each of the dust power spectra, with a fixed index $\beta = -2.42$, as given by Equation 5.1. This is motivated by the *Planck* foreground analysis which finds the dust power spectra to be consistent with a power law in ℓ [235].

In data set 2, we increase the amplitude of all dust power spectra by an overall multiplicative factor, m, given by Equation 5.2. This represents measurements on patches larger and dustier than the BICEP2 region.

In data set 3, we write the EB and TB dust spectra as a correlated fraction, f_c, of the EE and BB and TT and BB spectra, respectively, as given by Equation 5.3. We use the correlation fraction to explore the possibility of proportionally large EB and TB cross-spectra while imposing the constraint that they do not exceed the level of the EE and BB or TT and BB power, respectively. The dashed lines in Figure 5.1b show the data set 3 EB dust cross-spectrum. These data sets provide realistic upper bounds on the observed dust power spectra at 150 GHz. We list the amplitude of the dust cross-spectra in each case in

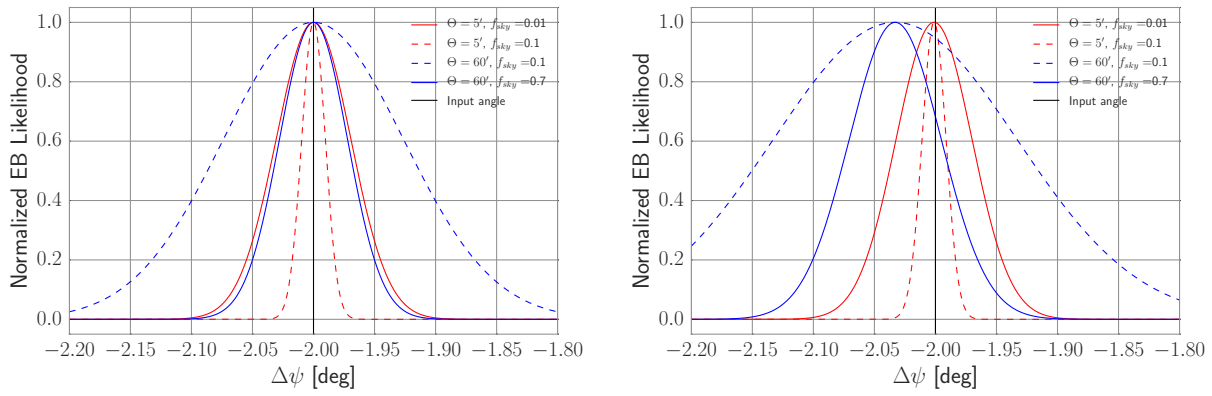

(a) (b)

Figure 5.2: (a) Clean sky EB likelihoods for various instrument configurations (see Section 5.3.1). Self-calibration likelihood for recovering $\Delta\psi_{EB}$ given an experiment misaligned by $\Delta\psi_{\text{in}} = -2°$. We exclude dust and consider only the effects of different beam sizes and sky fractions. We test experiment configurations with $\Theta_{\text{FWHM}} = 5'$ and $60'$ and $f_{sky} = 0.01$, 0.1, and 0.7. Red curves show the likelihood for $5'$ resolution experiments and blue curves show $60'$ resolution experiments. The two experiment configurations with nearly the same likelihood will be referred to as experiments E_{HR} and E_{LR} for the high-resolution and low-resolution configurations, respectively. (b) Dusty sky EB likelihoods for various instrument configurations (see Section 5.3.1). The same experiment specifications as Figure 5.2a but including dust in the rotated power spectrum. Dust dominates the polarized CMB at low multipoles and thus weakens the self-calibration procedure for low-resolution experiments. There is a small bias in the recovered alignment angle for large beam experiments.

Table 5.6.

5.2.2 Review of Self-Calibration Procedure

Following the self-calibration procedure of [167], a miscalibration of the instrument polarization angle, ψ_{design}, by an amount $\Delta\psi$ results in a rotation of the observed Stokes vector and thus the observed Stokes parameters, $\hat{Q}(\boldsymbol{p})$ and $\hat{U}(\boldsymbol{p})$, as given by Equations 5.4 and 5.5:

$$\hat{Q}(\boldsymbol{p}) = \cos(2\Delta\psi)Q(\boldsymbol{p}) - \sin(2\Delta\psi)U(\boldsymbol{p}) \tag{5.4}$$

$$\hat{U}(\boldsymbol{p}) = \sin(2\Delta\psi)Q(\boldsymbol{p}) + \cos(2\Delta\psi)U(\boldsymbol{p})\,, \tag{5.5}$$

where $Q(\mathbf{p})$ and $U(\mathbf{p})$ are the sky-synchronous linear polarization Stokes parameters, and $\boldsymbol{p}$ denotes the pointing on the sky (note we use the CMB convention for the polarization angle direction). The observed $\hat{E}(\boldsymbol{l})$ and $\hat{B}(\boldsymbol{l})$ modes are then rotated from the sky-synchronous $E(\boldsymbol{l})$ and $B(\boldsymbol{l})$ modes as given by Equations 5.6 and 5.7:

$$\hat{E}(\boldsymbol{l}) = \cos(2\Delta\psi)E(\boldsymbol{l}) + \sin(2\Delta\psi)B(\boldsymbol{l}) \tag{5.6}$$

$$\hat{B}(\boldsymbol{l}) = -\sin(2\Delta\psi)E(\boldsymbol{l}) + \cos(2\Delta\psi)B(\boldsymbol{l})\,, \tag{5.7}$$

where $\boldsymbol{l}$ is the conjugate variable to $\boldsymbol{p}$. To determine the best-fitting misalignment angle, $\Delta\psi$, we minimize the variance between the rotated spectra and theoretical CMB spectra and thus maximize the likelihood functions given by Equations 5.8 and 5.9, which are analytically solvable. We define f_{sky} as the observed sky fraction, Δ_X as the observation noise, Θ_{FWHM} as the telescope beam full-width at half-maximum, and let the subscript and superscript $X \in \{T, E, B\}$.

$$\mathcal{L}_{EB}(\Delta\psi) \propto \exp\left[-\sum_{\ell} \frac{\left(\hat{C}_\ell^{EB} + \frac{1}{2}\sin(4\Delta\psi)\left(C_\ell^{EE} - C_\ell^{BB}\right)\right)^2}{2\left(\delta\hat{C}_\ell^{EB}\right)^2}\right] \tag{5.8}$$

$$\mathcal{L}_{TB}(\Delta\psi) \propto \exp\left[-\sum_{\ell} \frac{\left(\hat{C}_\ell^{TB} + \sin(2\Delta\psi)C_\ell^{TE}\right)^2}{2\left(\delta\hat{C}_\ell^{TB}\right)^2}\right] \tag{5.9}$$

$$\left(\delta\hat{C}_\ell^{EB}\right)^2 = \frac{1}{(2\ell+1)f_{\mathrm{sky}}}\hat{C}_\ell^{EE,tot}\hat{C}_\ell^{BB,tot} \tag{5.10}$$

$$\left(\delta\hat{C}_\ell^{TB}\right)^2 = \frac{1}{(2\ell+1)f_{\mathrm{sky}}}\hat{C}_\ell^{TT,tot}\hat{C}_\ell^{BB,tot} \tag{5.11}$$

$$\hat{C}_\ell^{XX,tot} = \hat{C}_\ell^{XX} + \Delta_X^2 e^{\ell^2\Theta^2_{\mathrm{FWHM}}/(8\ln 2)} \tag{5.12}$$

The hat on $\hat{C}_\ell$ denotes rotated angular power spectra, which include foregrounds and a rotation angle in the model, and represent, in this Chapter, the power spectra that would be measured by an experiment. C_ℓ represents theoretical CMB power spectra. The rotated

power spectra are given by Equations 5.13 - 5.17 with the foregrounds given by C_ℓ^{fg}.

$$\begin{aligned}\hat{C}_\ell^{EE} =& \sin^2(2\Delta\psi)\left(C_\ell^{BB} + C_\ell^{fg,BB}\right) + \cos^2(2\Delta\psi) \\ &\times \left(C_\ell^{EE} + C_\ell^{fg,EE}\right) + \sin(4\Delta\psi)C_\ell^{fg,EB}\end{aligned} \tag{5.13}$$

$$\begin{aligned}\hat{C}_\ell^{BB} =& \cos^2(2\Delta\psi)\left(C_\ell^{BB} + C_\ell^{fg,BB}\right) + \sin^2(2\Delta\psi) \\ &\times \left(C_\ell^{EE} + C_\ell^{fg,EE}\right) - \sin(4\Delta\psi)C_\ell^{fg,EB}\end{aligned} \tag{5.14}$$

$$\hat{C}_\ell^{TE} = \cos(2\Delta\psi)\left(C_\ell^{TE} + C_\ell^{fg,TE}\right) + \sin(2\Delta\psi)C_\ell^{fg,TB} \tag{5.15}$$

$$\hat{C}_\ell^{TB} = \cos(2\Delta\psi)C_\ell^{fg,TB} - \sin(2\Delta\psi)\left(C_\ell^{TE} + C_\ell^{fg,TE}\right) \tag{5.16}$$

$$\begin{aligned}\hat{C}_\ell^{EB} =& \frac{1}{2}\sin(4\Delta\psi)\left(C_\ell^{BB} - C_\ell^{EE} + C_\ell^{fg,BB} - C_\ell^{fg,EE}\right) \\ &+ \cos(4\Delta\psi)C_\ell^{fg,EB}\end{aligned} \tag{5.17}$$

We use dust power spectra as defined by Equations 5.1 - 5.3 as the foreground spectra. Figure 5.1b shows the rotated EB spectrum, without dust, for various rotation angles. Figure 5.7 shows the CMB, dust, and rotated power spectra as well as noise for a fiducial experiment design.

Once $\Delta\psi$ is found it can be corrected for by a rotation of $-\Delta\psi$ applied to the measured Q and U maps, however any non-zero EB or TB foreground power will bias the calibration angle, as shown in the next Section. We write a complete formalism that takes the foregrounds into account in the likelihood itself in Section 5.4.

$\Delta\psi_{EB}$ [degrees]			
Θ_{FWHM}	f_{sky}	CMB Only	CMB + Dust
$5.0'$	0.01	-2.00 ± 0.03	-2.00 ± 0.03
	0.1	-2.00 ± 0.01	-2.00 ± 0.01
$60.0'$	0.1	-2.00 ± 0.07	-2.03 ± 0.10
	0.70	-2.00 ± 0.03	-2.03 ± 0.04
$\Delta\psi_{TB}$ [degrees]			
$5.0'$	0.01	-2.00 ± 0.09	-2.00 ± 0.09
	0.1	-2.00 ± 0.03	-2.00 ± 0.03
$60.0'$	0.1	-2.00 ± 0.12	-2.03 ± 0.13
	0.70	-2.00 ± 0.05	-2.03 ± 0.06

Table 5.1: Recovered angle with and without dust (see Figure 5.2a and 5.2b). Simulated misalignment $\Delta\psi_{in} = -2.0°$. The recovered $\Delta\psi$ and 1σ uncertainties for experiment configurations with different beams and sky coverage, with and without dust in the rotated spectra. The EB calibration is more precise than TB in all scenarios. The uncertainties scale inversely with f_{sky}.

5.3 Results

5.3.1 Foreground Biased Self-Calibration Angle

We perform the self-calibration procedure to measure the telescope misalignment $\Delta\psi$ using several different instrument configurations and compare the effects of foregrounds in each case. For all experiments we assume an effective instrument noise $\Delta_X = 5\mu K$ arcmin. We use three data sets of different dust spectra to characterize the effects of foregrounds on the self-calibration angle.

For convenience we define E_{HR} as the high-resolution and small sky fraction experiment with $\Theta_{FWHM} = 5'$ and $f_{sky} = 0.01$ and E_{LR} as the low-resolution and large sky fraction experiment with $\Theta_{FWHM} = 60'$ and $f_{sky} = 0.7$.

Self-Calibration with CMB Only

We reproduce the CMB-only results of [167] in Figure 5.2a and Table 5.1, with all the dust spectra set to zero. High angular resolution or large sky fraction experiments have inher-

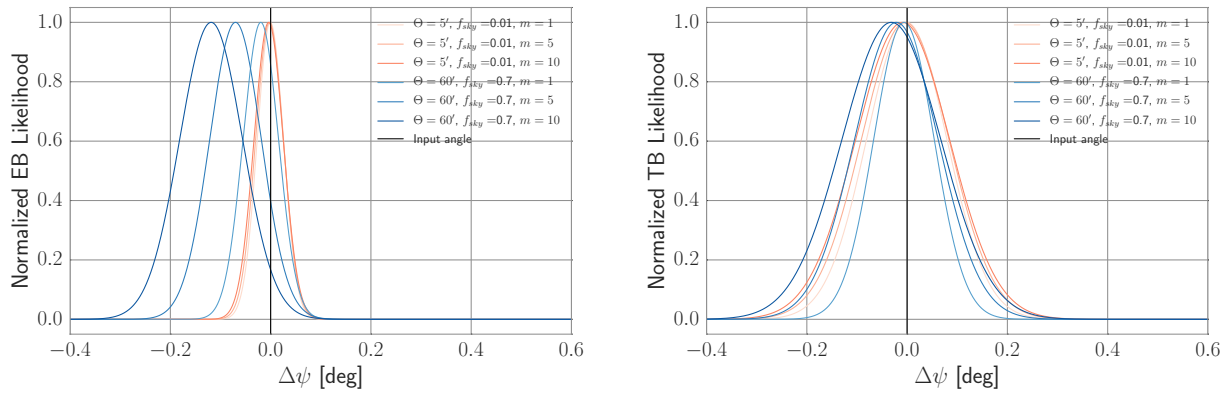

(a) (b)

Figure 5.3: (a) EB Likelihood with increased dust level (see Section 5.3.1). We increase the level of dust power and compare the results for experiment configurations E_{HR} and E_{LR}, with the simulated misalignment $\Delta\psi_{in} = 0.0°$. The low-resolution experiment is biased and has larger statistical uncertainty than the high-resolution experiment when high levels of foregrounds are observed. The multiplicative factor is $m = 1$, 5, and 10. (b) TB Likelihood with increased dust level. Same as Figure 5.3a but using TB as a calibrator. Notice the TB calibration has larger uncertainties than EB but is more robust in general to high power foregrounds.

ently less statistical uncertainty on the self-calibrated angle than low-resolution or small sky fraction experiments. Experiments E_{HR} and E_{LR} have approximately the same constraining power on $\Delta\psi_{EB}$ using the self-calibration procedure on the CMB-only sky.

Self-Calibration with Dust Measured in BICEP2 Region

We add dust, as measured in the BICEP2 region and fit to a power law, to the rotated spectra as in Equations 5.13 - 5.17, and show the results in Figure 5.2b and Table 5.1. The recovered $\Delta\psi$ for experiment E_{HR} is unbiased. However, the dust foreground produces a small bias in the calibration angle of experiment E_{LR} by $\Delta\psi_{in} - \Delta\psi_{out} = 0.03°$ at 0.75σ significance. The dust also increases the statistical error of the calibration. A bias of this size is negligible compared to current calibration uncertainties (of order 0.5°), but could prove relevant in the future. Also, the dust power spectra can be larger in other regions of the sky, producing a larger bias, as we show below.

Experiment Config.			$\Delta\psi$ [arcmin]	
Θ_{FWHM}	f_{sky}	m	EB	TB
$5.0'$	0.01	1	-0.0 ± 1.6	-0.1 ± 4.8
		5	-0.1 ± 1.7	-0.2 ± 5.2
		10	-0.2 ± 1.7	-0.6 ± 5.6
$60.0'$	0.70	1	-1.2 ± 2.1	-0.4 ± 3.6
		5	-4.2 ± 3.0	-1.3 ± 5.0
		10	-7.1 ± 3.8	-1.9 ± 5.9

Table 5.2: Increased dust level by multiplicative factor (see Figure 5.3a and 5.3b). Simulated misalignment $\Delta\psi_{in} = 0.0^\circ$ for experiment configurations E_{HR} and E_{LR} and $m = 1$, 5, and 10. An experiment observing large portions of the sky near the Galactic plane will observe high levels of dust which can bias the calibration angle, as evident in the second row of the table. Note the units of $\Delta\psi$ are arcminutes.

Self-Calibration with Brighter Dust Spectra

We increase the dust power in all spectra by a multiplicative factor as in Equation 5.2. This is motivated by the fact that we measured the dust spectra on only 1 per cent of the sky at high Galactic latitude, while larger sky fractions will see more dust. We increase the dust amplitude by up to an order of magnitude, which is consistent with *Planck* observed dust power on 70 per cent of the sky. Figure 5.3a and Table 5.2 illustrate the effect of increasing levels of dust power for experiments E_{HR} and E_{LR}. The dust power dominates the CMB at low ℓ and thus low resolution experiments using the self-calibration procedure are susceptible to a bias (as large as $1-2\sigma$). The calibration angle for high resolution experiments is robust to strong foregrounds.

Self-Calibration with Correlated Dust Spectra

We write the EB and TB spectra as a correlated fraction of the power in EE and BB and TT and BB, respectively, as in Equation 5.3. For simplicity we let the correlation fraction be the same and positive for both EB and TB, although the TB spectra measured in the BICEP2 region is slightly negatively correlated. To show an extreme case, we take the dust level to be $5\times$ that measured in the BICEP2 region and then set EB and TB using various

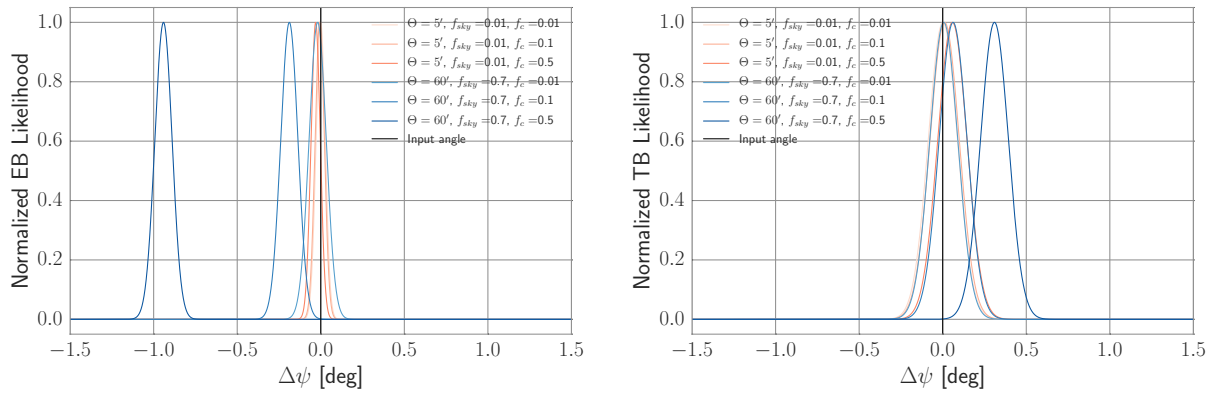

(a) (b)

Figure 5.4: (a) EB likelihood with correlated dust (see Section 5.3.1). Self-calibration likelihood using correlation fractions to set the EB and TB dust power. We set the overall dust level to be 5× that measured in the BICEP2 region and the correlation fraction f_c = 0.01, 0.1 and 0.5. The low-resolution experiment measures a calibration angle biased by up to 1°. Again the high resolution experiment is robust to foregrounds. (b) TB likelihood with correlated dust. Same as Figure 5.4a but using TB as a calibrator. The bias in $\Delta\psi_{TB}$ is of the opposite sign of the other $\Delta\psi_{TB}$ results because we have set the C_ℓ^{TB} dust spectrum to be positive when using the correlation fraction, however it is measured in the BICEP2 region to be slightly negative.

correlation fractions, as shown in Figure 5.4a and 5.4b and Table 5.3. We plot the EB cross-spectra derived using this method in Figure 5.1b.

The self-calibration angle in this scenario can be biased by up to 1°. There are several factors that must conspire together to achieve this bias. First, we used a relatively large beam telescope, although with a large sky fraction. Second, we used dust power 5× that in the BICEP2 region, which is generally only realistic for patches near the Galactic plane. Third, the dust correlation fraction is 50 per cent which is approximately 100× that measured by *Planck*. We do not expect this to be observed, although theoretically possible, and thus include it to show an upper bound. Using a small beam eliminates the bias and thus self-calibration for high resolution experiments is robust to bright polarized foregrounds.

Experiment Config.			$\Delta\psi$ [arcmin]	
Θ_{FWHM}	f_{sky}	f_c	EB	TB
$5.0'$	0.01	0.01	-0.1 ± 1.7	0.1 ± 5.2
		0.1	-0.4 ± 1.7	0.7 ± 5.2
		0.5	-1.9 ± 1.7	3.5 ± 5.2
$60.0'$	0.70	0.01	-1.1 ± 3.1	0.4 ± 5.0
		0.1	-11 ± 3.1	3.7 ± 5.0
		0.5	-57 ± 3.1	19 ± 5.0

Table 5.3: Increased dust by using a correlation fraction (see Figure 5.4a and 5.4b). Simulated misalignment $\Delta\psi_{in} = 0.0°$ for experiment configurations E_{HR} and E_{LR} and setting the dust EB and TB cross-spectra by $m = 5$ and $f_c = 0.01$, 0.1, 0.5. The low-resolution experiment measures significantly biased calibration angles. Disagreement between the EB and TB self-calibration angles would be a sign of foreground biases or other systematic errors.

5.3.2 Self-Calibration Angle Bias and Spurious B-mode Power

A miscalibration of the telescope angle will generate B-mode power from the rotation of E-modes into B-modes, as shown in Figure 5.4a. We estimate the tensor-to-scalar ratio from the spurious B-mode power for various rotation angles in Table 5.4. To estimate the equivalent r we take the rotated $\hat{C}_\ell^{BB}$ spectra divided by the $r = 1.0$ theoretical C_ℓ^{BB} spectrum and evaluate at $\ell = 80$, for a given angle $\Delta\psi$. We have neglected dust in the calculation as adding dust can produce an additional bias (i.e., we assume high-frequency data is used to clean polarized dust from the maps). We have also excluded lensing B-mode power in the calculation.

Current experiment systematic biases are generally larger than the potential foreground-induced bias. For example, BICEP2 measures a self-calibration angle of $\Delta\psi = -1.1°$ [34], POLARBEAR measures $\Delta\psi = -1.08°$ with a statistical uncertainty of $0.2°$ [301], and ACTPOL constrains their polarization offset angle to $-0.2 \pm 0.5°$ [209]. A 5σ detection of $r = 0.01$ requires a polarization angle uncertainty $< 0.5°$ for an otherwise ideal experiment with no other sources of systematic error. Accounting for other instrument systematics brings this requirement to $< 0.2°$ [36, 214, 167, 157], which approaches the foreground bias for low-resolution experiments observing particularly dusty regions. Similarly, a miscalibration of

$\Delta\psi$	0.0°	0.2°	0.5°	1.0°	2.0°
r	0.000	0.0003	0.002	0.008	0.033

Table 5.4: Estimated spurious r due to a rotation. We set r as the ratio of the rotated BB spectrum to the theoretical $r = 1.0$ BB spectrum at $\ell = 80$.

the telescope angle by $\gtrsim 0.5°$ greatly biases the measurement of gravitational lensing of E-modes into B-modes [272], as can be seen qualitatively in Figure 5.5.

5.4 Foreground Corrected Self-Calibration Method

We incorporate foregrounds into the calibration method by including them explicitly in the likelihood functions as given by Equations 5.18 and 5.19. This has the effect of eliminating the bias but increasing the uncertainty on the calibration angle, as shown in Figure 5.6. We marginalize over foreground amplitudes assuming a fixed index foreground power law spectrum, although this can be straightforwardly generalized:

$$\begin{aligned}\mathcal{L}_{EB}(\Delta\psi, \boldsymbol{A}') \propto \exp -\Bigg[\sum_\ell \Bigg(& \hat{C}_\ell^{EB} - \cos(4\Delta\psi) C_\ell'^{fg,EB} \\ & + \frac{1}{2}\sin(4\Delta\psi)\Big(C_\ell^{EE} - C_\ell^{BB} \\ & + C_\ell'^{fg,EE} - C_\ell'^{fg,BB}\Big)\Bigg)^2 \Big/ 2\big(\delta\hat{C}_\ell^{EB}\big)^2 \Bigg] \\ & \times \exp -\Bigg[\frac{(A'^{EB} - A^{EB})^2}{2\sigma_{EB}^2} \\ & + \frac{(A'^{EE} - A^{EE})^2}{2\sigma_{EE}^2} + \frac{(A'^{BB} - A^{BB})^2}{2\sigma_{BB}^2} \Bigg] \end{aligned} \tag{5.18}$$

Experiment Config.		$\Delta\psi$ [arcmin]	
Dust Level m	Corrected $\mathcal{L}$	EB	TB
0	No	0.0 ± 1.4	0.0 ± 2.6
5	No	-4.2 ± 3.1	-1.3 ± 5.0
5	Yes	0.0 ± 3.9	0.0 ± 5.3

Table 5.5: Likelihood corrected for foregrounds (see Figure 5.6). Simulated misalignment $\Delta\psi_{\rm in} = 0.0°$ for experiment E_{LR} and $m = 0$ or 5. Using the full likelihood calculation recovers the correct calibration angle as if there were no dust, but has larger uncertainty.

$$\mathcal{L}_{TB}(\Delta\psi, \boldsymbol{A}') \propto \exp - \Bigg[\sum_{\ell} \Big(\hat{C}_\ell^{TB} - \cos(2\Delta\psi) C_\ell'^{fg,TB} + \sin(2\Delta\psi)\big(C_\ell^{TE} + C_\ell'^{fg,TE}\big) \Big)^2 \Big/ 2\big(\delta\hat{C}_\ell^{TB}\big)^2 \Bigg] \times \exp - \left[\frac{(A'^{TB} - A^{TB})^2}{2\sigma_{TB}^2} + \frac{(A'^{TE} - A^{TE})^2}{2\sigma_{TE}^2} \right] \tag{5.19}$$

$$\mathcal{L}_{XB}(\Delta\psi) \propto \int d\boldsymbol{A}' \mathcal{L}_{XB}(\Delta\psi, \boldsymbol{A}') \,. \tag{5.20}$$

Here $C_\ell'^{fg,XY}$ represents the foreground power spectra determined by the amplitude A'^{XY}. We marginalize over the prime quantities in Equation 5.20. The Gaussians are centred on the best-fitting foreground amplitude, A^{XY}, with variance σ_{XY}^2, as determined from 353 GHz (or other high frequency) data. Figure 5.6 compares self-calibration results using the original and foreground-corrected likelihood functions. The corrected version accurately finds the calibration angle, with a slightly larger uncertainty due to the marginalization, as expected.

5.5 Discussion

Unmitigated foreground interference can bias and appreciably reduce the utility of the CMB self-calibration method because a foreground biased polarization angle will generate spurious B-mode power. We consider only dust in this Chapter, however, at lower frequencies other polarized sources such as synchrotron will likewise bias and reduce the effectiveness of the

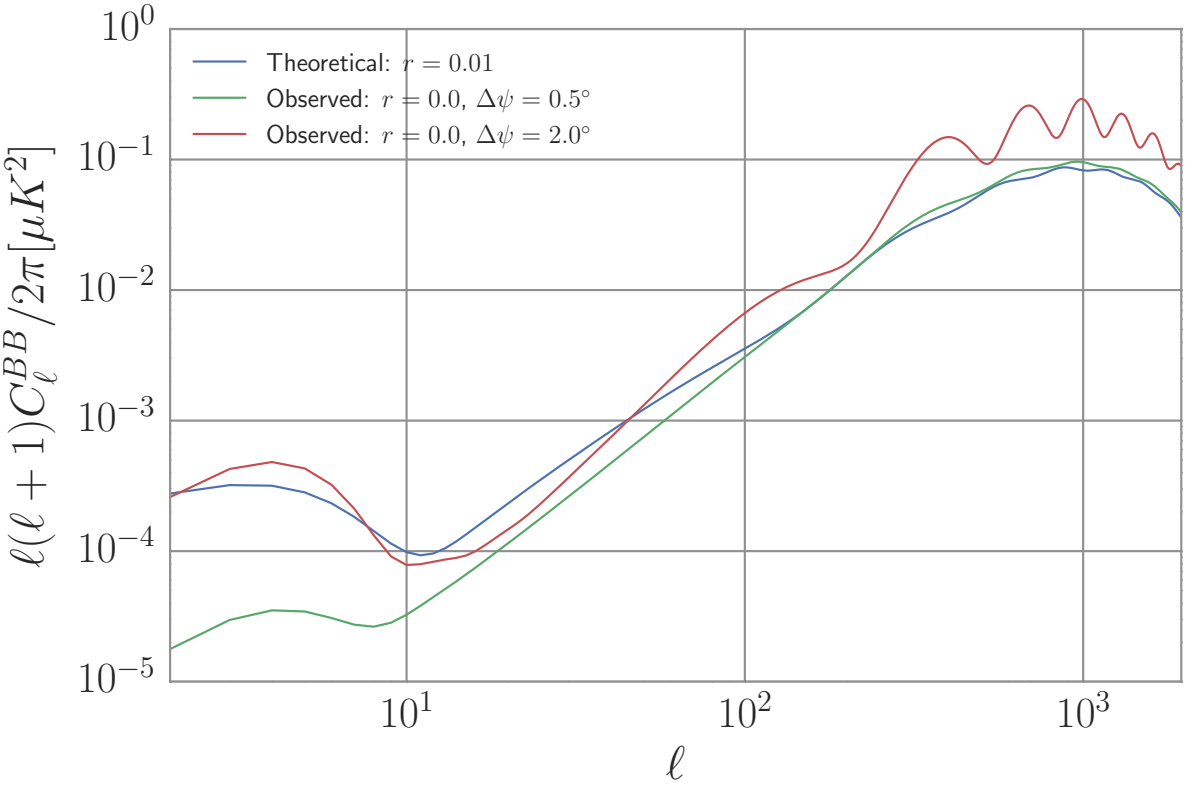

Figure 5.5: Rotated and theoretical BB power spectra. The blue curve shows the theoretical CMB BB power spectrum with $r = 0.01$, including lensing. We compare this to the rotated BB spectra, in the green and red curves, given a miscalibration of the telescope angle by $\Delta\psi = 0.5°$ and $2.0°$, respectively. The rotated spectra were calculated using $r = 0.0$, and thus consists of lensing and leaked $E-$ to B-modes only. For a misalignment of $\Delta\psi < 0.5°$, the E-mode leakage does not contribute significantly to the BB spectrum until $\ell \gtrsim 100$.

self-calibration procedure. To account for polarized foreground signals one can either include them in the self-calibration likelihood function or subtract them in the map domain. A map domain foreground cleaning may require an iterative method between self-calibration and component separation, especially if combining data from multiple instruments.

We note that, in principle, experiments should simultaneously estimate both the cosmological parameter values and the polarization angle because the cosmological parameters used as inputs to the theoretical CMB power spectra have non-zero uncertainty. Additionally, the likelihood functions for EB and TB should be maximized simultaneously, although the use of two separate estimators provides a consistency check.

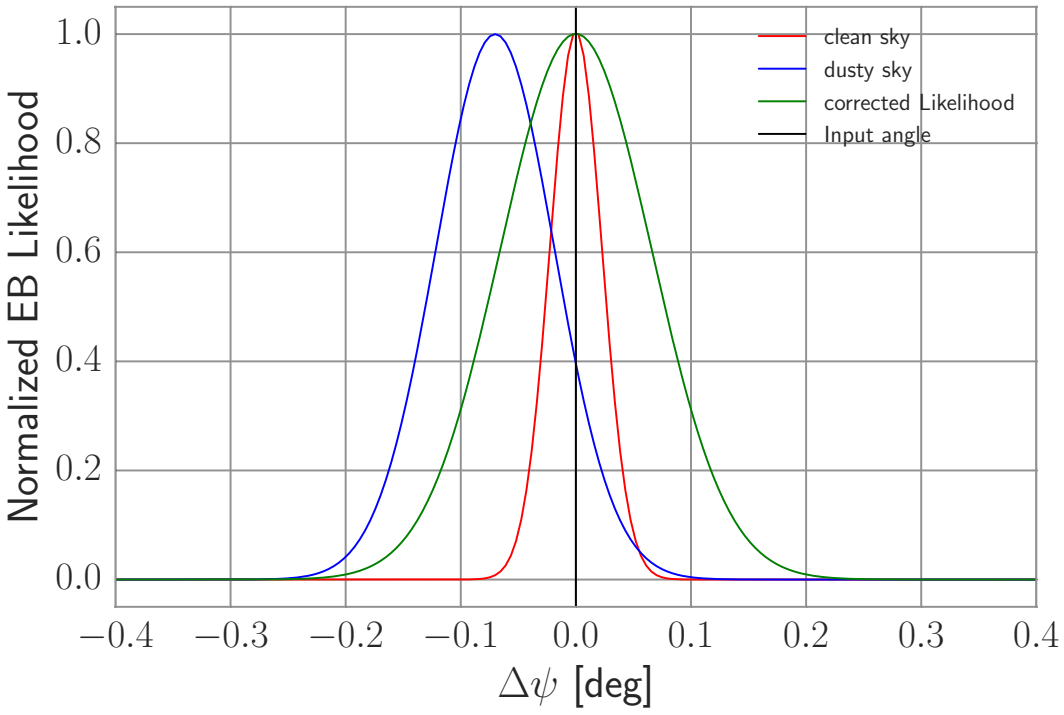

Figure 5.6: Likelihood corrected for foregrounds (see Section 5.4). We use experiment configuration E_{LR} and compare the uncorrected to the foreground-corrected likelihood. The red curve shows the likelihood without foregrounds for reference. The blue curve adds dust with $m = 5$ into the rotated spectra using the original (uncorrected) likelihood (Equation 5.8). The green curve includes the same dust power but corrects for foregrounds in the likelihood (Equation 5.18). Including the dust in the likelihood eliminates the bias but increases the statistical uncertainty (see also Table 5.5).

It is important to note that primordial magnetic fields and cosmic birefringence should produce faint non-zero EB and TB cross-spectra [231, 243]. Because the self-calibration method minimizes the EB and TB correlation, it is difficult to both search for these signals and self-calibrate. Nevertheless some experiments are investigating ways to make this observation [243].

We conclude that experiments using the self-calibration procedure should be aware of the potential bias of non-zero EB and TB power due to foregrounds. CMB experiments using foreground monitors at frequencies far above or below the foreground minimum need to account for foreground contamination in the self-calibration procedure. Self-calibration for experiments with access to high-ℓ multipoles is robust to foreground contamination, as

the foreground power spectra generally falls off as a power law. Low-resolution or low-ℓ experiments observing small sky fractions are vulnerable to foreground-induced biases.

Dust Data Set	Dust Power $[\ell(\ell+1)/2\pi\ \mu K^2] \times 1000$	
Dust Params	$C_{\ell=80}^{dust,EB}$	$C_{\ell=80}^{dust,TB}$
Measured	0.39 ± 3.5	5.66 ± 29
Best-Fitting	0.64 ± 3.2	-11.8 ± 24
$m = 5$	3.2	-59.2
$m = 10$	6.4	-118
$m = 5,\ f_c = 0.01$	0.86	17.0
$m = 5,\ f_c = 0.1$	8.6	171
$m = 5,\ f_c = 0.5$	43	853

Table 5.6: Dust EB and TB Power (see Section 5.2.1). We show the dust cross-spectra at $\ell = 80$ (multiplied by 1000 for ease of reading) for the three data sets we use in this Chapter (see Section 5.2.1). The best-fitting row refers to the amplitude of the power-law fit to all four band-powers (normalized at $\ell = 80$), whereas the measured row refers to the band-power measured at $\ell = 80$. The dust cross-spectra are currently not well-constrained and are consistent with zero in the BICEP2 region. We thus use these data sets to represent other possible measurements of the EB and TB dust cross-spectra, which are consistent with the bounds set by *Planck*, except for the $f_c = 0.5$ case.

5.6 Dust Cross-Correlation Spectra

For completeness, we list the amplitudes used in the EB and TB power-law spectra in Table 5.6. These can be compared to the EB and TB spectra in fig B.2 and B.3 of [225]. Briefly, *Planck* measures EB and TB power at 353 GHz in the range $0 - 10$ and $0 - 100$ μK^2, respectively, depending on the sky fraction analysed. Those upper limits correspond to approximately 0.017 and 0.17 μK^2 when scaled to 150 GHz using the grey-body frequency dependence of dust emission [235]. Comparing these to Table 5.6 (note we multiplied the Table by 1000 to ease readability), we see that all our spectra are within those bounds except the extreme case where $m = 5$ and $f_c = 0.5$.

Lastly, we reproduce fig. 2 of [167] using our data sets and show the resulting rotated BB spectra in Figure 5.7. The rotated BB spectra follows the dust spectra for $\ell \lesssim 100$ and

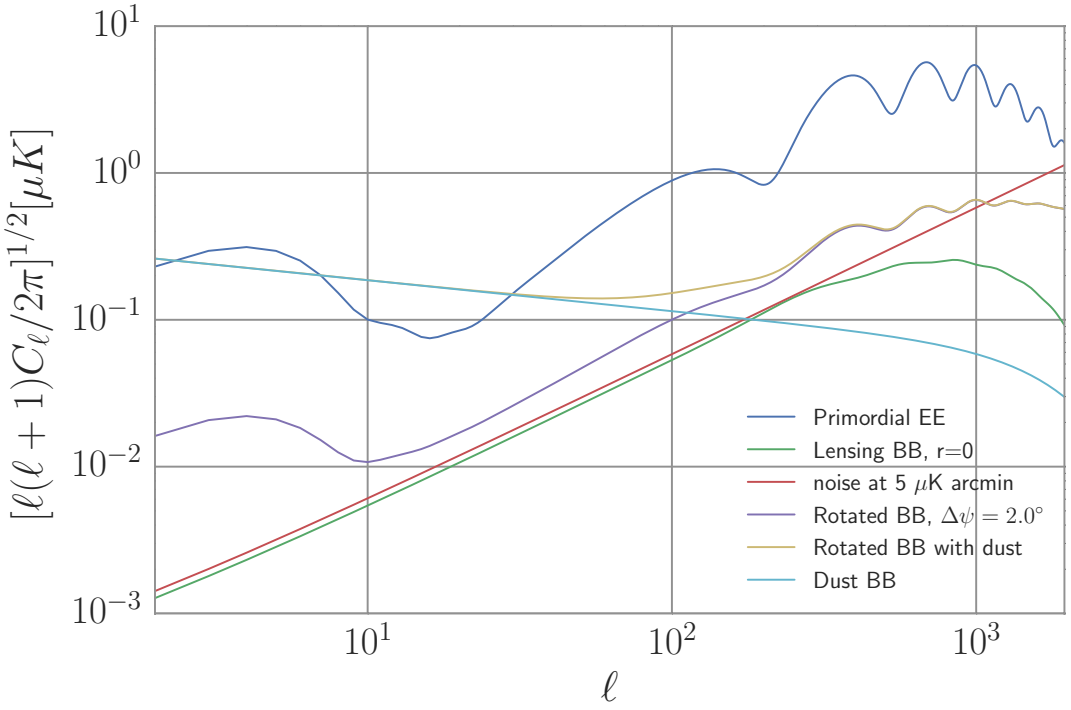

Figure 5.7: Theoretical and rotated amplitude spectra. CMB EE and BB amplitude spectra (square root of power spectra) with $r = 0$ and rotated BB spectra when including a telescope misalignment of $\Delta\psi_{in} = 2.0°$. Also shown is the dust BB spectrum and the noise amplitude spectrum given $\Delta_X = 5\mu K$ arcmin. The rotated spectra are shown both before and after adding dust to the sky in purple and gold lines, respectively. At low multipoles, $\ell \lesssim 100$, the dust contributes significantly to the rotated BB spectrum.

then follows the leaked EE component for $\ell \gtrsim 300$.

Part III

Experimental CMB Research

Chapter 6

The E and B Experiment Data Analysis

The E and B EXperiment (EBEX) was a balloon-borne CMB polarization experiment that flew over Antarctica in January 2013. EBEX was designed to measure the polarization of the CMB and foregrounds as well as serve as a pathfinder for new detector and readout technologies. EBEX observed in three frequency bands centered on 150, 250, and 410 GHz, using 1960 frequency domain multiplexed (FDM) transition edge sensor (TES) bolometers. EBEX used a continuously rotating cryogenic half-wave plate (HWP) to modulate the polarization signal in an effort to reduce polarized systematic errors. EBEX was designed to measure a 400 $\deg^2$ area of sky with an angular resolution of approximately $10'$. An attitude control motor malfunctioned during the flight, causing EBEX to lose control of its pointing. This resulted in observations covering 6000 $\deg^2$ of sky instead of 400 $\deg^2$. The expected noise per pixel was thus significantly increased and systematic errors were much more difficult to understand. See the three EBEX papers, The EBEX Collaboration et al. [299, 300, 298], for details about the experiment and flight.

This chapter describes my work for the EBEX experiment as we attempted to recover maps of the CMB despite the in-flight motor failure. The chapter is divided into two sections

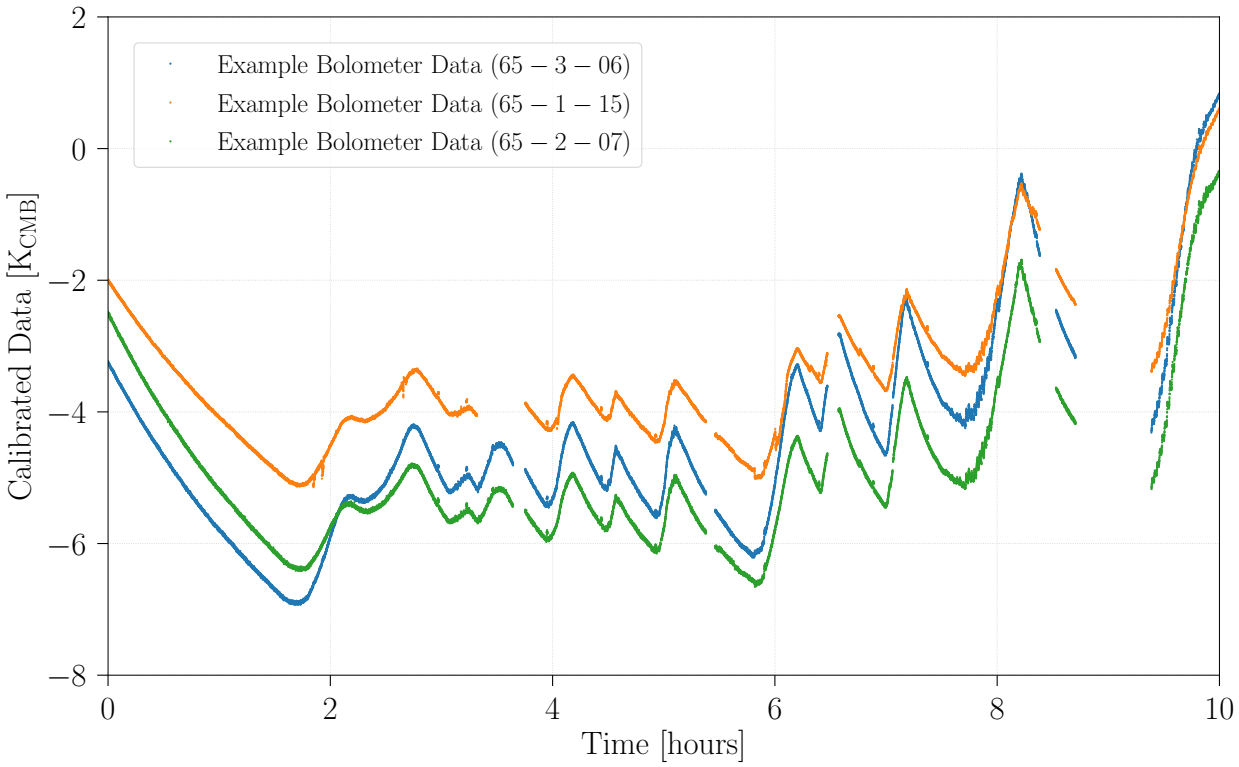

Figure 6.1: Example calibrated time-ordered data from three detectors at 250 GHz over the course of one data segment (approximately one day). The destriped map-making algorithm is designed to remove the long timescale drifts seen in the data.

i) noise modeling and ii) map-making. The noise modeling section summarizes my work characterizing the noise performance of the experiment by estimating the noise for each detector throughout the whole flight and using this information to inform the map-making algorithm and estimate the expected signal-to-noise on the sky. The map-making section discusses my work applying a destriped map-making code (*destriper*) to the EBEX data in order to make clean maps of the sky.

6.1 EBEX Noise Modeling

The goal of CMB experiments is to measure the angular power spectrum of the temperature and polarization anisotropies of the CMB. In order to do this, maps are made at different frequency using observations from many detectors. The frequency maps are then combined

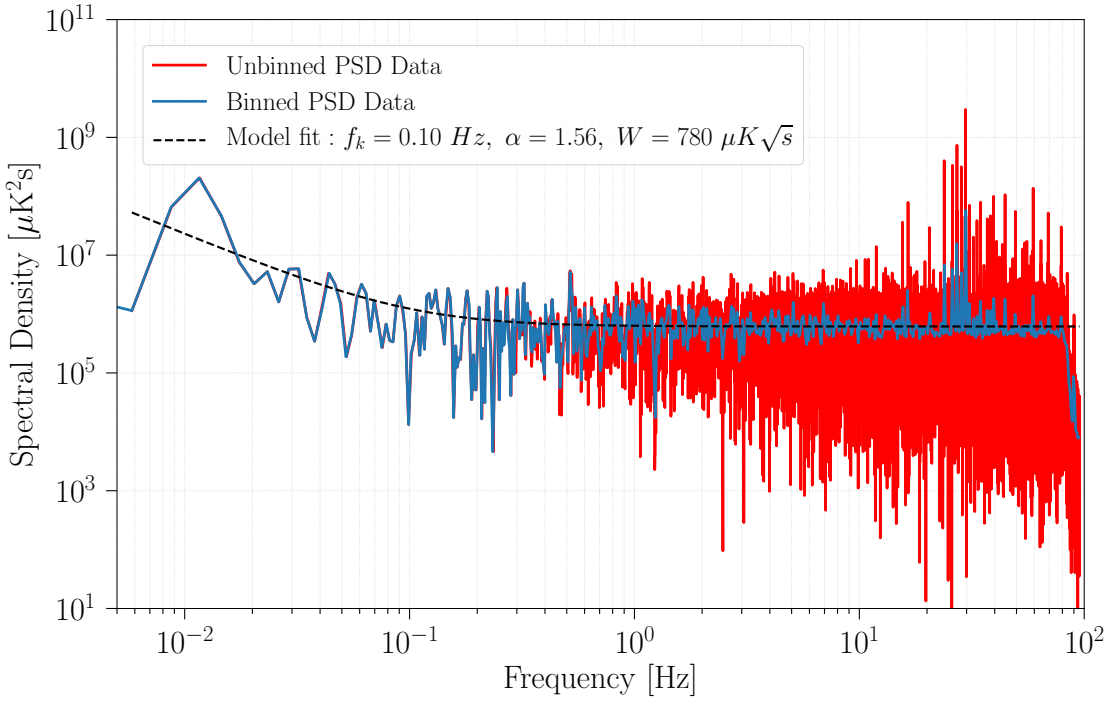

Figure 6.2: Example PSD of a 5.7 minute length of TOD for a 250 GHz detector (labeled 65-3-06) with the corresponding noise model fit. The red is the unbinned power spectrum and the blue is the logarithmically binned power spectrum. The dotted line is the best fit noise model of Equation 6.5 with $W = 780\ \mu K\sqrt{s}$, $f_k = 0.10$ Hz, and $\alpha = 1.56$. Below $f \leqslant 0.1$ Hz we see an increase in low-frequency noise power. The HWP template is subtracted only to 10 Hz and higher than this we see residual HWP signal harmonics. We apply this noise fitting to every detector TOD every 5.7 minutes for the entire flight to characterize the noise performance of EBEX.

to remove foregrounds and produce I, Q, and U maps of the CMB, which are then projected into T, E, and B modes. Cosmological parameters are then inferred from the angular power spectra of the T, E and B-mode maps. A variety of preprocessing steps are applied to the data before the map-making procedure. For EBEX, these steps include pointing reconstruction, half-wave plate template subtraction and demodulation, deglitching, data selection, and calibration. See Didier [86], Araujo [16], Aubin et al. [18] for information on these methods for EBEX. For my noise modeling and map-making work, I use data that has all the preprocessing applied and is ready for science analysis, which we will call time-ordered data (TOD). The data was gathered in segments of time lasting approximately

one day, which make for a natural timescale to organize the data. An example segment of TOD for three 250 GHz detectors is plotted in Figure 6.1. Several features stand out in the TOD. The TOD are correlated across detectors, which can come from a variety of sources including atmospheric drifts, sky signals, or cryogenic temperature changes. The high frequency noise (essentially the width of the lines) is much less than the size of the long-timescale drifts. To characterize the noise properties of the experiment, we will work in the power spectrum domain. Thus the long-timescale drifts are referred to as low-frequency noise and the short-timescale noise is related to the white-noise level of the TOD. The destriped map-making algorithm addresses the issue of drifts by combining multiple observations of the same location on the sky to separate signal from noise, and will be discussed in the map-making section. EBEX has the advantage of using a HWP to modulate the polarization signal which moves the polarization signal out of the low-frequency noise regime and into the white-noise regime.

EBEX flew with nearly 2000 detectors, producing approximately 1 Terabyte of data. In order to characterize the experiment performance and prepare for map-making, we produced a noise estimation method that would quickly analyze the noise for the entire dataset. There are two important characteristics of the noise that we would like to measure i) the Gaussian white-noise component and ii) the low-frequency red-noise component. The white-noise level determines how long observations must be conducted in order to average down the noise and detect the sky signal. The red-noise component does not average down in time and has to be removed by filtering or destriped map-making. The modeling procedure is performed in the power spectrum domain of the TOD. We first describe the noise estimation method and then describe the resulting noise statistics and map sensitivity.

6.1.1 Noise Estimation Method

We estimated the white-noise level and low-frequency behavior of the TOD, as well as the time variability of these noise characteristics. For each detector we calculated power spectral

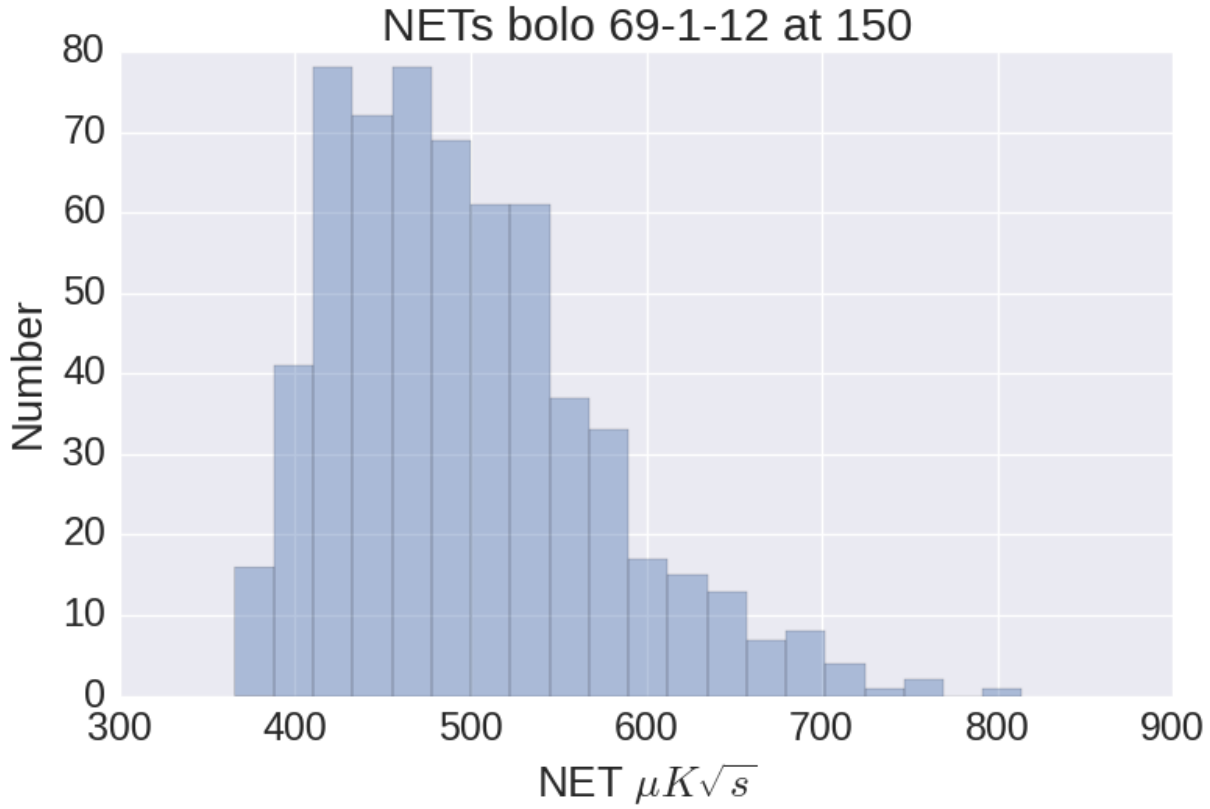

Figure 6.3: Example NET distribution for one 150 GHz detector (labeled 69-1-12). Each NET is measured from a 5.7 minute long length of TOD for the whole flight.

densities of 5.7 min sections of calibrated, deglitched, half-wave plate synchronous signal-subtracted TOD, and fit them with a three-parameter noise model $M(f)$ consisting of red and white noise terms as a function of frequency. Figure 6.2 shows an example PSD of a 5.7 minute section of TOD and the corresponding best-fit noise model. The fitting procedure is as follows.

We apply a Hanning window to the 5.7 minute chunk of TOD and then calculate a one-sided PSD as the magnitude squared Fast Fourier Transform (FFT) [245]. The zeroth and first lowest frequency bin are ignored due to the small bias induced by the windowing. Additionally, to avoid complications from the HWP harmonics, we fit PSD data only up to 10 Hz. The PSD measured in this way (also called a periodogram), $\hat{P}(f)$, is a biased estimator of the 'true' underlying noise power spectrum and is χ^2 distributed with two degrees

of freedom (χ^2_2) [218]. The source of this distribution can be understood as follows. The real and imaginary parts of the FFT data are Gaussian distributed so taking the magnitude squared produced a distribution that is the sum of two squared Gaussian distributions, which is the definition of a χ^2_2 distribution. Standard least squares fitting applies to Gaussian distributed data only, therefore we modify the least squares fitting procedure to correct for the χ^2_2 distributed data. We take the logarithm of the PSD which separates the expectation of the χ^2 distribution from the expectation value of the PSD,

$$\mathrm{E}\left[\log\left(\hat{\mathrm{P}}(\mathrm{f})\right)\right] = \log\left(\mathrm{P}(\mathrm{f})\right) + \mathrm{E}\left[\frac{\chi^2_2}{2}\right] = \log\left(\mathrm{P}(\mathrm{f})\right) - \gamma\,, \tag{6.1}$$

where $P(f)$ represents the true power spectral density and $\gamma = 0.57721...$ is the Euler-Mascheroni constant. The logarithm of the PSD is still a biased estimator, but we can correct for this by subtracting the constant, γ [30]. The variance of the logarithm of the PSD is then a constant given by,

$$\mathrm{VAR}\left[\log\left(\hat{\mathrm{P}}(\mathrm{f})\right)\right] = \pi^2/6\,. \tag{6.2}$$

The weighted least squares residuals are then minimized to produce unbiased estimators of the model parameters using,

$$\chi^2 = \sum \frac{\left(\log\left(\hat{P}(f)\right) - \log\left(M(f)\right) + \gamma\right)^2}{\pi^2/6}\,. \tag{6.3}$$

To account for the possibility of binning the PSD, which adds to the degrees of freedom of the PSD χ^2 distribution, we can calculate the correction needed for χ^2_{2N} distributions with any even number of degrees of freedom. The correction factor for χ^2 distributed data with $2N$ degrees of freedom is given by the digamma function,

$$\mathrm{E}\left[\frac{\chi^2_{2\mathrm{N}}}{2}\right] = \psi(\mathrm{N}) = \frac{\Gamma'(\mathrm{N})}{\Gamma(\mathrm{N})} = \sum_{\mathrm{k}=1}^{\mathrm{N}-1}\frac{1}{\mathrm{k}} - \gamma\,. \tag{6.4}$$

Note that the correction goes to zero as the number of degrees of freedom approaches infinity because the χ^2 distributions approaches a Gaussian (it is negligible after about 50 degrees of freedom) [218]. Binning the PSD this many times is a common way to reduce the bias in the estimator, however for our purposes this would require continuous TOD over long periods of time (hours). This is often not achievable experimentally (see for example the many gaps in the data in Figure 6.1) and so we used this method to estimate the noise PSD on fast timescales.

The noise model is given by

$$M(f) = W^2 \left[1 + \left(\frac{f_k}{f}\right)^{\alpha}\right] . \tag{6.5}$$

The noise model parameters are W, the white noise level in $\mathrm{K}/\sqrt{\mathrm{Hz}}$, which we will identify as the noise-equivalent temperature (NET) of the detectors; f_k, the frequency cutoff of the red-noise power law, also referred to as f_{knee}, in Hz; and α, the red-noise spectral index [218, 206]. In the case that the PSD is particularly flat, the f_k parameter should be zero, in which case we change the model to simply a constant white noise level. Figure 6.2 shows an example PSD and fit for one section of TOD for a 250 GHz detector.

This fitting procedure benefits from being a fast and simple method to estimate both the white-noise and low-frequency noise performance of the detectors as a function of time. The 5.7 minute length of time was chosen so that enough of the low-frequency noise was present in the PSD while being short enough that continuous sections of TOD could be chosen with no experimental glitches. The length is in fact 2^{16} samples which enables the FFT to be calculated efficiently. The model suffers somewhat from being non-linear in the parameters, however the logarithm separates the white noise level from f_k and α. The white noise parameter is log-normally distributed, which encourages use of the median and not the mean when examining the distribution of the white-noise levels. Figure 6.3 shows the distribution of white-noise levels measured throughout the flight for one 150 GHz detector. Additionally,

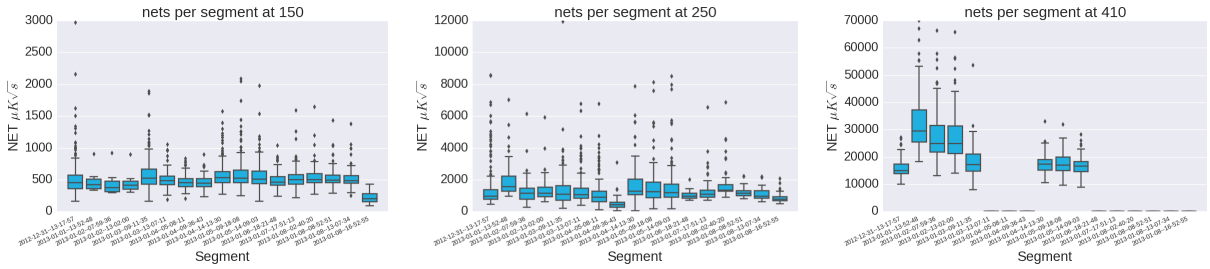

Figure 6.4: (From left to right) 150, 250, and 410 GHz detector NET distributions as a function of time. Each point is a box and whisker plot indicating the 25$^{\text{th}}$, 50$^{\text{th}}$, and 75$^{\text{th}}$ percentiles of the detector NET median values during one segment (approximately one day each). The whiskers indicate the outliers. We see the NET distribution does not change significantly as a function of time, except for the 410 GHz detectors.

non-linearity of the model implies that the reduced χ^2 statistic, e.g., χ^2/(number of data points - number of model parameters), is potentially rendered meaningless as a goodness-of-fit statistic, due to the degeneracy of f_k and α when either is near zero. The accuracy of this procedure was extensively tested using simulations and confirmed with the more conventional method of averaging many spectra together and estimating the white-noise level as the mean of the PSD in a certain bandwidth above f_{knee}.

6.1.2 Noise Statistics and Map Sensitivity

After applying the fitting procedure to all the detector data for all of the flight we have a set of parameters W, f_k, and α, which we can study to characterize the performance of the instrument. For each detector we calculate the three median parameter values over each segment and over the entire duration of the flight. Figure 6.4 shows the distribution of the detector median NET per segment. Figures 6.5, 6.6, and 6.7 show the NET, f_{knee}, and α histograms of detector median values for each parameter. The median NET is 400, 920, and 14590 $\mu\text{K}\sqrt{\text{s}}$ for the 150, 250, and 410 GHz detectors respectively. The white-noise level is used in conjunction with the pointing data to produce instrument effective sensitivity maps (see Chapman et al. [52] and Araujo [16] for details on the pointing reconstruction algorithm). The median f_{knee} is 0.15, 0.21, and 0.18 Hz for the 150, 250, and 410 GHz

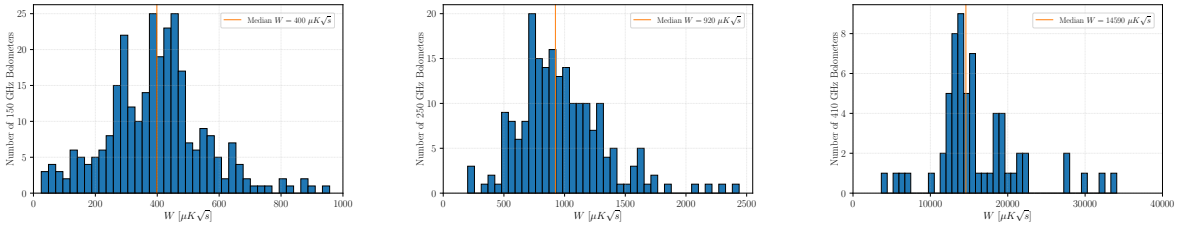

Figure 6.5: (Left to right) 150, 250, and 410 GHz distribution of median detector noise-equivalent temperatures, NET, for all available detectors in a given frequency band and the median of the distribution (vertical red). The median NET is 400, 920, and 14590 μK$\sqrt{\text{s}}$ for the 150, 250, and 410 GHz detectors respectively.

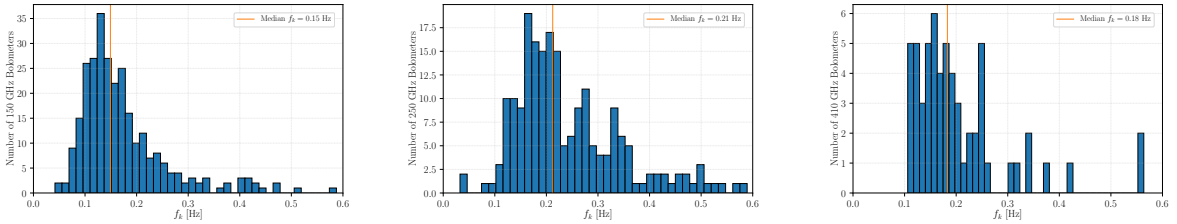

Figure 6.6: (Left to right) 150, 250, and 410 GHz distribution of median detector knee frequency, f_{knee}, for all available detectors in a given frequency band and the median of the distribution (vertical red). The median f_{knee} is 0.15, 0.21, and 0.18 Hz for the 150, 250, and 410 GHz detectors respectively.

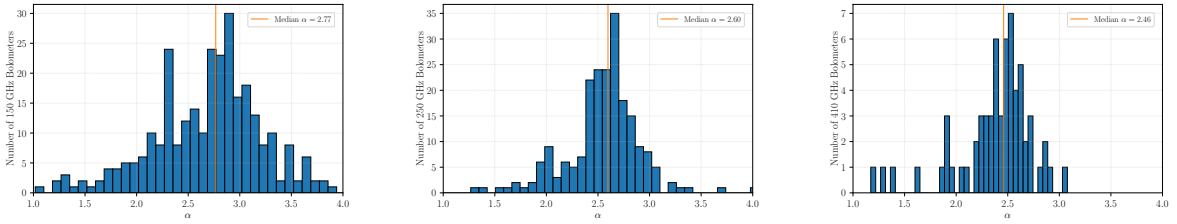

Figure 6.7: (Left to right) 150, 250, and 410 GHz distribution of median detector red noise index, α, for all available detectors in a given frequency band and the median of the distribution (vertical red). The median α is 2.77, 2.60, and 2.46 for the 150, 250, and 410 GHz detectors respectively.

detectors respectively. And the median α is 2.77, 2.60, and 2.46 for the 150, 250, and 410 GHz detectors respectively. The f_{knee} and α parameters characterize the low-frequency noise performance of the detectors and is provided as an input to the destriped map-making algorithm. The HWP modulates the polarization signal to a band around 5 Hz, far above the red-noise regime below approximately 0.2 Hz. The f_{knee} values of approximately 0.2 Hz indicate that the TOD contain drifts in the data on timescales longer than 5 seconds. These drifts will be subtracted by the destriping algorithm.

To estimate the map sensitivity we binned all the noise data onto the sky using HEALPix [122] with $N_{side} = 64$. Each sample is associated with an equivalent temperature noise N_s (in μK) equal to the product of the NET calculated during that time section and the square root of the sampling rate. We calculated depth per pixel D_p as,

$$D_p = \left(\sum \frac{1}{N_{s,p}^2} \right)^{-1/2}, \tag{6.6}$$

where the sum is over all samples that had pointing within a given pixel p. Figure 6.8 shows the estimated map sensitivity for the experiment and histogram of the sensitivity per pixel at a resolution of $\sim$1 deg^2. The map sensitivity is spatially inhomogeneous due to the motor malfunction, as described in The EBEX Collaboration et al. [300]. The median depth values per pixel for the 150, 250, and 410 GHz maps are 11, 28, and 1982 μK, respectively. These are several factors larger than sensitivity achieved by *Planck* and the expected CMB *E*-mode signal, indicating that even ideal maps without low-frequency noise residuals would not reveal many features of the CMB. We then combined these sensitivity maps with the expected polarized microwave sky (including Galactic foregrounds) determined by *Planck* to estimate the expected EBEX signal-to-noise maps. Figures 6.9 and 6.10 show the polarized signal-to-noise maps for the full dataset and zoomed in on the Galactic plane, where the signal is brightest.

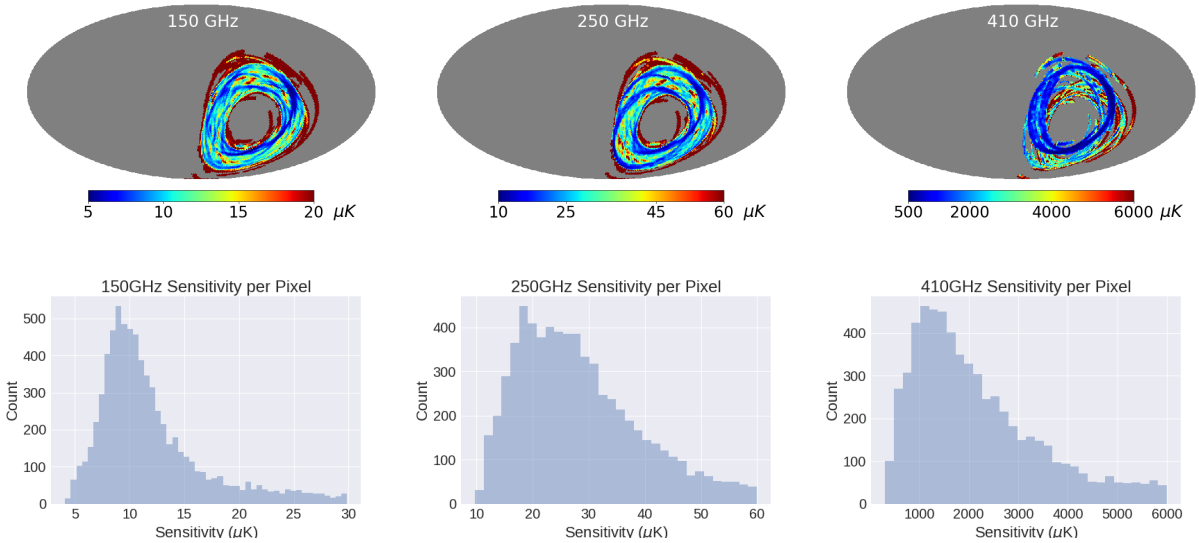

Figure 6.8: (Top from left to right) 150, 250, 410 GHz sensitivity depth maps in Galactic coordinates using the measured NET and EBEX pointing. The maps have resolution of about 1° (HEALPix $N_{side} = 64$ pixels) and the color scale is linear. At this pixelization the median pixel noise is 11, 28 and 1982 μK for the 150, 250, and 410 GHz bands, respectively. (Bottom from left to right) 150, 250, 410 GHz histograms of sensitivity per pixel.

6.2 Destriped Map-making

One of the most important steps for CMB experiments is the map-making procedure. The map-making procedure entails combining all the detector TOD back into a single map of the sky. The required components for map-making are the pointing, TOD, and TOD noise estimates. In general the TOD will contain a variety of systematic effects that are not representative of the sky. For EBEX, after deglitching and half-wave plate template subtraction, the most prominent signal in the TOD are low-frequency drifts in the data, as described above. A variety of approaches were tested and used to mitigate the effect of low-frequency noise. Here we will focus on a destriping algorithm that simultaneously solves for low-frequency noise in the data and produces cleaned maps of the sky.

The destriper we have used was developed by Sutton et al. [289, 290] and is called the DEStriping CARTographer (DESCART). DESCART is a FORTRAN code that I have

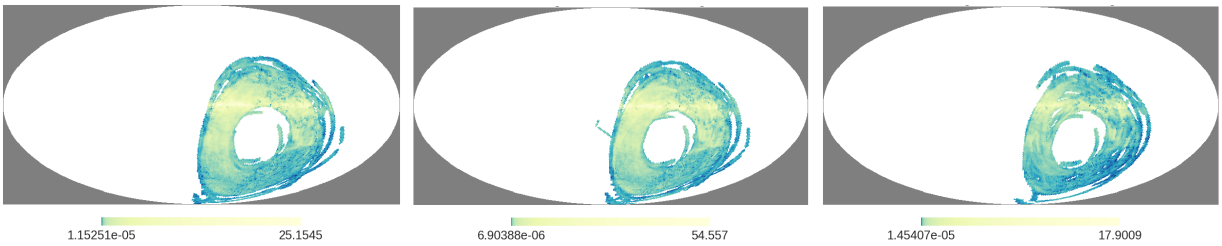

Figure 6.9: (Left to right) 150, 250, 410 GHz polarization signal-to-noise ratio maps. The maps have resolution of about 1° (HEALPix $N_{side} = 64$ pixels) and the color scale is logarithmic.

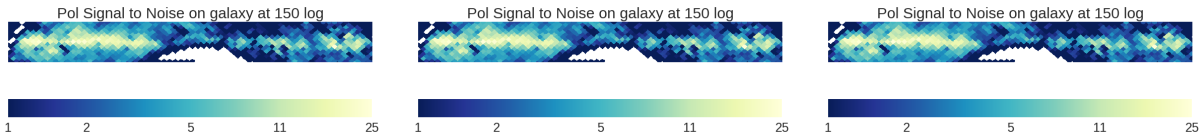

Figure 6.10: (Left to right) 150, 250, 410 GHz polarization signal-to-noise ratio maps zoomed in on Galactic plane. The maps have resolution of about 1° (HEALPix $N_{side} = 64$ pixels) and the color scale is logarithmic.

adapted and applied to EBEX data. A variety of data formatting modifications were made and most importantly I added capability for DESCART to handle polarization timestreams produced by an experiment with half-wave plate modulation. The modified DESCART algorithm was tested extensively in simulation with realistic signals, noise, and pointing before being applied to real EBEX data. The final EBEX polarization maps are statistical-noise dominated, as expected from the depth sensitivity maps, and the temperature map is systematic-noise dominated. The temperature systematic appears to be due to unexpected loading on the detectors, potentially from the sun, which produced a non-linear response in the detectors. Some of this effect is seen in the polarization maps as well. A discussion of the EBEX systematics errors can be found in Didier [86], Araujo [16]. Here I will summarize the destriping algorithm, then present results from realistic simulations, and finally I will present the destriped EBEX maps.

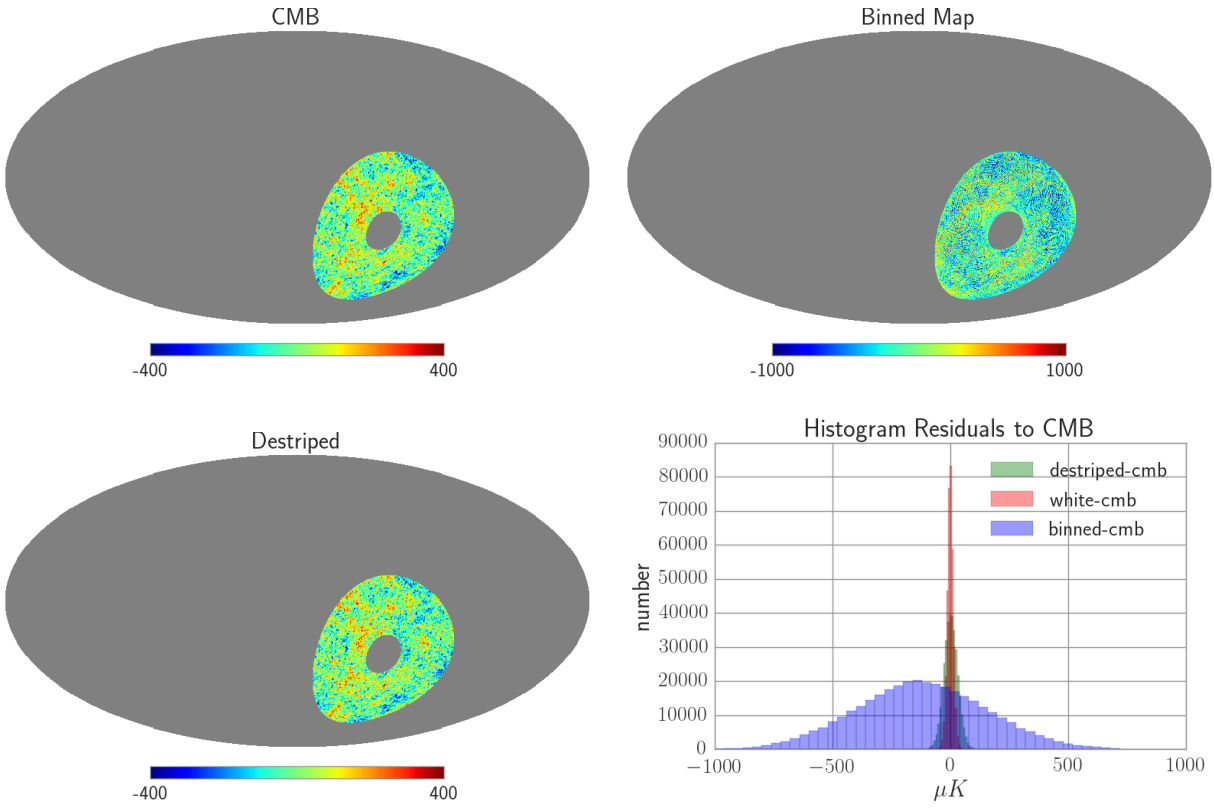

Figure 6.11: (Top left) Input CMB temperature map. (Top right) Binned and averaged map with simulated red-noise. (Bottom left) Destriped map. (Bottom right) Histogram of map residuals. The destriped map recovers the input CMB very well even in the presence of low-frequency red-noise. The destriped residuals (green in histogram) are approximately the same as a white-noise only simulation, showing the destriper effectively removes the red-noise from the map. Note the scale of the color bar for the binned map is larger than the other maps by a factor of 2.5.

6.2.1 Destriping Algorithm

To estimate the sky map from the TOD we begin by writing down a model for the TOD [296],

$$\mathbf{d} = \mathbf{P}\mathbf{m} + \mathbf{n}\,, \tag{6.7}$$

where $\mathbf{d}$ is the TOD vector, $\mathbf{P}$ is the pointing matrix, $\mathbf{m}$ is the pixelated observed sky map, and $\mathbf{n}$ is the noise in the TOD. This equation assumes the detectors have a linear response and that the noise is additive. For polarized map-making the sky map, $\mathbf{m}$, has 3 components,

I, Q, and U, each with length n_p and so in total has length $3n_p$. A detector sensitive to one linear polarization will observe a signal,

$$s = I + Q\cos 2\psi + U\sin 2\psi\,, \tag{6.8}$$

where ψ is the polarization angle of the detector and I, Q, and U are the Stokes parameters in a given pixel. This equation is modified for EBEX due to the half-wave plate modulation, such that,

$$s = \frac{1}{2}(I + Q\cos(4\theta_{hwp} + 2\psi) + U\sin(4\theta_{hwp} + 2\psi))\,, \tag{6.9}$$

where θ_{hwp} is the angle of the half-wave plate. The pointing matrix identifies the corresponding pixel on the sky for every time and so has a size of the number of time samples by the number of map pixels, $(n_t, 3n_p)$. The TOD, $\mathbf{d}$, and noise, $\mathbf{n}$, have length n_t. For experiments with multiple detectors, the detector TODs are concatenated end-to-end (so n_t is the total observation time for all detectors). The sky-map, $\mathbf{m}$, is assumed to already have already been convolved with the beam (this assumes all the detectors have the same shape beam). The noise vector, $\mathbf{n}$, can in general contain correlations in time within a detector and correlations between detectors. This can be represented by the noise (time-time and detector-detector) covariance matrix, $\mathbf{N} = \langle \mathbf{n}\mathbf{n}^{\mathrm{T}} \rangle$. Thus, we have the TOD vector, the pointing matrix, and know statistical properties of the noise vector and would like to solve for the sky-map. The previous section describes our method to estimate the noise properties. Assuming a Gaussian likelihood, the maximum likelihood solution for the sky-map is [296],

$$\hat{\mathbf{m}} = (\mathbf{P}^{\mathrm{T}}\mathbf{N}^{-1}\mathbf{P})^{-1}\mathbf{P}^{\mathrm{T}}\mathbf{N}^{-1}\mathbf{d} \tag{6.10}$$

with the map (pixel-pixel) covariance matrix,

$$\mathbf{C} = (\mathbf{P}^{\mathrm{T}}\mathbf{N}^{-1}\mathbf{P})^{-1}\,. \tag{6.11}$$

For Gaussian uncorrelated noise, the noise covariance matrix is diagonal and this solution amounts to binning and averaging the data assigned to a pixel. For non-diagonal noise matrices this solution is computationally infeasible to implement due to the size of the datasets. For EBEX, even with assumptions to estimate $\mathbf{N}^{-1}$ which otherwise has size $10^9 \times 10^9$, the inversion of $(\mathbf{P}^{\mathrm{T}}\mathbf{N}^{-1}\mathbf{P})$ would require 10^{16} operations ($\approx$ 1 CPU-year) and Terabits of memory. Instead, various approximations are made about the statistical properties of the noise and this allows us to reduce the computational complexity. A variety of map-making algorithms exist to solve this problem including Weiner filtering, time-domain filtering, Fourier-domain filtering, and maximum-entropy algorithms [296]. The method we apply here is a destriping algorithm as its main goal is to reduce the effect of correlated low-frequency noise on the map, which produce stripes along the scan path [182, 168, 310]. This method benefits from being computationally and practically efficient for producing high fidelity maps.

The destriping algorithm is based on the principle that the noise can be linearly decomposed into two components: a Gaussian uncorrelated white-noise component, $\mathbf{n}_w$, and a low-frequency correlated component, $\mathbf{n}_{corr}$ [290],

$$\mathbf{n} = \mathbf{n}_w + \mathbf{n}_{corr}\,. \tag{6.12}$$

The correlated noise is then modeled as a series of parameterized basis functions over a set baseline duration. The length of the baseline duration, n_b, is determined by where the low-frequency noise cuts off, which was measured in the previous section as f_{knee}. For DESCART, the basis functions are step functions with a free amplitude and therefore the low-frequency noise is modeled as a series of constant offsets [290],

$$\mathbf{n}_{corr} = \mathbf{F}\mathbf{a}\,. \tag{6.13}$$

Here the matrix $\mathbf{F}$ describes the basis functions composed of step functions with length n_b.

The model for the TOD is now,

$$\mathbf{d} = \mathbf{P}\mathbf{m} + \mathbf{F}\mathbf{a} + \mathbf{n}_w \,. \tag{6.14}$$

The white-noise component obeys,

$$\langle \mathbf{n}_w \rangle = 0 \,, \tag{6.15}$$

and has a diagonal covariance matrix,

$$\mathbf{C}_w = \langle \mathbf{n}_w \mathbf{n}_w^{\mathrm{T}} \rangle \tag{6.16}$$

with diagonal elements given by the white-noise variance, σ_t^2. This matrix, $\mathbf{C}_w$, is estimated in the previous section using the white-noise levels measured every 5.7 minutes. The destriper solves simultaneously for the sky-map and the correlated noise offsets, then iteratively updates both and repeats the procedure until they converge to a final map. The maximum likelihood sky-map is given by [290],

$$\hat{\mathbf{m}} = (\mathbf{P}^{\mathrm{T}} \mathbf{C}_w^{-1} \mathbf{P})^{-1} \mathbf{P}^{\mathrm{T}} \mathbf{C}_w^{-1} (\mathbf{d} - \mathbf{F}\mathbf{a}) \,, \tag{6.17}$$

with map variance,

$$\mathbf{C} = (\mathbf{P}^{\mathrm{T}} \mathbf{C}_w^{-1} \mathbf{P})^{-1} \,. \tag{6.18}$$

This solution is computationally efficient to solve because $\mathbf{C}_w^{-1}$ is diagonal. All the matrices in Equation 6.17 are known except the offset amplitudes, $\mathbf{a}$.

Before we address the solution of the offsets, let me briefly remark on the importance of the scan strategy for map-making. Let us define the matrix $\mathbf{M}$,

$$\mathbf{M} = (\mathbf{P}^{\mathrm{T}} \mathbf{C}_w^{-1} \mathbf{P}) \,, \tag{6.19}$$

which consists of the white-noise covariance matrix assigned to each map domain pixel [182].

The matrix $\mathbf{M}$ is block diagonal with a 3×3 block, $\mathbf{M}_p$, assigned to each pixel to represent the I, Q, and U terms. We can use Equation 6.9 to write,

$$\mathbf{M}_p = \begin{pmatrix} \sum_t \frac{1}{\sigma_t^2} & \sum_t \frac{\cos\alpha_t}{\sigma_t^2} & \sum_t \frac{\sin\alpha_t}{\sigma_t^2} \\ \sum_t \frac{\cos\alpha_t}{\sigma_t^2} & \sum_t \frac{\cos^2\alpha_t}{\sigma_t^2} & \sum_t \frac{\cos\alpha_t \sin\alpha_t}{\sigma_t^2} \\ \sum_t \frac{\sin\alpha_t}{\sigma_t^2} & \sum_t \frac{\sin\alpha_t \cos\alpha_t}{\sigma_t^2} & \sum_t \frac{\sin^2\alpha_t}{\sigma_t^2} \end{pmatrix}, \tag{6.20}$$

where we have defined $\alpha_t = 4\theta_{hwp} + 2\psi$ as the effective angle at a time t (θ_{hwp} can be set to 0 for polarization experiments without a half-wave plate). The sum is taken over all times t that are associated with observations of pixel p. The I, Q, and U parameters can only be measured if each pixel is observed with at least three different angles (optimally the angles are distributed uniformly between 0 and π). If the angles are too similar, then I, Q, and U are degenerate and $\mathbf{M}_p$ becomes singular and cannot be inverted. This is accounted for in the destriper by ignoring the TOD that are associated with pixels with singular $\mathbf{M}_p$.

Now, to estimate the destriping offsets, we assume the offset amplitudes are Gaussian distributed and uncorrelated, and solve the equation [290],

$$(\mathbf{F}^{\mathrm{T}}\mathbf{C}_w^{-1}\mathbf{Z}\mathbf{F})\hat{\mathbf{a}} = \mathbf{F}^{\mathrm{T}}\mathbf{C}_w^{-1}\mathbf{Z}\mathbf{d}\,, \tag{6.21}$$

to get the maximum likelihood solution for $\hat{\mathbf{a}}$. We have introduced the definition,

$$\mathbf{Z} = \mathbf{I} - \mathbf{P}\mathbf{M}^{-1}\mathbf{P}^{\mathrm{T}}\mathbf{C}_w^{-1}\,, \tag{6.22}$$

which operates in the time-domain and subtracts the uncorrelated component from the TOD (leaving only the correlated component). $\mathbf{Z}$ is a projection matrix such that $\mathbf{Z}^2 = \mathbf{Z}$, meaning we project out the uncorrelated TOD and then solve for the correlated offset amplitudes. Equation 6.21 is solved using a preconditioned conjugate gradient method [290].

This concludes the summary of the destriping algorithm. The algorithm takes the TOD and noise estimate as input and the baseline offset length as a parameter and returns the de-

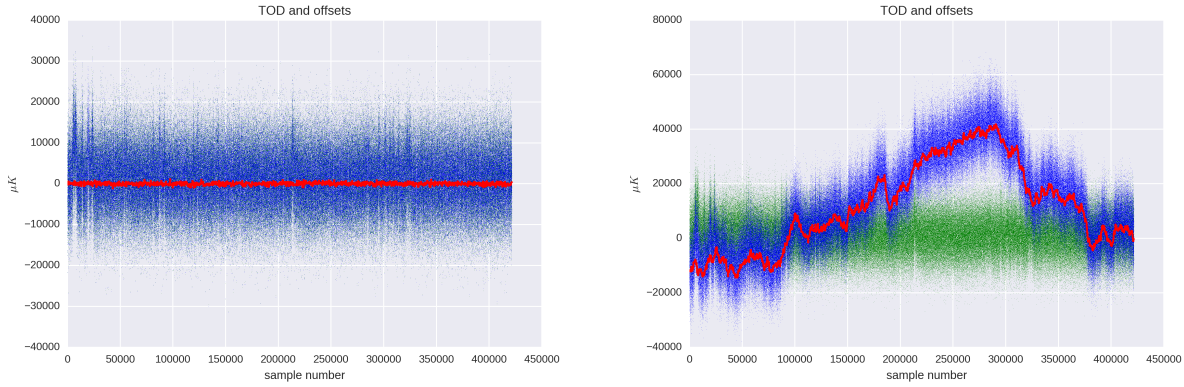

Figure 6.12: Simulated TOD shown with destriping offsets overplotted. (Left) White-noise only simulation. (Right) Red-noise simulation. The destriper solves for the offsets and subtracts them from the data to produce maps without red-noise biases. For both figures, the blue points are the simulated TOD and the red points are the destriping offsets. In the right figure, the green shows the TOD minus the destriping offsets to reveal the resulting destriped TOD.

striped approximation to the maximum likelihood map. The results of the destriper applied to simulation and EBEX data are discussed in the next section.

6.2.2 Simulated Data

The destriper was tested extensively in simulation. We began with full sky temperature only, white-noise only, simulations and step-by-step added more complexity and capability including realistic red-noise, real EBEX pointing, multiple detectors, and polarization. The final simulation before applying the destriper to EBEX data was to use the EBEX pointing but with simulated timestreams. Here we show the results of the simulations, beginning with temperature only maps and advancing to the polarization simulation.

To make the simulations realistic we used pointing that resembled the EBEX scan strategy and we used the measured noise statistics from the previous section to add noise to the timestreams. The sky was modeled using the EBEX sky-map which was based on the Planck results at the time. The first simulation was temperature only maps with one detector over the approximate EBEX region. Red-noise typical of EBEX detectors was added to the

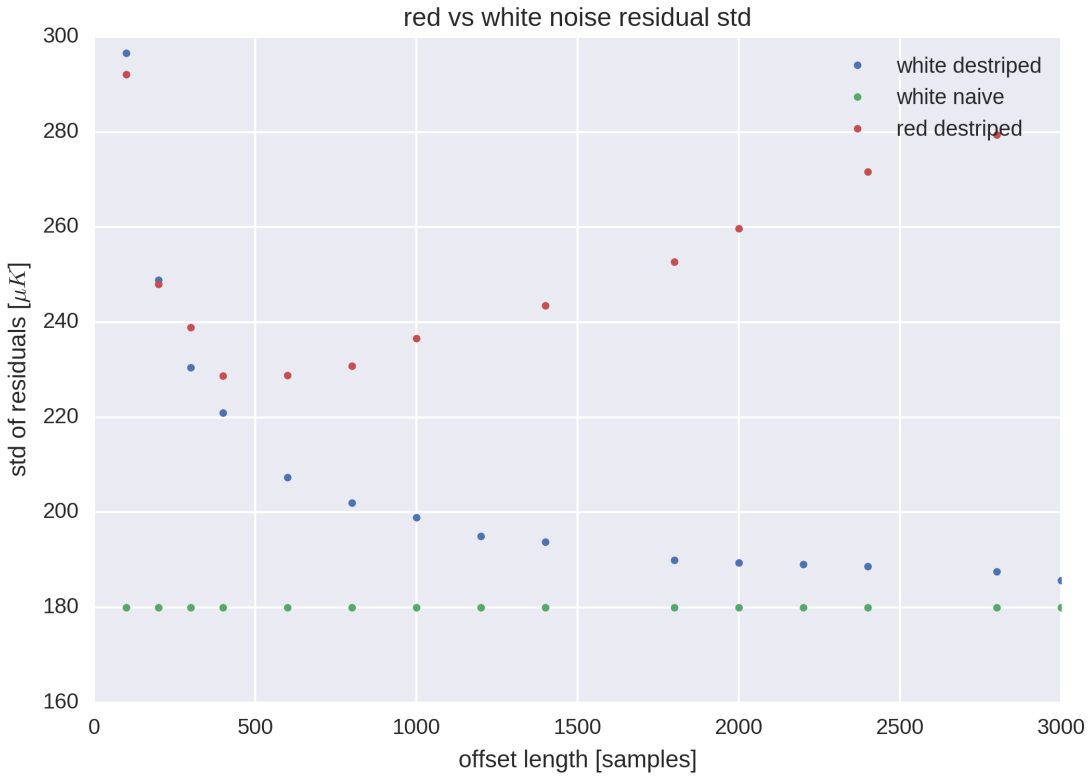

Figure 6.13: Standard deviation of map residuals as a function of destriping length for three different simulation scenarios (white-noise destriped, red-noise destriped, and white-noise binned and averaged). For white-noise only simulations the destriper converges to binning and averaging as the offset length increases. For the red-noise simulation, there is an optimal offset length dictated by the f_{knee} low-frequency noise cutoff. For this red-noise simulation the f_{knee} corresponds to 477 samples, which, as expected, is approximately where the minimum in the residuals is located.

timestream. Examples of the simulated timestream are shown in Figure 6.12. Figure 6.11 shows the results of the destriper on the maps.

First we simulated white noise only timestreams and then compared these to the input CMB maps. Next we added red-noise (with the same white noise level) and compared the destriped red-noise maps again to the input CMB maps and the white noise maps. Ideally if the destriper performs well the destriped map should converge to the white-noise only map. Figure 6.11 shows the simulated maps and a histogram of the map residuals between the red-noise binned, red-noise destriped, and white-noise binned and the input CMB. Figure 6.12

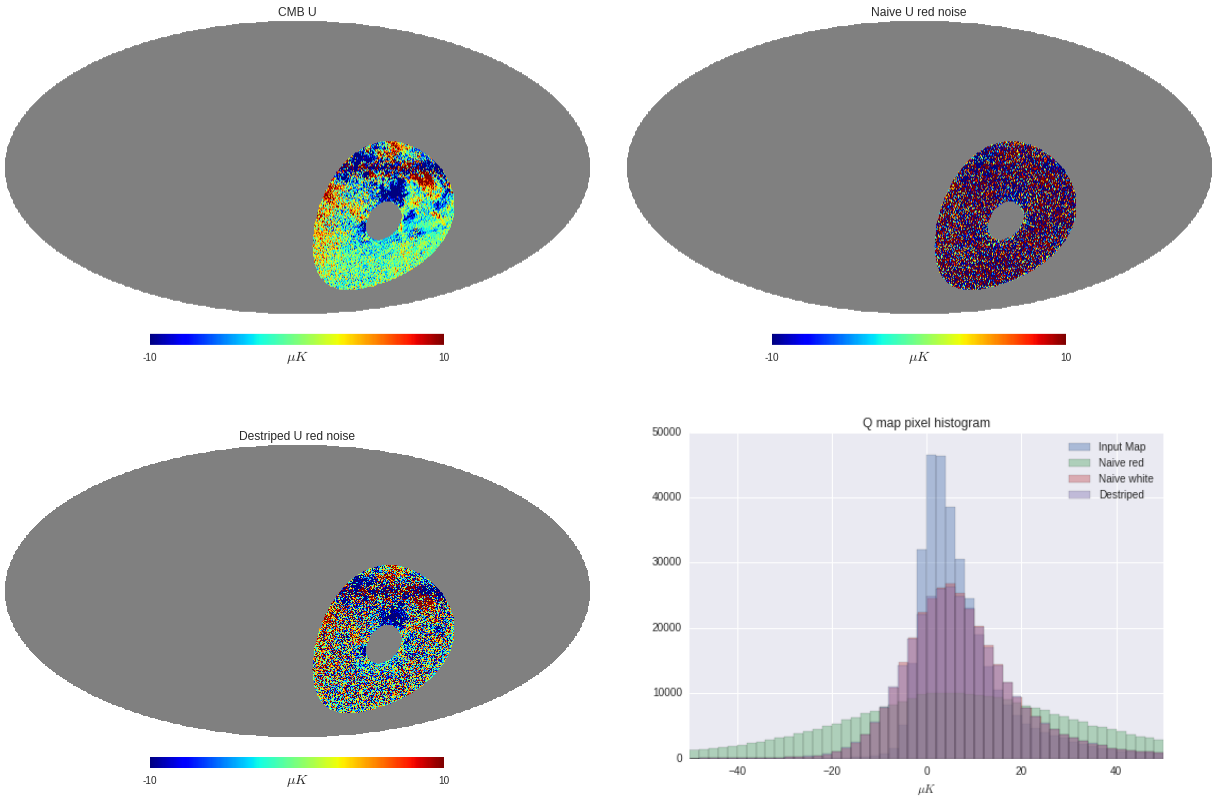

Figure 6.14: (Top left) Input CMB U map. (Top right) Binned and averaged map with added simulated red-noise. (Bottom left) Destriped map. (Bottom right) Histogram of output minus input map residuals. The destriped map recovers the input CMB very well even in the presence of low-frequency red-noise. Note the scale of the color bar for the binned plot is larger than the others by a factor of 2.5.

shows the destriped offsets in the red-noise and the resulting cleaned timestream.

Next we considered how the length of the destriping baseline offsets effects the maps and determined what is the optimal baseline length. We confirmed that the optimal baseline length should correspond approximately to the f_{knee} frequency in samples. This is shown in Figure 6.13. We compared the performance of the destriper with various offset lengths for red- and white-noise simulations compared this to the white-noise binned residuals. If the baseline is too short then the destriper will remove signal from the maps. If the baseline is too long then the destriper will not remove all of the low-frequency drifts. Additionally, applying the destriper to white-noise only simulations does increase the noise in the map as there are correlations in the map that are not accounted for in the destriper. The destriper

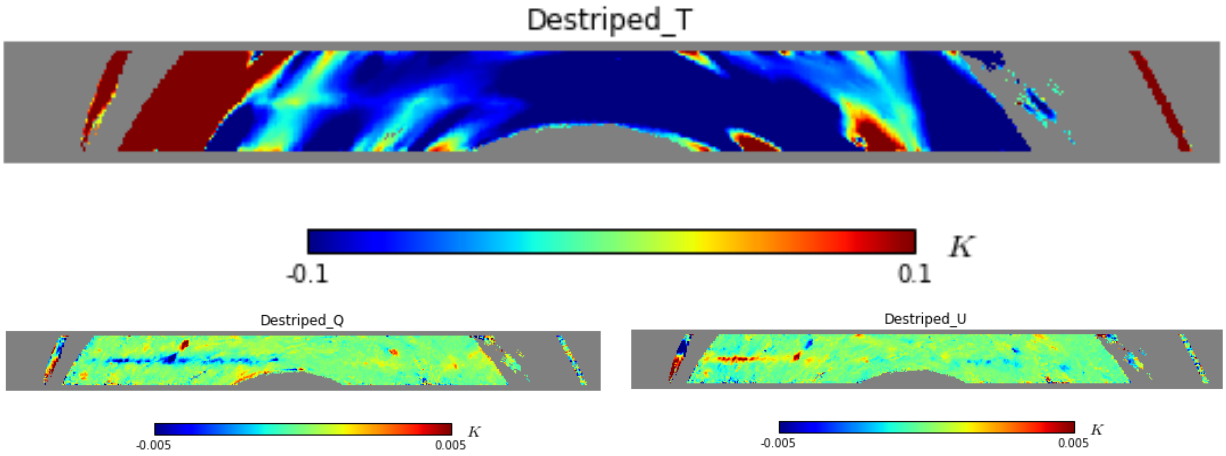

Figure 6.15: (Top I, bottom left Q, bottom right U) Destriped EBEX maps zoomed in on Galactic plane. The maps are strongly dominated by systematics in temperature. The polarization maps reveal features along the Galactic plane, but these appear to be from instrumental polarization.

assumes uncorrelated baseline offsets but this requirement is not always satisfied if the signal dominates over the noise. For EBEX data, the low-frequency noise is dominant and so the destriper performs optimally. Additional residuals due to sub-pixel fluctuations are also possible but not taken into account here as EBEX has a high enough resolution to resolve most of the strong gradients on the sky, except towards the center of the Galactic plane.

Finally, we introduced polarization into the simulations. We assumed the TOD model from Equation 6.9 and added red- and white-noise to the TOD. Figure 6.14 shows the maps and histogrammed residuatls for the polarization simulation. The destriper again performs well and recovers the sky-map at the expected white-noise level.

6.2.3 Destriped EBEX Maps

We first applied the destriper to EBEX data on the Galactic plane only (defined as $|b| < 5$ degrees) and produced I, Q, and U maps as shown in Figure 6.15. The temperature maps revealed only systematic artifacts. Time domain filtered temperature maps reveal more features of the Galaxy implying the systematic effects are inherent and dominant on long

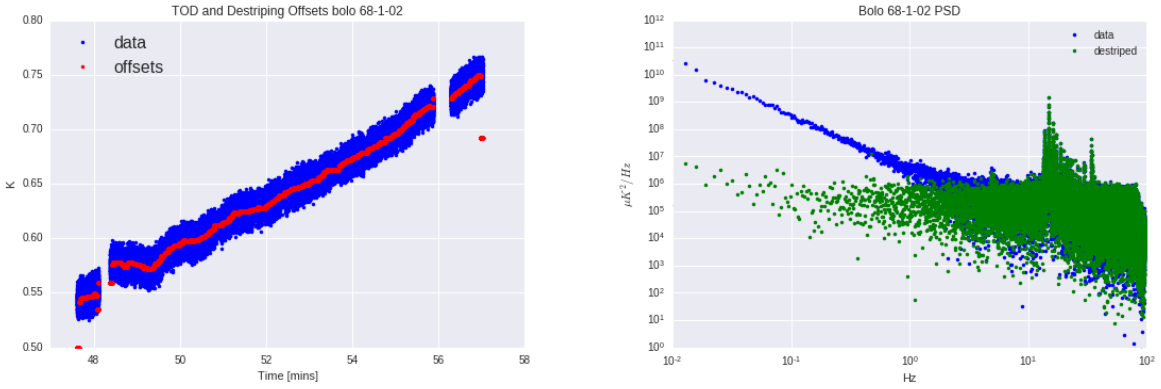

Figure 6.16: Example EBEX data before and after destriping. (Left) The example TOD in blue and the destriping offsets in red. (Right) The PSD of the TOD before and after destriping. The blue is the PSD of the raw TOD and the green is the PSD of the destriped TOD. The raw PSD shows the low-frequency noise and the destriped PSD is reduced to nearly white-noise.

time scales in the data. These effects could be due to sunlight leaking into the detector beams. The motor failure meant that EBEX pointed closer to the sun than was allowed by the specifications of the baffles. The Galactic plane polarization maps reveal some of the expected Galactic structure due to the half-wave plate modulation avoiding the low-frequency noise, however there are still clear systematics in the maps. The issue is that the observed polarization signal switches sign on opposite sides of the Galaxy for both the Q and U maps, which is not expected and indicative of an experimental systematics. This feature is also present in the filtered maps. The source of this instrumental polarization feature and attempts to remove it are discussed in Didier et al. [87].

We double checked that the destriper was performing as expected by inspecting the TOD and the solved destriper offsets, as shown in Figure 6.16. From this test we found additional detectors that performed poorly and removed them from the science selected data, however this did not resolve the systematic features in the temperature maps. The power spectrum of the destriped TOD shows that the destriper performed as expected and removed a majority of the low-frequency noise.

We then applied the destiper to the full flight data for all the 250 GHz data and produced

the maps shown in 6.17. Again the temperature maps show no discernible signal. The polarization maps show structure along the Galactic plane, but again this is most likely an instrumental polarization artifact of temperature leaking into polarization. These maps are made with the baseline offset length set based on the measured f_{knee}, however we also checked a variety of shorter and longer baselines as a test. The maps at 150 GHz are similar. The 410 GHz detectors did not produce very much usable data so we did not make destriped maps at 410 GHz.

We tested the possibility that a reflection of the sun was producing a signal by producing set of sun-centered coordinates. The motion of the sun was then subtracted from the pointing coordinates. We then made destriped temperature maps in the sun-centered coordinates, as shown in Figure 6.18. The figure shows that the side facing the sun sees a very bright signal and there could be a second reflection on the opposite side but it is hard to confirm whether is is purely from the sun or not. As another test we produced sun-signal subtracted maps by scanning the sun template and subtracting this sun template from the TOD. We then made maps with the sun subtracted TOD, as shown in Figure 6.18. The polarization maps were not strongly effected by the sun subtraction. The large signal on the left side of the temperature map was successfully removed by this method and some more features of the Galaxy could be seen but the maps was still dominated by systematics. For these reasons, EBEX sky-maps were not published, using either the destriping algorithm or a filtering method.

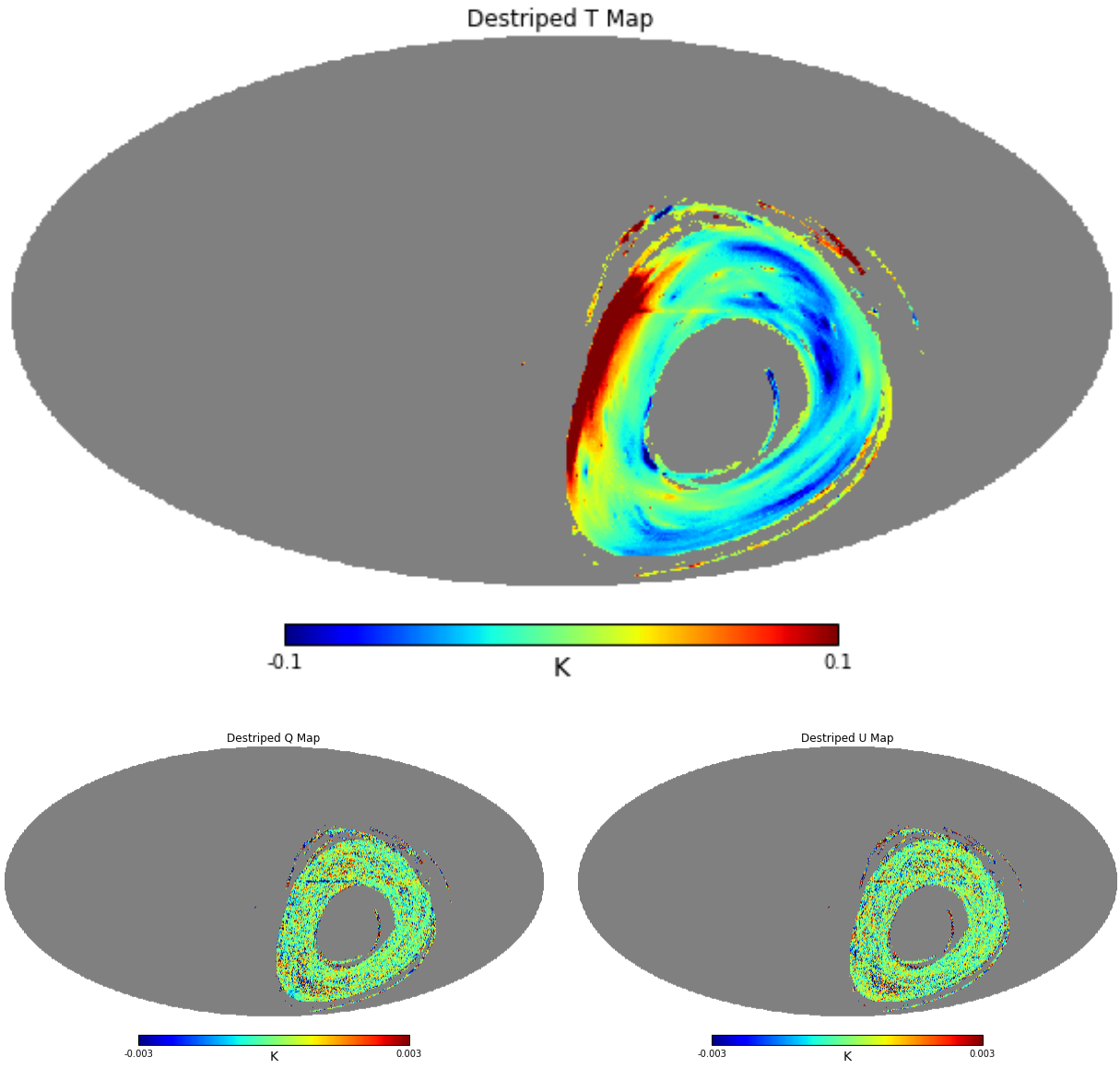

Figure 6.17: (From left to right) I, Q, U destriped EBEX maps. The temperature map is dominated by systematics, potentially related to sunlight leaking into the beam. The polarization maps are random noise dominated away from the Galaxy.

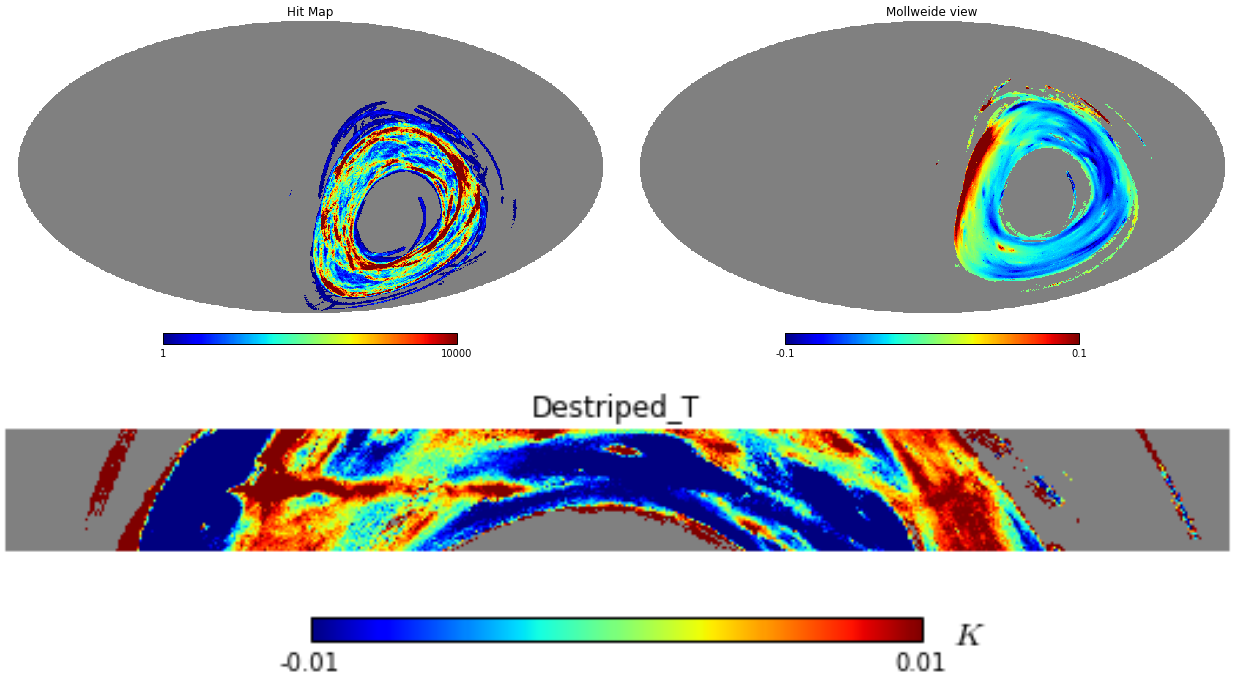

Figure 6.18: (Left) Total hit map of EBEX 250 GHz observations. (Right) Sun-centered map. (Bottom) Sun subtracted T map zoomed in on Galactic plane.

Chapter 7

Microwave Kinetic Inductance Detector Readout

One of the major design considerations for CMB experiments is the detector and readout system. Microwave Kinetic Inductance Detectors (MKIDs) are superconducting resonators that are designed to be highly sensitive photon detectors for astrophysical observations [77, 78]. At Columbia, MKIDs are being developed for cosmic microwave background polarization observations [199, 200, 198, 110, 158, 159, 160]. MKIDs are a strong candidate technology for CMB experiments because they are inherently multiplexable, meaning that many detectors can be read out at once. A variety of experiments have deployed or are planning to deploy KIDs for millimeter and sub-millimeter observations including BLAST-TNG, NIKA-2, TolTEC, and C-CAT Prime [49, 46, 88, 114, 20, 219]. Future CMB experiments such as CMB-S4 may also benefit from deploying KIDs [4]. This Chapter will focus on the readout system for MKIDs, which is one of the main advantages of MKIDs for CMB experiments.

7.1 Readout System Overview

MKID arrays are readout using frequency division multiplexing [38, 197, 304, 308, 40, 88, 202]. See Figure 7.1 for a diagram of the MKID multiplexing scheme. MKID readout requires

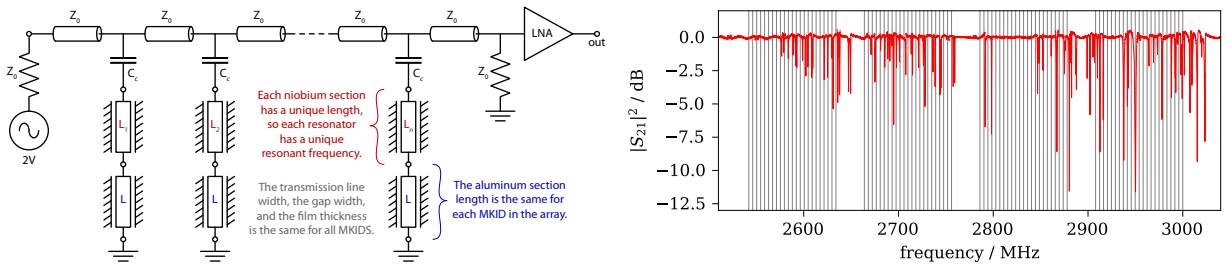

Figure 7.1: (Left) Example MKID multiplexing circuit schematic. In this design, each MKID is based on a quarter-wavelength coplanar waveguide (CPW) resonator. The length of the niobium section of the CPW is tuned to give each detector a unique resonance frequency. Tones at the appropriate frequencies are then passed down a single transmission line to resonant and read out all the detectors simultaneously. Photons are absorbed by the MKID which produces small changes in the inductance and therefore resonance frequency of the MKID. The resulting amplitude and phase shifts in the tone are then readout and calibrated into sky signals. (Right) Measured transmission as a function of frequency for an array of multi-chroic MKIDs. Each red line corresponds to an observed MKID resonance. Figures reproduced from Johnson et al. [158, 159].

playing a tone at the detector resonance frequency while simultaneously reading out that tone and measuring the resulting amplitude and phase shift. Changes in the amplitude and phase of the probe tone are due to changes in the resonance of the devices, which are caused by changes in the surface impedance of the device film [194, 196, 309, 212, 198, 110, 24]. Photons incident on the detectors with energy greater than the superconducting gap break Cooper pairs, changing the quasi-particle density and kinetic inductance, and thus surface impedance which is read out as a change in the probe tone amplitude and phase.

MKID readout systems must satisfy several basic requirements [304, 195, 95, 39, 41, 130]. The system must operate at the range of the resonance frequencies of the detectors, which is typically 100 - 8,000 MHz. The readout noise must be much less than the intrinsic detector noise (below ~ -90 dBc/Hz). The system needs to support a large enough bandwidth to read out hundreds or thousands of detectors at once. Lastly the readout needs to have the frequency resolution to readout resonators with very high quality factors, $Q \sim 100,000$.

The system is designed as follows (see Figure 7.2 for a diagram of the readout setup). A field-programmable gate array (FGPA) and digital-to-analog converter (DAC) generate complex IQ signals. The signals are mixed with a local oscillator to the required frequency

of the resonators. The tones are passed into the cryostat on a single coax line and excite the detectors at their resonance frequencies. The resulting signal is then demodulated by an IQ mixer and digitized by an analog-to-digital converter (ADC). The detector signal channels are selected and read out using a polyphase filterbank on the FPGA and sent to a computer for processing and storage. The resulting amplitude and phase shifts of the tones are then analyzed and calibrated into intensity units [114, 41, 39, 198, 110].

MKID readout requires a digital tone generator, such as an FPGA, connected to a DAC to produce the probe tones [121]. The waveforms are generated on the FPGA by taking a length N inverse Fast Fourier Transform (IFFT) of a delta function comb. The length of the IFFT sets the frequency resolution of the tones. For example, an FPGA with 500 MHz of bandwidth spaced with $N = 2^{18}$ bins gives a frequency resolution of about 1.9 kHz. The initial waveform amplitude should be maximal within the range of the DAC and the waveform crest factor should be minimized. This is achieved by randomly generating the probe tone phases (more advanced techniques are unnecessary because the MKID devices themselves will quasi-randomly shift the tone phases).

A mixing circuit is used to bring the signals to the required frequency. For example, to readout devices with resonances between 1000 to 1500 MHz, one would use the FPGA to generate tones from -250 to 250 MHz and mix them with a 1250 MHz local oscillator and IQ modulator to the required frequency. The same LO is used to demodulate the tones after passing through the MKID array. The tones are fed into the cryostat via coaxial cables and vacuum feedthroughs. The coax is wired through the cold stages and attenuated before interacting with the detectors. The signal is passed into a cold low noise amplifier and then back out of the cryostat. The signal is again amplified and mixed down before going into an ADC and back into the digital readout. Signals are then demodulated into amplitude and phase shifts, which can be calibrated to power variations on the detectors.

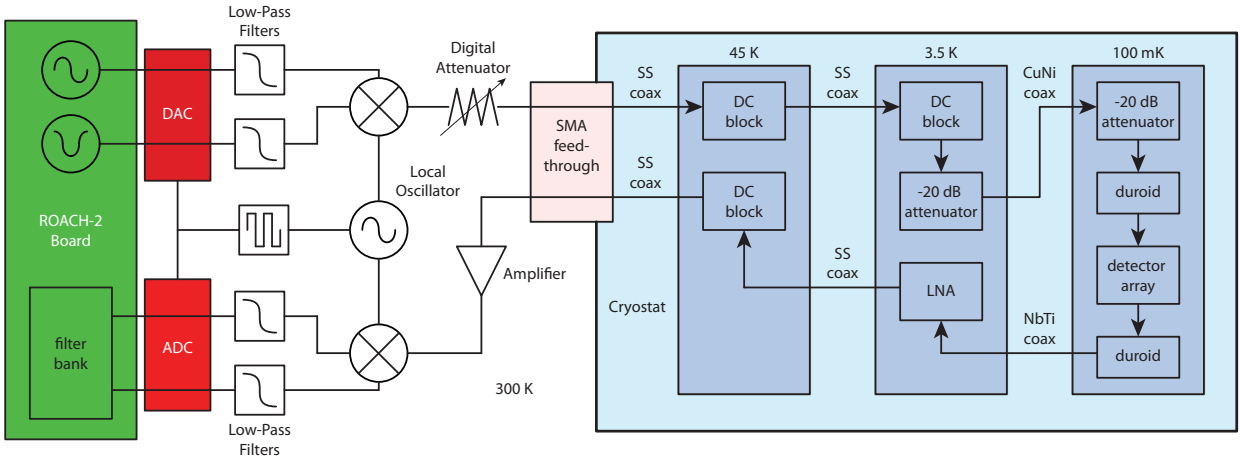

Figure 7.2: Schematic of the readout electronics. The top left shows the signal generation, digital-to-analog conversion, and IQ mixing. The blue portion shows the cryogenic electronics. The bottom left shows the demodulation and filtering scheme. Figure reproduced from Johnson et al. [158].

7.2 Readout Development

My work for the Columbia readout consisted of two projects, (i) building an analog signals condition circuit to operate high frequency MKIDs and (ii) updating the FPGA firmware to accommodate a 1 Gbit/s Ethernet connection directly from the FPGA to the local readout computer.

7.2.1 Analog Signal Conditioning and Mixing Circuit

The signals conditioning circuit for the testbed at Columbia was built to allow for devices to be readout at frequencies between 500 MHz and 4 GHz. The previous heterodyne readout system operated between 1 and 2 GHz and the baseband readout operates between 0 and 256 MHz. The new electronics circuit I built, which we named the MkII Heterodyne Readout Box, is shown in Figure 7.3. The purpose of the circuit is to convert between the baseband frequencies of the FPGA and the resonance frequencies of the MKIDs. A ROACH-2 [1] generates readout tones between -256 to $+256$ MHz while the detectors have resonance frequencies that could be anywhere between 500 MHz to 4 GHz.

[1] https://casper.berkeley.edu/

The signals conditioning circuit is composed of a series of amplifiers, attenuators, mixers, filters and a frequency synthesizer. The circuit is constructed as follows. Quadrature (IQ) signals are generated by the ROACH-2 and passed to the MkII Readout Box. The signals are low-pass filtered (Minicircuits Low Pass Filter SLP-200+) and then sent to quadrature modulator (Polyphase Microwave AM0350A Quadrature Modulator) where the signals are mixed with a local oscillator (LO) to the desired frequency range. The LO is produced by a frequency synthesizer (Valon 5008 Dual Frequency Synthesizer). The LO frequency can be set by communicating with the Valon via USB. This is done using the Python readout software developed at Columbia. The modulated signals are then attenuated to the desired level before being sent sent into the cryostat and to the MKID devices. The attenuator (Minicircuits Programmable Attenuator RCDAT-6000-60) can be controlled via Ethernet, which again is done automatically using the Python readout software. The signals resonant the MKIDs and then are amplified by a cold low-noise amplifier in the cryostat before being sent back to the MkII Readout Box. On the return side, the signals are again amplified by a series of two room-temperature amplifiers (Minicircuits Connectorized Amplifier ZX60-6013E). The signals are then demodulated back down to baseband using the LO and a quadrature demodulator (Polyphase Microwave AD0540B Quadrature Demodulator). The demodulator sets the high edge of the operating band with a cutoff at 4 GHz. The demodulated signals are then low-pass filtered and sent back to the ROACH-2. The ROACH-2 box houses both the ADC and DAC (Techne Instruments ADC2X550-12 and DAC2X1000-16).

The components and circuit were tested extensively for ensure the noise properties and performance satisfied the requirements for MKID testing. We studied the stability and phase noise of the LO from the Valon as well as the phase error of the modulators. We did find that the LO leakage through the modulators can be unacceptably high and so the LO is typically set at a frequency at least 50 MHz away from the nearest MKID resonance. All the components operated to the necessary specification.

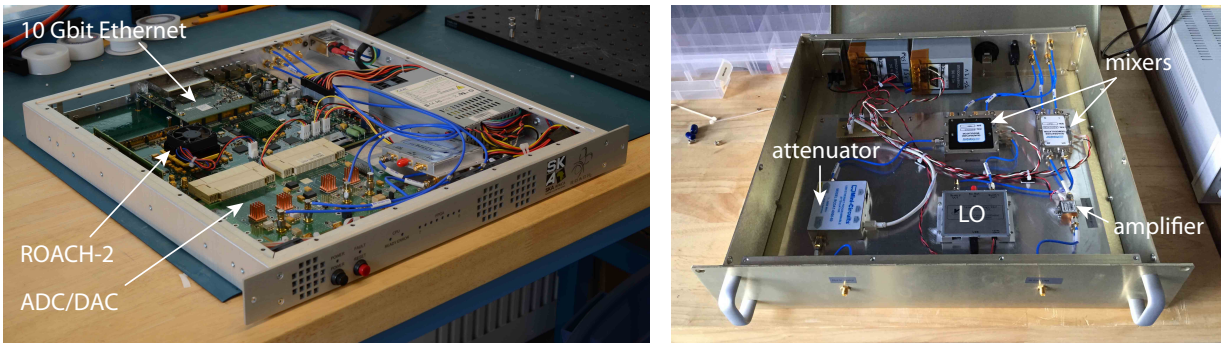

Figure 7.3: (Left) Image of the ROACH-2 board, which houses the FPGA and ADC/DAC. Signals are generated on the ROACH-2 and then passed to the heterodyne mixing circuit before going into the cryostat. (Right) MkII heterodyne readout circuit. The heterodyne readout circuit mixes the baseband signals from the ROACH-2 with a local oscillator to produce tones between 500 MHz and 4 GHz. The tones are then fed into the cryostat and resonant the MKIDs. On the return path, the mixing circuit demodulates the signal back to baseband and then sends it back to the ROACH-2 for channelizing and processing. Images reproduced from Johnson et al. [158].

7.2.2 FPGA Programming

Another upgrade I made to the readout system was to program the ROACH-2 FPGA (the FPGA is programmed using MATLAB Simulink and the CASPER tookit [137]) to enable 1 Gbit/s Ethernet speeds directly from the ROACH-2 to the readout computer. This upgrade meant that the system was capable of simultaneously reading out 800 MKIDs at once. (Other issues that were never addressed limited the actual readout capability to 128 MKIDs.) The previous system was only capable of reading out 16 tones and the largest array of MKIDs tested at Columbia had 256 MKIDs so this was satisfactory at the time. I will briefly review how the ROACH-2 FPGA produces the readout tones which are sent out to the MkII readout box and then the MKIDs. First, a set of readout tones is synthesized on the ROACH-2 computer (PowerPC 440EPx) and saved to a memory that is shared with the ROACH-2 FPGA (Virtex-6 SX475T FPGA). The ROACH-2 reads from this memory and outputs these tones to the DAC. The tones are then conditioned as described above and sent to the MKID devices and back. On return, the signals are sent to the ADC and then passed to the ROACH-2 FPGA. The FPGA takes an FFT of the signal using a poly-phase filter

bank (PPFB). The PPFB is a multi-rate digital signals processing algorithm that allows us to divide the incoming signal into an array of its constituent frequencies while maintaining high fidelity of the signals (in particular avoiding windowing and leakage issues between FFT bins). The result is that the FPGA now outputs a time-series of data for each input readout frequency (i.e. a time series for each MKID). The code I wrote took these time-series and arranged them into memory buffers and then User Datagram Protocol (UDP) packets in such a way that packets were continuously streaming from the ROACH-2 to the local readout computer at a rate fast enough to accommodate reading out up to 800 tones. The FPGA Simulink block diagram code is shown in Figure 7.4.

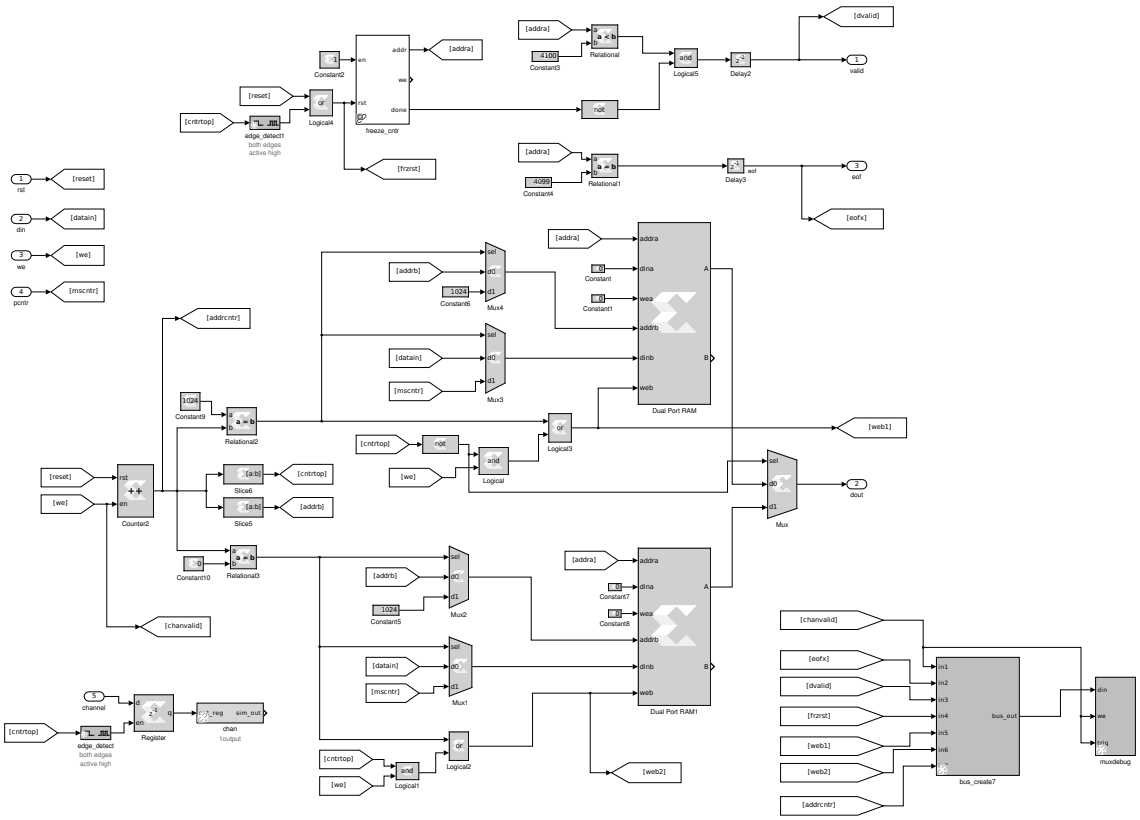

Figure 7.4: FPGA block diagram firmware I wrote to enable 1 Gbit/s data link from the ROACH-2 to the readout computer. The code works by implementing a state machine that fills alternating UDP packets while maintaining a memory buffer to collect data as the packets are being processed.

Chapter 8

Conclusion

This concludes my graduate research. I plan to build upon several of these projects in the future, in particular the self-calibration, spectral distortions, and GBT research. In terms of the self-calibration foreground biases, experiments like Simons Observatory [115] are currently developing their calibration methods and I plan to study how best to calibrate the polarization angle given the foregrounds. For the spectral distortions forecast, recently I have been updating the forecast and applying it to a newly proposed satellite experiment called PRISTINE. I am adding additional complexity to the forecast as well as adding functionality for more general experiment designs. For the GBT project, there are radio recombination lines and polarization data that we plan to study using our existing data set. I will also apply for time with GBT to observe the S140 region at Ku-band. Additionally, the GBT could be used to make high spatial and spectral resolution maps of other small regions for low-frequency foreground studies. It may also be possible to study Faraday rotation of Galactic synchrotron emission with the high spectral resolution of the VEGAS backend.

Lastly, one of the main projects I will work on is studying a new parametric foreground modeling method, called the moments method [69]. The moments method was developed by Jens Chluba, with Colin Hill and me, while we were working on the spectral distortions forecast. The moments method aims to generalize the parametric foreground modeling idea

to include the effect of line of sight and non-zero angular resolution integration. Current foreground subtraction methods can be dividing into what domain they operate in: the map domain, harmonic domain, or a combination of both, using spectral information and prior constraints to inform each method. The latest Planck release has five separate CMB removal methods, which each operate in different domains with different assumptions. For example, a common method is to assume the CMB blackbody spectrum and apply a linear combination of available frequency maps to produce a minimum variance result. Extensions to this involve applying constraints to the foreground models or using harmonic information to inform the statistics of the map. Another method is to simply apply physical constraints for the foreground models and gather a wide range of spectral information and fit for each foreground and CMB parameter. The principle of the moments method is that foregrounds are known to vary spatially, and in general should even vary along the line of sight and within the beam of current observations. This integration will produce a deviation from the assumed model since most models are not linear in the parameters. Assuming there exists an individual foreground element that follows a certain parametric model with a set number of parameters, then the spatial integration will be over a distribution of parameter values. The method is to model the effect of this integration by estimating the parameter distribution with the statistical moments of the distribution (mean, variance, skewness, kurtosis etc). The effect of the integration on the foreground model can then be taken into account by adding additional parameters to the model that are related to the moments of the underlying parameter distribution (hence naming it moments method). Future research in this area is warranted.

References

[1] K. N. Abazajian, K. Arnold, J. Austermann, B. A. Benson, C. Bischoff, J. Bock, J. R. Bond, J. Borrill, E. Calabrese, J. E. Carlstrom, C. S. Carvalho, C. L. Chang, H. C. Chiang, S. Church, A. Cooray, T. M. Crawford, K. S. Dawson, S. Das, M. J. Devlin, M. Dobbs, S. Dodelson, O. Doré, J. Dunkley, J. Errard, A. Fraisse, J. Gallicchio, N. W. Halverson, S. Hanany, S. R. Hildebrandt, A. Hincks, R. Hlozek, G. Holder, W. L. Holzapfel, K. Honscheid, W. Hu, J. Hubmayr, K. Irwin, W. C. Jones, M. Kamionkowski, B. Keating, R. Keisler, L. Knox, E. Komatsu, J. Kovac, C.-L. Kuo, C. Lawrence, A. T. Lee, E. Leitch, E. Linder, P. Lubin, J. McMahon, A. Miller, L. Newburgh, M. D. Niemack, H. Nguyen, H. T. Nguyen, L. Page, C. Pryke, C. L. Reichardt, J. E. Ruhl, N. Sehgal, U. Seljak, J. Sievers, E. Silverstein, A. Slosar, K. M. Smith, D. Spergel, S. T. Staggs, A. Stark, R. Stompor, A. G. Vieregg, G. Wang, S. Watson, E. J. Wollack, W. L. K. Wu, K. W. Yoon, and O. Zahn. Neutrino physics from the cosmic microwave background and large scale structure. *Astroparticle Physics*, 63:66–80, March 2015. doi: 10.1016/j.astropartphys.2014.05.014.

[2] K. N. Abazajian, P. Adshead, Z. Ahmed, S. W. Allen, D. Alonso, K. S. Arnold, C. Baccigalupi, J. G. Bartlett, N. Battaglia, B. A. Benson, C. A. Bischoff, J. Borrill, V. Buza, E. Calabrese, R. Caldwell, J. E. Carlstrom, C. L. Chang, T. M. Crawford, F.-Y. Cyr-Racine, F. De Bernardis, T. de Haan, S. di Serego Alighieri, J. Dunkley, C. Dvorkin, J. Errard, G. Fabbian, S. Feeney, S. Ferraro, J. P. Filippini, R. Flauger, G. M. Fuller, V. Gluscevic, D. Green, D. Grin, E. Grohs, J. W. Henning, J. C. Hill, R. Hlozek, G. Holder, W. Holzapfel, W. Hu, K. M. Huffenberger, R. Keskitalo, L. Knox, A. Kosowsky, J. Kovac, E. D. Kovetz, C.-L. Kuo, A. Kusaka, M. Le Jeune, A. T. Lee, M. Lilley, M. Loverde, M. S. Madhavacheril, A. Mantz, D. J. E. Marsh, J. McMahon, P. D. Meerburg, J. Meyers, A. D. Miller, J. B. Munoz, H. N. Nguyen, M. D. Niemack, M. Peloso, J. Peloton, L. Pogosian, C. Pryke, M. Raveri, C. L. Reichardt, G. Rocha, A. Rotti, E. Schaan, M. M. Schmittfull, D. Scott, N. Sehgal, S. Shandera, B. D. Sherwin, T. L. Smith, L. Sorbo, G. D. Starkman, K. T. Story, A. van Engelen, J. D. Vieira, S. Watson, N. Whitehorn, and W. L. Kimmy Wu. CMB-S4 Science Book, First Edition. *ArXiv e-prints*, October 2016.

[3] M. H. Abitbol, J. C. Hill, and B. R. Johnson. Foreground-induced biases in CMB polarimeter self-calibration. *MNRAS*, 457:1796–1803, April 2016. doi: 10.1093/mnras/stw030.

[4] M. H. Abitbol, Z. Ahmed, D. Barron, R. Basu Thakur, A. N. Bender, B. A. Benson, C. A. Bischoff, S. A. Bryan, J. E. Carlstrom, C. L. Chang, D. T. Chuss, K. T. Crowley,

A. Cukierman, T. de Haan, M. Dobbs, T. Essinger-Hileman, J. P. Filippini, K. Ganga, J. E. Gudmundsson, N. W. Halverson, S. Hanany, S. W. Henderson, C. A. Hill, S.-P. P. Ho, J. Hubmayr, K. Irwin, O. Jeong, B. R. Johnson, S. A. Kernasovskiy, J. M. Kovac, A. Kusaka, A. T. Lee, S. Maria, P. Mauskopf, J. J. McMahon, L. Moncelsi, A. W. Nadolski, J. M. Nagy, M. D. Niemack, R. C. O'Brient, S. Padin, S. C. Parshley, C. Pryke, N. A. Roe, K. Rostem, J. Ruhl, S. M. Simon, S. T. Staggs, A. Suzuki, E. R. Switzer, O. Tajima, K. L. Thompson, P. Timbie, G. S. Tucker, J. D. Vieira, A. G. Vieregg, B. Westbrook, E. J. Wollack, K. W. Yoon, K. S. Young, and E. Y. Young. CMB-S4 Technology Book, First Edition. *ArXiv e-prints*, June 2017.

[5] M. H. Abitbol, J. Chluba, J. C. Hill, and B. R. Johnson. Prospects for measuring cosmic microwave background spectral distortions in the presence of foregrounds. *MNRAS*, 471:1126–1140, October 2017. doi: 10.1093/mnras/stx1653.

[6] M. H. Abitbol, B. R. Johnson, G. Jones, C. Dickinson, and S. Harper. Constraining the Anomalous Microwave Emission Mechanism in the S140 Star Forming Region with Spectroscopic Observations Between 4 and 8 GHz at the Green Bank Telescope. *ArXiv e-prints*, May 2018.

[7] H. Akaike. A New Look at the Statistical Model Identification. *IEEE Transactions on Automatic Control*, 19:716–723, 1974.

[8] Y. Ali-Haïmoud. Effective conductance method for the primordial recombination spectrum. *Phys. Rev. D*, 87(2):023526, January 2013. doi: 10.1103/PhysRevD.87.023526.

[9] Y. Ali-Haïmoud. Spinning Dust Radiation: A Review of the Theory. *Advances in Astronomy*, 2013:462697, 2013. doi: 10.1155/2013/462697.

[10] Y. Ali-Haïmoud and M. Kamionkowski. Cosmic microwave background limits on accreting primordial black holes. *ArXiv:1612.05644*, December 2016.

[11] Y. Ali-Haïmoud, C. M. Hirata, and C. Dickinson. A refined model for spinning dust radiation. *MNRAS*, 395:1055–1078, May 2009. doi: 10.1111/j.1365-2966.2009.14599.x.

[12] D. Alonso, J. Dunkley, B. Thorne, and S. Næss. Simulated forecasts for primordial B -mode searches in ground-based experiments. *Phys. Rev. D*, 95(4):043504, February 2017. doi: 10.1103/PhysRevD.95.043504.

[13] R. A. Alpher and R. C. Herman. On the Relative Abundance of the Elements. *Physical Review*, 74:1737–1742, December 1948. doi: 10.1103/PhysRev.74.1737.

[14] R. A. Alpher, H. Bethe, and G. Gamow. The Origin of Chemical Elements. *Physical Review*, 73:803–804, April 1948. doi: 10.1103/PhysRev.73.803.

[15] P. André, C. Baccigalupi, A. Banday, D. Barbosa, B. Barreiro, J. Bartlett, N. Bartolo, E. Battistelli, R. Battye, G. Bendo, A. Beno#523t, J.-P. Bernard, M. Bersanelli, M. Béthermin, P. Bielewicz, A. Bonaldi, F. Bouchet, F. Boulanger, J. Brand, M. Bucher, C. Burigana, Z.-Y. Cai, P. Camus, F. Casas, V. Casasola, G. Castex, A. Challinor, J. Chluba, G. Chon, S. Colafrancesco, B. Comis, F. Cuttaia,

G. D'Alessandro, A. Da Silva, R. Davis, M. de Avillez, P. de Bernardis, M. de Petris, A. de Rosa, G. de Zotti, J. Delabrouille, F.-X. Désert, C. Dickinson, J. M. Diego, J. Dunkley, T. Enßlin, J. Errard, E. Falgarone, P. Ferreira, K. Ferrière, F. Finelli, A. Fletcher, P. Fosalba, G. Fuller, S. Galli, K. Ganga, J. García-Bellido, A. Ghribi, M. Giard, Y. Giraud-Héraud, J. Gonzalez-Nuevo, K. Grainge, A. Gruppuso, A. Hall, J.-C. Hamilton, M. Haverkorn, C. Hernandez-Monteagudo, D. Herranz, M. Jackson, A. Jaffe, R. Khatri, M. Kunz, L. Lamagna, M. Lattanzi, P. Leahy, J. Lesgourgues, M. Liguori, E. Liuzzo, M. Lopez-Caniego, J. Macias-Perez, B. Maffei, D. Maino, A. Mangilli, E. Martinez-Gonzalez, C. Martins, S. Masi, M. Massardi, S. Matarrese, A. Melchiorri, J.-B. Melin, A. Mennella, A. Mignano, M.-A. Miville-Deschênes, A. Monfardini, A. Murphy, P. Naselsky, F. Nati, P. Natoli, M. Negrello, F. Noviello, C. O'Sullivan, F. Paci, L. Pagano, R. Paladino, N. Palanque-Delabrouille, D. Paoletti, H. Peiris, F. Perrotta, F. Piacentini, M. Piat, L. Piccirillo, G. Pisano, G. Polenta, A. Pollo, N. Ponthieu, M. Remazeilles, S. Ricciardi, M. Roman, C. Rosset, J.-A. Rubino-Martin, M. Salatino, A. Schillaci, P. Shellard, J. Silk, A. Starobinsky, R. Stompor, R. Sunyaev, A. Tartari, L. Terenzi, L. Toffolatti, M. Tomasi, N. Trappe, M. Tristram, T. Trombetti, M. Tucci, R. Van de Weijgaert, B. Van Tent, L. Verde, P. Vielva, B. Wandelt, R. Watson, and S. Withington. PRISM (Polarized Radiation Imaging and Spectroscopy Mission): an extended white paper. *J. Cosmology Astropart. Phys.*, 2:006, February 2014. doi: 10.1088/1475-7516/2014/02/006.

[16] D. C. Araujo. *Data Analysis for the E and B EXperiment and Instrumentation Development for Cosmic Microwave Background Polarimetry.* PhD thesis, Columbia University, 2017.

[17] C. Armitage-Caplan, J. Dunkley, H. K. Eriksen, and C. Dickinson. Impact on the tensor-to-scalar ratio of incorrect Galactic foreground modelling. *MNRAS*, 424:1914–1924, August 2012. doi: 10.1111/j.1365-2966.2012.21314.x.

[18] F. Aubin, A. M. Aboobaker, P. Ade, D. Araujo, C. Baccigalupi, C. Bao, J. Borrill, D. Chapman, J. Didier, M. Dobbs, S. Feeney, C. Geach, S. Hanany, K. Helson, S. Hillbrand, G. Hilton, J. Hubmayr, A. Jaffe, B. Johnson, T. Jones, T. Kisner, J. Klein, A. Korotkov, A. Lee, L. Levinson, M. Limon, K. Macdermid, V. Marchenko, A. D. Miller, M. Milligan, E. Pascale, G. Puglisi, K. Raach, B. Reichborn-Kjennerud, C. Reintsema, I. Sagiv, G. Smecher, R. Stompor, M. Tristram, G. S. Tucker, B. Westbrook, K. Young, and K. Zilic. Temperature calibration of the E and B experiment. *ArXiv e-prints*, January 2016.

[19] J. Aumont, L. Conversi, C. Thum, H. Wiesemeyer, E. Falgarone, J. F. Macias-Perez, F. Piacentini, E. Pointecouteau, N. Ponthieu, J. L. Puget, C. Rosset, J. A. Tauber, and M. Tristram. Measurement of the Crab nebula polarization at 90 GHz as a calibrator for CMB experiments. *ArXiv e-prints*, December 2009.

[20] J. E. Austermann, J. A. Beall, S. A. Bryan, B. Dober, J. Gao, G. Hilton, J. Hubmayr, P. Mauskopf, C. M. McKenney, S. M. Simon, J. N. Ullom, M. R. Vissers,

and G. W. Wilson. Millimeter-Wave Polarimeters Using Kinetic Inductance Detectors for TolTEC and Beyond. *Journal of Low Temperature Physics*, May 2018. doi: 10.1007/s10909-018-1949-5.

[21] S. A. Balashev, E. E. Kholupenko, J. Chluba, A. V. Ivanchik, and D. A. Varshalovich. Spectral Distortions of the CMB Dipole. *ApJ*, 810:131, September 2015. doi: 10.1088/0004-637X/810/2/131.

[22] D. Barkats, R. Aikin, C. Bischoff, I. Buder, J. P. Kaufman, B. G. Keating, J. M. Kovac, M. Su, P. A. R. Ade, J. O. Battle, E. M. Bierman, J. J. Bock, H. C. Chiang, C. D. Dowell, L. Duband, J. Filippini, E. F. Hivon, W. L. Holzapfel, V. V. Hristov, W. C. Jones, C. L. Kuo, E. M. Leitch, P. V. Mason, T. Matsumura, H. T. Nguyen, N. Ponthieu, C. Pryke, S. Richter, G. Rocha, C. Sheehy, S. S. Kernasovskiy, Y. D. Takahashi, J. E. Tolan, and K. W. Yoon. Degree-scale Cosmic Microwave Background Polarization Measurements from Three Years of BICEP1 Data. *ApJ*, 783:67, March 2014. doi: 10.1088/0004-637X/783/2/67.

[23] J. D. Barrow and P. Coles. Primordial density fluctuations and the microwave background spectrum. *MNRAS*, 248:52–57, January 1991.

[24] J. Baselmans, S. J. C. Yates, R. Barends, Y. J. Y. Lankwarden, J. R. Gao, H. Hoevers, and T. M. Klapwijk. Noise and Sensitivity of Aluminum Kinetic Inductance Detectors for Sub-mm Astronomy. *Journal of Low Temperature Physics*, 151:524–529, April 2008. doi: 10.1007/s10909-007-9684-3.

[25] K. Basu, C. Hernández-Monteagudo, and R. A. Sunyaev. CMB observations and the production of chemical elements at the end of the dark ages. *A&A*, 416:447–466, March 2004. doi: 10.1051/0004-6361:20034298.

[26] N. Battaglia, J. C. Hill, I. G. McCarthy, J. Chluba, S. Ferraro, E. Schaan, and D. N. Spergel. CMB Spectral Distortions from Reionization and Cosmic Structure Formation. in prep.

[27] E. S. Battistelli, E. Carretti, A. Cruciani, P. de Bernardis, R. Génova-Santos, S. Masi, A. Naldi, R. Paladini, F. Piacentini, C. T. Tibbs, L. Verstraete, and N. Ysard. New Radio Observations of Anomalous Microwave Emission in the H II Region RCW175. *ApJ*, 801:111, March 2015. doi: 10.1088/0004-637X/801/2/111.

[28] C. L. Bennett, R. S. Hill, G. Hinshaw, M. R. Nolta, N. Odegard, L. Page, D. N. Spergel, J. L. Weiland, E. L. Wright, M. Halpern, N. Jarosik, A. Kogut, M. Limon, S. S. Meyer, G. S. Tucker, and E. Wollack. First-Year Wilkinson Microwave Anisotropy Probe (WMAP) Observations: Foreground Emission. *ApJS*, 148:97–117, September 2003. doi: 10.1086/377252.

[29] C. L. Bennett, D. Larson, J. L. Weiland, N. Jarosik, G. Hinshaw, N. Odegard, K. M. Smith, R. S. Hill, B. Gold, M. Halpern, E. Komatsu, M. R. Nolta, L. Page, D. N. Spergel, E. Wollack, J. Dunkley, A. Kogut, M. Limon, S. S. Meyer, G. S. Tucker, and

E. L. Wright. Nine-year Wilkinson Microwave Anisotropy Probe (WMAP) Observations: Final Maps and Results. *ApJS*, 208:20, October 2013. doi: 10.1088/0067-0049/208/2/20. URL http://arxiv.org/abs/1212.5225.

[30] K. Berg-Sørensen and H. Flyvbjerg. Power spectrum analysis for optical tweezers. *Review of Scientific Instruments*, 75:594–612, March 2004. doi: 10.1063/1.1645654.

[31] BICEP2 and Keck Array Collaborations, P. A. R. Ade, Z. Ahmed, R. W. Aikin, K. D. Alexander, D. Barkats, S. J. Benton, C. A. Bischoff, J. J. Bock, R. Bowens-Rubin, J. A. Brevik, I. Buder, E. Bullock, V. Buza, J. Connors, B. P. Crill, L. Duband, C. Dvorkin, J. P. Filippini, S. Fliescher, J. Grayson, M. Halpern, S. Harrison, G. C. Hilton, H. Hui, K. D. Irwin, K. S. Karkare, E. Karpel, J. P. Kaufman, B. G. Keating, S. Kefeli, S. A. Kernasovskiy, J. M. Kovac, C. L. Kuo, E. M. Leitch, M. Lueker, K. G. Megerian, C. B. Netterfield, H. T. Nguyen, R. O'Brient, R. W. Ogburn, IV, A. Orlando, C. Pryke, S. Richter, R. Schwarz, C. D. Sheehy, Z. K. Staniszewski, B. Steinbach, R. V. Sudiwala, G. P. Teply, K. L. Thompson, J. E. Tolan, C. Tucker, A. D. Turner, A. G. Vieregg, A. C. Weber, D. V. Wiebe, J. Willmert, C. L. Wong, W. L. K. Wu, and K. W. Yoon. BICEP2 / Keck Array VI: Improved Constraints On Cosmology and Foregrounds When Adding 95 GHz Data From Keck Array. *ArXiv e-prints*, October 2015.

[32] BICEP2 and Keck Array Collaborations, P. A. R. Ade, Z. Ahmed, R. W. Aikin, K. D. Alexander, D. Barkats, S. J. Benton, C. A. Bischoff, J. J. Bock, J. A. Brevik, I. Buder, E. Bullock, V. Buza, J. Connors, B. P. Crill, C. D. Dowell, C. Dvorkin, L. Duband, J. P. Filippini, S. Fliescher, S. R. Golwala, M. Halpern, S. Harrison, M. Hasselfield, S. R. Hildebrandt, G. C. Hilton, V. V. Hristov, H. Hui, K. D. Irwin, K. S. Karkare, J. P. Kaufman, B. G. Keating, S. Kefeli, S. A. Kernasovskiy, J. M. Kovac, C. L. Kuo, E. M. Leitch, M. Lueker, P. Mason, K. G. Megerian, C. B. Netterfield, H. T. Nguyen, R. O'Brient, R. W. Ogburn, IV, A. Orlando, C. Pryke, C. D. Reintsema, S. Richter, R. Schwarz, C. D. Sheehy, Z. K. Staniszewski, R. V. Sudiwala, G. P. Teply, K. L. Thompson, J. E. Tolan, A. D. Turner, A. G. Vieregg, A. C. Weber, J. Willmert, C. L. Wong, and K. W. Yoon. BICEP2/Keck Array V: Measurements of B-mode Polarization at Degree Angular Scales and 150 GHz by the Keck Array. *ApJ*, 811:126, October 2015. doi: 10.1088/0004-637X/811/2/126.

[33] BICEP2 Collaboration. BICEP2 I: Detection Of B-mode Polarization at Degree Angular Scales. *ArXiv e-prints*, March 2014. URL http://arxiv.org/abs/1403.3985.

[34] BICEP2 Collaboration, P. A. R. Ade, R. W. Aikin, D. Barkats, S. J. Benton, C. A. Bischoff, J. J. Bock, J. A. Brevik, I. Buder, E. Bullock, C. D. Dowell, L. Duband, J. P. Filippini, S. Fliescher, S. R. Golwala, M. Halpern, M. Hasselfield, S. R. Hildebrandt, G. C. Hilton, K. D. Irwin, K. S. Karkare, J. P. Kaufman, B. G. Keating, S. A. Kernasovskiy, J. M. Kovac, C. L. Kuo, E. M. Leitch, M. Lueker, C. B. Netterfield, H. T. Nguyen, R. O'Brient, R. W. Ogburn, IV, A. Orlando, C. Pryke, S. Richter, R. Schwarz, C. D. Sheehy, Z. K. Staniszewski, R. V. Sudiwala, G. P. Teply, J. E. Tolan, A. D. Turner, A. G. Vieregg, C. L. Wong, and K. W. Yoon. BICEP2 III: Instrumental Systematics. *ApJ*, 814:110, December 2015. doi: 10.1088/0004-637X/814/2/110.

[35] BICEP2/Keck and Planck Collaborations, P. A. R. Ade, N. Aghanim, Z. Ahmed, R. W. Aikin, K. D. Alexander, M. Arnaud, J. Aumont, C. Baccigalupi, A. J. Banday, and et al. Joint Analysis of BICEP2/Keck Array and Planck Data. *Physical Review Letters*, 114(10):101301, March 2015. doi: 10.1103/PhysRevLett.114.101301.

[36] J. Bock, S. Church, M. Devlin, G. Hinshaw, A. Lange, A. Lee, L. Page, B. Partridge, J. Ruhl, M. Tegmark, P. Timbie, R. Weiss, B. Winstein, and M. Zaldarriaga. Task Force on Cosmic Microwave Background Research. *ArXiv Astrophysics e-prints*, April 2006.

[37] J. R. Bond and G. Efstathiou. The statistics of cosmic background radiation fluctuations. *MNRAS*, 226:655–687, June 1987. doi: 10.1093/mnras/226.3.655.

[38] O. Bourrion, A. Bideaud, A. Benoit, A. Cruciani, J. F. Macias-Perez, A. Monfardini, M. Roesch, L. Swenson, and C. Vescovi. Electronics and data acquisition demonstrator for a kinetic inductance camera. *Journal of Instrumentation*, 6:6012, June 2011. doi: 10.1088/1748-0221/6/06/P06012.

[39] O. Bourrion, C. Vescovi, J. L. Bouly, A. Benoit, M. Calvo, L. Gallin-Martel, J. F. Macias-Perez, and A. Monfardini. NIKEL: Electronics and data acquisition for kilopixels kinetic inductance camera. *Journal of Instrumentation*, 7:7014, July 2012. doi: 10.1088/1748-0221/7/07/P07014.

[40] O. Bourrion, C. Vescovi, A. Catalano, M. Calvo, A. D'Addabbo, J. Goupy, N. Boudou, J. F. Macias-Perez, and A. Monfardini. High speed readout electronics development for frequency-multiplexed kinetic inductance detector design optimization. *Journal of Instrumentation*, 8:C12006, December 2013. doi: 10.1088/1748-0221/8/12/C12006.

[41] O. Bourrion, A. Benoit, J. L. Bouly, J. Bouvier, G. Bosson, M. Calvo, A. Catalano, J. Goupy, C. Li, J. F. Macías-Pérez, A. Monfardini, D. Tourres, N. Ponchant, and C. Vescovi. NIKEL_AMC: Readout electronics for the NIKA2 experiment. *ArXiv e-prints*, February 2016.

[42] M. Bucher. Physics of the cosmic microwave background anisotropy. *International Journal of Modern Physics D*, 24:1530004-303, January 2015. doi: 10.1142/S0218271815300049.

[43] C. Burigana, L. Danese, and G. de Zotti. Formation and evolution of early distortions of the microwave background spectrum - A numerical study. *A&A*, 246:49–58, June 1991.

[44] G. Cabass, A. Melchiorri, and E. Pajer. μ distortions or running: A guaranteed discovery from CMB spectrometry. *Phys. Rev. D*, 93(8):083515, April 2016. doi: 10.1103/PhysRevD.93.083515.

[45] E. Calabrese, D. Alonso, and J. Dunkley. Complementing the ground-based CMB Stage-4 experiment on large scales with the PIXIE satellite. *ArXiv:1611.10269*, November 2016.

[46] M. Calvo, A. Benoît, A. Catalano, J. Goupy, A. Monfardini, N. Ponthieu, E. Barria, G. Bres, M. Grollier, G. Garde, J.-P. Leggeri, G. Pont, S. Triqueneaux, R. Adam, O. Bourrion, J.-F. Macías-Pérez, M. Rebolo, A. Ritacco, J.-P. Scordilis, D. Tourres, A. Adane, G. Coiffard, S. Leclercq, F.-X. Désert, S. Doyle, P. Mauskopf, C. Tucker, P. Ade, P. André, A. Beelen, B. Belier, A. Bideaud, N. Billot, B. Comis, A. D'Addabbo, C. Kramer, J. Martino, F. Mayet, F. Pajot, E. Pascale, L. Perotto, V. Revéret, A. Ritacco, L. Rodriguez, G. Savini, K. Schuster, A. Sievers, and R. Zylka. The NIKA2 Instrument, A Dual-Band Kilopixel KID Array for Millimetric Astronomy. *Journal of Low Temperature Physics*, 184:816–823, August 2016. doi: 10.1007/s10909-016-1582-0.

[47] C. L. Carilli, J. Chluba, R. Decarli, F. Walter, M. Aravena, J. Wagg, G. Popping, P. Cortes, J. Hodge, A. Weiss, F. Bertoldi, and D. Riechers. The ALMA Spectroscopic Survey in the Hubble Ultra Deep Field: Implications for Spectral Line Intensity Mapping at Millimeter Wavelengths and CMB Spectral Distortions. *ApJ*, 833:73, December 2016. doi: 10.3847/1538-4357/833/1/73.

[48] B. J. Carr, K. Kohri, Y. Sendouda, and J. Yokoyama. New cosmological constraints on primordial black holes. *Phys. Rev. D*, 81(10):104019–+, May 2010. doi: 10.1103/PhysRevD.81.104019.

[49] A. Catalano, M. Calvo, N. Ponthieu, R. Adam, A. Adane, P. Ade, P. André, A. Beelen, B. Belier, A. Benoît, A. Bideaud, N. Billot, N. Boudou, O. Bourrion, G. Coiffard, B. Comis, A. D'Addabbo, F.-X. Désert, S. Doyle, J. Goupy, C. Kramer, S. Leclercq, J. F. Macías-Pérez, J. Martino, P. Mauskopf, F. Mayet, A. Monfardini, F. Pajot, E. Pascale, L. Perotto, V. Revéret, L. Rodriguez, G. Savini, K. Schuster, A. Sievers, C. Tucker, and R. Zylka. Performance and calibration of the NIKA camera at the IRAM 30 m telescope. *A&A*, 569:A9, September 2014. doi: 10.1051/0004-6361/201423557.

[50] A. Challinor. CMB anisotropy science: a review. In M. G. Burton, X. Cui, and N. F. H. Tothill, editors, *Astrophysics from Antarctica*, volume 288 of *IAU Symposium*, pages 42–52, January 2013. doi: 10.1017/S1743921312016663.

[51] A. Challinor and A. Lasenby. Relativistic Corrections to the Sunyaev-Zeldovich Effect. *ApJ*, 499:1–+, May 1998. doi: 10.1086/305623.

[52] D. Chapman, J. Didier, S. Hanany, S. Hillbrand, M. Limon, A. Miller, B. Reichborn-Kjennerud, G. Tucker, and Y. Vinokurov. STARS: a software application for the EBEX autonomous daytime star cameras. In *Software and Cyberinfrastructure for Astronomy III*, volume 9152 of *Proc. SPIE*, page 915212, July 2014. doi: 10.1117/12.2057181.

[53] J. Chluba. *Spectral Distortions of the Cosmic Microwave Background*. PhD thesis, LMU München, March 2005.

[54] J. Chluba. Green's function of the cosmological thermalization problem. *MNRAS*, 434:352–357, September 2013. doi: 10.1093/mnras/stt1025.

[55] J. Chluba. Distinguishing different scenarios of early energy release with spectral distortions of the cosmic microwave background. *MNRAS*, 436:2232–2243, December 2013. doi: 10.1093/mnras/stt1733.

[56] J. Chluba. Science with CMB spectral distortions. *ArXiv:1405.6938*, May 2014.

[57] J. Chluba. Green's function of the cosmological thermalization problem - II. Effect of photon injection and constraints. *MNRAS*, 454:4182–4196, December 2015. doi: 10.1093/mnras/stv2243.

[58] J. Chluba. Which spectral distortions does ΛCDM actually predict? *MNRAS*, 460: 227–239, July 2016. doi: 10.1093/mnras/stw945.

[59] J. Chluba and Y. Ali-Haïmoud. COSMOSPEC: fast and detailed computation of the cosmological recombination radiation from hydrogen and helium. *MNRAS*, 456:3494–3508, March 2016. doi: 10.1093/mnras/stv2691.

[60] J. Chluba and D. Jeong. Teasing bits of information out of the CMB energy spectrum. *MNRAS*, 438:2065–2082, March 2014. doi: 10.1093/mnras/stt2327.

[61] J. Chluba and R. A. Sunyaev. Superposition of blackbodies and the dipole anisotropy: A possibility to calibrate CMB experiments. *A&A*, 424:389–408, September 2004. doi: 10.1051/0004-6361:20041016.

[62] J. Chluba and R. A. Sunyaev. Free-bound emission from cosmological hydrogen recombination. *A&A*, 458:L29–L32, November 2006. doi: 10.1051/0004-6361:20066191.

[63] J. Chluba and R. A. Sunyaev. Is there a need and another way to measure the cosmic microwave background temperature more accurately? *A&A*, 478:L27–L30, February 2008. doi: 10.1051/0004-6361:20078200.

[64] J. Chluba and R. A. Sunyaev. The evolution of CMB spectral distortions in the early Universe. *MNRAS*, 419:1294–1314, January 2012. doi: 10.1111/j.1365-2966.2011.19786.x.

[65] J. Chluba, G. M. Vasil, and L. J. Dursi. Recombinations to the Rydberg states of hydrogen and their effect during the cosmological recombination epoch. *MNRAS*, 407: 599–612, September 2010. doi: 10.1111/j.1365-2966.2010.16940.x.

[66] J. Chluba, A. L. Erickcek, and I. Ben-Dayan. Probing the Inflaton: Small-scale Power Spectrum Constraints from Measurements of the Cosmic Microwave Background Energy Spectrum. *ApJ*, 758:76, October 2012. doi: 10.1088/0004-637X/758/2/76.

[67] J. Chluba, R. Khatri, and R. A. Sunyaev. CMB at 2×2 order: the dissipation of primordial acoustic waves and the observable part of the associated energy release. *MNRAS*, 425:1129–1169, September 2012. doi: 10.1111/j.1365-2966.2012.21474.x.

[68] J. Chluba, E. Switzer, K. Nelson, and D. Nagai. Sunyaev-Zeldovich signal processing and temperature-velocity moment method for individual clusters. *MNRAS*, 430:3054–3069, April 2013. doi: 10.1093/mnras/stt110.

[69] J. Chluba, J. C. Hill, and M. H. Abitbol. Rethinking CMB foregrounds: systematic extension of foreground parameterizations. *ArXiv:1701.00274*, 472:1195–1213, January 2017. doi: 10.1093/mnras/stx1982.

[70] G. Chon, A. Challinor, S. Prunet, E. Hivon, and I. Szapudi. Fast estimation of polarization power spectra using correlation functions. *MNRAS*, 350:914–926, May 2004. doi: 10.1111/j.1365-2966.2004.07737.x.

[71] S. Clesse, B. Garbrecht, and Y. Zhu. Testing inflation and curvaton scenarios with CMB distortions. *J. Cosmology Astropart. Phys.*, 10:046, October 2014. doi: 10.1088/1475-7516/2014/10/046.

[72] A. T. Crites, J. W. Henning, P. A. R. Ade, K. A. Aird, J. E. Austermann, J. A. Beall, A. N. Bender, B. A. Benson, L. E. Bleem, J. E. Carlstrom, C. L. Chang, H. C. Chiang, H.-M. Cho, R. Citron, T. M. Crawford, T. de Haan, M. A. Dobbs, W. Everett, J. Gallicchio, J. Gao, E. M. George, A. Gilbert, N. W. Halverson, D. Hanson, N. Harrington, G. C. Hilton, G. P. Holder, W. L. Holzapfel, S. Hoover, Z. Hou, J. D. Hrubes, N. Huang, J. Hubmayr, K. D. Irwin, R. Keisler, L. Knox, A. T. Lee, E. M. Leitch, D. Li, C. Liang, D. Luong-Van, J. J. McMahon, J. Mehl, S. S. Meyer, L. Mocanu, T. E. Montroy, T. Natoli, J. P. Nibarger, V. Novosad, S. Padin, C. Pryke, C. L. Reichardt, J. E. Ruhl, B. R. Saliwanchik, J. T. Sayre, K. K. Schaffer, G. Smecher, A. A. Stark, K. T. Story, C. Tucker, K. Vanderlinde, J. D. Vieira, G. Wang, N. Whitehorn, V. Yefremenko, and O. Zahn. Measurements of E-Mode Polarization and Temperature-E-Mode Correlation in the Cosmic Microwave Background from 100 Square Degrees of SPTpol Data. *ApJ*, 805:36, May 2015. doi: 10.1088/0004-637X/805/1/36.

[73] R. A. Daly. Spectral distortions of the microwave background radiation resulting from the damping of pressure waves. *ApJ*, 371:14–28, April 1991. doi: 10.1086/169866.

[74] L. Danese and G. de Zotti. The relic radiation spectrum and the thermal history of the Universe. *Nuovo Cimento Rivista Serie*, 7:277–362, September 1977. doi: 10.1007/BF02747276.

[75] L. Danese and G. de Zotti. Dipole anisotropy and distortions of the spectrum of the cosmic microwave background. *A&A*, 94:L33, February 1981.

[76] S. Das, T. Louis, M. R. Nolta, G. E. Addison, E. S. Battistelli, J. R. Bond, E. Calabrese, D. Crichton, M. J. Devlin, S. Dicker, J. Dunkley, R. Dünner, J. W. Fowler, M. Gralla, A. Hajian, M. Halpern, M. Hasselfield, M. Hilton, A. D. Hincks, R. Hlozek, K. M. Huffenberger, J. P. Hughes, K. D. Irwin, A. Kosowsky, R. H. Lupton, T. A. Marriage, D. Marsden, F. Menanteau, K. Moodley, M. D. Niemack, L. A. Page, B. Partridge, E. D. Reese, B. L. Schmitt, N. Sehgal, B. D. Sherwin, J. L. Sievers, D. N. Spergel, S. T. Staggs, D. S. Swetz, E. R. Switzer, R. Thornton, H. Trac, and E. Wollack. The Atacama Cosmology Telescope: temperature and gravitational lensing power spectrum measurements from three seasons of data. *J. Cosmology Astropart. Phys.*, 4:014, April 2014. doi: 10.1088/1475-7516/2014/04/014.

[77] P. K. Day, H. G. LeDuc, B. A. Mazin, A. Vayonakis, and J. Zmuidzinas. A broadband superconducting detector suitable for use in large arrays. *Nature*, 425:817–821, October 2003. doi: 10.1038/nature02037.

[78] P. K. Day, H. G. Leduc, A. Goldin, T. Vayonakis, B. A. Mazin, S. Kumar, J. Gao, and J. Zmuidzinas. Antenna-coupled microwave kinetic inductance detectors. *Nuclear Instruments and Methods in Physics Research A*, 559:561–563, April 2006. doi: 10.1016/j.nima.2005.12.057.

[79] A. de Oliveira-Costa, M. Tegmark, B. M. Gaensler, J. Jonas, T. L. Landecker, and P. Reich. A model of diffuse Galactic radio emission from 10 MHz to 100 GHz. *MNRAS*, 388:247–260, July 2008. doi: 10.1111/j.1365-2966.2008.13376.x.

[80] G. De Zotti, M. Negrello, G. Castex, A. Lapi, and M. Bonato. Another look at distortions of the Cosmic Microwave Background spectrum. *J. Cosmology Astropart. Phys.*, 3:047, March 2016. doi: 10.1088/1475-7516/2016/03/047.

[81] J. Delabrouille. Analysis of the accuracy of a destriping method for future cosmic microwave background mapping with the PLANCK SURVEYOR satellite. *A&AS*, 127:555–567, February 1998. doi: 10.1051/aas:1998119.

[82] V. Desjacques, J. Chluba, J. Silk, F. de Bernardis, and O. Doré. Detecting the cosmological recombination signal from space. *MNRAS*, 451:4460–4470, August 2015. doi: 10.1093/mnras/stv1291.

[83] C. Dickinson. Observations of Anomalous Microwave Emission from HII Regions. *Advances in Astronomy*, 2013:162478, 2013. doi: 10.1155/2013/162478.

[84] C. Dickinson, M. Peel, and M. Vidal. New constraints on the polarization of anomalous microwave emission in nearby molecular clouds. *MNRAS*, 418:L35–L39, November 2011. doi: 10.1111/j.1745-3933.2011.01138.x.

[85] C. Dickinson, Y. Ali-Haïmoud, A. Barr, E. S. Battistelli, A. Bell, L. Bernstein, S. Casassus, K. Cleary, B. T. Draine, R. Génova-Santos, S. E. Harper, B. Hensley, J. Hill-Valler, T. Hoang, F. P. Israel, L. Jew, A. Lazarian, J. P. Leahy, J. Leech, C. H. López-Caraballo, I. McDonald, E. J. Murphy, T. Onaka, R. Paladini, M. W. Peel, Y. Perrott, F. Poidevin, A. C. S. Readhead, J.-A. Rubiño-Martín, A. C. Taylor, C. T. Tibbs, M. Todorović, and M. Vidal. The State-of-Play of Anomalous Microwave Emission (AME) research. *New A Rev.*, 80:1–28, February 2018. doi: 10.1016/j.newar.2018.02.001.

[86] J. Didier. *Construction, Deployment and Data Analysis of the E and B EXperiment: A Cosmic Microwave Background Polarimeter*. PhD thesis, Columbia University, 2016.

[87] J. Didier, A. D. Miller, D. Araujo, F. Aubin, C. Geach, B. Johnson, A. Korotkov, K. Raach, B. Westbrook, K. Young, A. M. Aboobaker, P. Ade, C. Baccigalupi, C. Bao, D. Chapman, M. Dobbs, W. Grainger, S. Hanany, K. Helson, S. Hillbrand, J. Hubmayr, A. Jaffe, T. Jones, J. Klein, A. Lee, M. Limon, K. MacDermid, M. Milligan, E. Pascale,

B. Reichborn-Kjennerud, I. Sagiv, C. Tucker, G. S. Tucker, and K. Zilic. Intensity-Coupled-Polarization in Instruments with a Continuously Rotating Half-Wave Plate. *ArXiv e-prints*, November 2017.

[88] B. J. Dober, P. A. R. Ade, P. Ashton, F. E. Angilè, J. A. Beall, D. Becker, K. J. Bradford, G. Che, H.-M. Cho, M. J. Devlin, L. M. Fissel, Y. Fukui, N. Galitzki, J. Gao, C. E. Groppi, S. Hillbrand, G. C. Hilton, J. Hubmayr, K. D. Irwin, J. Klein, J. Van Lanen, D. Li, Z.-Y. Li, N. P. Lourie, H. Mani, P. G. Martin, P. Mauskopf, F. Nakamura, G. Novak, D. P. Pappas, E. Pascale, F. P. Santos, G. Savini, D. Scott, S. Stanchfield, J. N. Ullom, M. Underhill, M. R. Vissers, and D. Ward-Thompson. The next-generation BLASTPol experiment. In *Millimeter, Submillimeter, and Far-Infrared Detectors and Instrumentation for Astronomy VII*, volume 9153 of *Proc. SPIE*, page 91530H, July 2014. doi: 10.1117/12.2054419.

[89] S. Dodelson. *Modern cosmology*. 2003.

[90] B. T. Draine. *Physics of the Interstellar and Intergalactic Medium*. 2011.

[91] B. T. Draine and B. S. Hensley. Quantum Suppression of Alignment in Ultrasmall Grains: Microwave Emission from Spinning Dust will be Negligibly Polarized. *ApJ*, 831:59, November 2016. doi: 10.3847/0004-637X/831/1/59.

[92] B. T. Draine and A. Lazarian. Electric Dipole Radiation from Spinning Dust Grains. *ApJ*, 508:157–179, November 1998. doi: 10.1086/306387.

[93] B. T. Draine and A. Lazarian. Diffuse Galactic Emission from Spinning Dust Grains. *ApJ*, 494:L19–L22, February 1998. doi: 10.1086/311167.

[94] B. T. Draine and A. Lazarian. Magnetic Dipole Microwave Emission from Dust Grains. *ApJ*, 512:740–754, February 1999. doi: 10.1086/306809.

[95] R. Duan, S. McHugh, B. Serfass, B. A. Mazin, A. Merrill, S. R. Golwala, T. P. Downes, N. G. Czakon, P. K. Day, J. Gao, J. Glenn, M. I. Hollister, H. G. Leduc, P. R. Maloney, O. Noroozian, H. T. Nguyen, J. Sayers, J. A. Schlaerth, S. Siegel, J. E. Vaillancourt, A. Vayonakis, P. R. Wilson, and J. Zmuidzinas. An open-source readout for MKIDs. In *Millimeter, Submillimeter, and Far-Infrared Detectors and Instrumentation for Astronomy V*, volume 7741 of *Proc. SPIE*, page 77411V, July 2010. doi: 10.1117/12.856832.

[96] V. K. Dubrovich. Hydrogen recombination lines of cosmological origin. *Soviet Astronomy Letters*, 1:196–+, October 1975.

[97] J. Dunkley, A. Amblard, C. Baccigalupi, M. Betoule, D. Chuss, A. Cooray, J. Delabrouille, C. Dickinson, G. Dobler, J. Dotson, H. K. Eriksen, D. Finkbeiner, D. Fixsen, P. Fosalba, A. Fraisse, C. Hirata, A. Kogut, J. Kristiansen, C. Lawrence, A. M. Magalha˜Es, M. A. Miville-Deschenes, S. Meyer, A. Miller, S. K. Naess, L. Page, H. V. Peiris, N. Phillips, E. Pierpaoli, G. Rocha, J. E. Vaillancourt, and L. Verde. Prospects for polarized foreground removal. In S. Dodelson, D. Baumann, A. Cooray, J. Dunkley,

A. Fraisse, M. G. Jackson, A. Kogut, L. Krauss, M. Zaldarriaga, and K. Smith, editors, *American Institute of Physics Conference Series*, volume 1141 of *American Institute of Physics Conference Series*, pages 222–264, June 2009. doi: 10.1063/1.3160888.

[98] J. Dunkley, R. Hlozek, J. Sievers, V. Acquaviva, P. A. R. Ade, P. Aguirre, M. Amiri, J. W. Appel, L. F. Barrientos, E. S. Battistelli, J. R. Bond, B. Brown, B. Burger, and J. Chervenak. The Atacama Cosmology Telescope: Cosmological Parameters from the 2008 Power Spectrum. *ApJ*, 739:52, September 2011. doi: 10.1088/0004-637X/739/1/52.

[99] M. B. Einhorn and K. Sato. Monopole production in the very early universe in a first-order phase transition. *Nuclear Physics B*, 180:385–404, May 1981. doi: 10.1016/0550-3213(81)90057-2.

[100] J. Ellis, G. B. Gelmini, J. L. Lopez, D. V. Nanopoulos, and S. Sarkar. Astrophysical constraints on massive unstable neutral relic particles. *Nuclear Physics B*, 373:399–437, April 1992. doi: 10.1016/0550-3213(92)90438-H.

[101] W. C. Erickson. A Mechanism of Non-Thermal Radio-Noise Origin. *ApJ*, 126:480, November 1957. doi: 10.1086/146421.

[102] J. Errard, S. M. Feeney, H. V. Peiris, and A. H. Jaffe. Robust forecasts on fundamental physics from the foreground-obscured, gravitationally-lensed CMB polarization. *J. Cosmology Astropart. Phys.*, 3:052, March 2016. doi: 10.1088/1475-7516/2016/03/052.

[103] T. Essinger-Hileman, A. Ali, M. Amiri, J. W. Appel, D. Araujo, C. L. Bennett, F. Boone, M. Chan, H.-M. Cho, D. T. Chuss, F. Colazo, E. Crowe, K. Denis, R. Dünner, J. Eimer, D. Gothe, M. Halpern, K. Harrington, G. C. Hilton, G. F. Hinshaw, C. Huang, K. Irwin, G. Jones, J. Karakla, A. J. Kogut, D. Larson, M. Limon, L. Lowry, T. Marriage, N. Mehrle, A. D. Miller, N. Miller, S. H. Moseley, G. Novak, C. Reintsema, K. Rostem, T. Stevenson, D. Towner, K. U-Yen, E. Wagner, D. Watts, E. J. Wollack, Z. Xu, and L. Zeng. CLASS: the cosmology large angular scale surveyor. In *Millimeter, Submillimeter, and Far-Infrared Detectors and Instrumentation for Astronomy VII*, volume 9153 of *Proc. SPIE*, page 91531I, July 2014. doi: 10.1117/12.2056701.

[104] J. P. Filippini, P. A. R. Ade, M. Amiri, S. J. Benton, R. Bihary, J. J. Bock, J. R. Bond, J. A. Bonetti, S. A. Bryan, B. Burger, H. C. Chiang, C. R. Contaldi, B. P. Crill, O. Doré, M. Farhang, L. M. Fissel, N. N. Gandilo, S. R. Golwala, J. E. Gudmundsson, M. Halpern, M. Hasselfield, G. Hilton, W. Holmes, V. V. Hristov, K. D. Irwin, W. C. Jones, C. L. Kuo, C. J. MacTavish, P. V. Mason, T. E. Montroy, T. A. Morford, C. B. Netterfield, D. T. O'Dea, A. S. Rahlin, C. D. Reintsema, J. E. Ruhl, M. C. Runyan, M. A. Schenker, J. A. Shariff, J. D. Soler, A. Trangsrud, C. Tucker, R. S. Tucker, and A. D. Turner. SPIDER: a balloon-borne CMB polarimeter for large angular scales. In *Millimeter, Submillimeter, and Far-Infrared Detectors and Instrumentation for Astronomy V*, volume 7741 of *Society of Photo-Optical Instrumentation Engineers (SPIE) Conference Series*, page 77411N, July 2010. doi: 10.1117/12.857720.

[105] D. P. Finkbeiner. A Full-Sky Hα Template for Microwave Foreground Prediction. *ApJS*, 146:407–415, June 2003. doi: 10.1086/374411.

[106] D. J. Fixsen. The Temperature of the Cosmic Microwave Background. *ApJ*, 707: 916–920, December 2009. doi: 10.1088/0004-637X/707/2/916.

[107] D. J. Fixsen and J. C. Mather. The Spectral Results of the Far-Infrared Absolute Spectrophotometer Instrument on COBE. *ApJ*, 581:817–822, December 2002. doi: 10.1086/344402.

[108] D. J. Fixsen, E. S. Cheng, J. M. Gales, J. C. Mather, R. A. Shafer, and E. L. Wright. The Cosmic Microwave Background Spectrum from the Full COBE FIRAS Data Set. *ApJ*, 473:576–+, December 1996. doi: 10.1086/178173.

[109] D. Flanigan, B. R. Johnson, M. H. Abitbol, S. Bryan, R. Cantor, P. Day, G. Jones, P. Mauskopf, H. McCarrick, A. Miller, and J. Zmuidzinas. Magnetic field dependence of the internal quality factor and noise performance of lumped-element kinetic inductance detectors. *Applied Physics Letters*, 109(14):143503, October 2016. doi: 10.1063/1.4964119.

[110] D. Flanigan, H. McCarrick, G. Jones, B. R. Johnson, M. H. Abitbol, P. Ade, D. Araujo, K. Bradford, R. Cantor, G. Che, P. Day, S. Doyle, C. B. Kjellstrand, H. Leduc, M. Limon, V. Luu, P. Mauskopf, A. Miller, T. Mroczkowski, C. Tucker, and J. Zmuidzinas. Photon noise from chaotic and coherent millimeter-wave sources measured with horn-coupled, aluminum lumped-element kinetic inductance detectors. *Applied Physics Letters*, 108(8):083504, February 2016. doi: 10.1063/1.4942804.

[111] R. Flauger, J. C. Hill, and D. N. Spergel. Toward an understanding of foreground emission in the BICEP2 region. *J. Cosmology Astropart. Phys.*, 8:039, August 2014. doi: 10.1088/1475-7516/2014/08/039.

[112] D. Foreman-Mackey, D. W. Hogg, D. Lang, and J. Goodman. emcee: The MCMC Hammer. *ArXiv:1202.3665*, February 2012.

[113] U. Fuskeland, I. K. Wehus, H. K. Eriksen, and S. K. Næss. Spatial Variations in the Spectral Index of Polarized Synchrotron Emission in the 9 yr WMAP Sky Maps. *ApJ*, 790:104, August 2014. doi: 10.1088/0004-637X/790/2/104.

[114] N. Galitzki, P. Ade, F. E. Angilè, P. Ashton, J. Austermann, T. Billings, G. Che, H.-M. Cho, K. Davis, M. Devlin, S. Dicker, B. J. Dober, L. M. Fissel, Y. Fukui, J. Gao, S. Gordon, C. E. Groppi, S. Hillbrand, G. C. Hilton, J. Hubmayr, K. D. Irwin, J. Klein, D. Li, Z.-Y. Li, N. P. Lourie, I. Lowe, H. Mani, P. G. Martin, P. Mauskopf, C. McKenney, F. Nati, G. Novak, E. Pascale, G. Pisano, F. P. Santos, D. Scott, A. Sinclair, J. D. Soler, C. Tucker, M. Underhill, M. Vissers, and P. Williams. Instrumental performance and results from testing of the BLAST-TNG receiver, submillimeter optics, and MKID detector arrays. In *Millimeter, Submillimeter, and Far-Infrared Detectors and Instrumentation for Astronomy VIII*, volume 9914 of *Proc. SPIE*, page 99140J, July 2016. doi: 10.1117/12.2231167.

[115] N. Galitzki, A. Ali, K. S. Arnold, P. C. Ashton, J. E. Austermann, C. Baccigalupi, T. Baildon, D. Barron, J. A. Beall\, S. Beckman, S. M. M. Bruno, S. Bryan, P. G. Calisse, G. E. Chesmore, Y. Chinone, S. K. Choi, G. Coppi, K. D. Crowley, K. T. Crowley, A. Cukierman, M. J. Devlin, S. Dicker, B. Dober, S. M. Duff, J. Dunkley, G. Fabbian, P. A. Gallardo, M. Gerbino, N. Goeckner-Wald, J. E. Golec, J. E. Gudmundsson, E. E. Healy, S. Henderson, C. A. Hill, G. C. Hilton, S.-P. P. Ho, L. A. Howe, J. Hubmayr, O. Jeong, B. Keating, B. J. Koopman, K. Kuichi, A. Kusaka, J. Lashner, A. T. Lee, Y. Li, M. Limon, M. Lungu, F. Matsuda, P. D. Mauskopf, A. J. May, N. McCallum, J. McMahon, F. Nati, M. D. Niemack, J. L. Orlowski-Scherer, S. C. Parshley, L. Piccirillo, M. Sathyanarayana Rao, C. Raum, M. Salatino, J. S. Seibert, C. Sierra, M. Silva-Feaver, S. M. Simon, S. T. Staggs, J. R. Stevens, A. Suzuki\, G. Teply, R. Thornton, C. Tsai, J. N. Ullom, E. M. Vavagiakis, M. R. Vissers, B. Westbrook, E. J. Wollack, Z. Xu\, and N. Zhu. The Simons Observatory: Instrument Overview. *ArXiv e-prints*, August 2018.

[116] G. Gamow. The Evolution of the Universe. *Nature*, 162:680–682, October 1948. doi: 10.1038/162680a0.

[117] R. Génova-Santos, J. A. Rubiño-Martín, R. Rebolo, M. Aguiar, F. Gómez-Reñasco, C. Gutiérrez, R. J. Hoyland, C. López-Caraballo, A. E. Peláez-Santos, M. R. Pérez-de-Taoro, F. Poidevin, V. Sánchez de la Rosa, D. Tramonte, A. Vega-Moreno, T. Viera-Curbelo, R. Vignasa, E. Martínez-González, R. B. Barreiro, B. Casaponsa, F. J. Casas, J. M. Diego, R. Fernández-Cobos, D. Herranz, M. López-Caniego, D. Ortiz, P. Vielva, E. Artal, B. Aja, J. Cagigas, J. L. Cano, L. de la Fuente, A. Mediavilla, J. V. Terán, E. Villa, L. Piccirillo, R. Davies, R. J. Davis, C. Dickinson, K. Grainge, S. Harper, B. Maffei, M. McCulloch, S. Melhuish, G. Pisano, R. A. Watson, A. Lasenby, M. Ashdown, M. Hobson, Y. Perrott, N. Razavi-Ghods, R. Saunders, D. Titterington, and P. Scott. The QUIJOTE experiment: project overview and first results. In A. J. Cenarro, F. Figueras, C. Hernández-Monteagudo, J. Trujillo Bueno, and L. Valdivielso, editors, *Highlights of Spanish Astrophysics VIII*, pages 207–212, May 2015.

[118] R. Génova-Santos, J. A. Rubiño-Martín, R. Rebolo, A. Peláez-Santos, C. H. López-Caraballo, S. Harper, R. A. Watson, M. Ashdown, R. B. Barreiro, B. Casaponsa, C. Dickinson, J. M. Diego, R. Fernández-Cobos, K. J. B. Grainge, C. M. Gutiérrez, D. Herranz, R. Hoyland, A. Lasenby, M. López-Caniego, E. Martínez-González, M. McCulloch, S. Melhuish, L. Piccirillo, Y. C. Perrott, F. Poidevin, N. Razavi-Ghods, P. F. Scott, D. Titterington, D. Tramonte, P. Vielva, and R. Vignaga. QUIJOTE scientific results - I. Measurements of the intensity and polarisation of the anomalous microwave emission in the Perseus molecular complex. *MNRAS*, 452:4169–4182, October 2015. doi: 10.1093/mnras/stv1405.

[119] R. Génova-Santos, J. A. Rubiño-Martín, A. Peláez-Santos, F. Poidevin, R. Rebolo, R. Vignaga, E. Artal, S. Harper, R. Hoyland, A. Lasenby, E. Martínez-González, L. Piccirillo, D. Tramonte, and R. A. Watson. QUIJOTE scientific results - II. Polarisation measurements of the microwave emission in the Galactic molecular complexes

W43 and W47 and supernova remnant W44. *MNRAS*, 464:4107–4132, February 2017. doi: 10.1093/mnras/stw2503.

[120] M. Gervasi, M. Zannoni, A. Tartari, G. Boella, and G. Sironi. TRIS. II. Search for CMB Spectral Distortions at 0.60, 0.82, and 2.5 GHz. *ApJ*, 688:24-31, November 2008. doi: 10.1086/592134.

[121] S. Gordon, B. Dober, A. Sinclair, S. Rowe, S. Bryan, P. Mauskopf, J. Austermann, M. Devlin, S. Dicker, J. Gao, G. C. Hilton, J. Hubmayr, G. Jones, J. Klein, N. P. Lourie, C. McKenney, F. Nati, J. D. Soler, M. Strader, and M. Vissers. An Open Source, FPGA-Based LeKID Readout for BLAST-TNG: Pre-Flight Results. *Journal of Astronomical Instrumentation*, 5:1641003, December 2016. doi: 10.1142/S2251171716410038.

[122] K. M. Górski, E. Hivon, A. J. Banday, B. D. Wandelt, F. K. Hansen, M. Reinecke, and M. Bartelmann. HEALPix: A Framework for High-Resolution Discretization and Fast Analysis of Data Distributed on the Sphere. *ApJ*, 622:759–771, April 2005. doi: 10.1086/427976.

[123] H. P. Gush, M. Halpern, and E. H. Wishnow. Rocket measurement of the cosmic-background-radiation mm-wave spectrum. *Phys. Rev. Lett.*, 65:537–540, Jul 1990. doi: 10.1103/PhysRevLett.65.537. URL http://link.aps.org/doi/10.1103/PhysRevLett.65.537.

[124] A. H. Guth. Inflationary universe: A possible solution to the horizon and flatness problems. *Phys. Rev. D*, 23:347–356, January 1981. doi: 10.1103/PhysRevD.23.347.

[125] D. Hanson, S. Hoover, A. Crites, P. A. R. Ade, K. A. Aird, J. E. Austermann, J. A. Beall, A. N. Bender, B. A. Benson, L. E. Bleem, J. J. Bock, J. E. Carlstrom, C. L. Chang, H. C. Chiang, H.-M. Cho, A. Conley, T. M. Crawford, T. de Haan, M. A. Dobbs, W. Everett, J. Gallicchio, J. Gao, E. M. George, N. W. Halverson, N. Harrington, J. W. Henning, G. C. Hilton, G. P. Holder, W. L. Holzapfel, J. D. Hrubes, N. Huang, J. Hubmayr, K. D. Irwin, R. Keisler, L. Knox, A. T. Lee, E. Leitch, D. Li, C. Liang, D. Luong-Van, G. Marsden, J. J. McMahon, J. Mehl, S. S. Meyer, L. Mocanu, T. E. Montroy, T. Natoli, J. P. Nibarger, V. Novosad, S. Padin, C. Pryke, C. L. Reichardt, J. E. Ruhl, B. R. Saliwanchik, J. T. Sayre, K. K. Schaffer, B. Schulz, G. Smecher, A. A. Stark, K. T. Story, C. Tucker, K. Vanderlinde, J. D. Vieira, M. P. Viero, G. Wang, V. Yefremenko, O. Zahn, and M. Zemcov. Detection of B-Mode Polarization in the Cosmic Microwave Background with Data from the South Pole Telescope. *Physical Review Letters*, 111(14):141301, October 2013. doi: 10.1103/PhysRevLett.111.141301. URL http://arxiv.org/abs/1307.5830.

[126] S. E. Harper, C. Dickinson, and K. Cleary. Observations of free-free and anomalous microwave emission from LDN 1622 with the 100 m Green Bank Telescope. *MNRAS*, 453:3375–3385, November 2015. doi: 10.1093/mnras/stv1863.

[127] K. Harrington, T. Marriage, A. Ali, J. W. Appel, C. L. Bennett, F. Boone, M. Brewer, M. Chan, D. T. Chuss, F. Colazo, S. Dahal, K. Denis, R. Dünner, J. Eimer, T. Essinger-Hileman, P. Fluxa, M. Halpern, G. Hilton, G. F. Hinshaw, J. Hubmayr, J. Iuliano, J. Karakla, J. McMahon, N. T. Miller, S. H. Moseley, G. Palma, L. Parker, M. Petroff, B. Pradenas, K. Rostem, M. Sagliocca, D. Valle, D. Watts, E. Wollack, Z. Xu, and L. Zeng. The Cosmology Large Angular Scale Surveyor. In *Millimeter, Submillimeter, and Far-Infrared Detectors and Instrumentation for Astronomy VIII*, volume 9914 of *Society of Photo-Optical Instrumentation Engineers (SPIE) Conference Series*, page 99141K, July 2016. doi: 10.1117/12.2233125.

[128] C. G. T. Haslam, U. Klein, C. J. Salter, H. Stoffel, W. E. Wilson, M. N. Cleary, D. J. Cooke, and P. Thomasson. A 408 MHz all-sky continuum survey. I - Observations at southern declinations and for the North Polar region. *A&A*, 100:209–219, July 1981.

[129] C. G. T. Haslam, C. J. Salter, H. Stoffel, and W. E. Wilson. A 408 MHz all-sky continuum survey. II - The atlas of contour maps. *A&AS*, 47:1, January 1982.

[130] K. Hattori, S. Ariyoshi, M. Hazumi, H. Ishino, A. Kibayashi, S. Mima, C. Otani, N. Satoh, T. Tomaru, M. Yoshida, and H. Watanabe. Novel Frequency-Domain Multiplexing MKID Readout for the LiteBIRD Satellite. *Journal of Low Temperature Physics*, 167:671–677, June 2012. doi: 10.1007/s10909-012-0506-x.

[131] M. G. Hauser, R. G. Arendt, T. Kelsall, E. Dwek, N. Odegard, J. L. Weiland, H. T. Freudenreich, W. T. Reach, R. F. Silverberg, S. H. Moseley, Y. C. Pei, P. Lubin, J. C. Mather, R. A. Shafer, G. F. Smoot, R. Weiss, D. T. Wilkinson, and E. L. Wright. The COBE Diffuse Infrared Background Experiment Search for the Cosmic Infrared Background. I. Limits and Detections. *ApJ*, 508:25–43, November 1998. doi: 10.1086/306379.

[132] B. S. Hensley and P. Bull. Mitigating Complex Dust Foregrounds in Future Cosmic Microwave Background Polarization Experiments. *ApJ*, 853:127, February 2018. doi: 10.3847/1538-4357/aaa489.

[133] B. S. Hensley and B. T. Draine. Modeling the Anomalous Microwave Emission with Spinning Nanoparticles: No PAHs Required. *ApJ*, 836:179, February 2017. doi: 10.3847/1538-4357/aa5c37.

[134] B. S. Hensley, B. T. Draine, and A. M. Meisner. A Case Against Spinning PAHs as the Source of the Anomalous Microwave Emission. *ApJ*, 827:45, August 2016. doi: 10.3847/0004-637X/827/1/45.

[135] C. Hervías-Caimapo, A. Bonaldi, and M. L. Brown. A new model of the microwave polarized sky for CMB experiments. *MNRAS*, 462:2063–2073, October 2016. doi: 10.1093/mnras/stw1787.

[136] C. Hervías-Caimapo, A. Bonaldi, and M. L. Brown. Impact of modelling foreground uncertainties on future CMB polarization satellite experiments. *ArXiv:1701.02277*, January 2017.

[137] J. Hickish, Z. Abdurashidova, Z. Ali, K. D. Buch, S. C. Chaudhari, H. Chen, M. Dexter, R. S. Domagalski, J. Ford, G. Foster, D. George, J. Greenberg, L. Greenhill, A. Isaacson, H. Jiang, G. Jones, F. Kapp, H. Kriel, R. Lacasse, A. Lutomirski, D. MacMahon, J. Manley, A. Martens, R. McCullough, M. V. Muley, W. New, A. Parsons, D. C. Price, R. A. Primiani, J. Ray, A. Siemion, V. van Tonder, L. Vertatschitsch, M. Wagner, J. Weintroub, and D. Werthimer. A Decade of Developing Radio-Astronomy Instrumentation using CASPER Open-Source Technology. *Journal of Astronomical Instrumentation*, 5:1641001-12, December 2016. doi: 10.1142/S2251171716410014.

[138] J. C. Hill, N. Battaglia, J. Chluba, S. Ferraro, E. Schaan, and D. N. Spergel. Taking the Universe's Temperature with Spectral Distortions of the Cosmic Microwave Background. *Physical Review Letters*, 115(26):261301, December 2015. doi: 10.1103/PhysRevLett.115.261301.

[139] G. Hinshaw, D. Larson, E. Komatsu, D. N. Spergel, C. L. Bennett, J. Dunkley, M. R. Nolta, M. Halpern, R. S. Hill, N. Odegard, L. Page, K. M. Smith, J. L. Weiland, B. Gold, N. Jarosik, A. Kogut, M. Limon, S. S. Meyer, G. S. Tucker, E. Wollack, and E. L. Wright. Nine-year Wilkinson Microwave Anisotropy Probe (WMAP) Observations: Cosmological Parameter Results. *ApJS*, 208:19, October 2013. doi: 10.1088/0067-0049/208/2/19.

[140] T. Hoang and A. Lazarian. A Unified Model of Grain Alignment: Radiative Alignment of Interstellar Grains with Magnetic Inclusions. *ApJ*, 831:159, November 2016. doi: 10.3847/0004-637X/831/2/159.

[141] W. Hu and S. Dodelson. Cosmic Microwave Background Anisotropies. *ARA&A*, 40: 171–216, 2002. doi: 10.1146/annurev.astro.40.060401.093926.

[142] W. Hu and J. Silk. Thermalization and spectral distortions of the cosmic background radiation. *Phys. Rev. D*, 48:485–502, July 1993. doi: 10.1103/PhysRevD.48.485.

[143] W. Hu and J. Silk. Thermalization constraints and spectral distortions for massive unstable relic particles. *Physical Review Letters*, 70:2661–2664, May 1993. doi: 10.1103/PhysRevLett.70.2661.

[144] W. Hu and N. Sugiyama. Anisotropies in the cosmic microwave background: an analytic approach. *ApJ*, 444:489–506, May 1995. doi: 10.1086/175624.

[145] W. Hu and M. White. CMB anisotropies: Total angular momentum method. *Phys. Rev. D*, 56:596–615, July 1997. doi: 10.1103/PhysRevD.56.596.

[146] W. Hu, D. Scott, and J. Silk. Power spectrum constraints from spectral distortions in the cosmic microwave background. *ApJ*, 430:L5–L8, July 1994. doi: 10.1086/187424.

[147] W. Hu, D. Scott, and J. Silk. Reionization and cosmic microwave background distortions: A complete treatment of second-order Compton scattering. *Phys. Rev. D*, 49: 648–670, January 1994. doi: 10.1103/PhysRevD.49.648.

[148] W. Hu, D. Scott, and J. Silk. Reionization and cosmic microwave background distortions: A complete treatment of second-order Compton scattering. *Phys. Rev. D*, 49: 648–670, January 1994. doi: 10.1103/PhysRevD.49.648.

[149] W. Hu, N. Sugiyama, and J. Silk. The physics of microwave background anisotropies. *Nature*, 386:37–43, March 1997. doi: 10.1038/386037a0.

[150] Wayne Hu, Matthew M. Hedman, and Matias Zaldarriaga. Benchmark parameters for cmb polarization experiments. *Phys. Rev. D*, 67(4):043004, Feb 2003. doi: 10.1103/PhysRevD.67.043004. URL http://link.aps.org/doi/10.1103/PhysRevD.67.043004.

[151] A. F. Illarionov and R. A. Sunyaev. Comptonization, the spectrum of RELICT radiation, and the thermal history of the universe. *Astronomicheskii Zhurnal*, 51:1162–1176, December 1974.

[152] N. Imara and A. Loeb. The Distortion of the Cosmic Microwave Background Spectrum Due to Intergalactic Dust. *ApJ*, 825:130, July 2016. doi: 10.3847/0004-637X/825/2/130.

[153] M. O. Irfan, C. Dickinson, R. D. Davies, C. Copley, R. J. Davis, P. G. Ferreira, C. M. Holler, J. L. Jonas, M. E. Jones, O. G. King, J. P. Leahy, J. Leech, E. M. Leitch, S. J. C. Muchovej, T. J. Pearson, M. W. Peel, A. C. S. Readhead, M. A. Stevenson, D. Sutton, A. C. Taylor, and J. Zuntz. C-Band All-Sky Survey: a first look at the Galaxy. *MNRAS*, 448:3572–3586, April 2015. doi: 10.1093/mnras/stv212.

[154] N. Itoh, Y. Kohyama, and S. Nozawa. Relativistic Corrections to the Sunyaev-Zeldovich Effect for Clusters of Galaxies. *ApJ*, 502:7–+, July 1998. doi: 10.1086/305876.

[155] D. Jeong, J. Pradler, J. Chluba, and M. Kamionkowski. Silk Damping at a Redshift of a Billion: New Limit on Small-Scale Adiabatic Perturbations. *Physical Review Letters*, 113(6):061301, August 2014. doi: 10.1103/PhysRevLett.113.061301.

[156] P. R. Jewell and R. M. Prestage. The green bank telescope. *Proc. SPIE*, 5489:5489 – 5489 – 12, 2004. doi: 10.1117/12.550631. URL http://dx.doi.org/10.1117/12.550631.

[157] B. R. Johnson, C. J. Vourch, T. D. Drysdale, A. Kalman, S. Fujikawa, B. Keating, and J. Kaufman. A CubeSat for Calibrating Ground-Based and Sub-Orbital Millimeter-Wave Polarimeters (CalSat). *Journal of Astronomical Instrumentation*, 4:1550007, October 2015. doi: 10.1142/S2251171715500075.

[158] B. R. Johnson, D. Flanigan, M. H. Abitbol, P. A. R. Ade, S. Bryan, H.-M. Cho, R. Datta, P. Day, S. Doyle, K. Irwin, G. Jones, S. Kernasovskiy, D. Li, P. Mauskopf, H. McCarrick, J. McMahon, A. Miller, G. Pisano, Y. Song, H. Surdi, and C. Tucker. Polarization sensitive Multi-Chroic MKIDs. In *Millimeter, Submillimeter, and Far-Infrared Detectors and Instrumentation for Astronomy VIII*, volume 9914 of *Proc. SPIE*, page 99140X, July 2016. doi: 10.1117/12.2233243.

[159] B. R. Johnson, D. Flanigan, M. H. Abitbol, P. A. R. Ade, S. Bryan, H.-M. Cho, R. Datta, P. Day, S. Doyle, K. Irwin, G. Jones, D. Li, P. Mauskopf, H. McCarrick, J. McMahon, A. Miller, G. Pisano, Y. Song, H. Surdi, and C. ˜Tucker. Development of Multi-Chroic MKIDs for Next-Generation CMB Polarization Studies. *ArXiv e-prints*, November 2017.

[160] G. Jones, B. R. Johnson, M. H. Abitbol, P. A. R. Ade, S. Bryan, H.-M. Cho, P. Day, D. Flanigan, K. D. Irwin, D. Li, P. Mauskopf, H. McCarrick, A. Miller, Y. R. Song, and C. Tucker. High quality factor manganese-doped aluminum lumped-element kinetic inductance detectors sensitive to frequencies below 100 GHz. *Applied Physics Letters*, 110(22):222601, May 2017. doi: 10.1063/1.4984105.

[161] M. E. Jones, A. C. Taylor, M. Aich, C. J. Copley, H. C. Chiang, R. J. Davis, C. Dickinson, R. D. P. Grumitt, Y. Hafez, H. M. Heilgendorff, C. M. Holler, M. O. Irfan, L. R. P. Jew, J. J. John, J. Jonas, O. G. King, J. P. Leahy, J. Leech, E. M. Leitch, S. J. C. Muchovej, T. J. Pearson, M. W. Peel, A. C. S. Readhead, J. Sievers, M. A. Stevenson, and J. Zuntz. The C-Band All-Sky Survey (C-BASS): Design and capabilities. *MNRAS*, July 2018. doi: 10.1093/mnras/sty1956.

[162] M. Kamionkowski, A. Kosowsky, and A. Stebbins. Statistics of cosmic microwave background polarization. *Phys. Rev. D.*, 55:7368–7388, June 1997. doi: 10.1103/PhysRevD.55.7368.

[163] D. Kandel, A. Lazarian, and D. Pogosyan. Statistical properties of Galactic CMB foregrounds: dust and synchrotron. *MNRAS*, 478:530–540, July 2018. doi: 10.1093/mnras/sty1115.

[164] J. P. Kaufman, N. J. Miller, M. Shimon, D. Barkats, C. Bischoff, I. Buder, B. G. Keating, J. M. Kovac, P. A. R. Ade, R. Aikin, J. O. Battle, E. M. Bierman, J. J. Bock, H. C. Chiang, C. D. Dowell, L. Duband, J. Filippini, E. F. Hivon, W. L. Holzapfel, V. V. Hristov, W. C. Jones, S. S. Kernasovskiy, C. L. Kuo, E. M. Leitch, P. V. Mason, T. Matsumura, H. T. Nguyen, N. Ponthieu, C. Pryke, S. Richter, G. Rocha, C. Sheehy, M. Su, Y. D. Takahashi, J. E. Tolan, and K. W. Yoon. Self-calibration of BICEP1 three-year data and constraints on astrophysical polarization rotation. *Phys. Rev. D*, 89(6):062006, March 2014. doi: 10.1103/PhysRevD.89.062006.

[165] D. Kazanas. Dynamics of the universe and spontaneous symmetry breaking. *ApJ*, 241: L59–L63, October 1980. doi: 10.1086/183361.

[166] D. Kazanas. Cosmological Inflation: A Personal Perspective. *Astrophysics and Space Science Proceedings*, 8:485, 2009. doi: 10.1007/978-3-540-75826-6_49.

[167] B. G. Keating, M. Shimon, and A. P. S. Yadav. Self-calibration of Cosmic Microwave Background Polarization Experiments. *ApJ*, 762:L23, January 2013. doi: 10.1088/2041-8205/762/2/L23.

[168] E. Keihänen, R. Keskitalo, H. Kurki-Suonio, T. Poutanen, and A.-S. Sirviö. Making cosmic microwave background temperature and polarization maps with MADAM. *A&A*, 510:A57, February 2010. doi: 10.1051/0004-6361/200912813.

[169] R. Keisler, C. L. Reichardt, K. A. Aird, B. A. Benson, L. E. Bleem, J. E. Carlstrom, C. L. Chang, H. M. Cho, T. M. Crawford, A. T. Crites, T. de Haan, M. A. Dobbs, J. Dudley, and E. M. George. A Measurement of the Damping Tail of the Cosmic Microwave Background Power Spectrum with the South Pole Telescope. *ApJ*, 743:28, December 2011. doi: 10.1088/0004-637X/743/1/28.

[170] R. Keisler, S. Hoover, N. Harrington, J. W. Henning, P. A. R. Ade, K. A. Aird, J. E. Austermann, J. A. Beall, A. N. Bender, B. A. Benson, L. E. Bleem, J. E. Carlstrom, C. L. Chang, H. C. Chiang, H.-M. Cho, R. Citron, T. M. Crawford, A. T. Crites, T. de Haan, M. A. Dobbs, W. Everett, J. Gallicchio, J. Gao, E. M. George, A. Gilbert, N. W. Halverson, D. Hanson, G. C. Hilton, G. P. Holder, W. L. Holzapfel, Z. Hou, J. D. Hrubes, N. Huang, J. Hubmayr, K. D. Irwin, L. Knox, A. T. Lee, E. M. Leitch, D. Li, D. Luong-Van, D. P. Marrone, J. J. McMahon, J. Mehl, S. S. Meyer, L. Mocanu, T. Natoli, J. P. Nibarger, V. Novosad, S. Padin, C. Pryke, C. L. Reichardt, J. E. Ruhl, B. R. Saliwanchik, J. T. Sayre, K. K. Schaffer, E. Shirokoff, G. Smecher, A. A. Stark, K. T. Story, C. Tucker, K. Vanderlinde, J. D. Vieira, G. Wang, N. Whitehorn, V. Yefremenko, and O. Zahn. Measurements of Sub-degree B-mode Polarization in the Cosmic Microwave Background from 100 Square Degrees of SPTpol Data. *ApJ*, 807: 151, July 2015. doi: 10.1088/0004-637X/807/2/151.

[171] R. Khatri and R. A. Sunyaev. Beyond y and μ: the shape of the CMB spectral distortions in the intermediate epoch, $1.5 \times 10^4 \lesssim$ z *lesssim*2×10^5. *J. Cosmology Astropart. Phys.*, 9:016, September 2012. doi: 10.1088/1475-7516/2012/09/016.

[172] A. Kogut and D. J. Fixsen. Foreground Bias from Parametric Models of Far-IR Dust Emission. *ApJ*, 826:101, August 2016. doi: 10.3847/0004-637X/826/2/101.

[173] A. Kogut, A. J. Banday, C. L. Bennett, K. M. Gorski, G. Hinshaw, and W. T. Reach. High-Latitude Galactic Emission in the COBE Differential Microwave Radiometer 2 Year Sky Maps. *ApJ*, 460:1, March 1996. doi: 10.1086/176947.

[174] A. Kogut, A. J. Banday, C. L. Bennett, K. M. Gorski, G. Hinshaw, G. F. Smoot, and E. I. Wright. Microwave Emission at High Galactic Latitudes in the Four-Year DMR Sky Maps. *ApJ*, 464:L5, June 1996. doi: 10.1086/310072.

[175] A. Kogut, D. Fixsen, S. Fixsen, S. Levin, M. Limon, L. Lowe, P. Mirel, M. Seiffert, J. Singal, P. Lubin, and E. Wollack. ARCADE: Absolute radiometer for cosmology, astrophysics, and diffuse emission. *New Astronomy Reviews*, 50:925–931, December 2006. doi: 10.1016/j.newar.2006.09.023.

[176] A. Kogut, D. J. Fixsen, D. T. Chuss, J. Dotson, E. Dwek, M. Halpern, G. F. Hinshaw, S. M. Meyer, S. H. Moseley, M. D. Seiffert, D. N. Spergel, and E. J. Wollack. The Primordial Inflation Explorer (PIXIE): a nulling polarimeter for cosmic microwave

background observations. *J. Cosmology Astropart. Phys.*, 7:25–+, July 2011. doi: 10.1088/1475-7516/2011/07/025.

[177] A. Kogut, D. J. Fixsen, S. M. Levin, M. Limon, P. M. Lubin, P. Mirel, M. Seiffert, J. Singal, T. Villela, E. Wollack, and C. A. Wuensche. ARCADE 2 Observations of Galactic Radio Emission. *ApJ*, 734:4–+, June 2011. doi: 10.1088/0004-637X/734/1/4.

[178] A. Kogut, J. Chluba, D. J. Fixsen, S. Meyer, and D. Spergel. The Primordial Inflation Explorer (PIXIE). In *Space Telescopes and Instrumentation 2016: Optical, Infrared, and Millimeter Wave*, volume 9904 of *Society of Photo-Optical Instrumentation Engineers (SPIE) Conference Series*, page 99040W, July 2016. doi: 10.1117/12.2231090.

[179] P. M. Korngut, S. R. Dicker, E. D. Reese, B. S. Mason, M. J. Devlin, T. Mroczkowski, C. L. Sarazin, M. Sun, and J. Sievers. MUSTANG High Angular Resolution Sunyaev-Zel'dovich Effect Imaging of Substructure in Four Galaxy Clusters. *ApJ*, 734:10, June 2011. doi: 10.1088/0004-637X/734/1/10.

[180] A. Kosowsky. Cosmic microwave background polarization. *Annals of Physics*, 246: 49–85, February 1996. doi: 10.1006/aphy.1996.0020.

[181] N. Krachmalnicoff, E. Carretti, C. Baccigalupi, G. Bernardi, S. Brown, B. M. Gaensler, M. Haverkorn, M. Kesteven, F. Perrotta, S. Poppi, and L. Staveley-Smith. The S-PASS view of polarized Galactic Synchrotron at 2.3 GHz as a contaminant to CMB observations. *ArXiv e-prints*, February 2018.

[182] H. Kurki-Suonio, E. Keihänen, R. Keskitalo, T. Poutanen, A.-S. Sirviö, D. Maino, and C. Burigana. Destriping CMB temperature and polarization maps. *A&A*, 506: 1511–1539, November 2009. doi: 10.1051/0004-6361/200912361.

[183] S. Kurtz. Ultracompact HII Regions. In P. Crowther, editor, *Hot Star Workshop III: The Earliest Phases of Massive Star Birth*, volume 267 of *Astronomical Society of the Pacific Conference Series*, page 81, October 2002.

[184] A. Lazarian and B. T. Draine. Resonance Paramagnetic Relaxation and Alignment of Small Grains. *ApJ*, 536:L15–L18, June 2000. doi: 10.1086/312720.

[185] E. M. Leitch, A. C. S. Readhead, T. J. Pearson, and S. T. Myers. An anomalous component of galactic emission. *The Astrophysical Journal Letters*, 486(1):L23, 1997. URL http://stacks.iop.org/1538-4357/486/i=1/a=L23.

[186] J. Lesgourgues. The Cosmic Linear Anisotropy Solving System (CLASS) III: Comparision with CAMB for LambdaCDM. *ArXiv e-prints*, April 2011.

[187] A. Lewis, A. Challinor, and A. Lasenby. Efficient Computation of Cosmic Microwave Background Anisotropies in Closed Friedmann-Robertson-Walker Models. *ApJ*, 538: 473–476, August 2000. doi: 10.1086/309179.

[188] Antony Lewis, Anthony Challinor, and Anthony Lasenby. Efficient computation of CMB anisotropies in closed FRW models. *Astrophys. J.*, 538:473–476, 2000.

[189] A. Li and B. T. Draine. Infrared Emission from Interstellar Dust. II. The Diffuse Interstellar Medium. *ApJ*, 554:778–802, June 2001. doi: 10.1086/323147.

[190] A. D. Linde. A new inflationary universe scenario: A possible solution of the horizon, flatness, homogeneity, isotropy and primordial monopole problems. *Physics Letters B*, 108:389–393, February 1982. doi: 10.1016/0370-2693(82)91219-9.

[191] N. Mashian, A. Loeb, and A. Sternberg. Spectral Distortion of the CMB by the Cumulative CO Emission from Galaxies throughout Cosmic History. *MNRAS*, February 2016. doi: 10.1093/mnrasl/slw027.

[192] J. C. Mather, E. S. Cheng, R. E. Eplee, Jr., R. B. Isaacman, S. S. Meyer, R. A. Shafer, R. Weiss, E. L. Wright, C. L. Bennett, N. W. Boggess, E. Dwek, S. Gulkis, M. G. Hauser, M. Janssen, T. Kelsall, P. M. Lubin, S. H. Moseley, Jr., T. L. Murdock, R. F. Silverberg, G. F. Smoot, and D. T. Wilkinson. A preliminary measurement of the cosmic microwave background spectrum by the Cosmic Background Explorer (COBE) satellite. *ApJ*, 354:L37–L40, May 1990. doi: 10.1086/185717.

[193] T. Matsumura, P. Ade, D. Barkats, D. Barron, J. O. Battle, E. M. Bierman, J. J. Bock, H. C. Chiang, B. P. Crill, C. D. Dowell, L. Duband, E. F. Hivon, W. L. Holzapfel, V. V. Hristov, W. C. Jones, B. G. Keating, J. M. Kovac, C.-l. Kuo, A. E. Lange, E. M. Leitch, P. V. Mason, H. T. Nguyen, N. Ponthieu, C. Pryke, S. Richter, G. M. Rocha, Y. D. Takahashi, and K. W. Yoon. Absolute polarization angle calibration using polarized diffuse Galactic emission observed by BICEP. In *Society of Photo-Optical Instrumentation Engineers (SPIE) Conference Series*, volume 7741 of *Society of Photo-Optical Instrumentation Engineers (SPIE) Conference Series*, page 2, July 2010. doi: 10.1117/12.856855.

[194] P. D. Mauskopf, S. Doyle, P. Barry, S. Rowe, A. Bidead, P. A. R. Ade, C. Tucker, E. Castillo, A. Monfardini, J. Goupy, and M. Calvo. Photon-Noise Limited Performance in Aluminum LEKIDs. *Journal of Low Temperature Physics*, 176:545–552, August 2014. doi: 10.1007/s10909-013-1069-1.

[195] B. A. Mazin. Microwave Kinetic Inductance Detectors: The First Decade. In B. Young, B. Cabrera, and A. Miller, editors, *American Institute of Physics Conference Series*, volume 1185 of *American Institute of Physics Conference Series*, pages 135–142, December 2009. doi: 10.1063/1.3292300.

[196] B. A. Mazin, P. K. Day, J. Zmuidzinas, and H. G. Leduc. Multiplexable kinetic inductance detectors. *Low Temperature Detectors*, 605:309–312, February 2002. doi: 10.1063/1.1457652.

[197] B. A. Mazin, P. K. Day, K. D. Irwin, C. D. Reintsema, and J. Zmuidzinas. Digital readouts for large microwave low-temperature detector arrays. *Nuclear Instruments and Methods in Physics Research A*, 559:799–801, April 2006. doi: 10.1016/j.nima.2005.12.208.

[198] H. McCarrick, D. Flanigan, G. Jones, B. R. Johnson, P. Ade, D. Araujo, K. Bradford, R. Cantor, G. Che, P. Day, S. Doyle, H. Leduc, M. Limon, V. Luu, P. Mauskopf, A. Miller, T. Mroczkowski, C. Tucker, and J. Zmuidzinas. Horn-coupled, commercially-fabricated aluminum lumped-element kinetic inductance detectors for millimeter wavelengths. *Review of Scientific Instruments*, 85(12):123117, December 2014. doi: 10.1063/1.4903855.

[199] H. McCarrick, M. H. Abitbol, P. A. R. Ade, P. Barry, S. Bryan, G. Che, P. Day, S. Doyle, D. Flanigan, B. R. Johnson, G. Jones, H. G. LeDuc, M. Limon, P. Mauskopf, A. Miller, C. Tucker, and J. Zmuidzinas. Development of dual-polarization LEKIDs for CMB observations. In *Millimeter, Submillimeter, and Far-Infrared Detectors and Instrumentation for Astronomy VIII*, volume 9914 of *Proc. SPIE*, page 99140O, July 2016. doi: 10.1117/12.2231830.

[200] H. McCarrick, G. Jones, B. R. Johnson, M. H. Abitbol, P. A. R. Ade, S. Bryan, P. Day, T. Essinger-Hileman, D. Flanigan, H. G. Leduc, M. Limon, P. Mauskopf, A. Miller, and C. Tucker. Design and performance of dual-polarization lumped-element kinetic inductance detectors for millimeter-wave polarimetry. *A&A*, 610:A45, February 2018. doi: 10.1051/0004-6361/201732044.

[201] P. McDonald, R. J. Scherrer, and T. P. Walker. Cosmic microwave background constraint on residual annihilations of relic particles. *Phys. Rev. D*, 63(2):023001–+, January 2001. doi: 10.1103/PhysRevD.63.023001.

[202] S. McHugh, B. A. Mazin, B. Serfass, S. Meeker, K. O'Brien, R. Duan, R. Raffanti, and D. Werthimer. A readout for large arrays of microwave kinetic inductance detectors. *Review of Scientific Instruments*, 83(4):044702–044702, April 2012. doi: 10.1063/1.3700812.

[203] A. M. Meisner and D. P. Finkbeiner. Modeling Thermal Dust Emission with Two Components: Application to the Planck High Frequency Instrument Maps. *ApJ*, 798:88, January 2015. doi: 10.1088/0004-637X/798/2/88.

[204] N. J. Miller, M. Shimon, and B. G. Keating. CMB polarization systematics due to beam asymmetry: Impact on cosmological birefringence. *Phys. Rev. D*, 79(10):103002, May 2009. doi: 10.1103/PhysRevD.79.103002.

[205] M.-A. Miville-Deschênes and G. Lagache. IRIS: A New Generation of IRAS Maps. *ApJS*, 157:302–323, April 2005. doi: 10.1086/427938.

[206] P. Mohan, A. Mangalam, and S. Chattopadhyay. Parametric Models of Periodogram. *Journal of Astrophysics and Astronomy*, 35:397–400, September 2014. doi: 10.1007/s12036-014-9240-x.

[207] I. Moskalenko. Modeling cosmic ray propagation and associated interstellar emissions. In *39th COSPAR Scientific Assembly*, volume 39 of *COSPAR Meeting*, page 1281, July 2012.

[208] T. Murphy, M. Cohen, R. D. Ekers, A. J. Green, R. M. Wark, and V. Moss. Ultra- and hyper-compact HII regions at 20 GHz. *MNRAS*, 405:1560–1572, July 2010. doi: 10.1111/j.1365-2966.2010.16589.x.

[209] S. Naess, M. Hasselfield, J. McMahon, M. D. Niemack, G. E. Addison, P. A. R. Ade, R. Allison, M. Amiri, N. Battaglia, J. A. Beall, F. de Bernardis, J. R. Bond, J. Britton, E. Calabrese, H.-m. Cho, K. Coughlin, D. Crichton, S. Das, R. Datta, M. J. Devlin, S. R. Dicker, J. Dunkley, R. Dünner, J. W. Fowler, A. E. Fox, P. Gallardo, E. Grace, M. Gralla, A. Hajian, M. Halpern, S. Henderson, J. C. Hill, G. C. Hilton, M. Hilton, A. D. Hincks, R. Hlozek, P. Ho, J. Hubmayr, K. M. Huffenberger, J. P. Hughes, L. Infante, K. Irwin, R. Jackson, S. Muya Kasanda, J. Klein, B. Koopman, A. Kosowsky, D. Li, T. Louis, M. Lungu, M. Madhavacheril, T. A. Marriage, L. Maurin, F. Menanteau, K. Moodley, C. Munson, L. Newburgh, J. Nibarger, M. R. Nolta, L. A. Page, C. Pappas, B. Partridge, F. Rojas, B. L. Schmitt, N. Sehgal, B. D. Sherwin, J. Sievers, S. Simon, D. N. Spergel, S. T. Staggs, E. R. Switzer, R. Thornton, H. Trac, C. Tucker, M. Uehara, A. Van Engelen, J. T. Ward, and E. J. Wollack. The Atacama Cosmology Telescope: CMB polarization at $200 < l < 9000$. *J. Cosmology Astropart. Phys.*, 10: 007, October 2014. doi: 10.1088/1475-7516/2014/10/007.

[210] C. B. Netterfield, P. A. R. Ade, J. J. Bock, J. R. Bond, J. Borrill, A. Boscaleri, K. Coble, C. R. Contaldi, B. P. Crill, P. de Bernardis, P. Farese, K. Ganga, M. Giacometti, E. Hivon, V. V. Hristov, A. Iacoangeli, and A. H. Jaffe. A Measurement by BOOMERANG of Multiple Peaks in the Angular Power Spectrum of the Cosmic Microwave Background. *ApJ*, 571:604–614, June 2002. doi: 10.1086/340118.

[211] G. M. Nita and D. E. Gary. The generalized spectral kurtosis estimator. *MNRAS*, 406:L60–L64, July 2010. doi: 10.1111/j.1745-3933.2010.00882.x.

[212] O. Noroozian. *Superconducting Microwave Resonator Arrays for Submillimeter/Far-Infrared Imaging*. PhD thesis, California Institute of Technology, 2012.

[213] S. Nozawa, N. Itoh, Y. Suda, and Y. Ohhata. An improved formula for the relativistic corrections to the kinematical Sunyaev-Zeldovich effect for clusters of galaxies. *Nuovo Cimento B Serie*, 121:487–500, May 2006. doi: 10.1393/ncb/i2005-10223-0.

[214] D. O'Dea, A. Challinor, and B. R. Johnson. Systematic errors in cosmic microwave background polarization measurements. *MNRAS*, 376:1767–1783, April 2007. doi: 10.1111/j.1365-2966.2007.11558.x.

[215] J. P. Ostriker and C. Thompson. Distortion of the cosmic background radiation by superconducting strings. *ApJ*, 323:L97–L101, December 1987. doi: 10.1086/185065.

[216] M. Ott, A. Witzel, A. Quirrenbach, T. P. Krichbaum, K. J. Standke, C. J. Schalinski, and C. A. Hummel. An updated list of radio flux density calibrators. *A&A*, 284: 331–339, April 1994.

[217] R. Paladini, A. Ingallinera, C. Agliozzo, C. T. Tibbs, A. Noriega-Crespo, G. Umana, C. Dickinson, and C. Trigilio. Anomalous Microwave Emission in HII Regions: Is

it Really Anomalous? The Case of RCW 49. *ApJ*, 813:24, November 2015. doi: 10.1088/0004-637X/813/1/24.

[218] I. E. Papadakis and A. Lawrence. Improved Methods for Power Spectrum Modelling of Red Noise. *MNRAS*, 261:612, April 1993. doi: 10.1093/mnras/261.3.612.

[219] S. C. Parshley, J. Kronshage, J. Blair, T. Herter, M. Nolta, G. J. Stacey, A. Bazarko, F. Bertoldi, R. Bustos, D. B. Campbell, S. Chapman, N. Cothard, M. Devlin, J. Erler, M. Fich, P. A. Gallardo, R. Giovanelli, U. Graf, S. Gramke, M. P. Haynes, R. Hills, M. Limon, J. G. Mangum, J. McMahon, M. D. Niemack, T. Nikola, M. Omlor, D. A. Riechers, K. Steeger, J. Stutzki, and E. M. Vavagiakis. CCAT-prime: a novel telescope for sub-millimeter astronomy. In *Society of Photo-Optical Instrumentation Engineers (SPIE) Conference Series*, volume 10700 of *Society of Photo-Optical Instrumentation Engineers (SPIE) Conference Series*, page 107005X, July 2018. doi: 10.1117/12.2314046.

[220] T. J. Pearson, B. S. Mason, A. C. S. Readhead, M. C. Shepherd, J. L. Sievers, P. S. Udomprasert, J. K. Cartwright, A. J. Farmer, S. Padin, S. T. Myers, J. R. Bond, C. R. Contaldi, U.-L. Pen, S. Prunet, D. Pogosyan, J. E. Carlstrom, J. Kovac, E. M. Leitch, C. Pryke, N. W. Halverson, W. L. Holzapfel, P. Altamirano, L. Bronfman, S. Casassus, J. May, and M. Joy. The Anisotropy of the Microwave Background to l = 3500: Mosaic Observations with the Cosmic Background Imager. *ApJ*, 591:556–574, July 2003. doi: 10.1086/375508.

[221] A. A. Penzias and R. W. Wilson. A Measurement of Excess Antenna Temperature at 4080 Mc/s. *ApJ*, 142:419–421, July 1965. doi: 10.1086/148307.

[222] R. A. Perley and B. J. Butler. An Accurate Flux Density Scale from 1 to 50 GHz. *ApJS*, 204:19, February 2013. doi: 10.1088/0067-0049/204/2/19.

[223] Y. C. Perrott, A. M. M. Scaife, N. Hurley-Walker, and K. J. B. Grainge. Investigating the Source of Planck-Detected AME: High-Resolution Observations at 15 GHz. *Advances in Astronomy*, 2013:354259, 2013. doi: 10.1155/2013/354259.

[224] Planck Collaboration, Ade, P. A. R., Aghanim, N., Arnaud, M., Ashdown, M., Aumont, J., Baccigalupi, C., Balbi, A., Banday, A. J., Barreiro, R. B., Bartlett, J. G., Battaner, E., Benabed, K., Beno??t, A., Bernard, J.-P., Bersanelli, M., Bhatia, R., Bock, J. J., Bonaldi, A., Bond, J. R., Borrill, J., Bouchet, F. R., Boulanger, F., Bucher, M., Burigana, C., Cabella, P., Cappellini, B., Cardoso, J.-F., Casassus, S., Catalano, A., Cay??n, L., Challinor, A., Chamballu, A., Chary, R.-R., Chen, X., Chiang, L.-Y., Chiang, C., Christensen, P. R., Clements, D. L., Colombi, S., Couchot, F., Coulais, A., Crill, B. P., Cuttaia, F., Danese, L., Davies, R. D., Davis, R. J., de Bernardis, P., de Gasperis, G., de Rosa, A., de Zotti, G., Delabrouille, J., Delouis, J.-M., Dickinson, C., Donzelli, S., Dor??, O., D??rl, U., Douspis, M., Dupac, X., Efstathiou, G., En??lin, T. A., Eriksen, H. K., Finelli, F., Forni, O., Frailis, M., Franceschi, E., Galeotta, S., Ganga, K., G??nova-Santos, R. T., Giard, M., Giardino, G., Giraud-H??raud, Y., Gonz??lez-Nuevo, J., G??rski, K. M., Gratton, S., Gregorio, A., Gruppuso, A.,

Hansen, F. K., Harrison, D., Helou, G., Henrot-Versill??, S., Herranz, D., Hildebrandt, S. R., Hivon, E., Hobson, M., Holmes, W. A., Hovest, W., Hoyland, R. J., Huffenberger, K. M., Jaffe, T. R., Jaffe, A. H., Jones, W. C., Juvela, M., Keih??nen, E., Keskitalo, R., Kisner, T. S., Kneissl, R., Knox, L., Kurki-Suonio, H., Lagache, G., L??hteenm??ki, A., Lamarre, J.-M., Lasenby, A., Laureijs, R. J., Lawrence, C. R., Leach, S., Leonardi, R., Lilje, P. B., Linden-V??rnle, M., L??pez-Caniego, M., Lubin, P. M., Mac??as-P??rez, J. F., MacTavish, C. J., Maffei, B., Maino, D., Mandolesi, N., Mann, R., Maris, M., Marshall, D. J., Mart??nez-Gonz??lez, E., Masi, S., Matarrese, S., Matthai, F., Mazzotta, P., McGehee, P., Meinhold, P. R., Melchiorri, A., Mendes, L., Mennella, A., Mitra, S., Miville-Desch??nes, M.-A., Moneti, A., Montier, L., Morgante, G., Mortlock, D., Munshi, D., Murphy, A., Naselsky, P., Natoli, P., Netterfield, C. B., N??rgaard-Nielsen, H. U., Noviello, F., Novikov, D., Novikov, I., O???Dwyer, I. J., Osborne, S., Pajot, F., Paladini, R., Partridge, B., Pasian, F., Patanchon, G., Pearson, T. J., Peel, M., Perdereau, O., Perotto, L., Perrotta, F., Piacentini, F., Piat, M., Plaszczynski, S., Platania, P., Pointecouteau, E., Polenta, G., Ponthieu, N., Poutanen, T., Pr??zeau, G., Procopio, P., Prunet, S., Puget, J.-L., Reach, W. T., Rebolo, R., Reich, W., Reinecke, M., Renault, C., Ricciardi, S., Riller, T., Ristorcelli, I., Rocha, G., Rosset, C., Rowan-Robinson, M., Rubi??o-Mart??n, J. A., Rusholme, B., Sandri, M., Santos, D., Savini, G., Scott, D., Seiffert, M. D., Shellard, P., Smoot, G. F., Starck, J.-L., Stivoli, F., Stolyarov, V., Stompor, R., Sudiwala, R., Sygnet, J.-F., Tauber, J. A., Terenzi, L., Toffolatti, L., Tomasi, M., Torre, J.-P., Tristram, M., Tuovinen, J., Umana, G., Valenziano, L., Varis, J., Verstraete, L., Vielva, P., Villa, F., Vittorio, N., Wade, L. A., Wandelt, B. D., Watson, R., Wilkinson, A., Ysard, N., Yvon, D., Zacchei, A., and Zonca, A. Planck early results. xx. new light on anomalous microwave emission from spinning dust grains??? *A&A*, 536:A20, 2011. doi: 10.1051/0004-6361/201116470. URL https://doi.org/10.1051/0004-6361/201116470.

[225] Planck Collaboration, R. Adam, P. A. R. Ade, N. Aghanim, M. Arnaud, J. Aumont, C. Baccigalupi, A. J. Banday, R. B. Barreiro, J. G. Bartlett, and et al. Planck intermediate results. XXX. The angular power spectrum of polarized dust emission at intermediate and high Galactic latitudes. *ArXiv e-prints*, September 2014.

[226] Planck Collaboration, P. A. R. Ade, N. Aghanim, M. I. R. Alves, C. Armitage-Caplan, M. Arnaud, M. Ashdown, F. Atrio-Barandela, J. Aumont, C. Baccigalupi, and et al. Planck 2013 results. XIII. Galactic CO emission. *A&A*, 571:A13, November 2014. doi: 10.1051/0004-6361/201321553.

[227] Planck Collaboration, P. A. R. Ade, N. Aghanim, F. Argüeso, C. Armitage-Caplan, M. Arnaud, M. Ashdown, F. Atrio-Barandela, J. Aumont, C. Baccigalupi, and et al. Planck 2013 results. XXVIII. The Planck Catalogue of Compact Sources. *A&A*, 571: A28, November 2014. doi: 10.1051/0004-6361/201321524.

[228] Planck Collaboration, P. A. R. Ade, N. Aghanim, C. Armitage-Caplan, M. Arnaud, M. Ashdown, F. Atrio-Barandela, J. Aumont, C. Baccigalupi, A. J. Banday, and et al. Planck 2013 results. XXX. Cosmic infrared background measure-

ments and implications for star formation. *A&A*, 571:A30, November 2014. doi: 10.1051/0004-6361/201322093.

[229] Planck Collaboration, P. A. R. Ade, N. Aghanim, C. Armitage-Caplan, M. Arnaud, M. Ashdown, F. Atrio-Barandela, J. Aumont, C. Baccigalupi, A. J. Banday, and et al. Planck 2013 results. XIV. Zodiacal emission. *A&A*, 571:A14, November 2014. doi: 10.1051/0004-6361/201321562.

[230] Planck Collaboration, Ade, P. A. R., Aghanim, N., Alves, M. I. R., Arnaud, M., Atrio-Barandela, F., Aumont, J., Baccigalupi, C., Banday, A. J., Barreiro, R. B., Battaner, E., Benabed, K., Benoit-L??vy, A., Bernard, J.-P., Bersanelli, M., Bielewicz, P., Bobin, J., Bonaldi, A., Bond, J. R., Borrill, J., Bouchet, F. R., Boulanger, F., Burigana, C., Cardoso, J.-F., Casassus, S., Catalano, A., Chamballu, A., Chen, X., Chiang, H. C., Chiang, L.-Y., Christensen, P. R., Clements, D. L., Colombi, S., Colombo, L. P. L., Couchot, F., Crill, B. P., Cuttaia, F., Danese, L., Davies, R. D., Davis, R. J., de Bernardis, P., de Rosa, A., de Zotti, G., Delabrouille, J., D??sert, F.-X., Dickinson, C., Diego, J. M., Donzelli, S., Dor??, O., Dupac, X., En??lin, T. A., Eriksen, H. K., Finelli, F., Forni, O., Franceschi, E., Galeotta, S., Ganga, K., G??nova-Santos, R. T., Ghosh, T., Giard, M., Gonz??lez-Nuevo, J., G??rski, K. M., Gregorio, A., Gruppuso, A., Hansen, F. K., Harrison, D. L., Helou, G., Hern??ndez-Monteagudo, C., Hildebrandt, S. R., Hivon, E., Hobson, M., Hornstrup, A., Jaffe, A. H., Jaffe, T. R., Jones, W. C., Keih??nen, E., Keskitalo, R., Kneissl, R., Knoche, J., Kunz, M., Kurki-Suonio, H., L??hteenm??ki, A., Lamarre, J.-M., Lasenby, A., Lawrence, C. R., Leonardi, R., Liguori, M., Lilje, P. B., Linden-V??rnle, M., L??pez-Caniego, M., Mac??as-P??rez, J. F., Maffei, B., Maino, D., Mandolesi, N., Marshall, D. J., Martin, P. G., Mart??nez-Gonz??lez, E., Masi, S., Massardi, M., Matarrese, S., Mazzotta, P., Meinhold, P. R., Melchiorri, A., Mendes, L., Mennella, A., Migliaccio, M., Miville-Desch??nes, M.-A., Moneti, A., Montier, L., Morgante, G., Mortlock, D., Munshi, D., Naselsky, P., Nati, F., Natoli, P., N??rgaard-Nielsen, H. U., Noviello, F., Novikov, D., Novikov, I., Oxborrow, C. A., Pagano, L., Pajot, F., Paladini, R., Paoletti, D., Patanchon, G., Pearson, T. J., Peel, M., Perdereau, O., Perrotta, F., Piacentini, F., Piat, M., Pierpaoli, E., Pietrobon, D., Plaszczynski, S., Pointecouteau, E., Polenta, G., Ponthieu, N., Popa, L., Pratt, G. W., Prunet, S., Puget, J.-L., Rachen, J. P., Rebolo, R., Reich, W., Reinecke, M., Remazeilles, M., Renault, C., Ricciardi, S., Riller, T., Ristorcelli, I., Rocha, G., Rosset, C., Roudier, G., Rubi??o-Mart??n, J. A., Rusholme, B., Sandri, M., Savini, G., Scott, D., Spencer, L. D., Stolyarov, V., Sutton, D., Suur-Uski, A.-S., Sygnet, J.-F., Tauber, J. A., Tavagnacco, D., Terenzi, L., Tibbs, C. T., Toffolatti, L., Tomasi, M., Tristram, M., Tucci, M., Valenziano, L., Valiviita, J., Van Tent, B., Varis, J., Verstraete, L., Vielva, P., Villa, F., Wandelt, B. D., Watson, R., Wilkinson, A., Ysard, N., Yvon, D., Zacchei, A., and Zonca, A. Planck intermediate results. xv. a study of anomalous microwave emission in galactic clouds. *A&A*, 565:A103, 2014. doi: 10.1051/0004-6361/201322612. URL https://doi.org/10.1051/0004-6361/201322612.

[231] Planck Collaboration, P. A. R. Ade, N. Aghanim, M. Arnaud, F. Arroja, M. Ashdown,

J. Aumont, C. Baccigalupi, M. Ballardini, A. J. Banday, and et al. Planck 2015 results. XIX. Constraints on primordial magnetic fields. *ArXiv e-prints*, February 2015.

[232] Planck Collaboration, P. A. R. Ade, N. Aghanim, M. Arnaud, M. Ashdown, J. Aumont, C. Baccigalupi, A. J. Banday, R. B. Barreiro, J. G. Bartlett, and et al. Planck 2015 results. XIII. Cosmological parameters. *ArXiv:1502.01589*, February 2015.

[233] Planck Collaboration, N. Aghanim, M. Arnaud, M. Ashdown, J. Aumont, C. Baccigalupi, A. J. Banday, R. B. Barreiro, J. G. Bartlett, N. Bartolo, and et al. Planck 2015 results. XI. CMB power spectra, likelihoods, and robustness of parameters. *ArXiv e-prints*, July 2015.

[234] Planck Collaboration, R. Adam, P. A. R. Ade, N. Aghanim, Y. Akrami, M. I. R. Alves, F. Argüeso, M. Arnaud, F. Arroja, M. Ashdown, and et al. Planck 2015 results. I. Overview of products and scientific results. *A&A*, 594:A1, September 2016. doi: 10.1051/0004-6361/201527101.

[235] Planck Collaboration, R. Adam, P. A. R. Ade, N. Aghanim, M. I. R. Alves, M. Arnaud, M. Ashdown, J. Aumont, C. Baccigalupi, A. J. Banday, and et al. Planck 2015 results. X. Diffuse component separation: Foreground maps. *A&A*, 594:A10, September 2016. doi: 10.1051/0004-6361/201525967.

[236] Planck Collaboration, P. A. R. Ade, N. Aghanim, M. I. R. Alves, M. Arnaud, M. Ashdown, J. Aumont, C. Baccigalupi, A. J. Banday, R. B. Barreiro, and et al. Planck 2015 results. XXV. Diffuse low-frequency Galactic foregrounds. *A&A*, 594:A25, September 2016. doi: 10.1051/0004-6361/201526803.

[237] Planck Collaboration, N. Aghanim, Y. Akrami, M. I. R. Alves, M. Ashdown, J. Aumont, C. Baccigalupi, M. Ballardini, A. J. Banday, R. B. Barreiro, N. Bartolo, S. Basak, K. Benabed, J.-P. Bernard, M. Bersanelli, P. Bielewicz, J. J. Bock, J. R. Bond, J. Borrill, F. R. Bouchet, F. Boulanger, A. Bracco, M. Bucher, C. Burigana, E. Calabrese, J.-F. Cardoso, J. Carron, R.-R. Chary, H. C. Chiang, L. P. L. Colombo, C. Combet, B. P. Crill, F. Cuttaia, P. de Bernardis, G. de Zotti, J. Delabrouille, J.-M. Delouis, E. Di Valentino, C. Dickinson, J. M. Diego, O. Doré, M. Douspis, A. Ducout, X. Dupac, G. Efstathiou, F. Elsner, T. A. Enßlin, H. K. Eriksen, Y. Fantaye, R. Fernandez-Cobos, K. Ferrière, F. Forastieri, M. Frailis, A. A. Fraisse, E. Franceschi, A. Frolov, S. Galeotta, S. Galli, K. Ganga, R. T. Génova-Santos, M. Gerbino, T. Ghosh, J. González-Nuevo, K. M. Górski, S. Gratton, G. Green, A. Gruppuso, J. E. Gudmundsson, V. Guillet, W. Handley, F. K. Hansen, G. Helou, D. Herranz, E. Hivon, Z. Huang, A. H. Jaffe, W. C. Jones, E. Keihänen, R. Keskitalo, K. Kiiveri, J. Kim, N. Krachmalnicoff, M. Kunz, H. Kurki-Suonio, G. Lagache, J.-M. Lamarre, A. Lasenby, M. Lattanzi, C. R. Lawrence, M. Le Jeune, F. Levrier, M. Liguori, P. B. Lilje, V. Lindholm, M. López-Caniego, P. M. Lubin, Y.-Z. Ma, J. F. Macías-Pérez, G. Maggio, D. Maino, N. Mandolesi, A. Mangilli, A. Marcos-Caballero, M. Maris, P. G. Martin, E. Martínez-González, S. Matarrese, N. Mauri, J. D. McEwen, A. Melchiorri, A. Mennella, M. Migliaccio, M.-A. Miville-Deschênes, D. Molinari, A. Moneti, L. Montier, G. Morgante, A. Moss, P. Natoli, L. Pagano, D. Paoletti, G. Patanchon, F. Perrotta,

V. Pettorino, F. Piacentini, L. Polastri, G. Polenta, J.-L. Puget, J. P. Rachen, M. Reinecke, M. Remazeilles, A. Renzi, I. Ristorcelli, G. Rocha, C. Rosset, G. Roudier, J. A. Rubiño-Martín, B. Ruiz-Granados, L. Salvati, M. Sandri, M. Savelainen, D. Scott, C. Sirignano, R. Sunyaev, A.-S. Suur-Uski, J. A. Tauber, D. Tavagnacco, M. Tenti, L. Toffolatti, M. Tomasi, T. Trombetti, J. Valiviita, B. Van Tent, P. Vielva, F. Villa, N. Vittorio, B. D. Wandelt, I. K. Wehus, A. Zacchei, and A. Zonca. Planck 2018 results. XII. Galactic astrophysics using polarized dust emission. *ArXiv e-prints*, July 2018.

[238] Planck Collaboration, N. Aghanim, Y. Akrami, M. Ashdown, J. Aumont, C. Baccigalupi, M. Ballardini, A. J. Banday, R. B. Barreiro, N. Bartolo, S. Basak, R. Battye, K. Benabed, J.-P. Bernard, M. Bersanelli, P. Bielewicz, J. J. Bock, J. R. Bond, J. Borrill, F. R. Bouchet, F. Boulanger, M. Bucher, C. Burigana, R. C. Butler, E. Calabrese, J.-F. Cardoso, J. Carron, A. Challinor, H. C. Chiang, J. Chluba, L. P. L. Colombo, C. Combet, D. Contreras, B. P. Crill, F. Cuttaia, P. de Bernardis, G. de Zotti, J. Delabrouille, J.-M. Delouis, E. Di Valentino, J. M. Diego, O. Doré, M. Douspis, A. Ducout, X. Dupac, S. Dusini, G. Efstathiou, F. Elsner, T. A. Enßlin, H. K. Eriksen, Y. Fantaye, M. Farhang, J. Fergusson, R. Fernandez-Cobos, F. Finelli, F. Forastieri, M. Frailis, E. Franceschi, A. Frolov, S. Galeotta, S. Galli, K. Ganga, R. T. Génova-Santos, M. Gerbino, T. Ghosh, J. González-Nuevo, K. M. Górski, S. Gratton, A. Gruppuso, J. E. Gudmundsson, J. Hamann, W. Handley, D. Herranz, E. Hivon, Z. Huang, A. H. Jaffe, W. C. Jones, A. Karakci, E. Keihänen, R. Keskitalo, K. Kiiveri, J. Kim, T. S. Kisner, L. Knox, N. Krachmalnicoff, M. Kunz, H. Kurki-Suonio, G. Lagache, J.-M. Lamarre, A. Lasenby, M. Lattanzi, C. R. Lawrence, M. Le Jeune, P. Lemos, J. Lesgourgues, F. Levrier, A. Lewis, M. Liguori, P. B. Lilje, M. Lilley, V. Lindholm, M. López-Caniego, P. M. Lubin, Y.-Z. Ma, J. F. Macías-Pérez, G. Maggio, D. Maino, N. Mandolesi, A. Mangilli, A. Marcos-Caballero, M. Maris, P. G. Martin, M. Martinelli, E. Martínez-González, S. Matarrese, N. Mauri, J. D. McEwen, P. R. Meinhold, A. Melchiorri, A. Mennella, M. Migliaccio, M. Millea, S. Mitra, M.-A. Miville-Deschênes, D. Molinari, L. Montier, G. Morgante, A. Moss, P. Natoli, H. U. Nørgaard-Nielsen, L. Pagano, D. Paoletti, B. Partridge, G. Patanchon, H. V. Peiris, F. Perrotta, V. Pettorino, F. Piacentini, L. Polastri, G. Polenta, J.-L. Puget, J. P. Rachen, M. Reinecke, M. Remazeilles, A. Renzi, G. Rocha, C. Rosset, G. Roudier, J. A. Rubiño-Martín, B. Ruiz-Granados, L. Salvati, M. Sandri, M. Savelainen, D. Scott, E. P. S. Shellard, C. Sirignano, G. Sirri, L. D. Spencer, R. Sunyaev, A.-S. Suur-Uski, J. A. Tauber, D. Tavagnacco, M. Tenti, L. Toffolatti, M. Tomasi, T. Trombetti, L. Valenziano, J. Valiviita, B. Van Tent, L. Vibert, P. Vielva, F. Villa, N. Vittorio, B. D. Wandelt, I. K. Wehus, M. White, S. D. M. White, A. Zacchei, and A. Zonca. Planck 2018 results. VI. Cosmological parameters. *ArXiv e-prints*, July 2018.

[239] Planck Collaboration, Y. Akrami, F. Arroja, M. Ashdown, J. Aumont, C. Baccigalupi, M. Ballardini, A. J. Banday, R. B. Barreiro, N. Bartolo, S. Basak, R. Battye, K. Benabed, J.-P. Bernard, M. Bersanelli, P. Bielewicz, J. J. Bock, J. R. Bond, J. Borrill, F. R. Bouchet, F. Boulanger, M. Bucher, C. Burigana, R. C. Butler, E. Calabrese, J.-F. Cardoso, J. Carron, B. Casaponsa, A. Challinor, H. C. Chiang, L. P. L. Colombo, C. Com-

bet, D. Contreras, B. P. Crill, F. Cuttaia, P. de Bernardis, G. de Zotti, J. Delabrouille, J.-M. Delouis, F.-X. Désert, E. Di Valentino, C. Dickinson, J. M. Diego, S. Donzelli, O. Doré, M. Douspis, A. Ducout, X. Dupac, G. Efstathiou, F. Elsner, T. A. Enßlin, H. K. Eriksen, E. Falgarone, Y. Fantaye, J. Fergusson, R. Fernandez-Cobos, F. Finelli, F. Forastieri, M. Frailis, E. Franceschi, A. Frolov, S. Galeotta, S. Galli, K. Ganga, R. T. Génova-Santos, M. Gerbino, T. Ghosh, J. González-Nuevo, K. M. Górski, S. Gratton, A. Gruppuso, J. E. Gudmundsson, J. Hamann, W. Handley, F. K. Hansen, G. Helou, D. Herranz, E. Hivon, Z. Huang, A. H. Jaffe, W. C. Jones, A. Karakci, E. Keihänen, R. Keskitalo, K. Kiiveri, J. Kim, T. S. Kisner, L. Knox, N. Krachmalnicoff, M. Kunz, H. Kurki-Suonio, G. Lagache, J.-M. Lamarre, M. Langer, A. Lasenby, M. Lattanzi, C. R. Lawrence, M. Le Jeune, J. P. Leahy, J. Lesgourgues, F. Levrier, A. Lewis, M. Liguori, P. B. Lilje, M. Lilley, V. Lindholm, M. López-Caniego, P. M. Lubin, Y.-Z. Ma, J. F. Macías-Pérez, G. Maggio, D. Maino, N. Mandolesi, A. Mangilli, A. Marcos-Caballero, M. Maris, P. G. Martin, E. Martínez-González, S. Matarrese, N. Mauri, J. D. McEwen, P. D. Meerburg, P. R. Meinhold, A. Melchiorri, A. Mennella, M. Migliaccio, M. Millea, S. Mitra, M.-A. Miville-Deschênes, D. Molinari, A. Moneti, L. Montier, G. Morgante, A. Moss, S. Mottet, M. Münchmeyer, P. Natoli, H. U. Nørgaard-Nielsen, C. A. Oxborrow, L. Pagano, D. Paoletti, B. Partridge, G. Patanchon, T. J. Pearson, M. Peel, H. V. Peiris, F. Perrotta, V. Pettorino, F. Piacentini, L. Polastri, G. Polenta, J.-L. Puget, J. P. Rachen, M. Reinecke, M. Remazeilles, A. Renzi, G. Rocha, C. Rosset, G. Roudier, J. A. Rubiño-Martín, B. Ruiz-Granados, L. Salvati, M. Sandri, M. Savelainen, D. Scott, E. P. S. Shellard, M. Shiraishi, C. Sirignano, G. Sirri, L. D. Spencer, R. Sunyaev, A.-S. Suur-Uski, J. A. Tauber, D. Tavagnacco, M. Tenti, L. Terenzi, L. Toffolatti, M. Tomasi, T. Trombetti, J. Valiviita, B. Van Tent, L. Vibert, P. Vielva, F. Villa, N. Vittorio, B. D. Wandelt, I. K. Wehus, M. White, S. D. M. White, A. Zacchei, and A. Zonca. Planck 2018 results. I. Overview and the cosmological legacy of Planck. *ArXiv e-prints*, July 2018.

[240] Planck Collaboration, Y. Akrami, M. Ashdown, J. Aumont, C. Baccigalupi, M. Ballardini, A. J. Banday, R. B. Barreiro, N. Bartolo, S. Basak, K. Benabed, J.-P. Bernard, M. Bersanelli, P. Bielewicz, J. R. Bond, J. Borrill, F. R. Bouchet, F. Boulanger, A. Bracco, M. Bucher, C. Burigana, E. Calabrese, J.-F. Cardoso, J. Carron, H. C. Chiang, C. Combet, B. P. Crill, P. de Bernardis, G. de Zotti, J. Delabrouille, J.-M. Delouis, E. Di Valentino, C. Dickinson, J. M. Diego, A. Ducout, X. Dupac, G. Efstathiou, F. Elsner, T. A. Enßlin, E. Falgarone, Y. Fantaye, K. Ferrière, F. Finelli, F. Forastieri, M. Frailis, A. A. Fraisse, E. Franceschi, A. Frolov, S. Galeotta, S. Galli, K. Ganga, R. T. Génova-Santos, T. Ghosh, J. González-Nuevo, K. M. Górski, A. Gruppuso, J. E. Gudmundsson, V. Guillet, W. Handley, F. K. Hansen, D. Herranz, Z. Huang, A. H. Jaffe, W. C. Jones, E. Keihänen, R. Keskitalo, K. Kiiveri, J. Kim, N. Krachmalnicoff, M. Kunz, H. Kurki-Suonio, J.-M. Lamarre, A. Lasenby, M. Le Jeune, F. Levrier, M. Liguori, P. B. Lilje, V. Lindholm, M. López-Caniego, P. M. Lubin, Y.-Z. Ma, J. F. Macías-Pérez, G. Maggio, D. Maino, N. Mandolesi, A. Mangilli, P. G. Martin, E. Martínez-González, S. Matarrese, J. D. McEwen, P. R. Meinhold, A. Melchiorri, M. Migliaccio, M.-A. Miville-Deschênes, D. Molinari, A. Moneti, L. Montier, G. Morgante, P. Natoli, L. Pagano, D. Paoletti, V. Pettorino, F. Piacentini, G. Polenta, J.-L.

Puget, J. P. Rachen, M. Reinecke, M. Remazeilles, A. Renzi, G. Rocha, C. Rosset, G. Roudier, J. A. Rubiño-Martín, B. Ruiz-Granados, L. Salvati, M. Sandri, M. Savelainen, D. Scott, J. D. Soler, L. D. Spencer, J. A. Tauber, D. Tavagnacco, L. Toffolatti, M. Tomasi, T. Trombetti, J. Valiviita, F. Vansyngel, F. Van Tent, P. Vielva, F. Villa, N. Vittorio, I. K. Wehus, A. Zacchei, and A. Zonca. Planck 2018 results. XI. Polarized dust foregrounds. *ArXiv e-prints*, January 2018.

[241] Planck Collaboration, Y. Akrami, M. Ashdown, J. Aumont, C. Baccigalupi, M. Ballardini, A. J. Banday, R. B. Barreiro, N. Bartolo, S. Basak, K. Benabed, M. Bersanelli, P. Bielewicz, J. R. Bond, J. Borrill, F. R. Bouchet, F. Boulanger, M. Bucher, C. Burigana, E. Calabrese, J.-F. Cardoso, J. Carron, B. Casaponsa, A. Challinor, L. P. L. Colombo, C. Combet, B. P. Crill, F. Cuttaia, P. de Bernardis, A. de Rosa, G. de Zotti, J. Delabrouille, J.-M. Delouis, E. Di Valentino, C. Dickinson, J. M. Diego, S. Donzelli, O. Doré, A. Ducout, X. Dupac, G. Efstathiou, F. Elsner, T. A. Enßlin, H. K. Eriksen, E. Falgarone, R. Fernandez-Cobos, F. Finelli, F. Forastieri, M. Frailis, A. A. Fraisse, E. Franceschi, A. Frolov, S. Galeotta, S. Galli, K. Ganga, R. T. Génova-Santos, M. Gerbino, T. Ghosh, J. González-Nuevo, K. M. Górski, S. Gratton, A. Gruppuso, J. E. Gudmundsson, W. Handley, F. K. Hansen, G. Helou, D. Herranz, Z. Huang, A. H. Jaffe, A. Karakci, E. Keihänen, R. Keskitalo, K. Kiiveri, J. Kim, T. S. Kisner, N. Krachmalnicoff, M. Kunz, H. Kurki-Suonio, G. Lagache, J.-M. Lamarre, A. Lasenby, M. Lattanzi, C. R. Lawrence, M. Le Jeune, F. Levrier, M. Liguori, P. B. Lilje, V. Lindholm, M. López-Caniego, P. M. Lubin, Y.-Z. Ma, J. F. Macías-Pérez, G. Maggio, D. Maino, N. Mandolesi, A. Mangilli, A. Marcos-Caballero, P. G. Martin, E. Martínez-González, S. Matarrese, N. Mauri, J. D. McEwen, P. R. Meinhold, A. Melchiorri, A. Mennella, M. Migliaccio, M.-A. Miville-Deschênes, D. Molinari, A. Moneti, L. Montier, G. Morgante, P. Natoli, F. Oppizzi, L. Pagano, D. Paoletti, B. Partridge, M. Peel, V. Pettorino, F. Piacentini, G. Polenta, J.-L. Puget, J. P. Rachen, M. Reinecke, M. Remazeilles, A. Renzi, G. Rocha, G. Roudier, J. A. Rubiño-Martín, B. Ruiz-Granados, L. Salvati, M. Sandri, M. Savelainen, D. Scott, D. S. Seljebotn, C. Sirignano, L. D. Spencer, A.-S. Suur-Uski, J. A. Tauber, D. Tavagnacco, M. Tenti, H. Thommesen, L. Toffolatti, M. Tomasi, T. Trombetti, J. Valiviita, B. Van Tent, P. Vielva, F. Villa, N. Vittorio, B. D. Wandelt, I. K. Wehus, A. Zacchei, and A. Zonca. Planck 2018 results. IV. Diffuse component separation. *ArXiv e-prints*, July 2018.

[242] J. Poh and S. Dodelson. Line-of-sight extrapolation noise in dust polarization. *Phys. Rev. D*, 95(10):103511, May 2017. doi: 10.1103/PhysRevD.95.103511.

[243] POLARBEAR Collaboration, P. A. R. Ade, K. Arnold, M. Atlas, C. Baccigalupi, D. Barron, D. Boettger, J. Borrill, S. Chapman, Y. Chinone, A. Cukierman, M. Dobbs, A. Ducout, R. Dunner, T. Elleflot, J. Errard, G. Fabbian, S. Feeney, C. Feng, A. Gilbert, N. Goeckner-Wald, J. Groh, G. Hall, N. W. Halverson, M. Hasegawa, K. Hattori, M. Hazumi, C. Hill, W. L. Holzapfel, Y. Hori, L. Howe, Y. Inoue, G. C. Jaehnig, A. H. Jaffe, O. Jeong, N. Katayama, J. P. Kaufman, B. Keating, Z. Kermish, R. Keskitalo, T. Kisner, A. Kusaka, M. Le Jeune, A. T. Lee, E. M. Leitch, D. Leon, Y. Li, E. Linder, L. Lowry, F. Matsuda, T. Matsumura, N. Miller, J. Montgomery, M. J. Myers, M. Navaroli, H. Nishino, T. Okamura, H. Paar, J. Peloton, L. Pogosian,

D. Poletti, G. Puglisi, C. Raum, G. Rebeiz, C. L. Reichardt, P. L. Richards, C. Ross, K. M. Rotermund, D. E. Schenck, B. D. Sherwin, M. Shimon, I. Shirley, P. Siritanasak, G. Smecher, N. Stebor, B. Steinbach, A. Suzuki, J.-i. Suzuki, O. Tajima, S. Takakura, A. Tikhomirov, T. Tomaru, N. Whitehorn, B. Wilson, A. Yadav, A. Zahn, and O. Zahn. POLARBEAR Constraints on Cosmic Birefringence and Primordial Magnetic Fields. *ArXiv e-prints*, September 2015.

[244] R. M. Prestage, M. Bloss, J. Brandt, H. Chen, R. Creager, P. Demorest, J. Ford, G. Jones, A. A. Kepley, A. Kobelski, P. Marganian, M. Mello, D. McMahon, R. McCullough, J. Ray, D. A. Roshi, D. Werthimer, and M. Whitehead. The versatile gbt astronomical spectrometer (vegas): Current status and future plans. In *2015 USNC-URSI Radio Science Meeting (Joint with AP-S Symposium)*, pages 294–294, July 2015. doi: 10.1109/USNC-URSI.2015.7303578.

[245] J. G. Proakis and D. G. Manolakis. *Digital signal processing: principles, algorithms, and applications*. 1996.

[246] G. Puglisi, V. Galluzzi, L. Bonavera, J. Gonzalez-Nuevo, A. Lapi, M. Massardi, F. Perrotta, C. Baccigalupi, A. Celotti, and L. Danese. Forecasting Polarized Radio Sources for CMB observations. *ArXiv e-prints*, December 2017.

[247] QUIET Collaboration, D. Araujo, C. Bischoff, A. Brizius, I. Buder, Y. Chinone, K. Cleary, R. N. Dumoulin, A. Kusaka, R. Monsalve, S. K. Næss, L. B. Newburgh, R. Reeves, I. K. Wehus, J. T. L. Zwart, L. Bronfman, R. Bustos, S. E. Church, C. Dickinson, H. K. Eriksen, T. Gaier, J. O. Gundersen, M. Hasegawa, M. Hazumi, K. M. Huffenberger, K. Ishidoshiro, M. E. Jones, P. Kangaslahti, D. J. Kapner, D. Kubik, C. R. Lawrence, M. Limon, J. J. McMahon, A. D. Miller, M. Nagai, H. Nguyen, G. Nixon, T. J. Pearson, L. Piccirillo, S. J. E. Radford, A. C. S. Readhead, J. L. Richards, D. Samtleben, M. Seiffert, M. C. Shepherd, K. M. Smith, S. T. Staggs, O. Tajima, K. L. Thompson, K. Vanderlinde, and R. Williamson. Second Season QUIET Observations: Measurements of the Cosmic Microwave Background Polarization Power Spectrum at 95 GHz. *ApJ*, 760:145, December 2012. doi: 10.1088/0004-637X/760/2/145.

[248] A. Refregier and et al. Power spectrum of the Sunyaev-Zel'dovich effect. *Phys. Rev. D*, 61(12):123001, June 2000. doi: 10.1103/PhysRevD.61.123001.

[249] P. Reich and W. Reich. A radio continuum survey of the northern sky at 1420 MHz. II. *A&AS*, 63:205–288, February 1986.

[250] P. Reich and W. Reich. A map of spectral indices of the Galactic radio continuum emission between 408 MHz and 1420 MHz for the entire northern sky. *A&AS*, 74:7–23, July 1988.

[251] P. Reich, J. C. Testori, and W. Reich. A radio continuum survey of the southern sky at 1420 MHz. The atlas of contour maps. *A&A*, 376:861–877, September 2001. doi: 10.1051/0004-6361:20011000.

[252] W. Reich. A radio continuum survey of the northern sky at 1420 MHz. I. *A&AS*, 48: 219–297, May 1982.

[253] C. L. Reichardt, P. A. R. Ade, J. J. Bock, J. R. Bond, J. A. Brevik, C. R. Contaldi, M. D. Daub, J. T. Dempsey, J. H. Goldstein, W. L. Holzapfel, C. L. Kuo, A. E. Lange, M. Lueker, M. Newcomb, J. B. Peterson, J. Ruhl, M. C. Runyan, and Z. Staniszewski. High-Resolution CMB Power Spectrum from the Complete ACBAR Data Set. *ApJ*, 694:1200–1219, April 2009. doi: 10.1088/0004-637X/694/2/1200.

[254] M. Remazeilles, C. Dickinson, A. J. Banday, M.-A. Bigot-Sazy, and T. Ghosh. An improved source-subtracted and destriped 408-MHz all-sky map. *MNRAS*, 451:4311–4327, August 2015. doi: 10.1093/mnras/stv1274.

[255] M. Remazeilles, C. Dickinson, H. K. K. Eriksen, and I. K. Wehus. Sensitivity and foreground modelling for large-scale cosmic microwave background B-mode polarization satellite missions. *MNRAS*, 458:2032–2050, May 2016. doi: 10.1093/mnras/stw441.

[256] M. Remazeilles, A. J. Banday, C. Baccigalupi, S. Basak, A. Bonaldi, G. De Zotti, J. Delabrouille, C. Dickinson, H. K. Eriksen, J. Errard, R. Fernandez-Cobos, U. Fuskeland, C. Hervías-Caimapo, M. López-Caniego, E. Martinez-González, M. Roman, P. Vielva, I. Wehus, A. Achucarro, P. Ade, R. Allison, M. Ashdown, M. Ballardini, R. Banerji, J. Bartlett, N. Bartolo, D. Baumann, M. Bersanelli, M. Bonato, J. Borrill, F. Bouchet, F. Boulanger, T. Brinckmann, M. Bucher, C. Burigana, A. Buzzelli, Z.-Y. Cai, M. Calvo, C.-S. Carvalho, G. Castellano, A. Challinor, J. Chluba, S. Clesse, I. Colantoni, A. Coppolecchia, M. Crook, G. D'Alessandro, P. de Bernardis, G. de Gasperis, J.-M. Diego, E. Di Valentino, S. Feeney, S. Ferraro, F. Finelli, F. Forastieri, S. Galli, R. Genova-Santos, M. Gerbino, J. González-Nuevo, S. Grandis, J. Greenslade, S. Hagstotz, S. Hanany, W. Handley, C. Hernandez-Monteagudo, M. Hills, E. Hivon, K. Kiiveri, T. Kisner, T. Kitching, M. Kunz, H. Kurki-Suonio, L. Lamagna, A. Lasenby, M. Lattanzi, J. Lesgourgues, A. Lewis, M. Liguori, V. Lindholm, G. Luzzi, B. Maffei, C. J. A. P. Martins, S. Masi, S. Matarrese, D. McCarthy, J.-B. Melin, A. Melchiorri, D. Molinari, A. Monfardini, P. Natoli, M. Negrello, A. Notari, A. Paiella, D. Paoletti, G. Patanchon, M. Piat, G. Pisano, L. Polastri, G. Polenta, A. Pollo, V. Poulin, M. Quartin, J.-A. Rubino-Martin, L. Salvati, A. Tartari, M. Tomasi, D. Tramonte, N. Trappe, T. Trombetti, C. Tucker, J. Valiviita, R. Van de Weijgaert, B. van Tent, V. Vennin, N. Vittorio, K. Young, and M. Zannoni. Exploring cosmic origins with CORE: B-mode component separation. *J. Cosmology Astropart. Phys.*, 4:023, April 2018. doi: 10.1088/1475-7516/2018/04/023.

[257] M. Righi, C. Hernández-Monteagudo, and R. A. Sunyaev. Carbon monoxide line emission as a CMB foreground: tomography of the star-forming universe with different spectral resolutions. *A&A*, 489:489–504, October 2008. doi: 10.1051/0004-6361:200810199.

[258] J. A. Rubiño-Martin, R. Rebolo, P. Carreira, K. Cleary, R. D. Davies, R. J. Davis, C. Dickinson, K. Grainge, C. M. Gutiérrez, M. P. Hobson, M. E. Jones,

R. Kneissl, A. Lasenby, and K. Maisinger. First results from the Very Small Array - IV. Cosmological parameter estimation. *MNRAS*, 341:1084–1092, June 2003. doi: 10.1046/j.1365-8711.2003.06494.x.

[259] J. A. Rubiño-Martín, C. Hernández-Monteagudo, and R. A. Sunyaev. The imprint of cosmological hydrogen recombination lines on the power spectrum of the CMB. *A&A*, 438:461–473, August 2005. doi: 10.1051/0004-6361:20052939.

[260] J. A. Rubiño-Martín, J. Chluba, and R. A. Sunyaev. Lines in the cosmic microwave background spectrum from the epoch of cosmological hydrogen recombination. *MNRAS*, 371:1939–1952, (RMCS06), October 2006. doi: 10.1111/j.1365-2966.2006.10839.x.

[261] R. K. Sachs and A. M. Wolfe. Perturbations of a Cosmological Model and Angular Variations of the Microwave Background. *ApJ*, 147:73, January 1967. doi: 10.1086/148982.

[262] S. Sarkar and A. M. Cooper. Cosmological and experimental constraints on the tau neutrino. *Physics Letters B*, 148:347–354, November 1984. doi: 10.1016/0370-2693(84)90101-1.

[263] M. Sathyanarayana Rao, R. Subrahmanyan, N. Udaya Shankar, and J. Chluba. On the Detection of Spectral Ripples from the Recombination Epoch. *ApJ*, 810:3, September 2015. doi: 10.1088/0004-637X/810/1/3.

[264] M. Sathyanarayana Rao, R. Subrahmanyan, N. Udaya Shankar, and J. Chluba. GMOSS: All-sky Model of Spectral Radio Brightness Based on Physical Components and Associated Radiative Processes. *AJ*, 153:26, January 2017. doi: 10.3847/1538-3881/153/1/26.

[265] S. Y. Sazonov and R. A. Sunyaev. Cosmic Microwave Background Radiation in the Direction of a Moving Cluster of Galaxies with Hot Gas: Relativistic Corrections. *ApJ*, 508:1–5, November 1998. doi: 10.1086/306406.

[266] D. Scott and G. F. Smoot. Cosmic Microwave Background Mini-review. *ArXiv e-prints*, May 2010.

[267] M. Seiffert, D. J. Fixsen, A. Kogut, S. M. Levin, M. Limon, P. M. Lubin, P. Mirel, J. Singal, T. Villela, E. Wollack, and C. A. Wuensche. Interpretation of the ARCADE 2 Absolute Sky Brightness Measurement. *ApJ*, 734:6, June 2011. doi: 10.1088/0004-637X/734/1/6.

[268] U. Seljak and M. Zaldarriaga. A Line-of-Sight Integration Approach to Cosmic Microwave Background Anisotropies. *ApJ*, 469:437, October 1996. doi: 10.1086/177793.

[269] U. Seljak and M. Zaldarriaga. Signature of Gravity Waves in the Polarization of the Microwave Background. *Physical Review Letters*, 78:2054–2057, March 1997. doi: 10.1103/PhysRevLett.78.2054.

[270] P. Serra, O. Doré, and G. Lagache. Dissecting the High-z Interstellar Medium through Intensity Mapping Cross-correlations. *ApJ*, 833:153, December 2016. doi: 10.3847/1538-4357/833/2/153.

[271] S. Sharpless. A Catalogue of H II Regions. *ApJS*, 4:257, December 1959. doi: 10.1086/190049.

[272] M. Shimon, B. Keating, N. Ponthieu, and E. Hivon. CMB polarization systematics due to beam asymmetry: Impact on inflationary science. *Phys. Rev. D*, 77(8):083003, April 2008. doi: 10.1103/PhysRevD.77.083003.

[273] J. Silk. Cosmic Black-Body Radiation and Galaxy Formation. *ApJ*, 151:459, February 1968. doi: 10.1086/149449.

[274] J. Silk and J. Chluba. Next Steps for Cosmology. *Science*, 344:586–588, May 2014. doi: 10.1126/science.1252724.

[275] K. Silsbee, Y. Ali-Haïmoud, and C. M. Hirata. Spinning dust emission: the effect of rotation around a non-principal axis. *MNRAS*, 411:2750–2769, March 2011. doi: 10.1111/j.1365-2966.2010.17882.x.

[276] S. M. Simon, J. A. Beall, N. F. Cothard, S. M. Duff, P. A. Gallardo, S. P. Ho, J. Hubmayr, B. J. Koopman, J. J. McMahon, F. Nati, M. D. Niemack, S. T. Staggs, E. M. Vavagiakis, and E. J. Wollack. The Advanced ACTPol 27/39 GHz Array. *Journal of Low Temperature Physics*, May 2018. doi: 10.1007/s10909-018-1963-7.

[277] A. Soliman, P. A. R. Ade, Z. Ahmed, R. W. Aikin, K. D. Alexander, D. Barkats, S. J. Benton, C. A. Bischoff, J. J. Bock, R. Bowens-Rubin, J. A. Brevik, I. Buder, E. Bullock, V. Buza, J. Connors, J. Cornelison, B. P. Crill, M. Crumrine, M. Dierickx, L. Duband, C. Dvorkin, J. P. Filippini, S. Fliescher, J. Grayson, G. Hall, M. Halpern, S. Harrison, S. R. Hildebrandt, G. C. Hilton, H. Hui, K. D. Irwin, J. Kang, K. S. Karkare, E. Karpel, J. P. Kaufman, B. G. Keating, S. Kefeli, S. A. Kernasovskiy, J. M. Kovac, C. L. Kuo, K. Lau, N. A. Larsen, E. M. Leitch, M. Lueker, K. G. Megerian, L. Moncelsi, T. Namikawa, C. B. Netterfield, H. T. Nguyen, R. OBrient, R. W. Ogburn, IV, S. Palladino, C. Pryke, B. Racine, S. Richter, R. Schwarz, A. Schillaci, C. D. Sheehy, T. St. Germaine, Z. K. Staniszewski, B. Steinbach, R. V. Sudiwala, G. P. Teply, K. L. Thompson, J. E. Tolan, C. Tucker, A. D. Turner, C. Umilta, A. G. Vieregg, A. Wandui, A. C. Weber, D. V. Wiebe, J. Willmert, C. L. Wong, W. L. K. Wu, E. Yang, K. W. Yoon, and C. Zhang. Design and performance of wide-band corrugated walls for the BICEP Array detector modules at 30/40 GHz. *ArXiv e-prints*, August 2018.

[278] S. Staggs, J. Dunkley, and L. Page. Recent discoveries from the cosmic microwave background: a review of recent progress. *Reports on Progress in Physics*, 81(4):044901, April 2018. doi: 10.1088/1361-6633/aa94d5.

[279] A. A. Starobinsky. A new type of isotropic cosmological models without singularity. *Physics Letters B*, 91:99–102, March 1980. doi: 10.1016/0370-2693(80)90670-X.

[280] G. Steigman. Tracking the Post-Bbn Evolution of Deuterium. In M. E. van Steenberg, G. Sonneborn, H. W. Moos, and W. P. Blair, editors, *American Institute of Physics Conference Series*, volume 1135 of *American Institute of Physics Conference Series*, pages 94–101, May 2009. doi: 10.1063/1.3154093.

[281] R. Stompor, J. Errard, and D. Poletti. Forecasting performance of CMB experiments in the presence of complex foreground contaminations. *Phys. Rev. D*, 94(8):083526, October 2016. doi: 10.1103/PhysRevD.94.083526.

[282] R. A. Sunyaev and J. Chluba. Signals from the epoch of cosmological recombination (Karl Schwarzschild Award Lecture 2008). *Astronomische Nachrichten*, 330:657–+, 2009. doi: 10.1002/asna.200911237.

[283] R. A. Sunyaev and R. Khatri. Unavoidable CMB Spectral Features and Blackbody Photosphere of Our Universe. *International Journal of Modern Physics D*, 22:1330014, June 2013. doi: 10.1142/S0218271813300140.

[284] R. A. Sunyaev and Y. B. Zeldovich. The Spectrum of Primordial Radiation, its Distortions and their Significance. *Comments on Astrophysics and Space Physics*, 2:66, March 1970.

[285] R. A. Sunyaev and Y. B. Zeldovich. Small scale entropy and adiabatic density perturbations — Antimatter in the Universe. *Ap&SS*, 9:368–382, December 1970. doi: 10.1007/BF00649577.

[286] R. A. Sunyaev and Y. B. Zeldovich. The interaction of matter and radiation in the hot model of the Universe, II. *Ap&SS*, 7:20–30, April 1970. doi: 10.1007/BF00653472.

[287] R. A. Sunyaev and Y. B. Zeldovich. Small-Scale Fluctuations of Relic Radiation. *Ap&SS*, 7:3–19, April 1970. doi: 10.1007/BF00653471.

[288] R. A. Sunyaev and Y. B. Zeldovich. Formation of Clusters of Galaxies; Protocluster Fragmentation and Intergalactic Gas Heating. *A&A*, 20:189–+, August 1972.

[289] D. Sutton, B. R. Johnson, M. L. Brown, P. Cabella, P. G. Ferreira, and K. M. Smith. Map making in small field modulated CMB polarization experiments: approximating the maximum likelihood method. *MNRAS*, 393:894–910, March 2009. doi: 10.1111/j.1365-2966.2008.14195.x.

[290] D. Sutton, J. A. Zuntz, P. G. Ferreira, M. L. Brown, H. K. Eriksen, B. R. Johnson, A. Kusaka, S. K. Næss, and I. K. Wehus. Fast and precise map-making for massively multi-detector CMB experiments. *MNRAS*, 407:1387–1402, September 2010. doi: 10.1111/j.1365-2966.2010.16954.x.

[291] E. R. Switzer. Tracing the cosmological evolution of stars and cold gas with CMB spectral surveys. *ArXiv:1703.07832*, March 2017.

[292] H. Tashiro. CMB spectral distortions and energy release in the early universe. *Prog. of Theo. and Exp. Physics*, 2014(6):06B107, June 2014. doi: 10.1093/ptep/ptu066.

[293] H. Tashiro, E. Sabancilar, and T. Vachaspati. CMB distortions from superconducting cosmic strings. *Phys. Rev. D*, 85(10):103522, May 2012. doi: 10.1103/PhysRevD.85.103522.

[294] H. Tashiro, E. Sabancilar, and T. Vachaspati. CMB distortions from damping of acoustic waves produced by cosmic strings. *J. Cosmology Astropart. Phys.*, 8:035, August 2013. doi: 10.1088/1475-7516/2013/08/035.

[295] A. R. Taylor, S. J. Gibson, M. Peracaula, P. G. Martin, T. L. Landecker, C. M. Brunt, P. E. Dewdney, S. M. Dougherty, A. D. Gray, L. A. Higgs, C. R. Kerton, L. B. G. Knee, R. Kothes, C. R. Purton, B. Uyaniker, B. J. Wallace, A. G. Willis, and D. Durand. The Canadian Galactic Plane Survey. *AJ*, 125:3145–3164, June 2003. doi: 10.1086/375301.

[296] M. Tegmark. CMB mapping experiments: A designer's guide. *Phys. Rev. D*, 56: 4514–4529, October 1997. doi: 10.1103/PhysRevD.56.4514.

[297] The COrE Collaboration, C. Armitage-Caplan, M. Avillez, D. Barbosa, A. Banday, N. Bartolo, R. Battye, J. Bernard, P. de Bernardis, S. Basak, M. Bersanelli, P. Bielewicz, A. Bonaldi, M. Bucher, F. Bouchet, F. Boulanger, C. Burigana, P. Camus, A. Challinor, S. Chongchitnan, D. Clements, S. Colafrancesco, J. Delabrouille, M. De Petris, G. De Zotti, C. Dickinson, J. Dunkley, T. Ensslin, J. Fergusson, P. Ferreira, K. Ferriere, F. Finelli, S. Galli, J. Garcia-Bellido, C. Gauthier, M. Haverkorn, M. Hindmarsh, A. Jaffe, M. Kunz, J. Lesgourgues, A. Liddle, M. Liguori, M. Lopez-Caniego, B. Maffei, P. Marchegiani, E. Martinez-Gonzalez, S. Masi, P. Mauskopf, S. Matarrese, A. Melchiorri, P. Mukherjee, F. Nati, P. Natoli, M. Negrello, L. Pagano, D. Paoletti, T. Peacocke, H. Peiris, L. Perroto, F. Piacentini, M. Piat, L. Piccirillo, G. Pisano, N. Ponthieu, C. Rath, S. Ricciardi, J. Rubino Martin, M. Salatino, P. Shellard, R. Stompor, L. T. J. Urrestilla, B. Van Tent, L. Verde, B. Wandelt, and S. Withington. COrE (Cosmic Origins Explorer) A White Paper. *ArXiv:1102.2181*, February 2011.

[298] The EBEX Collaboration, A. Aboobaker, P. Ade, D. Araujo, F. Aubin, C. Baccigalupi, C. Bao, D. Chapman, J. Didier, M. Dobbs, W. Grainger, S. Hanany, K. Helson, S. Hillbrand, J. Hubmayr, A. Jaffe, B. Johnson, T. Jones, J. Klein, A. Korotkov, A. Lee, L. Levinson, M. Limon, K. MacDermid, A. D. Miller, M. Milligan, L. Moncelsi, E. Pascale, K. Raach, B. Reichborn-Kjennerud, I. Sagiv, C. Tucker, G. S. Tucker, B. Westbrook, K. Young, and K. Zilic. The EBEX Balloon-Borne Experiment - Gondola, Attitude Control, and Control Software. *ArXiv e-prints*, February 2017.

[299] The EBEX Collaboration, A. M. Aboobaker, P. Ade, D. Araujo, F. Aubin, C. Baccigalupi, C. Bao, D. Chapman, J. Didier, M. Dobbs, C. Geach, W. Grainger, S. Hanany, K. Helson, S. Hillbrand, J. Hubmayr, A. Jaffe, B. Johnson, T. Jones, J. Klein, A. Korotkov, A. Lee, L. Levinson, M. Limon, K. MacDermid, T. Matsumura, A. D. Miller, M. Milligan, K. Raach, B. Reichborn-Kjennerud, I. Sagiv, G. Savini, L. Spencer, C. Tucker, G. S. Tucker, B. Westbrook, K. Young, and K. Zilic. The EBEX Balloon Borne Experiment - Optics, Receiver, and Polarimetry. *ArXiv e-prints*, March 2017.

[300] The EBEX Collaboration, M. Abitbol, A. M. Aboobaker, P. Ade, D. Araujo, F. Aubin, C. Baccigalupi, C. Bao, D. Chapman, J. Didier, M. Dobbs, S. M. Feeney, C. Geach, W. Grainger, S. Hanany, K. Helson, S. Hillbrand, G. Hilton, J. Hubmayr, K. Irwin, A. Jaffe, B. Johnson, T. Jones, J. Klein, A. Korotkov, A. Lee, L. Levinson, M. Limon, K. MacDermid, A. D. Miller, M. Milligan, K. Raach, B. Reichborn-Kjennerud, C. Reintsema, I. Sagiv, G. Smecher, G. S. Tucker, B. Westbrook, K. Young, and K. Zilic. The EBEX Balloon Borne Experiment - Detectors and Readout. *ArXiv e-prints*, March 2018.

[301] The Polarbear Collaboration: P. A. R. Ade, Y. Akiba, A. E. Anthony, K. Arnold, M. Atlas, D. Barron, D. Boettger, J. Borrill, S. Chapman, Y. Chinone, M. Dobbs, T. Elleflot, J. Errard, G. Fabbian, C. Feng, D. Flanigan, A. Gilbert, W. Grainger, N. W. Halverson, M. Hasegawa, K. Hattori, M. Hazumi, W. L. Holzapfel, Y. Hori, J. Howard, P. Hyland, Y. Inoue, G. C. Jaehnig, A. H. Jaffe, B. Keating, Z. Kermish, R. Keskitalo, T. Kisner, M. Le Jeune, A. T. Lee, E. M. Leitch, E. Linder, M. Lungu, F. Matsuda, T. Matsumura, X. Meng, N. J. Miller, H. Morii, S. Moyerman, M. J. Myers, M. Navaroli, H. Nishino, A. Orlando, H. Paar, J. Peloton, D. Poletti, E. Quealy, G. Rebeiz, C. L. Reichardt, P. L. Richards, C. Ross, I. Schanning, D. E. Schenck, B. D. Sherwin, A. Shimizu, C. Shimmin, M. Shimon, P. Siritanasak, G. Smecher, H. Spieler, N. Stebor, B. Steinbach, R. Stompor, A. Suzuki, S. Takakura, T. Tomaru, B. Wilson, A. Yadav, and O. Zahn. A Measurement of the Cosmic Microwave Background B-mode Polarization Power Spectrum at Sub-degree Scales with POLARBEAR. *ApJ*, 794:171, October 2014. doi: 10.1088/0004-637X/794/2/171.

[302] B. Thorne, J. Dunkley, D. Alonso, and S. Næss. The Python Sky Model: software for simulating the Galactic microwave sky. *MNRAS*, 469:2821–2833, August 2017. doi: 10.1093/mnras/stx949.

[303] A. K. Tung, R. Kothes, T. L. Landecker, J. Geisbüsch, D. Del Rizzo, A. R. Taylor, C. M. Brunt, A. D. Gray, and S. M. Dougherty. A High Resolution Survey of the Galactic Plane at 408 MHz. *AJ*, 154:156, October 2017. doi: 10.3847/1538-3881/aa866d.

[304] J. van Rantwijk, M. Grim, D. van Loon, S. Yates, A. Baryshev, and J. Baselmans. Multiplexed readout for 1000-pixel arrays of microwave kinetic inductance detectors. *IEEE Transactions on Microwave Theory and Techniques*, 64(6):1876–1883, June 2016. ISSN 0018-9480. doi: 10.1109/TMTT.2016.2544303.

[305] S. Weinberg. *Cosmology*. Oxford University Press, 2008.

[306] J. C. Weingartner and B. T. Draine. Dust Grain-Size Distributions and Extinction in the Milky Way, Large Magellanic Cloud, and Small Magellanic Cloud. *ApJ*, 548: 296–309, February 2001. doi: 10.1086/318651.

[307] A. P. S. Yadav, M. Su, and M. Zaldarriaga. Primordial B-mode diagnostics and self-calibrating the CMB polarization. *Phys. Rev. D*, 81(6):063512, March 2010. doi: 10.1103/PhysRevD.81.063512.

[308] S. J. C. Yates, A. M. Baryshev, J. J. A. Baselmans, B. Klein, and R. Güsten. Fast Fourier transform spectrometer readout for large arrays of microwave kinetic inductance detectors. *Applied Physics Letters*, 95(4):042504, July 2009. doi: 10.1063/1.3159818.

[309] S. J. C. Yates, J. J. A. Baselmans, A. Endo, R. M. J. Janssen, L. Ferrari, P. Diener, and A. M. Baryshev. Photon noise limited radiation detection with lens-antenna coupled microwave kinetic inductance detectors. *Applied Physics Letters*, 99(7):073505, August 2011. doi: 10.1063/1.3624846.

[310] D. Yvon and F. Mayet. Mirage: A new iterative map-making code for CMB experiments. *A&A*, 436:729–739, June 2005. doi: 10.1051/0004-6361:20035920.

[311] M. Zaldarriaga. The Polarization of the Cosmic Microwave Background. *Measuring and Modeling the Universe*, page 309, 2004.

[312] M. Zaldarriaga and U. Seljak. All-sky analysis of polarization in the microwave background. *Phys. Rev. D.*, 55:1830–1840, February 1997. doi: 10.1103/PhysRevD.55.1830.

[313] M. Zaldarriaga and U. Seljak. CMBFAST for Spatially Closed Universes. *ApJS*, 129:431–434, August 2000. doi: 10.1086/313423.

[314] Y. B. Zeldovich and R. A. Sunyaev. The Interaction of Matter and Radiation in a Hot-Model Universe. *Ap&SS*, 4:301–316, July 1969. doi: 10.1007/BF00661821.

[315] Y. B. Zeldovich, V. G. Kurt, and R. A. Syunyaev. Recombination of Hydrogen in the Hot Model of the Universe. *Zhurnal Eksperimental noi i Teoreticheskoi Fiziki*, 55:278–286, July 1968.

[316] Y. B. Zeldovich, A. F. Illarionov, and R. A. Sunyaev. The Effect of Energy Release on the Emission Spectrum in a Hot Universe. *SJETP*, 35:643, 1972.

[317] H. Zheng, M. Tegmark, J. S. Dillon, D. A. Kim, A. Liu, A. R. Neben, J. Jonas, P. Reich, and W. Reich. An improved model of diffuse galactic radio emission from 10 MHz to 5 THz. *MNRAS*, 464:3486–3497, January 2017. doi: 10.1093/mnras/stw2525.